Influence of spin-orbit coupling on solid-state NMR parameters



Ava Dean

Brasenose College

University of Oxford

A thesis submitted for the degree of

Doctor of Philosophy

Hilary 2023

Acknowledgements

My time at Oxford has been amazing for so many reasons, and the support from the people around me has helped through many difficult but exciting years.

I want to thank my supervisor, Jonathan, for the support and guidance in what has been a very challenging but rewarding project.

My friends Mike, Tristan, Lillian and Francesca have all been so wonderful. Our pub quizzes, F1, croquet and punting activities have been so much fun and I hope there are more to come.

Also, Matt, Dilhan, Alex, Tom and the rest of the TMCS cohort have made my time here so fantastic, and we have so many good memories. As well, Ian, Matthew, and the rest of the Chemistry department as a whole.

I also want to thank my officemates Sabrina, Ted, Ewan, as well as Namu, Jack, Rebecca and the rest of the MML group. Tuesday morning coffees - most excitingly our Biscuit World Cup - made my time in the Materials department so much fun.

And finally, I want to thank my amazing mum, dad, brother and best friend Catty, as well as the rest of the family, for all of their love and support.

Abstract

Nuclear magnetic resonance is a widely utilised spectroscopic technique for the structural determination of molecules and solids. The development of density functional theory methods have allowed for the computation of many nuclear magnetic resonance parameters, supporting experimental studies. Heavy atoms introduce additional difficulties, that currently, are typically ignored. They require a fully relativistic treatment to include the effects of spin-orbit coupling, which ultimately dictates the magnetic response of nearby light nuclei.

In this thesis, we develop the theory to accommodate the prediction of nuclear magnetic resonance properties in the solid-state, with the inclusion of spin-orbit coupling. We develop the planewave pseudopotential method, in its application to density functional theory, to account for relativistic effects. This involves the extension of the projector augmented-wave method for two-component spinor wavefunctions, and its gauge-including counterpart. This allows for the investigation of the electric field gradient and magnetic shielding parameters of inorganic compounds and molecular crystals.

Contents

Acronyms and abbreviations **xi**

List of Figures **xv**

List of Tables **xvii**

1 Introduction **1**

2 Nuclear magnetic resonance **5**
2.1 Background 5
2.2 Chemical shifts 11
2.3 Electric field gradients 12
2.4 Other NMR parameters 13
2.5 Solid-state NMR 14
2.6 Calculations 19

3 First principles methodologies **23**
3.1 Non-relativistic quantum mechanics 24
3.1.1 Schrödinger equation 24
3.1.2 Born-Oppenheimer approximation 25
3.1.3 The variational principle 26
3.2 Mean-field techniques 26
3.2.1 Hartree-Fock 26
3.2.2 Electron correlation 27
3.2.3 Post Hartree-Fock techniques 28
3.3 Density functional theory 29
3.3.1 The Hohenberg-Kohn theorems 29
3.3.2 The Kohn-Sham equations 32
3.3.3 Exchange-correlation functionals 33
3.4 Implementation methodology 35
3.4.1 The reciprocal lattice 35
3.4.2 The Brillouin zone 36
3.4.3 Bloch's theorem 36

3.4.4 Planewaves . . . 38
3.4.5 Frozen core approximation . . . 40
3.4.6 Pseudopotentials . . . 40
3.4.7 Projector augmented-wave method . . . 46
3.5 Relativistic quantum mechanics . . . 48
3.5.1 Dirac equation . . . 49
3.5.2 Introducing an electromagnetic field . . . 50
3.5.3 Relativistic corrections . . . 51
3.5.4 Elimination of the small component . . . 53
3.5.5 Zeroth-order regular approximation . . . 55
3.5.6 Scalar-relativistic approaches . . . 56
3.5.7 Relativistic pseudopotentials . . . 56
3.5.8 Projector augmented-wave method with spinors . . . 59

4 Implementation 65
4.1 Finding the ground state . . . 65
4.2 Non-collinear magnetism considerations . . . 66
4.2.1 Exchange-correlation functional . . . 66
4.2.2 Self-consistent field cycle . . . 68
4.3 Spin-orbit splitting . . . 68
4.3.1 Atomic: lead, Pb . . . 68
4.3.2 Bandstructure: lead, Pb . . . 72
4.3.3 Bandstructure: bismuth telluride, Bi_2Te_3 . . . 72
4.4 Applied magnetic field . . . 76
4.4.1 Expression . . . 76
4.4.2 Implementation . . . 77
4.5 The implementation of the f-matrices . . . 78
4.6 Memory and calculation time considerations . . . 80
4.7 Symmetry breaking . . . 82
4.8 Towards nuclear magnetic resonance calculations . . . 83

5 Electric field gradients 85
5.1 Electric field gradient expression . . . 85
5.2 Implementation . . . 88
5.2.1 Testing spinor wavefunctions . . . 88
5.2.2 Testing norm-conserving pseudopotentials . . . 88
5.2.3 Calculations with relativistic pseudopotentials . . . 92
5.3 Results . . . 92
5.3.1 Convergence testing . . . 95
5.3.2 ^{133}Cs . . . 96
5.3.3 ^{209}Bi . . . 96

6 Magnetic shielding **105**
6.1 Induced and applied magnetic fields . . . 105
6.2 Gauge-including projector augmented-wave method . . . 107
6.3 Core shielding . . . 108
6.3.1 Expression . . . 108
6.3.2 Implementation . . . 109
6.4 Orbital shielding . . . 110
6.4.1 Expression . . . 110
6.4.2 Implementation . . . 121
6.5 Spin term . . . 124
6.5.1 Expression . . . 125
6.5.2 Implementation . . . 128
6.6 Results . . . 136
6.6.1 Hydrogen halide molecules . . . 136
6.6.2 L-Cysteine . . . 140
6.6.3 4-dimethylaminopyridinium halides . . . 148

7 Conclusions and future work **159**

Appendices

A Notation **165**
A.1 Spinors . . . 165
A.2 Pauli vector matrix elements, $\boldsymbol{\sigma}^{\sigma,\sigma'}$ . . . 167

B The rotation matrix, $\mathbf{U}^{\ell}$ **169**
B.1 Spherical coordinate system . . . 169
B.2 Complex spherical harmonics . . . 170
B.3 CASTEP choice of real spherical harmonics . . . 171
B.4 Common choice of real spherical harmonics . . . 173

C The $\mathbf{C}_{\alpha\beta}$ vector **175**
C.1 Definition . . . 175
C.2 Spherical operator form . . . 176

D Electric field gradient data **179**

References **189**

Acronyms and abbreviations

an	anhydrous
aniso	anisotropic
aug	augmentation
calc	calculated
class	classical
cut	cut-off
d	diamagnetic
ee	electron-electron
eff	effective
elec	electronic
eqn	equation
exp	experimental
hy	hydrated
in	induced
ion	ionic
iso	isotropic
-ive	negative
+ive	positive
kin	kinetic
loc	local
Ne	nuclear-electron
non-cl	non-classical
non-int	non-interacting
non-loc	non-local
opt	optimised
orb	orbital
p	paramagnetic
ref	reference
rel	relativity
tr	trial

AIRSS	ab initio random structure searching
BZ	Brillouin zone
C	correlation
CBM	conduction band minimum
CC	coupled cluster

CI	configuration interaction
CP	cross polarisation
CRAMPS	combined rotation and multiple pulse spectroscopy
CT	central transition
DAS	dynamic angle spinning
DFT	density functional theory
DMAP	dimethylaminopyridinium
DOR	double rotation
DUMBO	decoupling using mind-boggling optimisation
EFG	electric field gradient
EM	electromagnetic
ESC	elimination of the small component
FC	Fermi-contact
FFT	fast-Fourier transform
FLAPW	full-potential linearised augmented-plane-wave
FR	fully-relativistic
GEA	gradient expansion approximation
GGA	generalised gradient approximation
GIAO	gauge-including atomic orbital
GIPAW	gauge-including projector augmented-wave
HAHA	heavy-atom heavy-atom
HALA	heavy-atom light-atom
HF	Hartree-Fock
HK	Hohenberg-Kohn
IGLO	indiviual gauges for localised orbital
KS	Kohn-Sham
LAPW	linearised augmented-plane-wave
LDA	local-density approximation
LSDA	local-spin-density approximation
MAS	magic-angle spinning
MP	Møller-Plesset / Monkhorst-Pack
MQMAS	multiple-quantum magic-angle spinning
NCM	non-collinear magnetism
NCP	norm-conserving pseudopotential
NMR	nuclear magnetic resonance
NR	non-relativistic
PAW	projector augmented-wave
PBE	Perdew-Burke-Ernzerhof
PMLG	phase-modulated Lee-Goldburg
PP	pseudopotential
ppm	parts per million
PT	perturbation theory
PW	Perdew-Wang
RKE	relativistic kinetic energy

RMS	root-mean-square
rSCAN	regularised strongly-constrained and appropriately-normed
SCAN	strongly-constrained and appropriately-normed
SCF	self-consistent field
SD	spin-dipolar / Slater determinant
SOC	spin-orbit coupling
SR	scalar-relativistic
ST	satellite transition
STMAS	satellite transition magic-angle spinning
sX-LDA	screen exchanged local-density approximation
TPSS	Tao–Perdew–Staroverov–Scuseria
USP	ultra-soft pseudopotential
VBM	valence band maximum
X	exchange
XC	exchange-correlation
Z-FC	ZORA Fermi-contact
ZORA	zeroth-order regular approximation

List of Figures

2.1 Larmor precession 7
2.2 Splitting of nuclear spin state due to external magnetic field 9
2.3 Schematic diagram of chemical shift anisotropy 15
2.4 Schematic diagram of magic-angle spinning 17

3.1 Two-dimensional reciprocal space lattice 37
3.2 Pseudopotential for lead, Pb 42
3.3 Atomic all-electron and pseudo-wavefunctions with corresponding projector for lead, Pb 43
3.4 ZORA $K(r)$ for lead, Pb 57

4.1 Energy levels comparison between scalar and fully-relativistic atomic lead, Pb 69
4.2 j-splitting of eigenstates for lead, Pb 71
4.3 Bandstructures of lead, Pb 73
4.4 Bandstructures of bismuth telluride, Bi_2Te_3 74
4.5 Magnetisation of cell with respect to applied magnetic field 79
4.6 Comparison between scalar and spinor calculation times with respect to E_{cut} 81

5.1 EFG implementation validation 89
5.2 Comparison of norm-conserving and ultra-soft pseudopotentials for C_Q values against experiment 91
5.3 Comparison of C_Q values between fully-relativistic calculations and experiment 93
5.4 Comparison of the treatment of relativity in C_Q values against experiment 94
5.5 C_Q values calculated using the experimental geometry against experiment for ^{209}Bi compounds 98
5.6 C_Q values of optimised against experimental geometries for ^{209}Bi compounds 99
5.7 C_Q values using PBE against LDA functionals for ^{209}Bi compounds 100
5.8 $\mathcal{G}_{zz}$ against experimental C_Q values for ^{209}Bi compounds 103

6.1 Core shielding difference between fully and scalar-relativistic calculations . . . 111
6.2 Orbital shielding implementation validation . . . 122
6.3 Effects of relativity on each of the chemical shielding core and orbital terms . . . 123
6.4 Analogy of spin-orbit coupling effect on chemical shielding with J-coupling . . . 129
6.5 Non-relativistic and fully-relativistic 1s atomic wavefunctions for hydrogen, H . . . 131
6.6 Relative difference between fully-relativistic and non-relativistic atomic wavefunctions . . . 132
6.7 Convergence of the isotropic orbital and spin chemical shielding values with respect to E_{cut} . . . 135
6.8 Comparison of relativistic treatments on the ^{1}H chemical shielding value in the hydrogen halide molecules . . . 138
6.9 Spin density in the hydrogen iodide molecule . . . 141
6.10 Molecular structure of L-cysteine . . . 142
6.11 Structure of L-cysteine at low temperature with S-H$\cdots$S hydrogen bonding . . . 143
6.12 Structure of L-cysteine at high temperature with S-H$\cdots$O hydrogen bonding . . . 144
6.13 Correlation between calculated ^{1}H chemical shielding values against experimental shifts for L-cysteine . . . 146
6.14 Distances of hydrogen atoms to sulphur in the molecular crystal L-cysteine . . . 149
6.15 Spin density in the molecular crystal L-cysteine . . . 150
6.16 Molecular structures of the 4-dimethylaminopyridinium halides . . . 152
6.17 Structure of the molecular crystal 4-dimethylaminopyridinium iodide 153
6.18 Correlation between calculated ^{1}H chemical shielding values against experimental shifts for the 4-dimethylaminopyridinium halides . . . 155

D.1 Convergence of ^{133}Cs C_Q values with respect to E_{cut} . . . 184
D.2 Convergence of ^{209}Bi C_Q values with respect to E_{cut} . . . 185
D.3 Convergence of ^{133}Cs C_Q values with respect to **k**-point grid spacing 186
D.4 Convergence of ^{209}Bi C_Q values with respect to **k**-point grid spacing 187

List of Tables

2.1 Spins of nuclear isotopes 6
2.2 Common chemical shift reference compounds 12

4.1 Energy levels with respect to relativistic treatment for atomic lead, Pb 70

5.1 C_Q values for ^{133}Cs in the $CsClO_4$, Cs_2SO_4 and Cs_2CO_3 systems . . 97
5.2 η values for ^{133}Cs in the $CsClO_4$, Cs_2SO_4 and Cs_2CO_3 systems . . . 97
5.3 EFG parameters for ^{209}Bi in the BiOCl, BiOBr and BiOI systems . 102
5.4 EFG parameters for ^{209}Bi in the $BiAlTeO_6$ and $BiGaTeO_6$ systems . 103

6.1 Calculated core electrons through the core density 110
6.2 ^{1}H chemical shielding values for the hydrogen halides from fully-relativistic calculations 139
6.3 Contribution of heavy atom core states to ^{1}H chemical shielding values for fully-relativistic calculations 139
6.4 ^{1}H chemical shielding values for the L-cysteine crystal from fully-relativistic calculations 147
6.5 ^{1}H chemical shielding values for the 4-dimethylaminopyridinium halides from fully-relativistic calculations 156

D.1 Comparison of pseudopotentials for C_Q values of halides against experiment 180
D.2 Comparison of pseudopotentials for C_Q values of metals against experiment 181
D.3 Comparison of relativistic treatments for C_Q values of halides against experiment 182
D.4 Comparison of relativistic treatments for C_Q values of metals against experiment 183

1 Introduction

Nuclear magnetic resonance (NMR) allows the imaging of molecules and solids by probing their magnetic properties.[1–3] Its uses stem from medical imaging to the study of organic molecules and crystalline materials. Its high sensitivity to the local environment of the atoms allows for accurate insight into the structure of the subject compound. Despite this advantage, interpretation of spectra can be challenging, particularly for the solid-state where anisotropic interactions are present. Computational calculations are therefore becoming more widely used to validate experimental studies by providing a pathway between measurement and assignment. Density functional theory (DFT)[4, 5] enables the equations of quantum mechanics to be solved for real-world systems, and the gauge-including projector augmented-wave (GIPAW)[6] method has allowed for the calculation of solid-state NMR results.

These methods have been implemented into the CASTEP electronic structure code,[7, 8] which is widely used and freely available to researchers at academic and government institutions worldwide. All work and implementations discussed in this thesis are based on the CASTEP package.

The combination of NMR experiments and GIPAW calculations have particular uses for molecular crystals in the pharmaceutical industry. Small molecules do not necessarily form crystallites that can be probed by diffraction-based studies. Also, multiple conformers of crystals may also exist, which upon dissolution, lose their

crystal interactions and are not distinguishable in the liquid-state. In solid-state NMR, the range of active nuclei is huge in comparison to typical organic studies, and as a result, the complexity of obtained spectra is high and less commonly studied. The use of GIPAW calculations can improve confidence in the characterisation of these structures by the researcher.

Despite the success of the GIPAW theory, there exists a problem: heavy elements. These can greatly perturb the chemical shift values of nearby light atoms, causing calculation errors of up to 5-10 ppm for ^{1}H nuclei, which is a huge proportion of its active NMR range. Many pharmaceutical compounds contain heavy atoms and their effects are currently ignored in calculations.

The reason for these errors is due to neglecting relativistic effects. The solutions of the non-relativistic (NR) Schrödinger equation become inaccurate for electrons that travel at a considerable fraction of the speed of light, which is the case in heavy atoms. Corrections for this have been offered by scalar-relativistic (SR) equations, which account for some proportion of relativistic effects, but critically ignore spin-orbit coupling (SOC). This interaction causes polarisation of spin density at the heavy atom, affecting the induced magnetic field for its neighbours and ultimately their reported chemical shift. A fully-relativistic (FR) approach is needed: the Dirac equation.

In this work, we develop the theoretical and computational framework to include the effects of relativity in the GIPAW approach to solid-state NMR parameters. The extension of the wavefunction into a spinor basis, and consideration of the vector spin density was required to capture the effects of SOC on the chemical shielding values of nuclei.

In chapter 2, we discuss the background of NMR and the parameters that quantify experimental spectra, with emphasis on the solid-state. We also review the field of computational NMR calculations, and outline the current implementations that are available for the inclusion of SOC, which at present are restricted to molecular studies only.

In chapter 3, we outline the first principle methodologies that allow for the determination of the electronic structure of molecules and solids. We highlight the extension of the currently implemented methods to their relativistic models, and discuss the schemes that provide pathways to obtaining NMR results from calculations.

In chapter 4, we outline some considerations needed for the implementation of the theories discussed in previous chapters. We demonstrate what calculations can currently be performed, and observe some of the effects of SOC in applications to the electronic structure of molecules and solids.

In chapter 5, we apply the generalised theory of the projector augmented-wave (PAW) approach to the electric field gradient (EFG) NMR parameter. We introduce updated equations for the FR approach and give discussion on how they were implemented in this work. Benchmark calculations are performed to assess the validity of the approach and describe some current limitations. Results on ^{133}Cs and ^{209}Bi compounds are obtained for the newly implemented FR calculations with discussion.

In chapter 6, we outline the generalisation of the aforementioned GIPAW theory to the magnetic shielding NMR parameter. We introduce updated equations required for the FR approach and give discussion on how they were implemented in this work. The hydrogen halide molecules, the L-cysteine molecular crystal and the 4-dimethylaminopyridinium halides are investigated and discussed.

In chapter 7, we summarise the work presented here and give insight into the potential future work in this field.

Throughout the equations in this text, we use Hartree atomic units,

$$\hbar = e = m_{\mathrm{e}} = 1, \qquad c = \frac{1}{\alpha}, \qquad \frac{\mu_0}{4\pi} = \alpha^2, \tag{1.1}$$

where $\hbar$ is the reduced Planck constant, e is the elementary charge, m_{e} is the electron rest mass, c is the speed of light, α is the fine-structure constant and μ_0 is the magnetic constant.

We use the error notation $x(y)$ where x is the value and y is the error as $\pm$ the number of digits in x from right to left. For example, 3(1) means the value

of 3 with the error range $2 - 4$. Also, 0.05(0.1) means the value of 0.05 with the error range $0.045 - 0.055$.

2

Nuclear magnetic resonance

Contents

2.1 Background **5**
2.2 Chemical shifts **11**
2.3 Electric field gradients **12**
2.4 Other NMR parameters **13**
2.5 Solid-state NMR **14**
2.6 Calculations **19**

2.1 Background

Nuclear magnetic resonance (NMR) spectroscopy is a technique used to probe the structure of molecules and solids through the magnetic properties of the nuclei in the system. The method can be described from a classical or quantum approach, both of which highlight key concepts. The central quantity is a form of intrinsic angular momentum of the nucleus, $\mathbf{I}$, called nuclear spin. Its quantum number is I, and nuclei with $I > 0$, possess a magnetic dipole moment, $\boldsymbol{\mu}$. See table 2.1 for a list of common nuclei and their spins. It is this moment that interacts with an applied magnetic field, $\mathbf{B}$.[1]

[1] It is important to note that the applied magnetic field and the field experienced by a nucleus are different. In essence, it is this difference that is at the heart of NMR spectroscopy.

Table 2.1: Examples of common nuclear isotopes and their spins.

Spin / a.u.	Example isotopes
$I = 0$	^{12}C, ^{16}O, ^{32}S
$I = \frac{1}{2}$	^{1}H, ^{3}H, ^{13}C, ^{15}N, ^{19}F, ^{31}P
$I = 1$	^{2}H, ^{14}N
$I > 1$	^{10}B, ^{11}B, ^{17}O, ^{23}Na, ^{27}Al, ^{35}Cl, ^{59}Co

Classical description

The magnetic moment precesses around the applied field, due to a torque, $\boldsymbol{\tau}$,

$$\boldsymbol{\tau} = \boldsymbol{\mu} \times \mathbf{B}. \tag{2.1}$$

The frequency of this precession - known as the Larmor frequency - is proportional to the field and a nucleus-specific constant, the gyromagnetic ratio, γ,

$$\nu = -\frac{\gamma}{2\pi}|\mathbf{B}|. \tag{2.2}$$

The most important property of the Larmor frequency is that it does not depend on the angle between the magnetic moment and the applied field, θ. We therefore do not need to know anything about the spatial orientation of the nuclear spins. The change in energy due to the applied field, ΔE, does however depend on the angle,

$$\Delta E = -\boldsymbol{\mu} \cdot \mathbf{B} = -|\boldsymbol{\mu}||\mathbf{B}| \cos\theta. \tag{2.3}$$

If a second magnetic field, $\mathbf{B}_\perp$, is then applied, $\boldsymbol{\mu}$ will experience a second torque and the angle θ changes slightly. If we choose $\mathbf{B}_\perp$ to rotate around $\mathbf{B}$ at a frequency ν, then an energy difference is obtained. If the frequency is not ν, then the applied field, $\mathbf{B}_\perp$, and Larmor precession will be in and out of phase, resulting in an overall energy difference of zero.

Larmor precession is diagrammed in figure 2.1.

Quantum description

Quantum mechanics tells us that the energy levels of a magnetic moment in an externally applied magnetic field are,

$$E_{m_I} = -\gamma\, m_I |\mathbf{B}|, \tag{2.4}$$

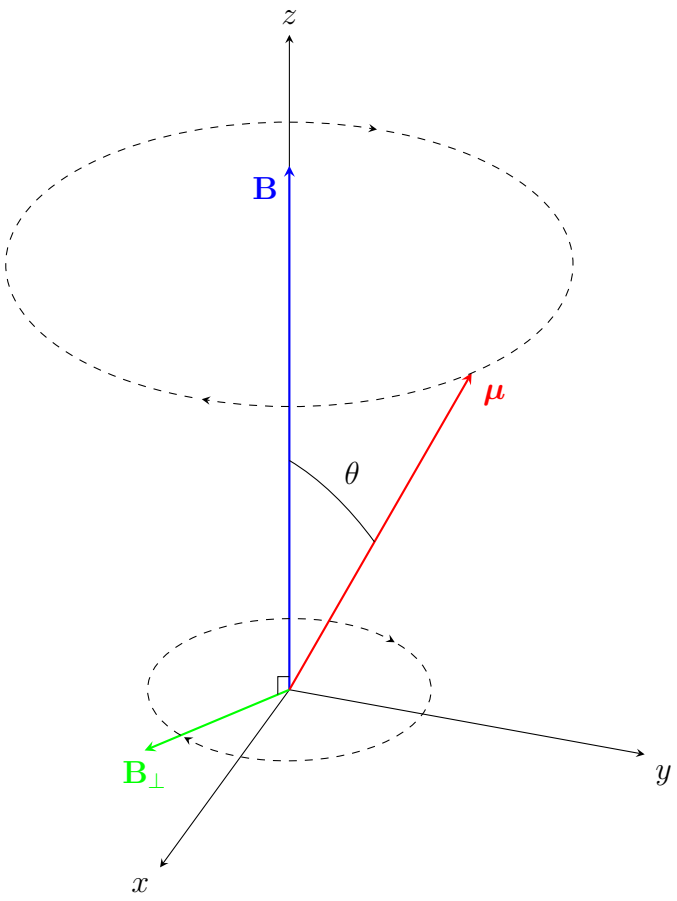


Figure 2.1: Classical representation of Larmor precession. A magnetic moment, $\boldsymbol{\mu}$, from a nucleus at the origin, precesses around the applied magnetic field, $\mathbf{B}$. The perpendicularly applied field, $\mathbf{B}_\perp$, is also indicated, along with its externally induced oscillatory motion.

where m_I is the quantum number that defines the nuclear spin momentum and takes values $-I, -I+1, \ldots, I-1, I$. There are thus $2I+1$ number of m_I values. These energy levels are diagrammed in figure 2.2.

As before, we may apply a second magnetic field, that is perpendicular to the first, which takes the oscillatory form,

$$\mathbf{B}_\perp(t) = B_\perp \begin{pmatrix} \cos \nu t \\ \sin \nu t \\ 0 \end{pmatrix}, \tag{2.5}$$

with magnitude, $B_\perp$. Assuming that $B_\perp$ is much smaller than $|\mathbf{B}|$, perturbation theory tells us that the probability of transmission between two energy levels, with quantum numbers m_I and m_I', is,

$$P_{m_I,m_I'}(\nu) = \gamma^2 B_\perp^2 I^2 g\left(h\nu - \Delta E_{m_I,m_I'}\right) \delta_{m_I \pm 1, m_I'}, \tag{2.6}$$

where $h = 2\pi$ is the Planck constant, and,

$$\Delta E_{m_I,m_I'} = -\gamma m_I |\mathbf{B}| - \left(-\gamma m_I' |\mathbf{B}|\right), \tag{2.7}$$

is the energy difference between two levels. The Kronecker delta in equation 2.6 highlights that only transitions between adjacent energy levels are allowed. By inserting $m_I' = m_I \pm 1$ into 2.7, we obtain their energy difference as,

$$\Delta E_{m_I,m_I'} \equiv \Delta E = \pm\gamma |\mathbf{B}|. \tag{2.8}$$

The function g is non-zero only when its argument equal to 0, which reflects the classical description that only allows for a detection in energy difference for a specific value of ν. Using this also allows us to recover equation 2.2.

The goal of both the classical and quantum viewpoints was to understand the change in energy that is observed when applying a magnetic field to a system of spins in a specific manner. When at resonance, the non-zero energy difference is detected by a change in voltage induced in a coil. The second magnetic field is typically of many orders of magnitude smaller than the first, and is chosen to be perpendicular to maximise the detected energy difference.

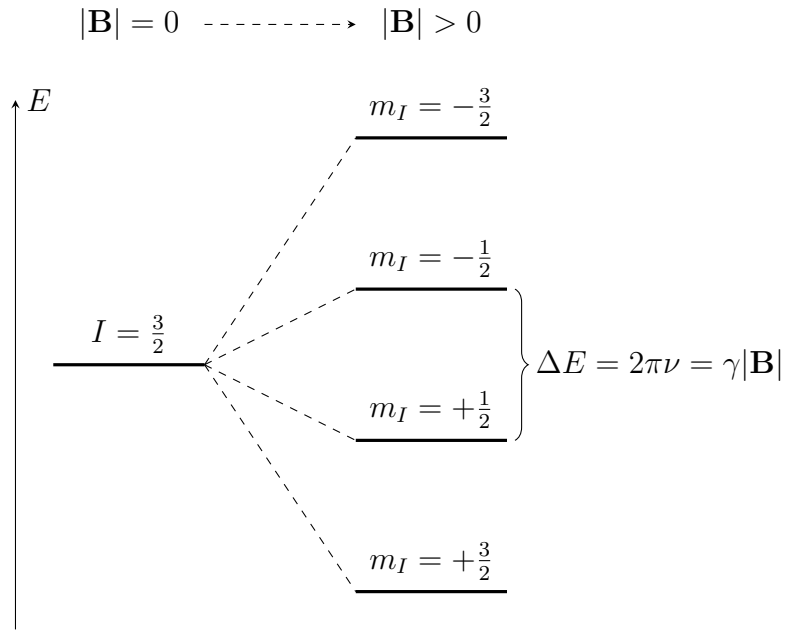


Figure 2.2: An example energy level diagram of a nuclear spin state, $I = \frac{3}{2}$. The quadrupedally degenerate state at $|\mathbf{B}| = 0$ is split into four distinct energy levels for $|\mathbf{B}| > 0$. The magnitude of the splitting is proportional to the applied field and gyromagnetic ratio of the nucleus, γ.

The discovery that the magnetic field experienced by a nucleus, $\mathbf{B}^{\text{in}}$, is altered by its surrounding chemical environment was of great importance.[9–14] These differences result in a different precession frequency for the nuclei in its environment. Determining these differences, typically from a reference compound, allows for a localised description of the atoms in the molecule or crystal. A range of $\mathbf{B}_{\perp}$ oscillation frequencies are tested,[2] and when a nucleus is in resonance with the field, the energy difference is detected and highlighted as a peak in the output spectrum. For a given nucleus, the field range needed to encompass all its resonances in a compound is relatively small. We therefore, typically, only probe one type of nucleus for a given study.

For an ensemble of nuclear spins, as in a sample of compound, the population of states is governed by the Boltzmann distribution,

$$\frac{n_+}{n_-} = \exp\left(-\frac{\Delta E}{k_{\text{B}}T}\right), \tag{2.9}$$

where n_+ is the population of the spin level at the higher energy and n_- the lower. ΔE is the difference between the - previously degenerate - nuclear spin energy levels, with k_{B} the Boltzmann constant and T as temperature. Equations 2.3 and 2.8 show that this difference depends on the applied magnetic field. A stronger field will therefore result in a greater number of spins undergoing the transition, meaning the peak is easier to detect.

The first experiments that observed the NMR phenomenon were by the teams of Purcell *et al.*[2] and Bloch *et al.*[3]. The heads of both these teams received the 1952 Nobel Prize in Physics for their work.

In the following subsections, we will discuss the main NMR parameters that are detailed in a spectrum. We will also discuss the field of solid-state NMR which has some additional challenges. And to set up the motivation for this project, we will consider how and why one may want to calculate NMR properties computationally, and what is currently missing from the state-of-the-art calculations.

[2]In modern NMR spectroscopy, it is typical to emit a very short pulse of radiowaves and measure the energy difference signal as the - now excited - states return to equilibrium. This technique is typically an order of magnitude more sensitive than the conventional approach, and is known as Fourier transform spectroscopy.[15]

2.2 Chemical shifts

As electrons are magnetically active, their density in compounds shield each nuclei from an applied field. This results in a change in Larmor frequency of the nucleus. In other words, the induced field, $\mathbf{B}^{\text{in}}$, at the nucleus is not exactly that of the applied, $\mathbf{B}$. This *shielding* effect is encompassed in a 3×3, tensor, $\overleftrightarrow{\sigma}$,

$$\mathbf{B}^{\text{in}} = -\overleftrightarrow{\sigma}\mathbf{B}. \tag{2.10}$$

The tensor denotes the shielding with respect to the orientation of the compound, relative to the applied field. Formally, this tensor describes how the energy, E, of the system changes with respect to the magnetic moment of a nucleus and the applied field,

$$\overleftrightarrow{\sigma} = \frac{\partial^2 E}{\partial \mathbf{B} \partial \boldsymbol{\mu}}. \tag{2.11}$$

The shielding tensor is thus a linear response function. That is, it denotes the amplitude to which a function changes in response to stimuli.

In liquids, due to the tumbling motion of molecules, the directional contributions cannot be seen and reduce to a number, the isotropic chemical shielding,

$$\sigma_{\text{iso}} = \frac{1}{3}\mathbb{T}\text{r}\,\overleftrightarrow{\sigma}. \tag{2.12}$$

In the solid-state, however, the static nature of the crystal does not allow the contributions to average themselves out. This results in a more complex picture, and anisotropic contributions can be detected.

Experimentally, the bare shielding of a nucleus cannot be obtained. A known reference compound is therefore chosen, and the difference in shielding - between this and a compound under study - obtained. A list of common reference compounds is given in table 2.2. This difference highlights the change in chemical environment of the nucleus, giving a localised description of the structure of the compound. This is known as the isotropic chemical *shift*, δ_{iso}, which is measured in units of parts per million (ppm),

$$\delta_{\text{iso}} = 10^6 \cdot \frac{\sigma_{\text{ref}} - \sigma_{\text{iso}}}{1 - \sigma_{\text{ref}}} \simeq 10^6 \cdot (\sigma_{\text{ref}} - \sigma_{\text{iso}}), \tag{2.13}$$

Table 2.2: Examples of common reference compounds used to obtained chemical shifts.

Nucleus	Reference compound(s)
^{1}H	$Si(CH_3)_4$, $(CH_3)_2CO$
^{13}C	$Si(CH_3)_4$
^{19}F	CCl_3F, C_6F_6
^{31}P	P_4O_6
^{14}N, ^{15}N	NH_3, NH_4^+
^{17}O	H_2O
^{11}B	BF_3, BCl_3

where σ_{ref} is the shielding of the reference compound.

The symmetric part of the chemical shielding tensor, $\frac{1}{2}\left(\overleftrightarrow{\sigma} + \overleftrightarrow{\sigma}^{\text{T}}\right)$, can be diagonalised into three principal components, δ_{11}, δ_{22} and δ_{33}, where,

$$\delta_{ii} = \sigma_{\text{ref}} - \sigma_{ii}, \tag{2.14}$$

and we follow the Haeberlen-Mehring-Spiess convention,[16–18]

$$|\delta_{33} - \delta_{\text{iso}}| \geq |\delta_{11} - \delta_{\text{iso}}| \geq |\delta_{22} - \delta_{\text{iso}}|. \tag{2.15}$$

The aforementioned anisotropic contribution, δ_{aniso}, is defined as,

$$\delta_{\text{aniso}} = \delta_{33} - \delta_{\text{iso}}, \tag{2.16}$$

and an asymmetry parameter, η_δ, is,

$$\eta_\delta = \frac{\delta_{22} - \delta_{11}}{\delta_{\text{aniso}}}. \tag{2.17}$$

2.3 Electric field gradients

Another NMR parameter of particular importance is the electric field gradient (EFG). Whilst not a magnetic quantity, nuclei with $I > \frac{1}{2}$ have their quadrupole moment, Q, interact with it. In solids, this typically broadens spectra, whilst in liquids, to first-order, its effects average to zero. The quadrupole of a nucleus represents its deviation from spherical charge symmetry, and for non-zero moments is prolate or oblate.

The EFG, $\overleftrightarrow{\mathcal{G}}(\mathbf{r})$, is given by,

$$\overleftrightarrow{\mathcal{G}}(\mathbf{r}) = \frac{\partial \mathbf{E}(\mathbf{r})}{\partial \mathbf{r}} - \frac{1}{3}\mathbb{1}_3 \left[\boldsymbol{\nabla} \cdot \mathbf{E}(\mathbf{r})\right], \tag{2.18}$$

where **E** is the electric field that depends on the ionic and electronic charge density. This function is evaluated at the nuclear position to obtain its EFG tensor, which is second-rank and 3×3 in dimension.

The tensor can be diagonalised into three components, $\mathcal{G}_{zz}$, $\mathcal{G}_{yy}$ and $\mathcal{G}_{xx}$, where,

$$|\mathcal{G}_{zz}| > |\mathcal{G}_{yy}| \geq |\mathcal{G}_{xx}|. \tag{2.19}$$

By definition, the tensor is traceless and its diagonal elements can therefore be fully defined using two parameters. The quadrupolar coupling constant, C_Q, quantifies the magnitude of the interaction,

$$C_Q = \frac{Q}{2\pi}\mathcal{G}_{zz}, \tag{2.20}$$

and the asymmetry quantified with η,

$$\eta = \frac{\mathcal{G}_{xx} - \mathcal{G}_{yy}}{\mathcal{G}_{zz}}. \tag{2.21}$$

2.4 Other NMR parameters

There exist other parameters that quantify the phenomena exhibited on NMR spectra. One example, of particular importance, is that of spin-spin coupling. An additional contribution to the magnetic field at a nucleus may arise due to the magnetic moments of other nuclei in the system. This may occur as a direct consequence of the coupling between the nuclei, dipolar coupling, or mediated through the electrons, J-coupling.

Dipolar coupling

The former is easily calculable, as it is a ground state property, but not easily detected in tumbling molecules experimentally. It is quantified by the traceless tensor, $\overleftrightarrow{D}_{KL}$, between ions K and L,

$$\overleftrightarrow{D}_{KL} = \frac{\gamma_I \gamma_J}{2\pi} \frac{1}{|\mathbf{r}_{KL}|^3} \left(\mathbb{1} - 3\hat{\mathbf{r}}_{KL} \otimes \hat{\mathbf{r}}_{KL}\right), \tag{2.22}$$

with $\mathbf{r}_{KL}$ their internuclear distance. This tensor is easily deduced in a calculation, as it is a function of the geometry of the ions only.

J-coupling

The latter arises due to two mechanisms. The first due to a magnetic moment interacting with the electronic structure and in turn inducing orbital currents, of which, create a magnetic field at the perturbed nucleus. The second is due to the interaction of the magnetic moment with the electronic spin, causing it to polarise and create a field at the perturbed nucleus. The $\overleftrightarrow{J}_{KL}$ tensor quantifies the weighting to which the perturbing ion, L, induces a magnetic field at the perturbed ion, K,

$$\mathbf{B}_K^{\text{in}} = \frac{1}{c^2}\frac{2\pi}{\gamma_K\gamma_L}\overleftrightarrow{J}_{KL}\cdot\boldsymbol{\mu}_L. \tag{2.23}$$

This second-rank tensor is formally defined as the interaction of the two magnetic moments,

$$\overleftrightarrow{J}_{KL} = \frac{\gamma_K\gamma_L}{2\pi}\frac{\partial^2 E}{\partial\boldsymbol{\mu}_K\partial\boldsymbol{\mu}_L}. \tag{2.24}$$

2.5 Solid-state NMR

Solid-state NMR is concerned with crystalline, repeating structures. These introduce challenges, not present in liquids or gases, because of anisotropic interactions. These, as mentioned before, do not average out due to the static nature of the ions in the system. As a result, spectral line peaks will be broadened dramatically due to the slightly differing orientation of each nuclear spin with the field. This broadening is quantified by the anisotropic shift, δ_{aniso}, and asymmetry parameter, η_δ. The latter is only defined when δ_{aniso} is non-zero, and indicates the nature of the symmetry of the interaction. Figure 2.3 shows a schematic diagram for non-zero chemical shift anisotropy, $\delta_{\text{aniso}} \neq 0$, for a range of asymmetry, η_δ, values. The top plot shows when the nucleus is at axial symmetry, meaning the δ_{11} and δ_{22} components are equal and η_δ necessarily 0. The two middle plots show non-zero asymmetry for the cases of $\delta_{11} > \delta_{22}$ and $\delta_{11} < \delta_{22}$. The seemingly odd choice of convention in equation 2.15 now becomes clear, as the three δ_{ii} components are in decreasing and increasing order from left to right, respectively. The bottom plot indicates the maximum asymmetry of 1, which on insertion into equation 2.17 indicates that

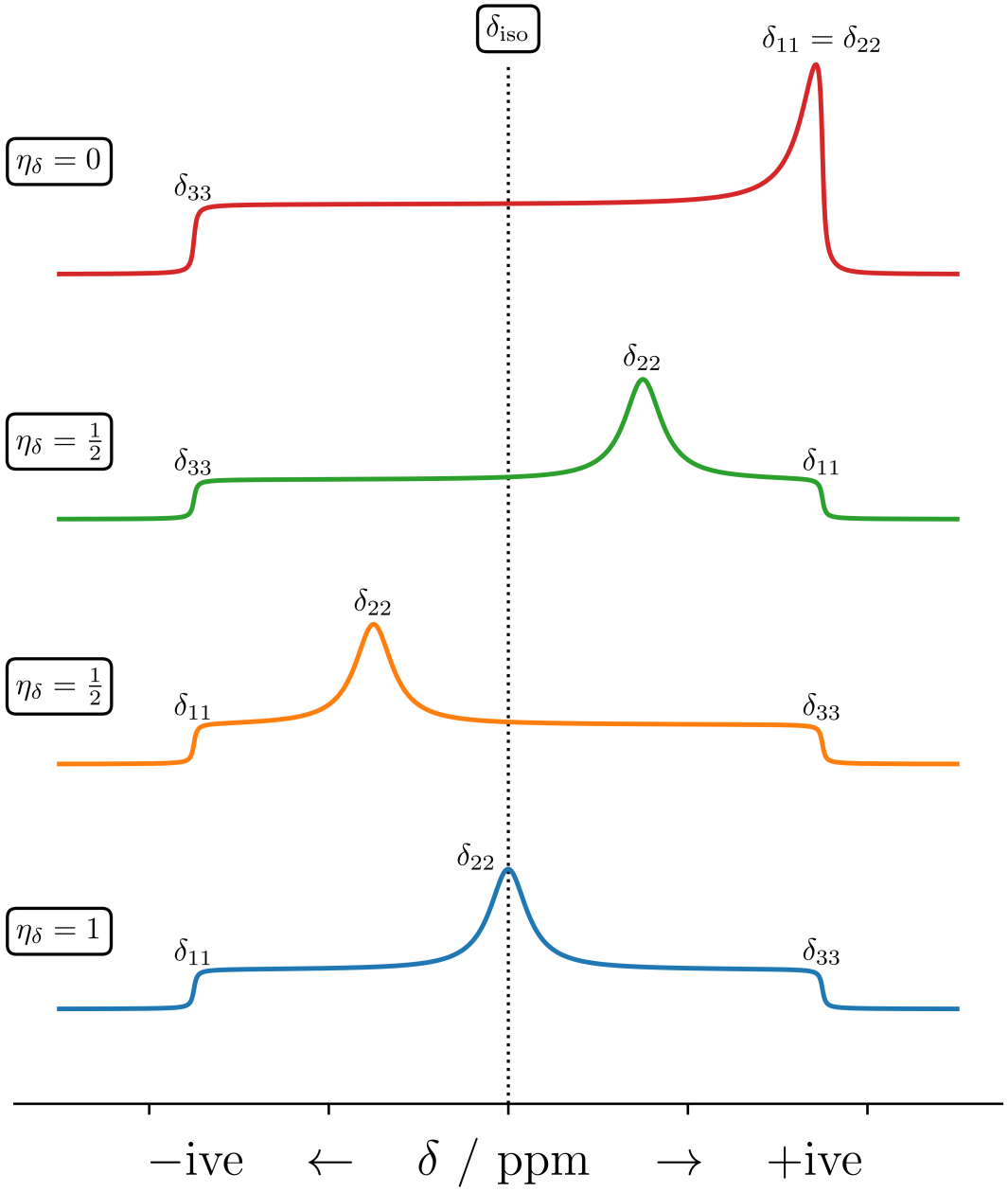


Figure 2.3: Schematic diagram of chemical shift anisotropy, that is δ_{aniso}, for different values of asymmetry, η_δ. Diagram recreated with reference to figure 2.2 of Apperley *et al.*.[19]

$\delta_{22} = \frac{\delta_{11}+\delta_{33}}{2}$ i.e δ_{22} is midway between δ_{11} and δ_{33}. We could have also recovered this relation by inserting $\delta_{\text{iso}} = \delta_{22}$ when $\eta_\delta = 1$, as seen on the plot.

The magnitude of these anisotropies can vary dramatically. For example, ^{1}H values are almost negligible but are much larger for ^{13}C; up to around 200 ppm.[19] Despite the extra difficulties created, they can be used to help assign spectra, often providing greater information than the isotropic shift alone.

There are further complications with $I > \frac{1}{2}$ nuclei, which have interactions with the EFG that often dominate over the anisotropies. An excellent review of the experimental and computational approaches towards obtaining solid-state NMR parameters is that of Bonhomme *et al.*.[20]

The most common technique to resolve the anisotropic issues is that of magic-angle spinning (MAS).[21, 22] The sample is spun rapidly, in a cylindrical container, at a 'magic' angle of 54.736°, that is the solution to $3\cos^2\theta = 1$, with respect to the applied field. At this angle, the principal axis of the material is orientated such that the anisotropic axes have their contributions cancelled when the container is spun fast enough. At slower rotation speeds, 'spinning sidebands' appear around peaks on the produced spectrum. As long as the rotation speed is greater than the frequency of the anisotropic interactions, a clean spectrum can be obtained. Figure 2.4 shows a schematic detailing the effects of MAS on a compound containing ^{1}H and ^{13}C. The ^{1}H spectra is dominated by dipolar coupling without MAS, broadening the line well beyond the expected δ_{H} range of 0-10 ppm. As mentioned, the anisotropy effects on ^{1}H are typically small and therefore do not appear. However, due to its very high gyromagnetic ratio, the dipolar couplings are huge - see equation 2.22. Spinning the sample at very high speeds is needed to sharpen the spectral resolution. The ^{13}C spectra indicate the nature of anisotropic interactions. Even at slow spinning speeds, we immediately see high resolution sharpening of line widths. The appearance of the aforementioned spinning sidebands appear at intervals of the spin rate from the centre band, and are only eliminated at very high speeds.

An additional technique is that of hetero and homonuclear dipolar decoupling. This is the averaging out of the spin contributions of one ion whilst obtaining

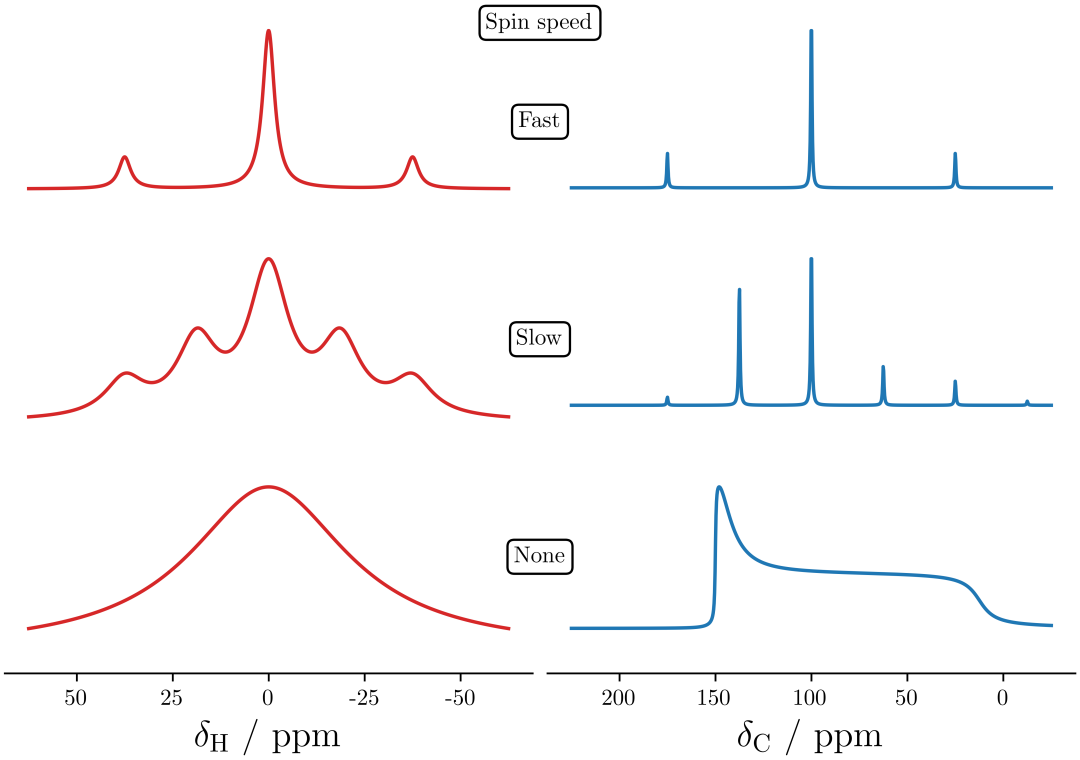


Figure 2.4: Schematic diagram of the effects of magic-angle spinning on an example compound containing ^{1}H and ^{13}C. Diagram recreated with reference to figure 2.12 of Apperley *et al.*.[19]

information about a second. Homonuclear decoupling is the more complex of the two, and requires a combination with MAS. This technique is known as Combined Rotation And Multiple Pulse Spectroscopy (CRAMPS). Advances in this area are Phase-Modulated Lee–Goldburg (PMLG)[23] and Decoupling Using Mind-Boggling Optimisation (DUMBO)[24, 25].

To increase the sensitivity of nuclei with naturally low abundance, the technique of cross-polarisation (CP) is commonly used.[26, 27] Naturally abundant nuclei with large gyromagnetic ratios are able to transfer magnetisation through dipolar couplings of the spins. There are restrictions on which nuclei can couple together due to certain relations and their proximity in space.

To obtain greater resolution spectra for quadrupolar nuclei, more advanced techniques must be used. The quadrupolar interaction has a greater complexity in its angular dependence with respect to the magnetic field. Therefore, even at very fast spinning rates, MAS techniques are not capable of averaging out the interaction. One natural choice of technique is double rotation (DOR), whereby the sample is spun at two angles simultaneously, with an inner and an outer rotor.[28, 29] Often, high enough spinning speeds are difficult to obtain, and a technique called dynamic angle spinning (DAS) may be preferable.[30, 31] This is similar to DOR, but the two rotations are performed sequentially. A difficulty in this technique is the speed at which the rotor angle is switched. The population of magnetised states must be maintained in this period, typically meaning only systems with slow relaxation of spin states may be probed.

An alternative to the DOR and DAS techniques are those that exploit the spin transitions in a quantum system. These are categorised into central (CT) and satellite (ST) transitions. To first order, the CT is not affected by the EFG, whereas STs are. It is typically only CTs that are observed experimentally. These quantum transitions can be utilised in a two-dimensional experiment and the technique is named multiple-quantum magic-angle spinning (MQMAS).[32] The more complicated approach of utilising the STs is named satellite-transition magic-angle spinning (STMAS)[33] and is typically much more sensitive than MQMAS.

These approaches are often preferred over DOR and DAS as only conventional probes are required for their implementation, rather than those that accommodate spinning the sample at two angles.

One final comment is in regard to recoupling techniques. These allow for the reintroduction of the anisotropic information lost due to techniques, such as MAS, in a controlled manner. Whilst problematic for attaining high resolution spectra, this information can provide valuable insight to the probed system. For example, the dipolar coupling - which typically broadens peaks - is highly sensitive to atomic positions, with an inverse proportionality of distance cubed. Retrieving the effects of this coupling can therefore provide excellent insight into the spatial distribution of nuclei in a system.

2.6 Calculations

Outlining the difficulties faced in attaining accurate experimental solid-state NMR spectra highlight the potential usefulness of computational studies. Density functional theory (DFT) provides an excellent tool for the study of periodic systems, because of its ability to consider large system sizes and both insulating and metallic compounds. For an experiment to be considered reliable, it is now almost a necessity to include comparisons between the experimental and computed data. Theoretical advancements over the last few decades now allow precise deduction of a wide range of NMR parameters, including all those discussed thus far.

The very high sensitivity of NMR parameters, with respect to system geometries, allows for changes in structure to be studied, such as atom substitution or bond length and angles changes. The solid-state introduces many previously discussed complications to the observed spectra, and along with the difficulty of many inorganic materials containing less well-studied elements, the necessity of combining experiment with calculation becomes more prominent. Ashbrook and McKay outline the recent advances of NMR calculations and their ability to support experiment, with particular emphasis on the field of NMR crystallography.[34] Martineau *et al.* highlight the combination of experiment with first-principles calculations through

their 'SMARTER' crystallography approach, whereby they apply both to studying a metal-organic-framework.[35] All of the atoms in the system have accessible NMR isotopes, providing great scope for comparison data between experimental and calculated. A Monte-Carlo search gave multiple potential structures, which were then geometrically optimised. Validation of NMR parameters, evaluated with DFT, gave a proposed structure, which when compared with single crystal x-ray diffraction data, highlighted the credibility of the multi-method approach. This technique can be applied to systems that have no, or incomplete, confirmed experimental structures. For example, Perras and Bryce improved the low-quality geometries of $Na_2Al_2B_2O_7$ by simultaneously refining the structures against experimental EFG data and those calculated using DFT.[36] Prediction methods can also give structural precursors, using typically only the elemental analysis. This has notably been done by Pickard and Needs in their ab initio random structure searching (AIRSS) method.[37]

Ramsey outlined the theoretical basis required for the computation of NMR parameters in the 1950s.[38–40] Many methods were developed over the following decades,[41–43] differing most notably in the choice of atomic orbitals used and their gauge dependence. This latter point refers to the problem that, for a long time, results of calculations would change on translation of the molecule, and only an infinite basis set would lead to no gauge-dependence. The most widely used techniques to deal with this problem were the individual gauges for localised orbitals (IGLO)[42, 44] and gauge-including atomic orbitals (GIAO)[45–47].

Mauri *et al.* were the first to present a method to calculate chemical shielding values in periodic systems,[48] which was critical to the development of NMR calculations in solids. The evaluation of position operators caused difficulties, resulting in divergent diamagnetic and paramagnetic terms. They outlined a reformulation of these terms into a single equation, that depends on the difference between position operators, and is well defined even for infinite systems.

The separation of core and valence electrons in the pseudopotential approach was once thought to be very problematic for the calculation of NMR parameters. This is because it was thought that the core contribution to the shielding was non-rigid, and

would thus need to be calculated in an all-electron fashion. However, it was shown by Gregor *et al.* that a careful choice of core and valence states allows their contributions to both remain gauge invariant, and thus a pseudopotential approach viable.[49]

A theory was required that 1) could utilise pseudopotentials; 2) was gauge-invariant and 3) implicitly contained periodic boundary conditions. It was Pickard and Mauri who introduced the groundbreaking theory that satisfied these strict requirements.[6] This extended the projector augmented-wave (PAW) method, devised by Blöchl,[50] into the gauge-including PAW (GIPAW) method. This paper showed how to recover the information contained in the core region, lost through the pseudopotentials, allowing for all-electron accuracy in infinite systems. All whilst satisfying gauge-invariance.

Advancements were then introduced by Yates *et al.*, who incorporated the use of the zeroth-order regular approximation (ZORA).[51] This provided a technique to calculate more accurate shielding values for systems that contain heavy elements. The mathematical extension required for the use of ultra-soft pseudopotentials (USPs) - which provide greater accuracy at lower computational cost compared to the regular norm-conserving pseudopotentials (NCPs) - was then also introduced by Yates *et al.*.[52]

Solid-state DFT calculations can be very time-consuming and memory intensive when employing high level functionals; those above generalised gradient approximations. Techniques have been devised to consider the periodic nature of the crystal using a lower level of DFT, but employ correctional terms based on isolated molecules computed at a higher level of theory.[53] Molecular crystals have been studied using this method, but it falls short in its ability to describe inorganic compounds well. Considering a single molecule works quite well for highly localised systems, but those that contain strong intermolecular interactions require a cluster of adjacent molecules to be considered.[54]

A method to calculate EFG tensors from first principles was initially presented by Blaha *et al.*.[55] This approach used the expensive linearised augmented-plane-wave (LAPW) method, which treat the core and valence electrons on the same footing

without any approximations on the potential. An approach for EFGs using the PAW method was first implemented by Petrilli *et al.*[56] and later by Profeta *et al.*[57]. The computation of J-coupling values were devised by Joyce *et al.*,[58] and their extension to use USPs and the ZORA approach were introduced by Green and Yates[59].

Despite the tremendous advancements described thus far, there still exists a problem: heavy atoms. The ZORA approach, implemented for both chemical shielding and J-coupling computations, is sometimes not sufficient in capturing the full effects. It is the spin-orbit coupling (SOC) phenomenon that is present in these atoms, of which, is included in the ZORA scheme but neglected in its current implementation. The proportionality scaling of SOC in hydrogen-like atoms is that of Z^4, where Z is the atomic number. Thus, as we descend down the periodic table, the effects become dramatically more important. Not only this, but light elements that are in close proximity to the heavy ones are affected. This is known as the heavy-atom light-atom (HALA) effect. These effects have been known about for a long time,[60, 61] and as early as the 1980s, it was shown that SOC effects from the heavy I atom in CI_4 can affect the ^{13}C shift as much as 300 ppm,[62] with formalisms progressing much of the understanding of the phenomenon later that decade[63–65]. Vícha *et al.* offer an extensive review of the effects of heavy atoms on NMR chemical shifts.[66] The addition of SOC in the calculation of NMR parameters has been implemented into DFT codes,[67–69] but unfortunately are suitable for molecular studies, only.

In this project, we have extended the work in this field to date by implementing the ability to calculate NMR shielding values with the inclusion of SOC effects in the pseudopotential and GIPAW formalisms. This provides the accurate calculation of NMR shielding values for, not only molecules, but extended systems, also.

3 First principles methodologies

Contents

3.1 Non-relativistic quantum mechanics 24
3.1.1 Schrödinger equation 24
3.1.2 Born-Oppenheimer approximation 25
3.1.3 The variational principle 26
3.2 Mean-field techniques 26
3.2.1 Hartree-Fock 26
3.2.2 Electron correlation 27
3.2.3 Post Hartree-Fock techniques 28
3.3 Density functional theory 29
3.3.1 The Hohenberg-Kohn theorems 29
3.3.2 The Kohn-Sham equations 32
3.3.3 Exchange-correlation functionals 33
3.4 Implementation methodology 35
3.4.1 The reciprocal lattice 35
3.4.2 The Brillouin zone 36
3.4.3 Bloch's theorem 36
3.4.4 Planewaves 38
3.4.5 Frozen core approximation 40
3.4.6 Pseudopotentials 40
3.4.7 Projector augmented-wave method 46
3.5 Relativistic quantum mechanics 48
3.5.1 Dirac equation 49
3.5.2 Introducing an electromagnetic field 50
3.5.3 Relativistic corrections 51
3.5.4 Elimination of the small component 53
3.5.5 Zeroth-order regular approximation 55
3.5.6 Scalar-relativistic approaches 56
3.5.7 Relativistic pseudopotentials 56

3.5.8 Projector augmented-wave method with spinors 59

3.1 Non-relativistic quantum mechanics

3.1.1 Schrödinger equation

The time dependent Schrödinger equation describes, in a non-relativistic manner, the wave-like nature of particles,[70]

$$H|\psi(t)\rangle = i\frac{\mathrm{d}}{\mathrm{d}t}|\psi(t)\rangle. \tag{3.1}$$

The Hamiltonian, H, an operator, is defined by the system. Any chemical property can be extracted from the complex wavefunction, $|\psi(t)\rangle$, for a given time, t. It is the Hamiltonian that propagates the wavefunction through time, as the dynamics of the system are dictated by the kinetic, T, and potential, V, energies,

$$H = T + V = \frac{p^2}{2} + V, \tag{3.2}$$

where the operator, V, is typically a function of position, only, $V = V(\mathbf{r})$. Here, $\mathbf{p}$ is the linear momentum operator, $\mathbf{p} = -i\boldsymbol{\nabla}$, and so, $p^2 = -\nabla^2$. The Schrödinger equation contains derivatives of second-order with respect to position but first-order with respect to time. We therefore know that it cannot satisfy the requirements of relativity that treat space and time only equal footing. Further discussion in regard to relativistic effects are found in later sections.

Assuming a time independent Hamiltonian, we can integrate equation 3.1 to recover the time independent Schrödinger equation,

$$H|\psi\rangle = E|\psi\rangle, \tag{3.3}$$

where E is the energy eigenvalue. The solutions are called stationary states and the real-space representation of the wavefunction, $\psi(\mathbf{r})$, is defined as,

$$\psi(\mathbf{r}) \equiv \langle \mathbf{r}|\psi\rangle. \tag{3.4}$$

To describe a system of interacting particles, such as in an atom or molecule, it is quite simple to write down the complete form of the Hamiltonian,

$$H = -\frac{1}{2}\sum_n \frac{\nabla_n^2}{m_n} + \sum_{m>n} \frac{q_n q_m}{r_{nm}}, \tag{3.5}$$

where n and m run over all electrons and nuclei. m_n is the mass of particle n and $m_n = 1(= m_e)$ for electrons. q_n is the charge of particle n and $q_n = -1(= -e)$ for electrons. Despite its simplicity, the Schrödinger equation, that arises due to this Hamiltonian, is only analytically solvable for the hydrogen-like atom.

3.1.2 Born-Oppenheimer approximation

To progress further, approximations and simplified models must be used. Let us split up the contributions from the electrons (labelled by i) and nuclei (labelled by I), and also expand the Coulomb term in this equation to identify its three components,

$$H = -\frac{1}{2}\sum_i \nabla_i^2 - \frac{1}{2}\sum_I \nabla_I^2 - \sum_{i,I} \frac{Z_I}{r_{iI}} + \sum_{j>i} \frac{1}{r_{ij}} + \sum_{J>I} \frac{Z_I Z_J}{R_{IJ}}, \tag{3.6}$$

with the first of the Coulomb terms denoting the nuclear-electron attraction, the second the electron-electron repulsion and the third the nuclear-nuclear repulsion. Z_I is the atomic number of nucleus I. Making the nuclear terms explicit in this equation allows us to introduce the Born-Oppenheimer approximation. This is the assumption that the dynamics of the electrons are considered instantaneous with respect to the nuclei. One may note the much larger mass values of nuclei, $m_I \gg 1$. We can therefore consider the nuclei as fixed, and treat them classically. The final term in the above equation is thus a constant and we can write down the electronic Hamiltonian,

$$H_{\text{elec}} = -\frac{1}{2}\sum_i \nabla_i^2 - \sum_{i,I} \frac{Z_I}{r_{iI}} + \sum_{j>i} \frac{1}{r_{ij}}. \tag{3.7}$$

We can resort to techniques, which are outlined later, to solve equation 3.1 with this Hamiltonian. The energy of the system can then be recovered as that found with this Hamiltonian plus the constant terms in equation 3.6.

3.1.3 The variational principle

Typically, the aim of computational studies of chemical systems is to solve for the wavefunction, $|\psi\rangle$. Currently, this seems an impossible task with no clear direction of progress. However, the variational principle can be used to guide the process of obtaining this wavefunction. Note that any trial wavefunction, say $|\psi^{\mathrm{tr}}\rangle$, can be written as a linear combination of the true spectrum of the Hamiltonian operator, that is $|\psi^{\mathrm{tr}}\rangle = \sum_n c_n|\psi_n\rangle$, where the eigenvalues are ordered, $E_0 < E_1 < E_2 < \cdots$. Now, with orthonormal wavefunctions,

$$\langle\psi^{\mathrm{tr}}|H|\psi^{\mathrm{tr}}\rangle = \sum_{n,m} c_n^* c_m \langle\psi_n|H|\psi_m\rangle = \sum_{n,m} c_n^* c_m E_m \langle\psi_n|\psi_m\rangle = \sum_n |c_n|^2 E_n. \quad 3.8$$

The sum of probability coefficients must always sum to unity, and so, using the identity $|c_0|^2 = 1 - \sum_{n>0} |c_n|^2$, we get,

$$\langle\psi^{\mathrm{tr}}|H|\psi^{\mathrm{tr}}\rangle = \sum_n |c_n|^2 E_n = E_0 + \sum_{n>0} |c_n|^2 (E_n - E_0) \geq E_0, \quad 3.9$$

as the energy terms in the summation are positive definite due to the ordered eigenvalues imposed earlier. As a result, we can systematically vary the trial wavefunction, using sensible algorithms, with the knowledge that a lower energy expectation value is a better approximate answer. The variation of this iterative cycle can act as a convergence tolerance indicator to highlight when a ground state has been found with desired accuracy. This process is typical of all quantum mechanical methods of determining wavefunctions.

3.2 Mean-field techniques

3.2.1 Hartree-Fock

The basis of the Hartree-Fock (HF) theory is to use a mean-field approximation towards the wavefunction that satisfies its parity.[71] This is achieved most simply by the use of a Slater determinant, Φ_{SD},

$$\psi(\mathbf{r}) \approx \Phi_{\mathrm{SD}}(\mathbf{r}_1, \mathbf{r}_2, ..., \mathbf{r}_N) = \frac{1}{\sqrt{N!}} \begin{vmatrix} \psi_1(\mathbf{r}_1) & \psi_2(\mathbf{r}_1) & \cdots & \psi_N(\mathbf{r}_1) \\ \psi_1(\mathbf{r}_2) & \psi_2(\mathbf{r}_2) & \cdots & \psi_N(\mathbf{r}_2) \\ \vdots & \vdots & \ddots & \vdots \\ \psi_1(\mathbf{r}_N) & \psi_2(\mathbf{r}_N) & \cdots & \psi_N(\mathbf{r}_N) \end{vmatrix}, \quad 3.10$$

where $\psi_i(\mathbf{r}_j)$ represents the real-space wavefunction for electron j in orbital i. Evaluating the Hamiltonian in equation 3.7, the electronic HF energy is,

$$E_{\mathrm{HF}} = \langle \Phi_{\mathrm{SD}} | H_{\mathrm{elec}} | \Phi_{\mathrm{SD}} \rangle = \sum_i (i|h|i) + \frac{1}{2} \sum_{i,j} (ii|jj) - (ij|ji), \tag{3.11}$$

where,

$$(i|h|i) = \int \psi_i^*(\mathbf{r}_1) \left[-\frac{1}{2} \nabla_i^2 - \sum_I \frac{Z_I}{r_{1I}} \right] \psi_i(\mathbf{r}_1) \, \mathrm{d}\mathbf{r}_1. \tag{3.12}$$

This defines the contribution of the kinetic energy of the electrons and their interaction with the nuclei. Also,

$$(ii|jj) = \int \int |\psi_i(\mathbf{r}_1)|^2 \frac{1}{r_{12}} |\psi_j(\mathbf{r}_2)|^2 \, \mathrm{d}\mathbf{r}_1 \, \mathrm{d}\mathbf{r}_2, \tag{3.13}$$

is the local Coulomb term, which is the mean-field interaction of electron i with electron j. Each experiences an averaged-out potential due to all electrons in the system, including themselves, and thus there is a so-called *self-interaction* error. Lastly,

$$(ij|ji) = \int \int \psi_i(\mathbf{r}_1) \psi_j^*(\mathbf{r}_1) \frac{1}{r_{12}} \psi_j(\mathbf{r}_2) \psi_i^*(\mathbf{r}_2) \, \mathrm{d}\mathbf{r}_1 \, \mathrm{d}\mathbf{r}_2, \tag{3.14}$$

is the non-local exchange term. Obtaining this explicit expression for the exchange interaction is a feature of the HF theory rarely found elsewhere, and we will not always have this luxury when we begin to solve the energy integrals in later methods. Another benefit to HF, not present in other theories, is that the Coulomb and exchange integrals are equal and opposite for an electron interacting with itself. Though computationally less efficient, this means the self-interaction error of the mean-field approximation is perfectly solved with this approach.

3.2.2 Electron correlation

Despite the benefits seen by the HF theory, there is one crucial element missing: electron correlation. The instantaneous movements of each electron are not correlated with each other, as they are simply responding to a mean-field. This smeared-out potential results in electrons typically spending too much time in close proximity with one another. This is known as dynamic correlation. Another effect, that is not accounted for, is from ignoring the results of antibonding-like orbitals.

Without these, ionic-like states begin to have too large of a contribution to the molecular orbital, giving incorrect results. Methods, such as unrestricted HF, may account for this.[72] This problem is known as static correlation.

As mentioned previously, the HF formalism deals with the exchange energy, $E_{\mathrm{X}}^{\mathrm{HF}}$, exactly, and thus the error in the HF energy is due to ignoring electron correlation energy, $E_{\mathrm{C}}^{\mathrm{HF}}$, *and* the energy difference in assuming the wavefunction to be a Slater determinant, $\Delta E_{\mathrm{SD}}^{\mathrm{HF}}$. We therefore define the HF correlation energy, $E_{\mathrm{C}}^{\mathrm{HF}}$, to be these differences, $E_{\mathrm{C}}^{\mathrm{HF}} = E_{\mathrm{exact}} - \Delta E^{\mathrm{HF}}$, where $\Delta E^{\mathrm{HF}} = E_{\mathrm{X}}^{\mathrm{HF}} - \Delta E_{\mathrm{SD}}^{\mathrm{HF}}$.

3.2.3 Post Hartree-Fock techniques

The correlation energy, $E_{\mathrm{C}}^{\mathrm{HF}}$, can be very large and the error in the Slater determinant approximation, $\Delta E_{\mathrm{SD}}^{\mathrm{HF}}$, is drastic. An exact formalism, i.e where this latter term is zero, that accounts for electron correlation (dynamic and static) is therefore of great importance. One approach is to learn from the static correlation problem and incorporate more configurations of determinants that account for additional excited states. This is named the Configuration Interaction (CI) approach.[73] If all configuration states are accounted for in the expansion, the approach is formally exact and solves equation 3.3. However, it is incredibly computationally expensive, and can only be practically applied to small molecules with a truncated expansion. The coupled cluster (CC) theory incorporates electron correlation by a cluster operator, which introduces electron excitations up to a defined level.[74–76] Single, double (D), triple (T) and quadrupole (Q) versions of CC are common, yet very large computational demands are still seen, particularly for the T and Q methods. Møller-Plesset perturbation theory (MP) is another common method that adds a small Rayleigh-Schrödinger perturbation to the Hamiltonian that characterises the electron correlation.[73, 77] Second, third and fourth-order corrections to the potential are standard in the literature, but fifth-order rarely seen. The technique is not typically chosen due to poor convergence for some systems.

3.3 Density functional theory

Until now, the most important mathematical object has been the wavefunction, $|\psi\rangle$. The electron density can be obtained via,

$$n(\mathbf{r}) = |\psi(\mathbf{r})|^2, \tag{3.15}$$

where $|\psi\rangle$ has been found by solving equation 3.3 with the electronic Hamiltonian defined in equation 3.7. This electron density is an observable quantity that becomes of great use as the fundamental variable of density functional theory (DFT). To treat many electrons in DFT, the above equation will extend to a summation of wavefunctions that represent the orbital nature of the electron in a mean field potential.

3.3.1 The Hohenberg-Kohn theorems

The use of the electron density as the fundamental variable in solving for the ground state of a chemical system was introduced by Hohenberg and Kohn in 1964.[4] A remarkable result from this is that we now only deal with the three spatial coordinates that the electron density depends on, $\mathbf{r}$. Previously, the wavefunction depended on the three spatial coordinates for each of the N electrons in the system. This improves the scalability of the problem dramatically.

First theorem

The external potential, V in equation 3.2, is the main component of the Hamiltonian that is dictated by the system. Suppose that there exists two external potentials, V and V', that correspond to the same electron density, $n(\mathbf{r})$. The pathways to obtaining this density are,

$$V \overset{\text{eqn 3.2}}{\Longrightarrow} H \overset{\text{eqn 3.3}}{\Longrightarrow} |\psi\rangle \overset{\text{eqn 3.15}}{\Longrightarrow} n(\mathbf{r}) \overset{\text{eqn 3.15}}{\Longleftarrow} |\psi'\rangle \overset{\text{eqn 3.3}}{\Longleftarrow} H' \overset{\text{eqn 3.2}}{\Longleftarrow} V', \tag{3.16}$$

where $|\psi\rangle$ and $|\psi'\rangle$ are the true, exact ground state wavefunctions of their respective Hamiltonians, which have expectation values,

$$E = \langle\psi|T + V|\psi\rangle, \tag{3.17}$$

$$E' = \langle\psi'|T + V'|\psi'\rangle. \tag{3.18}$$

From the variational principle, we know that using $|\psi'\rangle$ as a trial wavefunction for H will give us an energy larger than that of the true ground state energy. An analogous statement can be made for $|\psi\rangle$ with H'. And so,

$$E < \langle\psi'|T + V|\psi'\rangle, \tag{3.19}$$

$$E' < \langle\psi|T + V'|\psi\rangle. \tag{3.20}$$

A simple trick of algebra gives,

$$E < E' + \langle\psi'|V - V'|\psi'\rangle, \tag{3.21}$$

$$E' < E - \langle\psi|V - V'|\psi\rangle. \tag{3.22}$$

As equation 3.16 states that $|\psi\rangle$ and $|\psi'\rangle$ give the same density, $n(\mathbf{r})$, these equations are,

$$E < E' + \int [V(\mathbf{r}) - V'(\mathbf{r})]\, n(\mathbf{r})\, \mathrm{d}\mathbf{r}, \tag{3.23}$$

$$E' < E - \int [V(\mathbf{r}) - V'(\mathbf{r})]\, n(\mathbf{r})\, \mathrm{d}\mathbf{r}. \tag{3.24}$$

Then, by simply summing both sides of these equations, we get,

$$E + E' < E' + E, \tag{3.25}$$

which is physically unreasonable and, as a result, we have arrived at a contradiction. Thus, there cannot exist two distinct potentials that give rise to the same electron density. The electron density therefore is able to describe all variables of our system, Z_I and $\mathbf{R}_I$, the atomic number and position of each ion, respectively. These define H, and ultimately determine $|\psi\rangle$,

$$n(\mathbf{r}) \Rightarrow \{Z_I, \mathbf{R}_I\} \Rightarrow H \Rightarrow |\psi\rangle \Rightarrow E \quad \text{and all other properties.} \tag{3.26}$$

This is the first Hohenberg-Kohn theorem.

Second theorem

The energy is thus a functional of the ground state density, $E \equiv E[n(\mathbf{r})]$. By denoting the three energy terms found with the electronic Hamiltonian in equation 3.7 as E_{kin}, E_{Ne} and E_{ee}, respectively, the ground state energy is,

$$E_0[n_0] = E_{\text{kin}}[n_0] + E_{\text{Ne}}[n_0] + E_{\text{ee}}[n_0], \tag{3.27}$$

where $n_0 \equiv n_0(\mathbf{r})$ is the ground state density. $E_{\text{kin}}[n_0]$ and $E_{\text{ee}}[n_0]$ are universally valid for all systems, as they do not depend on Z_I or $\mathbf{R}_I$. $E_{\text{Ne}}[n_0]$ does, however, and thus it is sensible to group the universal terms into a new quantity, $F_{\text{HK}}[n_0]$, named the Hohenberg-Kohn functional, and explicitly express the nuclear-electron interactions,

$$E_0[n_0] = F_{\text{HK}}[n_0] + \int n_0(\mathbf{r}) V_{\text{Ne}}\, \mathrm{d}\mathbf{r}. \tag{3.28}$$

The Hohenberg-Kohn functional encapsulates the kinetic and electron-electron interaction terms and applies equivalently to all systems - from the hydrogen atom to proteins! This is the second Hohenberg-Kohn theorem.

Unfortunately, the complete, explicit expression of $F_{\text{HK}}[n_0]$ is not known. However, some progress can be made by noting that the classical Coulomb energy, can be extracted from $E_{\text{ee}}[n]$,

$$E_{\text{ee}}[n] = \frac{1}{2} \int \int \frac{n(\mathbf{r}_1) n(\mathbf{r}_2)}{r_{12}}\, \mathrm{d}\mathbf{r}_1\, \mathrm{d}\mathbf{r}_2 + E_{\text{non-cl}}[n] \equiv J[n] + E_{\text{non-cl}}[n], \tag{3.29}$$

where $E_{\text{non-cl}}[n]$ represents the non-classical parts of the electron-electron interactions: 1) the self-interaction error; 2) the exchange interaction; and 3) the electron correlation.

There is one final note to make at this point. We can solve for $E_{\text{kin}}^{\text{non-int}}[n]$, which is the kinetic energy of the same system, $E_{\text{kin}}[n]$, but considering the particles to be non-interacting. This can be solved for exactly. We finally define the

exchange-correlation energy functional, which shall be the focus of a large portion of the following discussions, as,

$$E_{\mathrm{XC}}[n] = \Delta E_{\mathrm{kin}}[n] + E_{\text{non-cl}}[n], \tag{3.30}$$

where,

$$\Delta E_{\mathrm{kin}}[n] = E_{\mathrm{kin}}[n] - E_{\mathrm{kin}}^{\text{non-int}}[n]. \tag{3.31}$$

So, the exchange-correlation energy functional contains all the unknown portions of information about our system. Namely, 1) the difference in kinetic energy between our true system and an equivalent system of non-interacting particles and 2) the non-classical interactions: self-interaction error, exchange interaction and electron correlation. We define a slightly modified Hohenberg-Kohn functional, $F[n]$, to give the ground state energy as,

$$E_0[n_0] = F[n_0] + \int n_0(\mathbf{r}) V_{\mathrm{Ne}}\, \mathrm{d}\mathbf{r}, \tag{3.32}$$

where,

$$F[n_0] = E_{\mathrm{kin}}^{\text{non-int}}[n_0] + J[n_0] + E_{\mathrm{XC}}[n_0]. \tag{3.33}$$

3.3.2 The Kohn-Sham equations

Kohn and Sham proposed to progress the problem of solving these equations by mapping it onto a set of non-interacting electrons.[5] The electron density is simply a sum of the individually solved densities,

$$n(\mathbf{r}) = \sum_i |\psi_i(\mathbf{r})|^2. \tag{3.34}$$

We have previously seen a model that produces a set of single particle equations - the HF method. Here, we take a similar approach, by introducing a Slater determinant, which results in the multiple one-electron equations,

$$f_{\mathrm{KS}}|\psi_i\rangle = \varepsilon_i|\psi_i\rangle, \tag{3.35}$$

where f_{KS} is the Kohn-Sham operator,

$$f_{\mathrm{KS}} = -\frac{1}{2}\nabla^2 + \int \frac{n(\mathbf{r}_2)}{r_{12}}\,\mathrm{d}\mathbf{r}_2 - \sum_I \frac{Z_I}{r_{1I}} + V_{\mathrm{XC}}(\mathbf{r}_1), \tag{3.36}$$

$$\equiv -\frac{1}{2}\nabla^2 + V_{\mathrm{eff}}(\mathbf{r}_1), \tag{3.37}$$

and $\psi_i(\mathbf{r})$ are named the Kohn-Sham orbitals, and the effective potential, $V_{\mathrm{eff}}(\mathbf{r})$, implicitly defined. This is a great improvement on the interacting picture, as these equations are much easier to solve now that they are uncoupled. The exchange-correlation energy functional, $E_{\mathrm{XC}}[n]$, is related to the exchange-correlation potential, $V_{\mathrm{XC}}(\mathbf{r})$, by,

$$V_{\mathrm{XC}}(\mathbf{r}) = \frac{\delta E_{\mathrm{XC}}[n(\mathbf{r})]}{\delta n(\mathbf{r})}. \tag{3.38}$$

Whilst the first three terms in equation 3.36 can be written explicitly, the exchange-correlation potential, $V_{\mathrm{XC}}(\mathbf{r})$, is not known. Its determination would allow for the calculation of the exact ground state of the system in question. Finding good approximations of the functional is very difficult to do and empirical methods are often resorted to.

3.3.3 Exchange-correlation functionals

We first begin with a simplification: to consider a local functional. We expect the true functional to be non-local, however. This approximation, named the local-density approximation (LDA), was suggested by Kohn and Sham in their original DFT paper. We consider the electrons to be non-interacting and that the potential due to the nuclei is a constant. For a further discussion, see, for example, reference [78]. This approximation is relatively poor, even for very smooth electron densities (where one may predict a uniform gas might be a good representation), primarily due to the neglect of spin. The local-spin-density approximation (LSDA) was then introduced, which is a functional of the up-spin electron density, $n_\uparrow(\mathbf{r})$, and down-spin electron density, $n_\downarrow(\mathbf{r})$,

$$V_{\mathrm{XC}}^{\mathrm{LSDA}}[n_\uparrow, n_\downarrow] = \int n(\mathbf{r})\varepsilon_{\mathrm{XC}}(n_\uparrow, n_\downarrow)\,\mathrm{d}\mathbf{r}, \tag{3.39}$$

where $\varepsilon_{\mathrm{XC}}$ is the exchange-correlation energy of the non-interacting, uniform electron gas. It was not until future work, that proposed a method to solve for this quantity,[79–81] where the L(S)DA functional was then able to be parametrised for use in DFT.[82–84] Despite its age and simplicity, it still remains a remarkably robust functional today. It still stands as a first-principles approximation, in that it has no empirically fitted parameters, and thus sensibly represents the physical nature of the exchange-correlation interaction.

Despite its trustworthiness, LSDA comes with some inaccuracies. It struggles to detail bonding and lattice structures well, as well as greatly overestimating atomisation energies[85]. To progress further, LSDA can be treated as a zeroth-order term in a Taylor expansion of $V_{\mathrm{XC}}[n_\uparrow, n_\downarrow]$. There are multiple examples of these gradient expansion approximations (GEAs),[86–88] however, they do not typically perform much better than LSDA. This is due to their violation of the physical nature of the exchange-correlation hole[89] through their Taylor expansion. This approximation breaks the physical nature of the exchange-correlation hole, which is respected by LSDA, and poor results may be found.

Slightly better advancements, that typically impose physically motivated restrictions in regard to the sum rule of the exchange-correlation hole, are the generalised gradient approximations (GGAs).[90–92] These also introduce a degree of freedom: the gradient of the electron density,

$$V_{\mathrm{XC}}^{\mathrm{GGA}}[n_\uparrow, n_\downarrow] = \int n(\mathbf{r})\varepsilon_{\mathrm{XC}}(n_\uparrow, n_\downarrow, \boldsymbol{\nabla} n_\uparrow, \boldsymbol{\nabla} n_\downarrow)\,\mathrm{d}\mathbf{r}, \tag{3.40}$$

and thus these functionals are semi-local. Many examples of this functional exist,[93–97] with the most notable examples are that of Perdew and Wang (PW91)[98] and that of Perdew, Burke and Ernzerhof (PBE)[99].

A further extension are meta-GGAs, which include the Laplacian (second-order derivative) of the electron density; and thus are still semi-local. They offer improvements on the energetics and structural properties of compounds, as well as improved band gap estimations. Examples of meta-GGA functionals include TPSS,[100] the modified Becke-Johnson potential,[101] SCAN[102] and rSCAN[103].

There exists a set of functionals that attempt to further improve results by incorporating a portion of the exchange energy deduced by the HF theory. Recall that this quantity is known exactly, equation 3.14. They also incorporate GGA exchange and correlation. Because of this, they are non-local and thus expensive to use, but are typically most accurate. These are known as hybrid functionals, and multiple, popular examples exist.[104–107]

Building on hybrid functionals, there exist double hybrids. These functionals attempt to incorporate virtual (unoccupied) Kohn–Sham orbitals via perturbation theory. Discussions regarding these functionals are available.[108]

Finally, there exists additional methods that can account for very highly correlated materials,[109, 110] dispersion corrections,[111–115] amongst others. There are many reviews that are dedicated to exchange-correlation functionals and their performance.[116]

3.4 Implementation methodology

Until this point, we have outlined how to solve the Kohn-Sham equations to obtain the Kohn-Sham orbitals, $\psi_i(\mathbf{r})$, but not detailed how this - seemingly daunting - process is implemented in a computer program. We now outline the tools required to turn the theory into practice.

3.4.1 The reciprocal lattice

We begin by defining a set of three basis vectors, $\mathbf{a}_1$, $\mathbf{a}_2$ and $\mathbf{a}_3$. We can then construct a repeating lattice, where the unit is defined by the three basis vectors, with a lattice point, $\mathbf{R}_{n_1,n_2,n_3}$, given as,

$$\mathbf{R}_{n_1,n_2,n_3} = n_1\mathbf{a}_1 + n_2\mathbf{a}_2 + n_3\mathbf{a}_3, \tag{3.41}$$

where n_1, n_2 and n_3 are integral. We now define three new basis vectors that satisfy, $\mathbf{a}_i \cdot \mathbf{b}_j = 2\pi\delta_{ij}$, and are given as,

$$\mathbf{b}_1 = \frac{2\pi}{\Omega}\mathbf{a}_2 \times \mathbf{a}_3, \tag{3.42}$$

$$\mathbf{b}_2 = \frac{2\pi}{\Omega}\mathbf{a}_3 \times \mathbf{a}_1, \tag{3.43}$$

$$\mathbf{b}_3 = \frac{2\pi}{\Omega}\mathbf{a}_1 \times \mathbf{a}_2, \tag{3.44}$$

where $\Omega = \mathbf{a}_1 \cdot \mathbf{a}_2 \times \mathbf{a}_3$ is the signed cell volume. From this point, we can define the reciprocal lattice vector, $\mathbf{G}_{m_1,m_2,m_3}$,

$$\mathbf{G}_{m_1,m_2,m_3} = m_1\mathbf{b}_1 + m_2\mathbf{b}_2 + m_3\mathbf{b}_3, \tag{3.45}$$

where each of m_1, m_2 and m_3 are integral. This defines the points in reciprocal space.

3.4.2 The Brillouin zone

The Brillouin zone is defined around the gamma point, $\mathbf{G} = \mathbf{0}$. All points in the reciprocal space that are closest to this lattice point are defined to be in the first Brillouin zone. All those where this point is second closest are defined to be in the second Brillouin zone, and so on. Each of the volume of these zones (cells) are equal and high points of symmetry are denoted certain letters e.g $\mathbf{\Gamma} = \mathbf{0}$. The simple cubic and simple hexagonal lattices are self-dual, in that their real space symmetry is the same as their reciprocal space symmetry. The face-centred cubic lattice, however, is body-centred cubic in reciprocal space; and vice-versa. For extra clarity, a representation of an example two-dimensional reciprocal lattice is displayed in figure 3.1.

3.4.3 Bloch's theorem

We wish to represent our Kohn-Sham orbitals on these lattices. Across unit cells, due to the repeating pattern of ions, our external potential, $V_{\text{eff}}[n(\mathbf{r})]$ (equation 3.37), will also periodically repeat. Our Hamiltonian must therefore be periodic and thus invariant to lattice translations. Supposing we have some translation

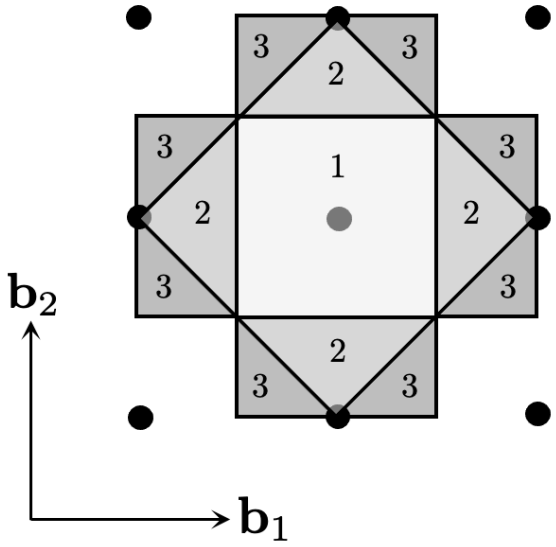


Figure 3.1: An example of a two-dimensional reciprocal space lattice with lattice vectors $\mathbf{b}_1$ and $\mathbf{b}_2$. The first three Brillouin zones are indicated.

operator, $T_{\mathbf{n}}$, it must commute with the Hamiltonian, and the Kohn-Sham orbitals are thus its appropriate eigenstates,

$$T_{\mathbf{n}}\psi_j(\mathbf{r}) = t_{\mathbf{n}}\psi_j(\mathbf{r}), \tag{3.46}$$

with $\mathbf{n}$ a composite index for n_1, n_2, n_3. A translation in space should not stretch or contract the state, $\psi_j(\mathbf{r})$, and so, $|t_{\mathbf{n}}| = 1$, meaning that $t_{\mathbf{n}} = e^{2\pi i q_{\mathbf{n}}}$. We have previously defined a useful basis to represent $2\pi q_{\mathbf{n}}$ by choosing,

$$2\pi q_{\mathbf{n}} = \mathbf{k} \cdot \mathbf{T}_{\mathbf{n}}, \tag{3.47}$$

where $\mathbf{k}$ is a vector in the reciprocal space.

We can write equation 3.46 as,

$$\psi_j(\mathbf{r} + \mathbf{T}_{\mathbf{n}}) = e^{i\mathbf{k}\cdot\mathbf{T}_{\mathbf{n}}}\psi_j(\mathbf{r}), \tag{3.48}$$

and so the wavefunction is periodic up to a phase factor. Choosing, $\psi_{j,\mathbf{k}}(\mathbf{r}) = e^{i\mathbf{k}\cdot\mathbf{r}}u_{j,\mathbf{k}}(\mathbf{r})$, we find,

$$e^{i\mathbf{k}\cdot(\mathbf{r}+\mathbf{T}_{\mathbf{n}})}u_{j,\mathbf{k}}(\mathbf{r} + \mathbf{T}_{\mathbf{n}}) = e^{i\mathbf{k}\cdot\mathbf{T}_{\mathbf{n}}}e^{i\mathbf{k}\cdot\mathbf{r}}u_{j,\mathbf{k}}(\mathbf{r}), \tag{3.49}$$

which is satisfied for $u_{j,\mathbf{k}}(\mathbf{r} + \mathbf{T}_{\mathbf{n}}) = u_{j,\mathbf{k}}(\mathbf{r})$.

Thus, for a periodic potential, V_{eff}, its Hamiltonian eigenstates will be Bloch waves, $\psi_{j,\mathbf{k}}(\mathbf{r}) = e^{i\mathbf{k}\cdot\mathbf{r}}u_{j,\mathbf{k}}(\mathbf{r})$, where $u_{j,\mathbf{k}}(\mathbf{r})$ is periodic, that is $u_{j,\mathbf{k}}(\mathbf{r}+\mathbf{T_n}) = u_{j,\mathbf{k}}(\mathbf{r})\ \forall\ \mathbf{T_n}$. This is Bloch's theorem.

The previous number of infinite electrons (and thus infinite eigenstates) have been cast over electronic *bands*, indexed by j. There will still exist an infinite number of conduction bands, but a finite number of valence bands. The higher energy conduction bands will have a lower contribution to the physics of the material, which is dominated by the bands near the Fermi level. Within each band, the infinite nature of the crystal has been mapped onto the index $\mathbf{k}$, however, these $\mathbf{k}$ values are only unique up to $\mathbf{k}+\mathbf{G_m}$. Therefore, we can restrict our consideration of $\mathbf{k}$ up to the first Brillouin zone and not lose generality.

3.4.4 Planewaves

We take advantage of Bloch's theorem and expand our wavefunction in terms of planewaves,

$$\psi_{j,\mathbf{k}}(\mathbf{r}) = \sum_{\mathbf{G}} c_{j,\mathbf{k}}(\mathbf{G})e^{i(\mathbf{k}+\mathbf{G})\cdot\mathbf{r}}, \tag{3.50}$$

where each of $\mathbf{G}$ are the lattice vectors. There are many choices of functions to expand the orbitals, including Gaussian functions ($\sim r^{\ell}e^{-\alpha r^2}$), Slater functions ($\sim r^{n-1}e^{-\alpha r}$) and linearised augmented planewaves. The latter of which uses a muffin-tin approximation to treat both valence and core electrons in the same manner. We choose planewaves here for the benefits of implicit periodicity and also because the kinetic energy operator, T, is diagonal in reciprocal space. The evaluation of T requires the computation of derivatives that, if performed on a real-space grid, require a finite difference method. The accuracy of this therefore depends on the grid density, and can lead to atoms experiencing fictitious forces if not exactly on a grid point. The transformation into reciprocal space is therefore highly valuable, and is done by a fast-Fourier transform (FFT). Codes for these type of transformations are incredibly fast (hence the name) and are widely available.

The infinite summation in equation 3.50 is truncated by choice of a *cut-off energy*, defined as,

$$E_{\text{cut}} \geq \frac{|\mathbf{k}+\mathbf{G}|^2}{2}, \tag{3.51}$$

which determines the number of **G** vectors to consider in the calculation that are commensurate with the unit cell. It is straightforward to determine a reasonable level of convergence on the truncation by systematically increasing E_{cut} until the change in value of the property under study is below a chosen tolerance value.

The electron density is calculated from the, now **k** dependent, wavefunctions over the first Brillouin zone,

$$n(\mathbf{r}) = \frac{1}{\Omega_{\text{BZ}_1}} \int_{\Omega_{\text{BZ}_1}} n_{\mathbf{k}}(\mathbf{r})\, \mathrm{d}\mathbf{k}, \tag{3.52}$$

where Ω_{BZ_1} is the volume of the first Brillouin zone and the **k**-dependent density is,

$$n_{\mathbf{k}}(\mathbf{r}) = \sum_i |\psi_{i,\mathbf{k}}(\mathbf{r})|^2. \tag{3.53}$$

In practice, equation 3.52 reduces to a sum over chosen **k**-vectors (or **k**-points),

$$n(\mathbf{r}) \simeq \sum_{\mathbf{k}} n_{\mathbf{k}}(\mathbf{r}). \tag{3.54}$$

Monkhorst and Pack outline methods to generate sets of **k**-points to consider.[117] In practice, we may apply the symmetries of the cell and consider a reduced set of points, which then have appropriate weightings to account for those excluded.

These **k**-points define the supercell, which approximates the infinitely repeating structure of real crystals very well for a sufficiently large **k**-point sample. Properties of molecules, of which do not have a repeating structure, are obtainable by considering only one **k**-point - typically the $\mathbf{\Gamma}$ point - provided the defined unit cell is large enough.

3.4.5 Frozen core approximation

Now we have a solid foundation for both representing our wavefunction with the planewave basis; and solving for it, using DFT. The approximations made thus far, in DFT for example, have allowed us to progress mathematically and physically with our theory. The following few sections, however, turn to computational considerations that must be made to ensure the calculations are not only accurate, but feasible in regard to computational time and power.

We begin with the frozen core approximation, whereby we split the core and valence electrons.[118] Those states that are bound tightly to the nucleus are considered core and the others considered valence. Exactly where the line is drawn in regard to this splitting is down to choice. Typically, the valence states will consist of only a few electrons of each atom (typically less than ten at most). This approximation provides the advantage of having to consider only the valence states in the calculation of chemical properties. The core states are typically highly rigid and are not greatly affected by the local chemical environment. As a general rule, we choose the core states to be that of the heaviest noble gas with atomic number lower than the element. For example, in silicon, we would typically choose its 3s and 3p states as valence and the 1s, 2s and 2p (neon) as core. Inclusion of lower energy states as valence, particularly d and f electrons, are typically decided on their participation in hybridisation and the ability to construct a reasonable pseudopotential, as discussed in the following section. Shallow states (those that are not deep in the low energy region) may also need to be included to avoid the creation of spurious ghost states that can invalidate the pseudopotential.

3.4.6 Pseudopotentials

The valence states pose problems nearer the nucleus. In this region, they are highly oscillatory - due to the orthogonality requirements to the core states - and thus require a very large number of planewaves to represent them accurately. The primary cause of these problems is the very strong, divergent Coulomb term in the effective potential, $V_{\text{eff}}[n(\mathbf{r})]$. We therefore introduce a weaker potential, that acts

below a defined cut-off radius, $\Omega_\ell^{\mathbf{R}}$, for each of angular momentum channel, ℓ, of atom, $\mathbf{R}$. It is typical that, $\Omega_\ell^{\mathbf{R}} = \Omega^{\mathbf{R}}\ \forall\ \ell$, but we keep the general notation here.

To construct a pseudopotential, we:

1. Solve the radial, all-electron (core and valence states) DFT calculation on the isolated atom. These are $\phi^{\mathbf{R}}_{\tau,\ell,m}(\mathbf{r})$ with eigenvalues $\varepsilon^{\mathbf{R}}_{\tau,\ell,m}$.

2. Within $\Omega_\ell^{\mathbf{R}}$, we modify the *valence* states of $\phi^{\mathbf{R}}_{\tau,\ell,m}(\mathbf{r})$ to be smooth and nodeless. This is done by ensuring that its Fourier transform decays rapidly. These are $\tilde{\phi}^{\mathbf{R}}_{\tau,\ell,m}(\mathbf{r})$.

3. The radial Kohn-Sham equations are then inverted to solve for a new effective potential, $\tilde{V}^{\mathbf{R}}_{\text{eff}}(\mathbf{r})$,

$$\tilde{V}^{\mathbf{R}}_{\text{eff}}(\mathbf{r}) = \frac{1}{2}\frac{1}{\tilde{\phi}^{\mathbf{R}}_{\tau,\ell,m}(\mathbf{r})}\nabla^2\tilde{\phi}^{\mathbf{R}}_{\tau,\ell,m}(\mathbf{r}) + \varepsilon^{\mathbf{R}}_{\tau,\ell,m}, \tag{3.55}$$

   in which we impose that we recover the scattering properties of each angular momentum channel, and above the cut-off radius we obtain the all-electron potential, $V^{\mathbf{R}}_{\text{eff}}$, that is, $|\mathbf{r}| \geq \Omega_\ell^{\mathbf{R}} \implies \tilde{V}^{\mathbf{R}}_{\text{eff}}(\mathbf{r}) = V^{\mathbf{R}}_{\text{eff}}(\mathbf{r})$.

We then name $\tilde{V}^{\mathbf{R}}_{\text{eff}}(\mathbf{r})$ as the pseudopotential for the atom at $\mathbf{R}$. We now have a weaker potential on the valence states of our calculation, with the core states as part of the frozen core potential. An all-electron potential, from which a pseudopotential is then generated, is shown in figure 3.2. We see the reduction in oscillatory nature in the pseudised states compared to the all-electron states in figure 3.3.

We may choose to have more than one state per angular momentum channel, hence we have included an index to account for this, τ. The total number of states per channel is denoted N_ε. In any case, we begin by solving the eigenvalue problem and thus obtain the state at its eigenenergy. For $N_\varepsilon > 1$, we solve for unbound states, typically with energies of 0.25, 0.5, ... a.u.. Normally, $N_\varepsilon \not> 3$. These unbound states, as the name suggests, do not tend toward zero at $r \to \infty$. One may be concerned that some of their integrals are thus formally ill-defined. However, we implicitly consider only the state inside its augmentation region. We also remember

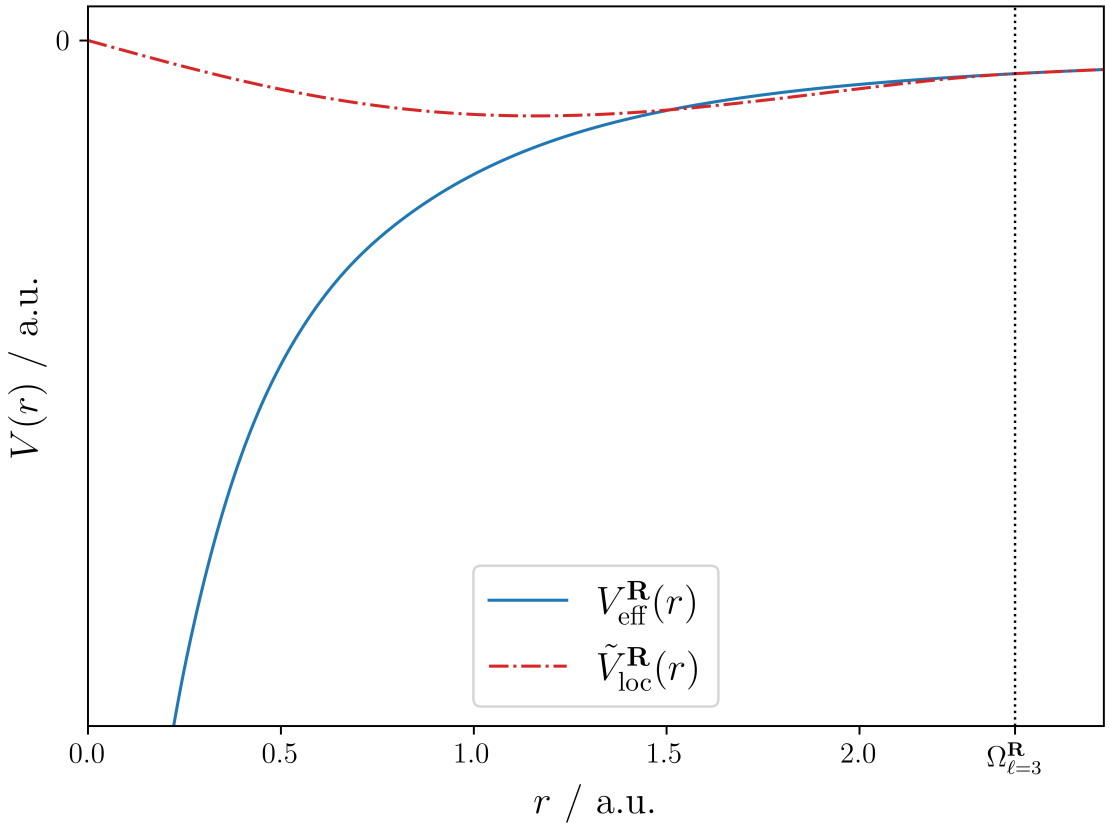


Figure 3.2: Plot of the local part of the pseudopotential, $\tilde{V}_{\text{loc}}^{\mathbf{R}}(r)$, and all-electron potential, $V_{\text{eff}}^{\mathbf{R}}(r)$, of a lead atom, Pb. The $\ell = 3$ angular momentum channel is chosen for the local part as it is chemically inactive. The pseudopotential is much weaker than the all-electron in the region nearer the nucleus. Above the cut-off radius, $\Omega_{\ell=3}^{\mathbf{R}} = 2.403$ / a.u., the projectors are zero, causing the non-local part to vanish and the local and all-electron to be equivalent.

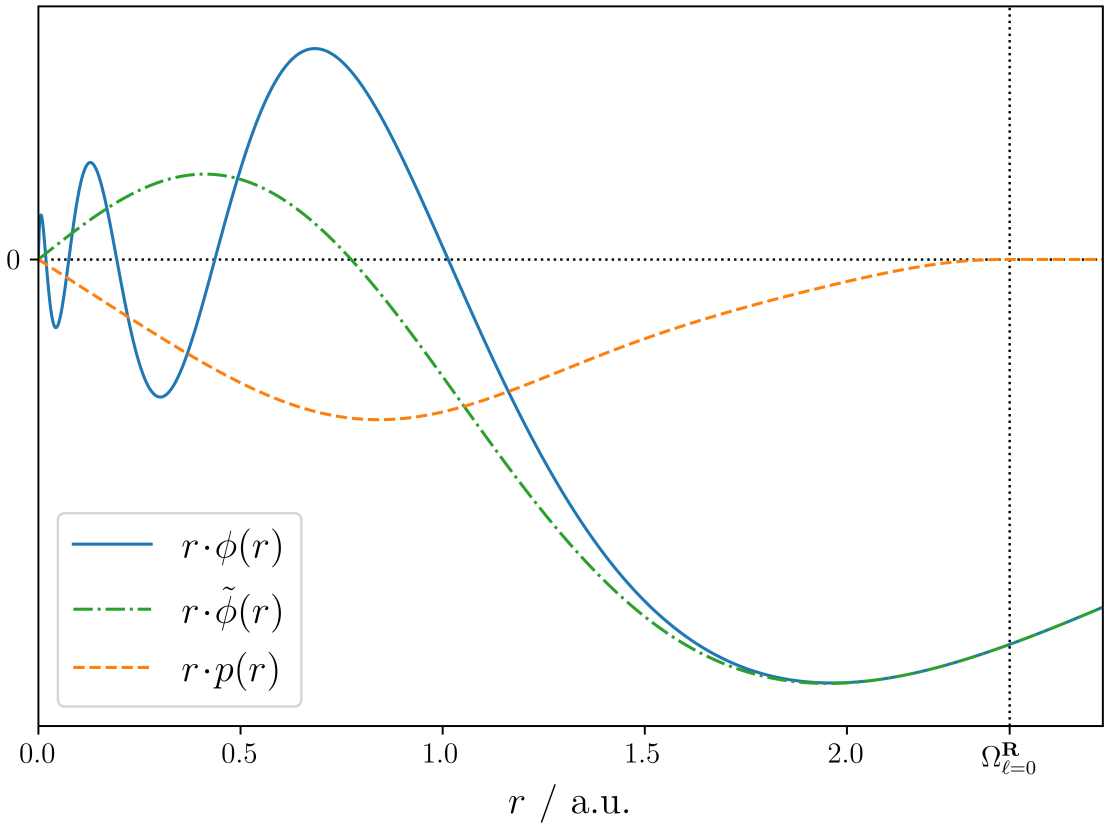


Figure 3.3: The atomic all-electron, $\phi(r)$, and pseudo-, $\tilde{\phi}(r)$, wavefunctions with the corresponding projector, $p(r)$, for lead, Pb, for $n = 6$ and $\ell = 0$. The pseudised state is much less oscillatory in nature than the all-electron. At $\Omega^{\mathbf{R}}_{\ell=0} = 2.403$ / a.u. and above, the states are equivalent, and the projector is zero. Irrelevant indices have been suppressed for brevity.

that these objects need not be physical and are only mathematical tools for use in the projector augmented-wave method; outlined later in 3.4.7.

One difficulty that must be considered for the pseudopotential are the appearance of unphysical 'ghost-states' that lie in energy near or below the valence states. A pseudopotential can be ensured to contain no 'ghost-states' by careful choice of the local potential (discussed in section 3.4.7), $\tilde{V}_{\text{loc}}$, and cut-off radius, $\Omega_\ell^{\mathbf{R}}$. Methods have been outlined on how to identify and remove these types of states.[119]

Beyond $\Omega_\ell^{\mathbf{R}}$, as with the potentials, the all-electron and pseudo-wavefunctions are also equal, $\tilde{\phi}^{\mathbf{R}}_{\tau,\ell,m}(\mathbf{r}) = \phi^{\mathbf{R}}_{\tau,\ell,m}(\mathbf{r})$. The larger $\Omega_\ell^{\mathbf{R}}$ is, the smaller the basis set, defined by E_{cut}, is able to be. The regions cannot be arbitrarily large, however, so as not to incorrectly describe the chemical bonding that is dictated by the interstitial regions of valence charge density. These pseudopotentials are typically 'descreened' by the Coulomb and exchange-correlation potentials to give what is named the ionic pseudopotential.

Hellmann is typically credited with the first use of pseudopotentials by devising a binding theory for metals.[120, 121] Their use became more common when Antončík[122, 123] and Phillips and Kleinman[124] devised a method to implement a weaker potential for the study of metals and semiconductors.

Norm-conserving pseudopotentials (NCPs) impose that the charge, within $\Omega_\ell^{\mathbf{R}}$, of the all-electron and pseudo-wavefunctions are equal, that is,

$$\langle \phi^{\mathbf{R}}_{\tau,\ell,m} | \phi^{\mathbf{R}}_{\tau,\ell,m} \rangle = \langle \tilde{\phi}^{\mathbf{R}}_{\tau,\ell,m} | \tilde{\phi}^{\mathbf{R}}_{\tau,\ell,m} \rangle, \tag{3.56}$$

for a given atom at $\mathbf{R}$. A popular choice of this type of pseudopotential was introduced by Troullier and Martins.[125] Unfortunately, this constraint can sometimes lead to high frequency pseudo-wavefunctions, particularly in d and f states, which was the initial problem the pseudopotentials attempted to solve. In these cases, more planewaves (higher E_{cut}) are required to achieve converged results.

To build on this, the constraint required by NCPs can be relaxed, to introduce ultrasoft pseudopotentials (USPs).[126] These pseudopotentials can provide much greater accuracy. Lower cut-off energies (and thus higher computational efficiency)

can be used whilst retaining converged results. The drawback with USPs is their implementation into electronic structure codes - there are some additional complexities involved in the mathematical equations.

We begin with the central quantity, the charge augmentation, which represents the difference in charge between the all-electron and pseudo-systems, within $\Omega_\ell^{\mathbf{R}}$,

$$q^{\mathbf{R}}_{\tau,\ell,m;\tau',\ell',m'} = \langle \phi^{\mathbf{R}}_{\tau,\ell,m} | \phi^{\mathbf{R}}_{\tau',\ell',m'} \rangle - \langle \tilde{\phi}^{\mathbf{R}}_{\tau,\ell,m} | \tilde{\phi}^{\mathbf{R}}_{\tau',\ell',m'} \rangle. \tag{3.57}$$

We also define the charge augmentation function,

$$\begin{aligned} Q^{\mathbf{R}}_{\tau,\ell,m;\tau',\ell',m'}(\mathbf{r}) &= \langle \phi^{\mathbf{R}}_{\tau,\ell,m} | \mathbf{r} \rangle \langle \mathbf{r} | \phi^{\mathbf{R}}_{\tau',\ell',m'} \rangle - \langle \tilde{\phi}^{\mathbf{R}}_{\tau,\ell,m} | \mathbf{r} \rangle \langle \mathbf{r} | \tilde{\phi}^{\mathbf{R}}_{\tau',\ell',m'} \rangle, \\ &= \left[\phi^{\mathbf{R}}_{\tau,\ell,m}(r) \phi^{\mathbf{R}}_{\tau',\ell',m'}(r) - \tilde{\phi}^{\mathbf{R}}_{\tau,\ell,m}(r) \tilde{\phi}^{\mathbf{R}}_{\tau',\ell',m'}(r) \right] Y^*_{\ell,m}(\theta,\varphi) Y_{\ell',m'}(\theta,\varphi), \end{aligned} \tag{3.58}$$

and notice that,

$$q^{\mathbf{R}}_{\tau,\ell,m;\tau',\ell',m'} = \int Q^{\mathbf{R}}_{\tau,\ell,m;\tau',\ell',m'}(\mathbf{r}) \, \mathrm{d}\mathbf{r}, \tag{3.59}$$

due to the resolution of the identity.

The pseudo-Hamiltonian, $\tilde{H}$, satisfies the following pseudo-eigenvalue problem,

$$\tilde{H} |\tilde{\psi}\rangle = \varepsilon S |\tilde{\psi}\rangle, \tag{3.60}$$

where we omit the band index, i, and $\mathbf{k}$-point index, $\mathbf{k}$, from this point onwards. The overlap matrix, S, is,

$$S = \mathbb{1} + \sum_{\mathbf{R}} \sum_{\tau,\ell,m} \sum_{\tau',\ell',m'} |p^{\mathbf{R}}_{\tau,\ell,m}\rangle q^{\mathbf{R}}_{\tau,\ell,m;\tau',\ell',m'} \langle p^{\mathbf{R}}_{\tau',\ell',m'}|, \tag{3.61}$$

that assures the norm of the wavefunction. Each of $|p^{\mathbf{R}}_{\tau,\ell,m}\rangle$ are localised, atomic projectors, exampled in figure 3.3. These are calculated alongside the generation of the pseudo-wavefunctions, and they satisfy the orthogonality, $\langle p^{\mathbf{R}}_{\tau,\ell,m} | \tilde{\phi}^{\mathbf{R}'}_{\tau',\ell',m'} \rangle = \delta_{\mathbf{R}\mathbf{R}'} \delta_{\tau\tau'} \delta_{\ell\ell'} \delta_{mm'}$, and completeness, $\sum_{\tau,\ell,m} |\tilde{\phi}^{\mathbf{R}}_{\tau,\ell,m}\rangle \langle p^{\mathbf{R}}_{\tau,\ell,m}| = \mathbb{1} \, \forall \, \mathbf{R}$, conditions.

One final point to note is required for the consideration of representing these quantities computationally. $Q^{\mathbf{R}}_{\tau,\ell,m;\tau',\ell',m'}(\mathbf{r})$ can itself be highly oscillatory in nature, and as a result, is pseudised itself with its own inner core region. In its construction, this pseudised augmentation is constrained to preserve the charge

moments, meaning the electrostatic potential in space remains unchanged.[127] This quantity is also represented on a finer grid of points, and meta-GGA functionals (such as rSCAN), result in the accuracy of the calculations being very sensitive to the chosen fine grid scale.

3.4.7 Projector augmented-wave method

So far, we have defined the use of planewaves as a basis set to expand our wavefunctions and the use of pseudopotentials to make this a feasible method computationally. The pseudopotentials have drastically reduced the size requirement of the basis set but have come at a cost of making the region near each nucleus non-physical. For those properties that are derived from outside the core region, such as total energies or geometries, the pseudopotential approach is sufficient. However, properties which originate from the inner region, such as nuclear magnetic resonance parameters, will be described very poorly by this method alone.

We turn to the projector augmented-wave (PAW) method, which allows us to recover the information lost due to the pseudisation of the wavefunction. This method was described by Van de Walle and Blöchl.[50, 128] We first define a linear transformation, T, that provides a mapping between the valence pseudo-wavefunction, $|\tilde{\psi}\rangle$, and the valence all-electron wavefunction, $|\psi\rangle = T|\tilde{\psi}\rangle$, with,

$$T = \mathbb{1} + \sum_{\mathbf{R}} \sum_{\tau,\ell,m} \left[|\phi^{\mathbf{R}}_{\tau,\ell,m}\rangle - |\tilde{\phi}^{\mathbf{R}}_{\tau,\ell,m}\rangle \right] \langle p^{\mathbf{R}}_{\tau,\ell,m}|. \tag{3.62}$$

We recall the augmentation region, $\Omega^{\mathbf{R}}_{\ell}$, and impose the following rules:

1. The atomic all-electron and pseudo-wavefunctions coincide outside this region, $|\mathbf{r}| \geq \Omega^{\mathbf{R}}_{\ell} \implies \phi^{\mathbf{R}}_{\tau,\ell,m}(\mathbf{r}) = \tilde{\phi}^{\mathbf{R}}_{\tau,\ell,m}(\mathbf{r}) \; \forall \; \tau, m.$

2. The projectors vanish outside this region, $|\mathbf{r}| \geq \Omega^{\mathbf{R}}_{\ell} \implies p^{\mathbf{R}}_{\tau,\ell,m}(\mathbf{r}) = 0 \; \forall \; \tau, m.$

3. The set of all-electron atomic wavefunctions form a complete set and can represent any physically reasonable all-electron wavefunction inside the region, $|\psi_{\Omega_{\mathbf{R}}}\rangle = \sum_{\tau,\ell,m} |\phi^{\mathbf{R}}_{\tau,\ell,m}\rangle\langle p^{\mathbf{R}}_{\tau,\ell,m}|\phi^{\mathbf{R}}_{\tau,\ell,m}\rangle$.

4. No two $\Omega_\ell^{\mathbf{R}}$ are defined such that there is any overlap in three-dimensional space.

From $\langle\psi|O|\psi\rangle = \langle\tilde{\psi}|T^\dagger OT|\tilde{\psi}\rangle \equiv \langle\tilde{\psi}|\tilde{O}|\tilde{\psi}\rangle$, we notice that an operator, O, has its pseudised form given as $\tilde{O} = T^\dagger OT$. The double summation of $\mathbf{R}$ reduces to one, as long as O is sufficiently local. This is true of most physically relevant operators, including the electronic Hamiltonian and those that appear in the calculation of chemical shifts and hyperfine parameters. Inserting the definition of the transformation gives,

$$\tilde{O} = O + \sum_{\mathbf{R}} \sum_{\tau,\ell,m} \sum_{\tau',\ell',m'} |p^{\mathbf{R}}_{\tau,\ell,m}\rangle \left[\langle\phi^{\mathbf{R}}_{\tau,\ell,m}|O|\phi^{\mathbf{R}}_{\tau',\ell',m'}\rangle - \langle\tilde{\phi}^{\mathbf{R}}_{\tau,\ell,m}|O|\tilde{\phi}^{\mathbf{R}}_{\tau',\ell',m'}\rangle\right] \langle p^{\mathbf{R}}_{\tau',\ell',m'}|. \tag{3.63}$$

We now have the tools to explicitly construct the aforementioned pseudo-Hamiltonian, which - along with the kinetic energy - consists of a local and a non-local part,

$$\tilde{H} = \frac{p^2}{2} + \tilde{V}_{\text{loc}} + \tilde{V}_{\text{non-loc}}, \tag{3.64}$$

by insertion of 3.2 into equation 3.63.

Typically, the local potential is chosen to represent the lowest angular momentum state that is not chemically active. With USPs, we have invalidated the physical nature of the active channels, due to the relaxation of the norm constraint, and thus this is a requirement. This means we need at least two projectors per angular momentum channel to reproduce the scattering properties; hence why we introduced the τ index. The drastically smaller basis set required for the computations typically outweighs this drawback, however. In the NCP scheme, if desired, we may choose the potential to be a chemically active channel, and we could drop the τ index.

The non-local contribution is,

$$\tilde{V}_{\text{non-loc}} = \sum_{\mathbf{R}} \sum_{\tau,\ell,m} \sum_{\tau',\ell',m'} |p^{\mathbf{R}}_{\tau,\ell,m}\rangle D^{\mathbf{R}}_{\tau,\ell,m;\tau',\ell',m'} \langle p^{\mathbf{R}}_{\tau',\ell',m'}|, \tag{3.65}$$

with,

$$D^{\mathbf{R}}_{\tau,\ell,m;\tau',\ell',m'} = D^{\mathbf{R},0}_{\tau,\ell,m;\tau',\ell',m'} + \int V_{\text{eff}}[n(\mathbf{r})]\, Q^{\mathbf{R}}_{\tau,\ell,m;\tau',\ell',m'}(\mathbf{r})\, \mathrm{d}\mathbf{r}. \tag{3.66}$$

The $D^{\mathbf{R},0}_{\tau,\ell,m;\tau',\ell',m'}$ coefficients characterise the pseudopotential, and depend on the arbitrary choice of the local potential.[127] They are chosen on the basis of the splitting between the local and non-local potentials, and ensure we recover the scattering properties of each angular momentum channel.

Finally, the valence charge density can be recovered by inserting the operator $|\mathbf{r}\rangle\langle\mathbf{r}|$ into equation 3.63,

$$n(\mathbf{r}) = |\tilde{\psi}(\mathbf{r})|^2 + \sum_{\mathbf{R}} \sum_{\tau,\ell,m} \sum_{\tau',\ell',m'} Q^{\mathbf{R}}_{\tau,\ell,m;\tau',\ell',m'}(\mathbf{r})\, \rho^{\mathbf{R}}_{\tau,\ell,m;\tau',\ell',m'}, \tag{3.67}$$

where,

$$\rho^{\mathbf{R}}_{\tau,\ell,m;\tau',\ell',m'} = \langle\tilde{\psi}|p^{\mathbf{R}}_{\tau,\ell,m}\rangle\langle p^{\mathbf{R}}_{\tau',\ell',m'}|\tilde{\psi}\rangle. \tag{3.68}$$

The first term is the 'soft' density: the contribution from the density extended throughout the unit cell. And the second term is the 'hard' density: the contribution that is localised on the atomic sites.

3.5 Relativistic quantum mechanics

So far, we have ignored the effects of relativity. This all stemmed from the non-relativistic Schrödinger equation, equation 3.3. It has been long known that the effects of Einstein's theory of special relativity play an important role in characterising the properties of molecules and crystals. There are many texts dedicated to outlining the theory of relativity in regard to quantum chemistry.[129–132] Capturing the effects for the computation of nuclear magnetic resonance parameters is of great importance, and often a non-relativistic treatment is not sufficient, even for some simple systems.[66, 133–135] The effects of relativity become more important with increasing atomic number. Typically, one would expect to substitute the non-relativistic wave equation with one that accounts for relativity. Within the PAW method, we will find, that we must also edit the form of the operators - and in cases even the formalism itself - to obtain the correct results.

The introduction of spinor wavefunctions and spin-dependent operators has some subtle notation considerations, which are detailed explicitly for clarity in appendix A.

3.5.1 Dirac equation

We can start from the time-independent Schrödinger equation, 3.3, and take Dirac's approach[136] of solving its inconsistency with special relativity by imposing that the kinetic part of the Hamiltonian follows the characteristic energy-momentum relation,

$$T^2 = c^4 + p^2c^2. \tag{3.69}$$

Making progress at this point might seem difficult, but we can demand that the right-hand side of this equation be the square of a - currently unknown - function that is linear in momentum,

$$c^4 + p^2c^2 = (\beta c^2 + c\boldsymbol{\alpha} \cdot \mathbf{p})^2. \tag{3.70}$$

This is the most general linear equation of $\mathbf{p}$, and we can impose that it reduces to the left-hand side with the following conditions,

$$\beta^2 = \mathbb{1}, \tag{3.71}$$

$$\{\alpha_i, \beta\} = \mathbb{0}, \tag{3.72}$$

$$\{\alpha_i, \alpha_j\} = \begin{cases} \mathbb{1} & i = j, \\ \mathbb{0} & i \neq j. \end{cases} \tag{3.73}$$

Evidently, the solution to these equations does not allow any of α_i or β to be scalar numbers. The simplest solution (or one of) to these equations is,

$$\alpha_i = \begin{pmatrix} \mathbb{0}_2 & \sigma_i \\ \sigma_i & \mathbb{0}_2 \end{pmatrix}, \qquad \beta = \begin{pmatrix} \mathbb{1}_2 & \mathbb{0}_2 \\ \mathbb{0}_2 & -\mathbb{1}_2 \end{pmatrix}, \tag{3.74}$$

where $\mathbb{0}_2$ is the 2×2 null matrix, $\mathbb{1}_2$ is the 2×2 identity matrix and σ_i are the Pauli matrices,

$$\sigma_1 = \begin{pmatrix} 0 & 1 \\ 1 & 0 \end{pmatrix}, \qquad \sigma_2 = \begin{pmatrix} 0 & -i \\ i & 0 \end{pmatrix}, \qquad \sigma_3 = \begin{pmatrix} 1 & 0 \\ 0 & -1 \end{pmatrix}. \tag{3.75}$$

Inserting $c\boldsymbol{\alpha} \cdot \mathbf{p} + \beta c^2$ as the kinetic energy into the Schrödinger equations leads us to,

$$\mathcal{H}|\boldsymbol{\Psi}\rangle = i\frac{\mathrm{d}}{\mathrm{d}t}|\boldsymbol{\Psi}\rangle, \tag{3.76}$$

which is the time-dependent Dirac equation, and,

$$\mathcal{H}|\boldsymbol{\Psi}\rangle = E|\boldsymbol{\Psi}\rangle, \tag{3.77}$$

which is the time-independent Dirac equation. The Hamiltonian is,

$$\mathcal{H} = \beta c^2 + c\boldsymbol{\alpha} \cdot \mathbf{p} + V\mathbb{1}_4, \tag{3.78}$$

as found in reference [136]. Notice that the spatial derivative is only first-order (from the linear momentum operator, $\mathbf{p} = -i\boldsymbol{\nabla}$). This contrasts to the time-dependent Schrödinger equation where it is second-order. From equation 3.76, time and space are now treated equally in this formalism, which satisfies the requirements of special relativity.

The new quantity, $|\boldsymbol{\Psi}\rangle$, is a four-component, complex spinor. The spectrum of the Dirac Hamiltonian, $\mathcal{H}$, can contain negative values. These states, which were initially concerning to Dirac, are described in his hole theory: The reason electrons do not fall into these lower energy eigenstates is because they are all already filled. The Pauli exclusion principle then stops electrons from occupying these filled states. It was hypothesised that if one were to be unfilled, then it would act as an electron with a positive charge. Whilst Dirac's reasoning was not entirely accurate (Feynman later giving a more formal explanation), the antimatter particle that followed the predicted properties, the positron, was found.[137]

3.5.2 Introducing an electromagnetic field

Incorporating the effects of an electromagnetic field, acting on an electron, requires two additional considerations in the Hamiltonian. Firstly, the momentum $\mathbf{p}$ becomes the canonical momentum, $\boldsymbol{\pi}$,

$$\mathbf{p} \to \boldsymbol{\pi} = \mathbf{p} + \frac{1}{c}\mathbf{A}, \tag{3.79}$$

where $\mathbf{A}$ is the magnetic vector potential for a magnetic field, $\mathbf{B} = \boldsymbol{\nabla} \times \mathbf{A}$. The potential term, V, will also contain the scalar electric potential, $-\Phi$. We keep the potential general for now, and so our Dirac Hamiltonian is,

$$\mathcal{H} = \beta c^2 + c\boldsymbol{\alpha} \cdot \boldsymbol{\pi} + V\mathbb{1}_4. \tag{3.80}$$

3.5.3 Relativistic corrections

The significance of the Dirac equation will not become fully clear without exploring it further and illuminating the physical terms encompassed in it. This can be done through, what is known as, a Foldy-Wouthuysen transformation.[138] This is algebraically demanding, but the process allows us to extract the three well-known corrections to the non-relativistic treatment, namely: 1) the first-order relativistic kinetic energy correction; 2) the Darwin term, and; 3) the spin-orbit coupling (SOC) term. The process also block-diagonalises the Hamiltonian, decoupling the Dirac spinor into two two-component spinors which still represent energy eigenstates. We jump to the final result in this section to allow for brevity and to focus on the physical interpretation of the key findings.

The Dirac Hamiltonian, expanded in terms of the relative sizes of its quantities to fourth-order, is as follows,

$$\mathcal{H} = \left(c^2 + \frac{\pi^2}{2} - \frac{p^4}{8c^2} - \frac{g}{4c}\boldsymbol{\Sigma}\cdot\mathbf{B}\right)\beta + \left(\frac{1}{8c^2}\nabla^2 V + V\right)\mathbb{1}_4 + \frac{1}{4c^2}\boldsymbol{\Sigma}\cdot\boldsymbol{\nabla}V\times\mathbf{p}, \quad 3.81$$

where we have inserted $g = 2$, and,

$$\Sigma_i = \begin{pmatrix}\sigma_i & \mathbb{0}_2\\ \mathbb{0}_2 & \sigma_i\end{pmatrix}. \quad 3.82$$

We also note that this Hamiltonian is block-diagonal and electronic energy eigenstates can be obtained from purely the upper components, which are,

$$\mathcal{H} = \left(c^2 + \frac{\pi^2}{2} - \frac{p^4}{8c^2} + \frac{1}{8c^2}\nabla^2 V + V\right)\mathbb{1}_2 + \frac{1}{2c^2}\mathbf{S}\cdot\boldsymbol{\nabla}V\times\mathbf{p} - \frac{g}{2c}\mathbf{S}\cdot\mathbf{B}, \quad 3.83$$

with $\mathbf{S} = \frac{1}{2}\boldsymbol{\sigma}$ and $\boldsymbol{\sigma}$ is the vector of Pauli matrices.

We now have all the foundations to discuss these relativistic corrections, of which, are order $\mathcal{O}\left(1/c^2\right)$.

Kinetic energy correction

The relativistic kinetic energy term is,

$$\mathcal{H}_{\mathrm{RKE}} = -\frac{p^4}{8c^2}\mathbb{1}_2. \quad 3.84$$

This correction term is relatively intuitive. Given that the energy of a relativistic particle is,

$$E = \sqrt{c^4 + c^2 p^2} \simeq c^2 + \frac{1}{2}p^2 - \frac{1}{8}\frac{p^4}{c^2} + \mathcal{O}\left(p^6/c^4\right), \tag{3.85}$$

where we have assumed that the momentum (equivalent to velocity; recall $m_e = 1$) of the particle is small in comparison to the speed of light, that is $\frac{p}{c} \ll 1$. The first term in this expression is the rest mass energy, the second is the non-relativistic kinetic energy and the third is the correction found through the expansion of the Dirac equation. Further Foldy-Wouthuysen transformations would extract the higher order terms found in this expansion.

Darwin term

The next term correction term is named the Darwin term,

$$\mathcal{H}_{\text{Darwin}} = \frac{1}{8c^2}\nabla^2 V, \tag{3.86}$$

which is particularly difficult to interpret physically. A rough description is that it represents the correction to the approximation of considering the electron to be a point-like particle. Near the nucleus, there exists the creation of electron-positron pairs. The positrons created may annihilate with a different electron to that which they originated with. This gives the illusion that the electrons 'hop' around in space and are therefore smeared.

Spin-orbit coupling term

The most important relativistic correction for this study is the introduction of the spin-orbit coupling term,

$$\mathcal{H}_{\text{SOC}} = \frac{1}{2c^2}\mathbf{S} \cdot \boldsymbol{\nabla} V \times \mathbf{p}. \tag{3.87}$$

This term can be best understood by observing the view from the rest frame of the electron. In this case, the nucleus - of which is positively charged - will be orbiting the electron. This moving charge creates a current loop which - according to the theory of special relativity - is equivalent to a magnetic field. The spin

of the electron therefore interacts with this field and splits the degeneracy of the eigenstates. In this framework, the orbital angular momentum, $\mathbf{L}$, is no longer a conserved quantity, as it now does not commute with our Hamiltonian. We must consider the total angular momentum, $\mathbf{J} = \mathbf{L} + \mathbf{S}$. The quantum number j is therefore the relevant quantity to uniquely identify our states, with $j = 1/2$ for $\ell = 0$ and $j = \ell \pm 1/2$ otherwise. The states are now said to be j-split in energy.

The magnitude of the splitting of the - previously degenerate - states increases with the atomic number, Z; proportionally Z^4 in hydrogen-like ions. As a result, this effect is of considerable importance when obtaining the energy levels of heavy atoms. Not only that, but light atoms that are bonded to heavier atoms will experience a large proportion of splitting, also. Typically, we may define 'heavy' to be selenium and beyond in the periodic table. These concepts are critical to the accurate determination of nuclear magnetic resonance parameters from first principles calculations. These factors motivate the requirement for the use of the Dirac equation to at least the two component level. From this, we need to modify the approach to incorporate the j split states in the pseudopotentials, and also to generalise the PAW method for use with spinor wavefunctions. These considerations are discussed in later sections.

As with all corrections discussed here, this effect is part of the fine structure corrections to the atomic energy levels. A magnetic field will also arise if a nucleus has a non-zero spin. The interactions of the electron spin with the nucleus spin are known as the hyperfine structure corrections. These, however, are an order of magnitude smaller than the fine structure.

3.5.4 Elimination of the small component

We can eliminate the positronic component of the states of the Dirac equation, which will later allow us to use an approximation that is easier to work with. We use the time-independent Dirac equation with an electromagnetic field.

The four-component wavefunction can be partitioned into two two-component spinors,

$$|\boldsymbol{\Psi}\rangle = \begin{pmatrix} |\Phi\rangle \\ |\chi\rangle \end{pmatrix}, \tag{3.88}$$

where $|\Phi\rangle$ is named the large component and $|\chi\rangle$ the small component. The Dirac equation, written explicitly, is then,

$$c\boldsymbol{\alpha}\cdot\boldsymbol{\pi}\begin{pmatrix} |\Phi\rangle \\ |\chi\rangle \end{pmatrix} + \beta c^2 \begin{pmatrix} |\Phi\rangle \\ |\chi\rangle \end{pmatrix} + V\begin{pmatrix} |\Phi\rangle \\ |\chi\rangle \end{pmatrix} = E\begin{pmatrix} |\Phi\rangle \\ |\chi\rangle \end{pmatrix}. \tag{3.89}$$

Recall the definitions of the $\boldsymbol{\alpha}$ and β matrices. These act on the spinor as follows,

$$c\boldsymbol{\sigma}\cdot\boldsymbol{\pi}\begin{pmatrix} |\chi\rangle \\ |\Phi\rangle \end{pmatrix} + c^2 \begin{pmatrix} |\Phi\rangle \\ -|\chi\rangle \end{pmatrix} + V\begin{pmatrix} |\Phi\rangle \\ |\chi\rangle \end{pmatrix} = E\begin{pmatrix} |\Phi\rangle \\ |\chi\rangle \end{pmatrix}. \tag{3.90}$$

Notice that the first spinor has had its components interchanged. We can shift the energy eigenvalue by the rest energy, $E \to E + c^2$. This is equivalent to introducing a phase factor in the wavefunction. We can then arrive to,

$$c\boldsymbol{\sigma}\cdot\boldsymbol{\pi}\begin{pmatrix} |\chi\rangle \\ |\Phi\rangle \end{pmatrix} + V\begin{pmatrix} |\Phi\rangle \\ |\chi\rangle \end{pmatrix} = E\begin{pmatrix} |\Phi\rangle \\ |\chi\rangle \end{pmatrix} + 2c^2 \begin{pmatrix} 0 \\ |\chi\rangle \end{pmatrix}. \tag{3.91}$$

We can form the following relation from the second components of each spinor,

$$|\chi\rangle = X|\Phi\rangle, \tag{3.92}$$

where,

$$X = \left(\frac{1}{E + 2c^2 - V}\right) c\boldsymbol{\sigma}\cdot\boldsymbol{\pi}. \tag{3.93}$$

One final note to make, before we construct the reduced Dirac equation, is that $|\Phi\rangle$ is not normalised. We thus introduce the normalised, spinor wavefunction, $|\Psi\rangle$, which is defined as,

$$|\Psi\rangle = \sqrt{\mathbb{1}_2 + X^\dagger X}|\Phi\rangle. \tag{3.94}$$

We can extract the first components of equation 3.91 and insert the relevant expressions for $|\Psi\rangle$ to arrive at,

$$\left(\mathbb{1}_2 + X^\dagger X\right)^{1/2} \mathcal{H}_{\mathrm{ESC}} \left(\mathbb{1}_2 + X^\dagger X\right)^{-1/2} |\Psi\rangle = E|\Psi\rangle, \tag{3.95}$$

with,

$$\mathcal{H}_{\text{ESC}} = c\boldsymbol{\sigma}\cdot\boldsymbol{\pi}\left(\frac{1}{E+2c^2-V}\right)c\boldsymbol{\sigma}\cdot\boldsymbol{\pi}+V\mathbb{1}_2. \tag{3.96}$$

This is the Dirac equation with the small-component eliminated. It may not be obvious yet, but this process has been important to lay a basis to solve this relativistic equation. Working at the two-spinor level has also halved the size of the wavefunction that would have to be stored computationally.

3.5.5 Zeroth-order regular approximation

The Hamiltonian in equation 3.95 is dependent on the energy, E. This is problematic but can be solved via a variety of methods, one most elegant being the zeroth-order regular approximation (ZORA).[139]

We expand the Hamiltonian in equation 3.96, as well as X, in powers of $E/(2c^2-V)$ due to the assumption $E \ll 2c^2-V$. This is valid even in the region of the divergent Coulomb potential. This can therefore be used to solve for our all-electron atomic states in the pseudopotential method. Typically, one may expand in terms of $p^2 \ll c^2$, leading to the Pauli Hamiltonian. However, this assumption can break down in regions very close to the nucleus and thus not be valid. Our expansion gives,

$$\mathcal{H}_{\text{ESC}} = c\boldsymbol{\sigma}\cdot\boldsymbol{\pi}\left\{\frac{1}{2c^2-V}\left[1-x+x^2+\mathcal{O}(x^3)\right]\right\}c\boldsymbol{\sigma}\cdot\boldsymbol{\pi}+V\mathbb{1}_2, \tag{3.97}$$

where,

$$x \equiv x(E) = \frac{E}{2c^2-V}. \tag{3.98}$$

As explained, we do not want the energy, E, appearing in the Hamiltonian. We can therefore take the expansion to zeroth-order to obtain,

$$\mathcal{H}_{\text{ZORA}} = \frac{1}{2}\boldsymbol{\sigma}\cdot\boldsymbol{\pi}\,K\,\boldsymbol{\sigma}\cdot\boldsymbol{\pi}+V\mathbb{1}_2, \tag{3.99}$$

where,

$$K = \frac{1}{1-\frac{V}{2c^2}}. \tag{3.100}$$

Typically, $V \equiv V(\mathbf{r})$, and so $K \equiv K(\mathbf{r})$. We can write equation 3.99 more explicitly,

$$\mathcal{H}_{\text{ZORA}} = \frac{1}{2}\boldsymbol{\pi}\cdot(K\boldsymbol{\pi})\,\mathbb{1}_2+\frac{K^2}{2c^2}\mathbf{S}\cdot\boldsymbol{\nabla}V\times\mathbf{p}-\frac{gK}{2c}\mathbf{S}\cdot\mathbf{B}+V\mathbb{1}_2, \tag{3.101}$$

with $g = 2$. Notice that, for a valence electron in a weak potential, that is $V \ll 2c^2$, $K \to 1$, and as a result, we recover the Levy-Leblond Hamiltonian.[140, 141] Close to the nucleus, however, the potential will be strong and $K < 1$. This factor represents the effects of relativity on the system. See figure 3.4. Notice that we have recovered several of the terms in equation 3.83, namely, the spin-orbit coupling term and the spin-magnetic field coupling term. The current ZORA scheme in the CASTEP package, implemented for the calculation of chemical shielding parameters,[51] neglects these terms, giving,

$$\mathcal{H}_{\mathrm{ZORA}} = \frac{1}{2}\boldsymbol{\pi} \cdot (K\boldsymbol{\pi}) + V, \tag{3.102}$$

which is now a scalar operator because it is diagonal in spin space.

3.5.6 Scalar-relativistic approaches

If we neglect the spin-orbit term, the ZORA equation reduces to, what is known as, a scalar-relativistic (SR) theory. One notable approach is that of Koelling and Harmon.[142] In this, only the SOC term of the Dirac equation is dropped, and all other relativistic effects - the kinetic energy correction, the Darwin term - are retained. As discussed, the spin-orbit effect splits the degenerate eigenstates at a given ℓ quantum number. The solutions calculated by the SR approaches typically represent that of a 'j-averaged' state. These energy eigenvalues are not split. One may introduce the effects of SOC through a perturbation treatment once the converged SR Kohn-Sham orbitals are found. As mentioned, the effects of the SOC increase strongly with atomic number, and as a result, calculations on systems containing heavy atoms will begin to yield inaccurate results with a SR approach. It becomes insufficient to treat the effects of relativity to only a scalar level and one may need to take a fully-relativistic (FR) approach.[129]

3.5.7 Relativistic pseudopotentials

In the scalar-relativistic approach, because we obtain an ℓ-dependent eigenstate (strictly *not* j labelled), spin remains a good quantum number. As a result, we can

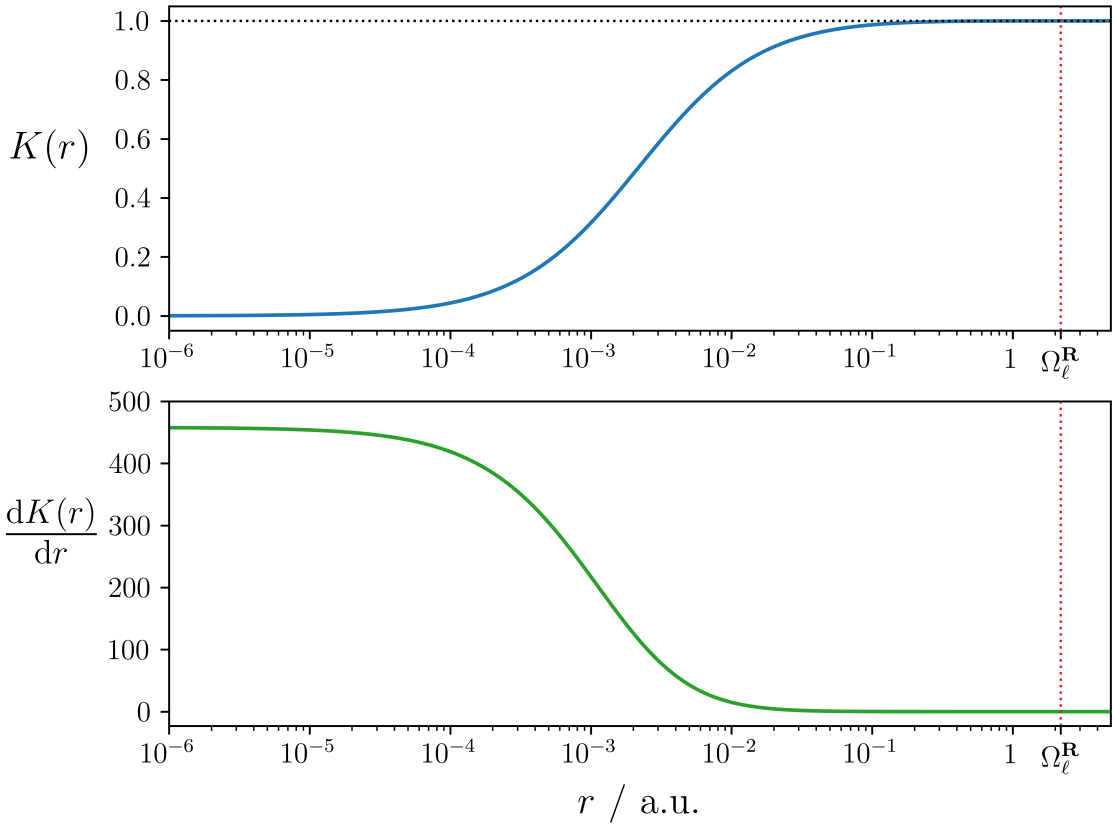


Figure 3.4: Plot of $K(r)$ and $\frac{\mathrm{d}K(r)}{\mathrm{d}r}$ for an all-electron, atomic, ZORA calculation on lead, Pb. We recover the expected results: near the nucleus, $K(r) < 1$ a.u., and; away from the nucleus, $K(r) \simeq 1$ a.u.. The derivative term is important for the relativistic effects in some nucleus magnetic resonance operators.

follow the exact procedure outlined in section 3.4.6 to construct the pseudopotential(s). We require that the scattering properties of the pseudopotential reproduce, typically for at least two eigenstates, those of the all-electron calculation.[126, 143, 144] NCPs have been introduced with SOC,[145, 146] where a scalar-relativistic part is treated with the approach in section 3.4.6 and the SOC calculated to first-order using perturbation theory. However, the larger the effect of the SOC, the more inaccurate this approach becomes. If we would like a FR treatment, we must solve the radial Dirac equation in the generation of the pseudopotentials.

We find the greatest spin-orbit splitting in the heavily localised core states from the all-electron calculation. SOC then arises in the valence states due to the orthogonality constraint imposed on the eigenstates. Through the requirement that the pseudopotential reproduces the valence scattering properties, the valence pseudo-states remain split and the pseudopotential will contain the spin-orbit splitting in its non-local part. The local part, however, can be chosen to be that of a j-averaged pseudopotential, without loss of generality.[126] We will now outline the mathematical scheme of the USPs with FR spinors; following that of dal Corso and Conte.[144]

We obtain the atomic all-electron and pseudo-states in an entirely analogous manner to that outlined in section 3.4.6, but where each are two-component spinors solved with the FR radial Dirac equation and are denoted $\Phi^{\mathbf{R}}_{\tau,\ell,j}(\mathbf{r})$ and $\tilde{\Phi}^{\mathbf{R}}_{\tau,\ell,j}(\mathbf{r})$ for the all-electron and pseudo-states, respectively. For each atom, we may choose j-dependent augmentation regions, $\Omega^{\mathbf{R}}_{\ell,j}$.

We aim to solve a similar eigenvalue problem as before,

$$\tilde{\mathcal{H}}|\tilde{\Psi}\rangle = \varepsilon\mathcal{S}|\tilde{\Psi}\rangle, \tag{3.103}$$

but now with spinors (note the capitalised 'Ψ', which contrasts equation 3.60 with 'ψ' from the Schrödinger approach). The pseudo-Hamiltonian, $\tilde{\mathcal{H}}$, is now 2×2 spin dependent.

We shall first generalise the PAW method to work with spinor wavefunctions before continuing. The final problem is to then derive our expression for the generalised pseudo-Hamiltonian, $\tilde{\mathcal{H}}$.

3.5.8 Projector augmented-wave method with spinors

The generalisation of the linear transformation is as follows,

$$\mathcal{T} = \mathbb{1} + \sum_{\mathbf{R}} \sum_{\tau,\ell,j,m_j} \left[|\Phi^{\mathbf{R}}_{\tau,\ell,j,m_j}\rangle - |\tilde{\Phi}^{\mathbf{R}}_{\tau,\ell,j,m_j}\rangle \right] \langle P^{\mathbf{R}}_{\tau,\ell,j,m_j}|, \tag{3.104}$$

with $|\Psi\rangle = \mathcal{T}|\tilde{\Psi}\rangle$. The quantities in this equation are two-component spinors,

$$|\Phi^{\sigma,\mathbf{R}}_{\tau,\ell,j,m_j}\rangle = |\phi^{\mathbf{R}}_{\tau,\ell,j}\bar{Y}^{\sigma}_{\ell,j,m_j}\rangle, \quad |\tilde{\Phi}^{\sigma,\mathbf{R}}_{\tau,\ell,j,m_j}\rangle = |\tilde{\phi}^{\mathbf{R}}_{\tau,\ell,j}\bar{Y}^{\sigma}_{\ell,j,m_j}\rangle, \quad |P^{\sigma,\mathbf{R}}_{\tau,\ell,j,m_j}\rangle = |p^{\mathbf{R}}_{\tau,\ell,j}\bar{Y}^{\sigma}_{\ell,j,m_j}\rangle, \tag{3.105}$$

with $\sigma = 1$ and $\sigma = 2$ corresponding to the first and second elements in the spinor, respectively. $\langle\hat{\mathbf{r}}|\bar{Y}_{\ell,j,m_j}\rangle \equiv \bar{Y}_{\ell,j,m_j}(\theta,\varphi)$ are the generalised version of the spherical harmonics: the spin-angle functions,

$$\bar{Y}_{\ell,j,m_j}(\theta,\varphi) = \begin{cases} \begin{pmatrix} \sqrt{\frac{\ell+m+1}{2\ell+1}} Y^{m}_{\ell}(\theta,\varphi) \\ \sqrt{\frac{\ell-m}{2\ell+1}} Y^{m+1}_{\ell}(\theta,\varphi) \end{pmatrix} & j = \ell + 1/2 \qquad m = m_j - 1/2, \\ \begin{pmatrix} \sqrt{\frac{\ell-m+1}{2\ell+1}} Y^{m-1}_{\ell}(\theta,\varphi) \\ -\sqrt{\frac{\ell+m}{2\ell+1}} Y^{m}_{\ell}(\theta,\varphi) \end{pmatrix} & j = \ell - 1/2 \qquad m = m_j + 1/2. \end{cases} \tag{3.106}$$

The *superscript* m indices in the spherical harmonics, $Y^{m}_{\ell}(\theta,\varphi)$, denote them as the *complex* versions.

We will now proceed to outline a key concept in the expressions involved in this section. We can extract the spin dependence of the above expressions and encapsulate it into a useful quantity, the f-matrix. This will allow us to continue to use the predefined PAW approach, with only minimal generalisations of the quantities involved. This way, we do not need to refactor an existing PAW implementation.

We allow for the use of any appropriate type of spherical harmonic functions in our derivation. We therefore can expand the complex versions as follows,

$$Y^{m}_{\ell} = \sum_{m'=-\ell}^{\ell} U^{\ell}_{m,m'} Y_{\ell,m'}. \tag{3.107}$$

Note the *subscript* m' indices on the right-hand side, denoting whatever choice of harmonics the reader may want to use.

An element of the spin-angle functions may therefore be written as,

$$\bar{Y}^{\sigma}_{\ell,j,m_j} = \alpha^{\sigma,\ell,j}_{m_j} \sum_{m'=-l}^{\ell} U^{\sigma,\ell,j}_{m_j,m'} Y_{\ell,m'}, \tag{3.108}$$

where $\alpha^{\sigma,\ell,j}_{m_j}$ are the Clebsch-Gordan coefficients that prefactor the harmonics in equation 3.106,

$$\alpha^{\sigma,\ell,j}_{m_j} = \begin{cases} \sqrt{\frac{\ell+m+1}{2\ell+1}} & \sigma = 1 \\ \sqrt{\frac{\ell-m}{2\ell+1}} & \sigma = 2 \end{cases} \quad j = \ell + 1/2 \qquad m = m_j - 1/2, \\ \begin{cases} \sqrt{\frac{\ell-m+1}{2\ell+1}} & \sigma = 1 \\ -\sqrt{\frac{\ell+m}{2\ell+1}} & \sigma = 2 \end{cases} \quad j = \ell - 1/2 \qquad m = m_j + 1/2, \tag{3.109}$$

and $U^{\sigma,\ell,j}_{m_j,m}$ is a spin dependent $(2j+1) \times (2\ell+1)$ matrix that reduces to $U^{\ell}_{m,m'}$ in the following ways,

$$U^{\sigma,\ell,j}_{m_j,m'} = \begin{cases} U^{\ell}_{m,m'} & \sigma = 1 \\ U^{\ell}_{m+1,m'} & \sigma = 2 \end{cases} \quad j = \ell + 1/2 \qquad m = m_j - 1/2, \\ \begin{cases} U^{\ell}_{m-1,m'} & \sigma = 1 \\ U^{\ell}_{m,m'} & \sigma = 2 \end{cases} \quad j = \ell - 1/2 \qquad m = m_j + 1/2. \tag{3.110}$$

We take $U^{1,\ell,j}_{m_j,m'} = 0$ when $m < -\ell$ and $U^{2,\ell,j}_{m_j,m'} = 0$ when $m + 1 > \ell$.

We now have the tools required to extract the spin dependence from the atomic wavefunctions and projectors, given in equation 3.105, by simply inserting equation 3.108,

$$\begin{aligned} |\phi^{\mathbf{R}}_{\tau,\ell,j} \bar{Y}^{\sigma}_{\ell,j,m_j}\rangle &= \alpha^{\sigma,\ell,j}_{m_j} \sum_{m'} U^{\sigma,\ell,j}_{m_j,m'} |\phi^{\mathbf{R}}_{\tau,\ell,j} Y_{\ell,m'}\rangle, \\ |\tilde{\phi}^{\mathbf{R}}_{\tau,\ell,j} \bar{Y}^{\sigma}_{\ell,j,m_j}\rangle &= \alpha^{\sigma,\ell,j}_{m_j} \sum_{m'} U^{\sigma,\ell,j}_{m_j,m'} |\tilde{\phi}^{\mathbf{R}}_{\tau,\ell,j} Y_{\ell,m'}\rangle, \\ |p^{\mathbf{R}}_{\tau,\ell,j} \bar{Y}^{\sigma}_{\ell,j,m_j}\rangle &= \alpha^{\sigma,\ell,j}_{m_j} \sum_{m'} U^{\sigma,\ell,j}_{m_j,m'} |p^{\mathbf{R}}_{\tau,\ell,j} Y_{\ell,m'}\rangle. \end{aligned} \tag{3.111}$$

The spinor nature of the spin-angle functions have reduced to summations of the j-split states, with appropriately defined spherical harmonics and Clebsch-Gordan coefficients.

We use entirely analogous rules to before regarding the behaviour of the atomic wavefunctions inside and outside the augmentation regions, $\Omega^{\mathbf{R}}_{\ell,j}$. And so, with the definitions above, we can define the generalised 2×2 spin dependent pseudo-operator, $\mathcal{O}$, in the spinor basis using equation 3.104. This is,

$$\begin{aligned}\langle\tilde{\Psi}|\mathcal{O}|\tilde{\Psi}\rangle = \langle\tilde{\Psi}|O|\tilde{\Psi}\rangle + \sum_{\mathbf{R}}\sum_{\tau,\ell,j,m_j}\sum_{\tau',\ell',j',m_{j'}}\langle\tilde{\Psi}|p^{\mathbf{R}}_{\tau,\ell,j}\bar{Y}_{\ell,j,m_j}\rangle \\ \times\Big[\langle\Phi^{\mathbf{R}}_{\tau,\ell,j}\bar{Y}_{\ell,j,m_j}|O|\Phi^{\mathbf{R}}_{\tau',\ell',j'}\bar{Y}_{\ell',j',m_{j'}}\rangle \\ -\langle\tilde{\Phi}^{\mathbf{R}}_{\tau,\ell,j}\bar{Y}_{\ell,j,m_j}|O|\tilde{\Phi}^{\mathbf{R}}_{\tau',\ell',j'}\bar{Y}_{\ell',j',m_{j'}}\rangle\Big] \\ \times\langle p^{\mathbf{R}}_{\tau',\ell',j'}\bar{Y}_{\ell',j',m_{j'}}|\tilde{\Psi}\rangle.\end{aligned} \tag{3.112}$$

Inserting the definitions in equation 3.111, we get,

$$\begin{aligned}\langle\tilde{\Psi}|\mathcal{O}|\tilde{\Psi}\rangle =&\langle\tilde{\Psi}|O|\tilde{\Psi}\rangle \\ &+\sum_{\mathbf{R}}\sum_{\tau,\ell,j}\sum_{\tau',\ell',j'}\sum_{m,m'}\sum_{\sigma,\sigma'}\Theta^{\mathbf{R}}_{\tau,\ell,j,m;\tau',\ell',j',m'}\,\rho^{\mathbf{R},\sigma,\sigma'}_{\tau,\ell,j,m;\tau',\ell',j',m'},\end{aligned} \tag{3.113}$$

where we have defined the augmentation operator,

$$\Theta^{\mathbf{R}}_{\tau,\ell,j,m;\tau',\ell',j',m'} = \langle\phi^{\mathbf{R}}_{\tau,\ell,j}Y_{\ell,m}|O|\phi^{\mathbf{R}}_{\tau',\ell',j'}Y_{\ell',m'}\rangle - \langle\tilde{\phi}^{\mathbf{R}}_{\tau,\ell,j}Y_{\ell,m}|O|\tilde{\phi}^{\mathbf{R}}_{\tau',\ell',j'}Y_{\ell',m'}\rangle, \tag{3.114}$$

and the density-like term,

$$\rho^{\mathbf{R},\sigma,\sigma'}_{\tau,\ell,j,m;\tau',\ell',j',m'} = \sum_{\sigma_A,\sigma_B}\sum_{m_A,m_B}\langle\tilde{\Psi}^{\sigma_A}|p^{\mathbf{R}}_{\tau,\ell,j}Y_{\ell,m_A}\rangle\langle p^{\mathbf{R}}_{\tau',\ell',j'}Y_{\ell',m_B}|\tilde{\Psi}^{\sigma_B}\rangle f^{\sigma_A,\sigma}_{\ell,j;m_A,m}f^{\sigma',\sigma_B}_{\ell',j';m',m_B}. \tag{3.115}$$

Analogously to dal Corso and Conte,[144] we have introduced the f-matrix, which is,

$$f^{\sigma,\sigma'}_{\ell,j;m,m'} = \sum_{m_j=-j}^{j}\alpha^{\sigma,\ell,j}_{m_j}U^{\sigma,\ell,j}_{m_j,m}\alpha^{\sigma',\ell,j}_{m_j}U^{\sigma',\ell,j,*}_{m_j,m'}. \tag{3.116}$$

This is the term that encapsulates all the spinor dependence of our equations. This, in principle, requires us only to generalise operators to 2×2 matrices, without the need for any spinor dependence, as it is managed by this term.

The generalised $\mathcal{S}$ matrix preserves the norm of the wavefunctions,

$$\mathcal{S}^{\sigma,\sigma'} = \delta_{\sigma\sigma'} + \sum_{\mathbf{R}}\sum_{\tau,\ell,j}\sum_{\tau',\ell',j'}\sum_{m,m'}|p^{\mathbf{R}}_{\tau,\ell,j}Y_{l,m}\rangle q^{\mathbf{R},\sigma,\sigma'}_{\tau,\ell,j,m;\tau',\ell',j',m'}\langle p^{\mathbf{R}}_{\tau',\ell',j'}Y_{l',m'}|. \tag{3.117}$$

The charge augmentation term is, in general, complex and has elements,

$$q^{\mathbf{R},\sigma,\sigma'}_{\tau,\ell,j,m;\tau',\ell',j',m'} = \sum_{m_A,m_B}\sum_{\sigma_A}q^{\mathbf{R}}_{\tau,\ell,j,m_A;\tau',\ell',j',m_B}f^{\sigma,\sigma_A}_{\ell,j;m,m_A}f^{\sigma_A,\sigma'}_{\ell',j';m_B,m'}, \tag{3.118}$$

where $q^{\mathbf{R}}_{\tau,\ell,j,m;\tau',\ell',j',m'}$ are generalised versions of the spin independent augmentation term in section 3.4.6. They follow a similar pattern with,

$$q^{\mathbf{R}}_{\tau,\ell,j,m;\tau',\ell',j',m'} = \int Q^{\mathbf{R}}_{\tau,\ell,j,m;\tau',\ell',j',m'}(\mathbf{r})\,\mathrm{d}\mathbf{r}, \tag{3.119}$$

where $Q^{\mathbf{R}}_{\tau,\ell,j,m;\tau',\ell',j',m'}(\mathbf{r})$ are recovered by inserting $O = |\mathbf{r}\rangle\langle\mathbf{r}|$, the density operator, into equation 3.114,

$$\begin{aligned} Q^{\mathbf{R}}_{\tau,\ell,j,m;\tau',\ell',j',m'}(\mathbf{r}) &= \langle\phi^{\mathbf{R}}_{\tau,\ell,j}Y_{\ell,m}|\mathbf{r}\rangle\langle\mathbf{r}|\phi^{\mathbf{R}}_{\tau',\ell',j'}Y_{\ell',m'}\rangle - \langle\tilde{\phi}^{\mathbf{R}}_{\tau,\ell,j}Y_{\ell,m}|\mathbf{r}\rangle\langle\mathbf{r}|\tilde{\phi}^{\mathbf{R}}_{\tau',\ell',j'}Y_{\ell',m'}\rangle, \\ &= \left[\phi^{\mathbf{R}}_{\tau,\ell,j}(r)\phi^{\mathbf{R}}_{\tau',\ell',j'}(r) - \tilde{\phi}^{\mathbf{R}}_{\tau,\ell,j}(r)\tilde{\phi}^{\mathbf{R}}_{\tau',\ell',j'}(r)\right] Y^*_{\ell,m}(\theta,\varphi)Y_{\ell',m'}(\theta,\varphi), \end{aligned} \tag{3.120}$$

where it is worth noting that the atomic functions are strictly real.

We now have the equations required to generalise our pseudo-Hamiltonian in the spinor framework, which is,

$$\tilde{\mathcal{H}} = \left(\frac{p^2}{2} + \tilde{V}_{\text{loc}}\right)\mathbb{1} + \tilde{\mathcal{V}}_{\text{non-loc}}. \tag{3.121}$$

As mentioned previously, we may choose the local potential part to be that of a j-averaged pseudopotential.[126] The only term that therefore needs review is the non-local part of our pseudopotential, of which, now becomes a 2×2 spin dependent matrix,

$$\tilde{\mathcal{V}}^{\sigma,\sigma'}_{\text{non-loc}} = \sum_{\mathbf{R}} \sum_{\tau,\ell,j,m} \sum_{\tau',\ell',j',m'} |p^{\mathbf{R}}_{\tau,\ell,j}Y_{\ell,m}\rangle D^{\mathbf{R},\sigma,\sigma'}_{\tau,\ell,j,m;\tau',\ell',j',m'}\langle p^{\mathbf{R}}_{\tau',\ell',j'}Y_{\ell',m'}|, \tag{3.122}$$

with the coefficients generalised,

$$\begin{aligned} D^{\mathbf{R},\sigma,\sigma'}_{\tau,\ell,j,m;\tau',\ell',j',m'} =& D^{\mathbf{R},0}_{\tau,\ell,j;\tau',\ell,j} f^{\sigma,\sigma'}_{\ell,j;m,m'}\delta_{\ell\ell'}\delta_{jj'} \\ &+ \sum_{m_A,m_B}\sum_{\sigma_A,\sigma_B}\sum_{\nu} \mathcal{A}^{\sigma_A,\sigma_B}_{\nu}\mathcal{I}^{\mathbf{R},\nu}_{\ell,j,m_A;\ell',j',m_B} f^{\sigma,\sigma_A}_{\ell,j;m,m_A} f^{\sigma_B,\sigma'}_{\ell',j';m_B,m'}. \end{aligned} \tag{3.123}$$

$D^{\mathbf{R},0}_{\tau,\ell,j;\tau',\ell,j}$ are, as before, generated with the pseudopotential, $\boldsymbol{\mathcal{A}} = (\mathbb{1}_2, \sigma_1, \sigma_2, \sigma_3)$ where σ_i are the Pauli matrices given in equation 3.75, and,

$$\mathcal{I}^{\mathbf{R},\nu}_{\tau,\ell,j,m;\tau',\ell',j',m'} = \int Q^{\mathbf{R}}_{\tau,\ell,j,m;\tau',\ell',j',m'}(\mathbf{r})\mathcal{B}_{\nu}(\mathbf{r})\,\mathrm{d}\mathbf{r}, \tag{3.124}$$

with $\boldsymbol{\mathcal{B}} = \left(V_{\text{eff}}, -\frac{1}{2}\mathcal{B}_{\text{XC},1}, -\frac{1}{2}\mathcal{B}_{\text{XC},2}, -\frac{1}{2}\mathcal{B}_{\text{XC},3}\right)$ and $\mathcal{B}_{\text{XC},i} = -\delta E_{\text{XC}}/\delta m_i$; known as the exchange-correlation magnetic field. Notice the V_{eff} in the first element here, reflecting the reduced equation 3.66. In $\mathcal{B}_{\text{XC},i}$, the magnetisation density, $\mathbf{m}(\mathbf{r})$, is,

$$\mathbf{m}(\mathbf{r}) = \frac{1}{2}\sum_{\sigma,\sigma'} n^{\sigma,\sigma'}(\mathbf{r})\boldsymbol{\sigma}^{\sigma,\sigma'}, \tag{3.125}$$

where the density matrix is,

$$n^{\sigma,\sigma'}(\mathbf{r}) = \langle\tilde{\Psi}^{\sigma}|\mathbf{r}\rangle\langle\mathbf{r}|\tilde{\Psi}^{\sigma'}\rangle + \sum_{\mathbf{R}}\sum_{\tau,\ell,j,m}\sum_{\tau',\ell',j',m'} Q^{\mathbf{R}}_{\tau,\ell,j,m;\tau',\ell',j',m'}(\mathbf{r})\,\rho^{\mathbf{R},\sigma,\sigma'}_{\tau,\ell,j,m;\tau',\ell',j',m'}, \tag{3.126}$$

and $n(\mathbf{r})$ obtained via its trace. The notation of $\boldsymbol{\sigma}^{\sigma,\sigma'}$ is outlined in appendix A.

We, again, note that there exists, in section 3.4.7, analogous equations for those presented here. Whilst the notation is intricate, these equations are just generalisations of those in 3.4.7 to spin dependent matrices; and the SOC alterations accounted for in the f-matrices, equation 3.116.

4 Implementation

Contents

4.1 Finding the ground state 65
4.2 Non-collinear magnetism considerations 66
4.2.1 Exchange-correlation functional 66
4.2.2 Self-consistent field cycle 68
4.3 Spin-orbit splitting 68
4.3.1 Atomic: lead, Pb 68
4.3.2 Bandstructure: lead, Pb 72
4.3.3 Bandstructure: bismuth telluride, Bi_2Te_3 72
4.4 Applied magnetic field 76
4.4.1 Expression 76
4.4.2 Implementation 77
4.5 The implementation of the f-matrices 78
4.6 Memory and calculation time considerations 80
4.7 Symmetry breaking 82
4.8 Towards nuclear magnetic resonance calculations . . . 83

4.1 Finding the ground state

Solving the Kohn-Sham equations, 3.35, is a non-linear problem, in that the operator requires the knowledge of the electron density, which in turn depends on the wavefunction. We implement a self-consistent field (SCF) cycle to solve this problem. We make use of the variational principle, in that a lower total

energy signifies a more accurate wavefunction. A sensible, initial guess of the electron density is performed, which constructs our Kohn-Sham operator and the wavefunction found. The new density is then constructed from this wavefunction and the cycle performed until a desired convergence level is reached. This iterative method is common among all electronic structure codes.

The cost of solving for the eigenvalues in equation 3.35 scales linearly with respect to the number of electrons. However, when solving for the eigenvalues of the pseudo-Hamiltonian with a planewave basis, the process scales with the numbers of planewaves cubed. Also, the memory required to store the Hamiltonian increases as the square of the planewaves.[147] To solve this problem, we take inspiration from a method introduced by Car and Parrinello, originally applied to molecular dynamics.[148] We use the conjugate gradient technique to minimise the Hamiltonian functional.[149] This involves a preconditioning factor for the kinetic energy that ensures the problem scales reasonably with increasing numbers of planewaves. It also allows for the Hamiltonian to be partitioned, meaning it never needs to be fully stored in memory.

One final remark, eluded to previously, is that we solve only the atomic states with the FR Dirac equation. This has required us to generalise the pseudopotential and PAW method, but has not required us to rework the ground state SCF solver in the main electronic structure code. We note that this has long been known to be a valid method in accounting for relativistic effects.[144, 150] The ground state electronic structure may therefore be calculated via the exact methods outlined in the non-relativistic portion of this chapter, as long as we work with pseudopotentials derived from the FR section and use the spinor PAW approach.

4.2 Non-collinear magnetism considerations

4.2.1 Exchange-correlation functional

One consideration worth noting is the difficulty of treating non-collinear magnetism (NCM) in regard to its definition in the exchange-correlation functional. In equation

3.39, the functional depends on the up-spin electron density, $n_{\uparrow}(\mathbf{r})$, and down-spin electron density, $n_{\downarrow}(\mathbf{r})$. The *collinear* magnetisation is a scalar, and is defined as,

$$m(\mathbf{r}) = n_{\uparrow}(\mathbf{r}) - n_{\downarrow}(\mathbf{r}). \tag{4.1}$$

However, in the *non-collinear* case, the magnetisation is a vector,

$$\mathbf{m}(\mathbf{r}) = \frac{1}{2}\sum_{\sigma,\sigma'} n^{\sigma,\sigma'}(\mathbf{r})\,\boldsymbol{\sigma}^{\sigma,\sigma'}, \tag{4.2}$$

where $n^{\sigma,\sigma'}(\mathbf{r})$ is the density matrix, with its trace being the electron density. The notation of $\boldsymbol{\sigma}^{\sigma,\sigma'}$ is outlined in appendix A. The important point is to note that the up-spin and down-spin densities are now not well defined in the NCM case.

In practice, we solve for the density matrix, meaning $\mathbf{m}(\mathbf{r})$ is well defined, and then evaluate the functional using the scalar magnetisation, $m(\mathbf{r})$. This quantity is obtained by projecting the non-collinear magnetisation in its local direction,

$$m(\mathbf{r}) = \mathbf{m}(\mathbf{r}) \cdot \frac{\mathbf{m}(\mathbf{r})}{|\mathbf{m}(\mathbf{r})|}. \tag{4.3}$$

We save the orientation of the magnetisation, $\mathbf{m}(\mathbf{r})/|\mathbf{m}(\mathbf{r})|$, to rotate it back later. Our exchange-correlation functionals, discussed in section 3.3.3, are now well defined within this spin basis with $m(\mathbf{r})$ and can be used as normal. This method, first suggested by Kübler *et al.*, is known as the *locally collinear approach.*[151] There have been a number of implementations of this method and its comparison to scalar calculations that use the collinear approach.[152–156]

However useful, this practice needs to be undertaken carefully, particularly in the case of GGAs and above, which have the electron density derivatives as extra degrees of freedom. Describing the magnetisation in this way, which formally should be a vector, may cause instabilities in the SCF solver.

A notable, recent article has discussed the limitations of the locally collinear approach, and outlined a method that satisfies a number of required criteria.[157] This includes 1) reproducing the correct collinear limit; 2) invariant to rotation of the magnetisation vector globally but not locally; 3) well-defined functional derivates; and 4) has zero global but non-zero local torque.

4.2.2 Self-consistent field cycle

Calculations on BiOBr and $BiGaTeO_6$ systems, which are investigated later in chapter 5, were performed to investigate the stability of the SCF solver with respect to the choice of exchange-correlation functional. It was found that the cut-off energy may affect the ability for the calculation to converge on a suitable ground-state wavefunction. Calculations from 500 eV to 1500 eV cut-off, with spacings of 100 eV, were performed for both the LDA and PBE functionals. Whilst all calculations for LDA converged satisfactorily for both systems, the BiOBr 1000 eV and $BiGaTeO_6$ 900 and 1000 eV for PBE did not. The failed calculations ran for 100 SCF iterations and oscillated between several different energy changes before stopping.

Due to the non-collinear spin problems described above, the potential energy landscape of the higher order functional (PBE) is likely highly complex. It is hypothesised that these specific cut-off energies happen to place the state wavefunction at an initial condition that leads the solver toward unstable local minima or even ill-defined points.

Consideration of this discussion in the CASTEP code is suggested as a suitable future project stemming from this work.

4.3 Spin-orbit splitting

The theory outlined so far allows us to perform calculations on molecules and crystals within the DFT framework using FR pseudopotentials. In this section, we demonstrate some key ideas in regard to the effects of SOC on atomic and solid-state systems. With some practical examples, we show the j-splitting of energy eigenstates and bandstructures, amongst other effects.

4.3.1 Atomic: lead, Pb

Figure 4.1 shows the energy level diagrams for SR and FR atomic calculations on lead, Pb. The degenerate 5d and 6p SR energy levels split on the inclusion of spin-orbit coupling in the FR scheme. The resultant levels also have degeneracy,

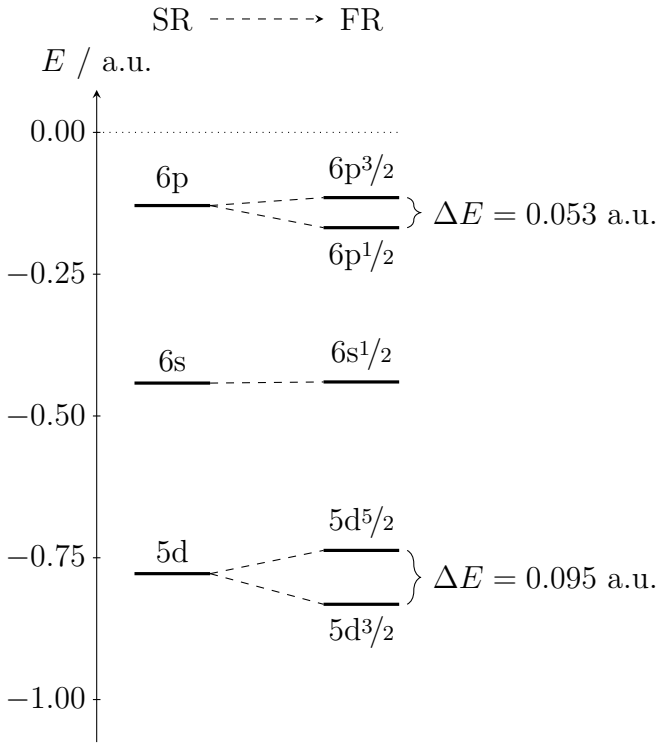


Figure 4.1: Energy level diagram comparison between scalar (SR) and fully-relativistic (FR) calculations on atomic lead, Pb. The effect of spin-orbit coupling splits the eigenenergies.

Table 4.1: Scalar and fully-relativistic atomic energy levels for lead, Pb. The former has notation n, ℓ and the latter n, ℓ, j.

Scalar-relativistic			Fully-relativistic		
Orbital	Occupation	Energy / a.u.	Orbital	Occupation	Energy / a.u.
6p	2.00	−0.129	$6p^3/_2$	1.33	−0.115
			$6p^1/_2$	0.67	−0.168
6s	2.00	−0.442	$6s^1/_2$	2.00	−0.440
5d	10.00	−0.778	$5d^5/_2$	6.00	−0.737
			$5d^3/_2$	4.00	−0.832

which could be broken by the inclusion of an external magnetic field. The splitting of the 5d levels is greater as they are more tightly bound and thus exhibit a higher relativistic character. As expected, the 6s state does has no degeneracy and does not greatly change in energy between the schemes. Table 4.1 details the specificities of the energy level diagram.

Figure 4.2 shows the splitting of the atomic wavefunctions in lead, Pb, for the $n = 6$, $\ell = 1$ state. One can notice that the $j = \frac{1}{2}$ state is more contracted. Its higher oscillatory nature corresponds to a more bound state, which is seen by its more negative energy compared to the scalar case. In contrast, the $j = \frac{3}{2}$ state is less negative in energy as it is a less bound state. This effect is evidenced in table 4.1.

A note of interest is the choice of occupation numbers for the FR states. The current implementation in the CASTEP code is to define the occupations for the j-split states as having the same ratios as the multiplicity of the states. In the SR 6p case, for example, the FR $6p^3/_2$ and $6p^1/_2$ states have degeneracies of 4 and 2, respectively. The occupation of 2 in the SR 6p state is therefore split up into $1.33 \equiv \frac{4}{3}$ and $0.67 \equiv \frac{2}{3}$ for the two FR states, respectively. An alternative approach would be to fill the FR eigenstates in order of their energies. This would result in occupations of 0 and 2 for the two FR states, respectively. Accuracy tests of the two choices against all-electron codes, such as in the *Delta Project*[158], would give insight into which approach is more formally appropriate.

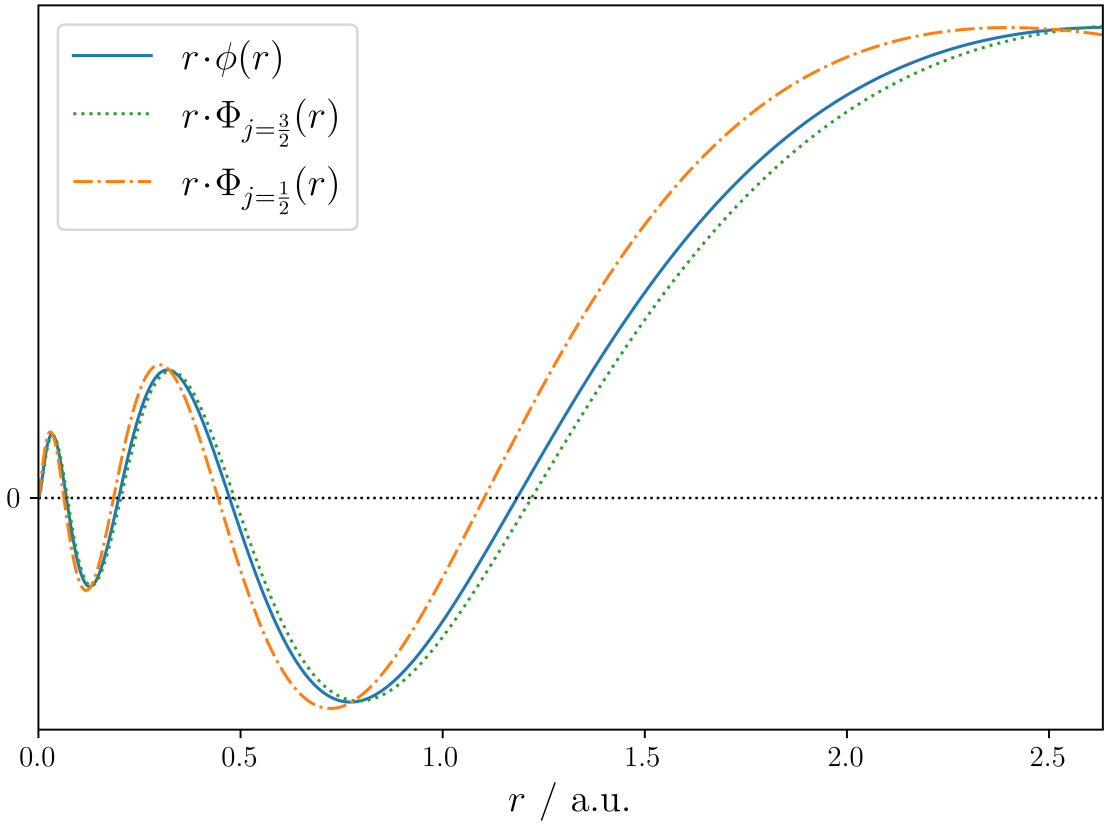


Figure 4.2: All-electron calculations of the $n = 6$ quantum number and $\ell = 1$ angular momentum channel for a lead atom, Pb. The relativistic eigenstates, $\Phi_{j=\frac{3}{2}}(r)$ and $\Phi_{j=\frac{1}{2}}(r)$, are split - and hence their energy eigenvalues split - in comparison to the non-relativistic eigenstate, $\phi(r)$. Irrelevant indices have been suppressed for brevity.

4.3.2 Bandstructure: lead, Pb

Calculations were performed to investigate the effects of SOC on the electronic bandstructure of lead, Pb. Figure 4.3 shows the calculated bandstructures with and without SOC. A cut-off energy of 1000 eV and **k**-point grid of $12 \times 12 \times 12$ was used. A path through the Brillouin zone of $\Gamma \rightarrow X \rightarrow K \rightarrow \Gamma \rightarrow L \rightarrow X \rightarrow W \rightarrow L$ was chosen, where $\Gamma \equiv (0.0, 0.0, 0.0)$, $X \equiv (0.0, 0.5, 0.5)$, $K \equiv (0.375, 0.75, 0.375)$, $L \equiv (0.5, 0.5, 0.5)$ and $W \equiv (0.25, 0.75, 0.5)$. The PBE functional and a set of NCPs, with FR capability, were used.

As observed in the atomic spectrum, we see splitting of eigenstates due to SOC. This is most prevalent at the Γ point, where the three 6p bands split into two and one. We also see large splitting of the tightly bound 6d states between -15 eV and -20 eV. These bands do not typically contribute to the electronic properties of lead, represented by their flat nature throughout the Brillouin zone. Other notable splittings occur along the $L \rightarrow X$ and $W \rightarrow L$ paths. We also observe crossings in the SR calculations around the K and W points that do not arise in the FR scheme. Our spectra map well to that recorded by Verstraete *et al.*,[159] who implemented a similar technique within the basis of DFT, utilising NCPs.

4.3.3 Bandstructure: bismuth telluride, Bi_2Te_3

Calculations were performed to investigate the effects of SOC on the electronic bandstructure of bismuth telluride, Bi_2Te_3. Figure 4.4 shows the calculated bandstructures with and without SOC. The structure was geometry optimised before the spectral calculations were performed. A cut-off energy of 1300 eV and **k**-point grid of $6 \times 6 \times 6$ was used. A path through the Brillouin zone of $U \rightarrow a \rightarrow \Gamma \rightarrow Z \rightarrow F \rightarrow L$ was chosen, where $U \equiv (0.823, 0.338, 0.338)$, $a \equiv (0.641, 0.430, 0.430)$, $\Gamma \equiv (0.0, 0.0, 0.0)$, $Z \equiv (0.5, 0.5, 0.5)$, $F \equiv (0.5, 0.5, 0.0)$ and $L \equiv (0.0, 0.5, 0.0)$. The PBE functional and a set of NCPs, with FR capability, were used. The SR and FR schemes required insulator and metal treatments, respectively.

Without SOC, our calculated band gap is 0.3677 eV. With SOC, however, our calculated gap reduced to 0.0870 eV, which is closer to the experimental values of

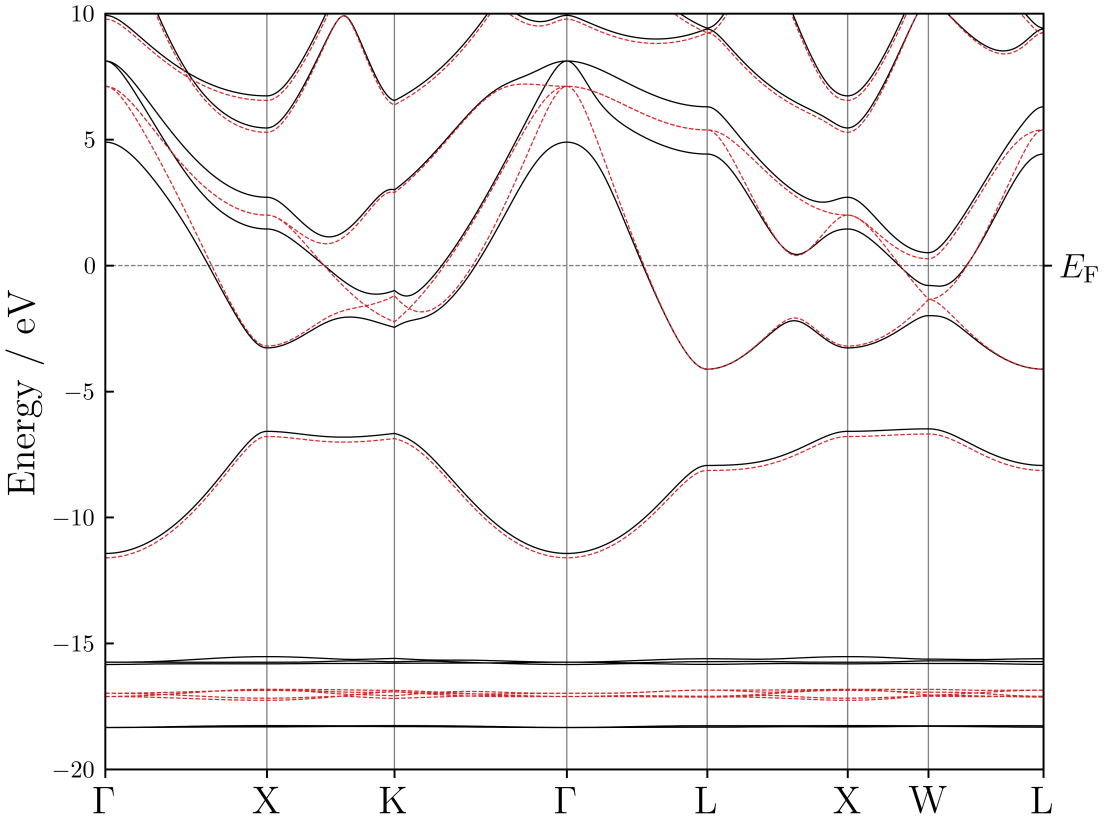


Figure 4.3: Calculated bandstructures of lead, Pb, with (black, solid line) and without (red, dashed line) spin-orbit coupling. The calculated Fermi energies of $E_F = 5.99$ eV, and $E_F = 6.12$ eV, respectively, have been set to the 0 energy level.

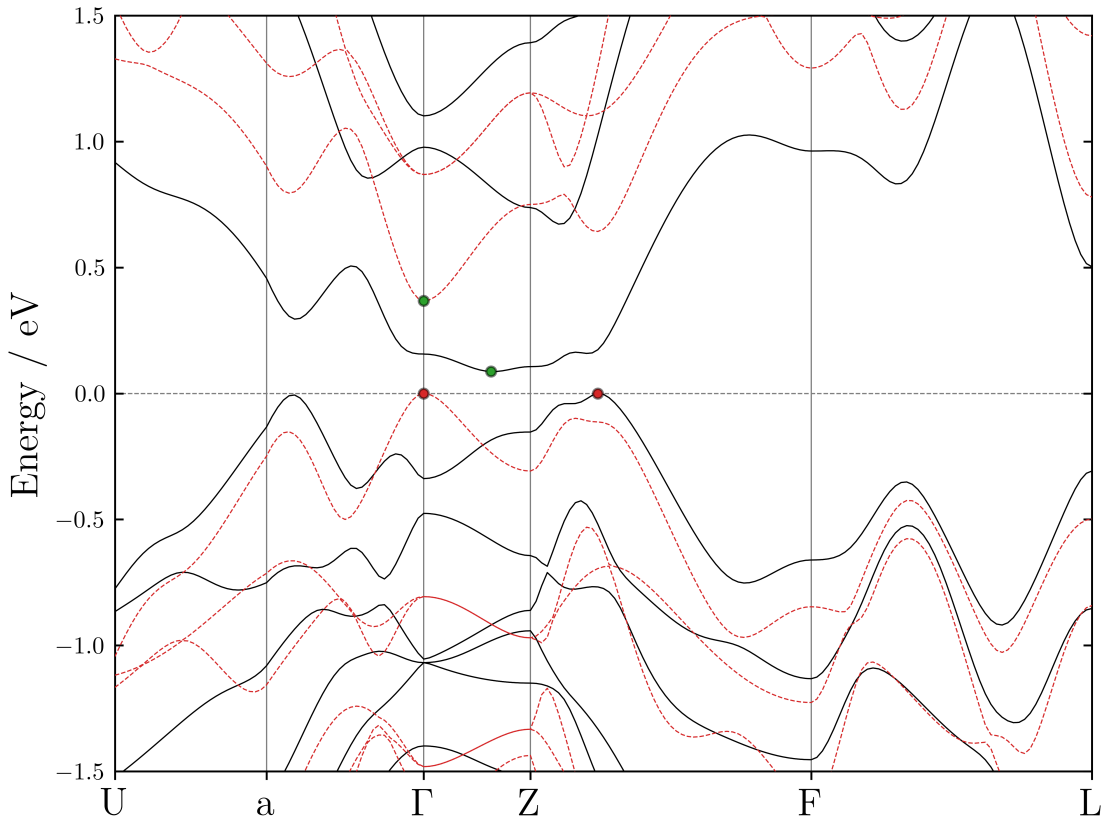


Figure 4.4: Calculated bandstructures of bismuth telluride, Bi_2Te_3, with (black, solid line) and without (red, dashed line) spin-orbit coupling. The valence band maxima, labelled with red dots, have been set to the 0 energy level. The conduction band minima have been labelled with green dots.

around 0.15 eV.[160–162] It is well-known that DFT methods typically underestimate the size of the band gap found (see, for example, reference [163]). The splitting of the bands due to SOC may reduce the gap calculated even further, creating additional difficulty. We also note that the use of USPs may yield better results. Employment of the full-potential linearised augmented-plane-wave method (FLAPW) by Youn *et al.*[164] and Larson[165] obtained slightly poorer results of 0.06 eV and 0.05 eV, respectively. The former used the LDA functional, whereas Larson used PBE and also implemented $p^1/_2$ corrections.[1] Scheidemantel *et al.* were then able to offer an improved value of 0.11 eV with the linearised augmented-plane-wave and local orbital method.[70] Kim *et al.* obtained an accurate value of 0.15 eV with the employment of the FLAPW method but using the sX-LDA functional, which offers an additional screening term specifically designed to aid in the poor ability of DFT to predict the band gap.[166] Huang *et al.* also recovered a good value of 0.13 eV with a similar method to Scheidemantel *et al.*, but with the aforementioned $p^1/_2$ and temperature effects. They noted, however, that the latter have negligible effects on the bandstructure, resulting in less than 2 % change in the predicted value.

The effects of SOC are dramatic in the bismuth telluride structure because both elements are heavy. Our results indicate that SOC causes band edges to move away from the Γ point, which corroborates the work of previous studies.[162, 167, 168] This results in an indirect band gap observed, contrasting to the direct Γ band gap found without SOC.

The valence band maximum (VBM) shifts from Γ to (0.500, 0.500, 0.380). There is also a maximum, near the *a* point, at (0.571, 0.571, 0.429), which is only 0.00610 eV lower in energy than the VBM. This is the VBM found by Huang and Kaviany.[169] Other authors report VBM coordinates around the (0.50, 0.38, 0.38)[164, 165, 170] and (0.65, 0.56, 0.56)[168] points.

[1] $p^1/_2$ corrections are required due to the treatment of SOC by a second-variational expansion. In this method, the ground-state eigenfunctions are solved for scalar-relativistically, and are then used as a basis to expand the spin-orbit split FR eigenfunctions. The p ($j = 1/2$) eigenstate is non-zero at the origin, but is expanded using the SR p state, which is. The corrections involve adding an additional basis function - that may be zero at the nucleus - specifically for the $p^1/_2$ state. In CASTEP, because the FR eigenfunctions are solved for using the full Dirac equation, these corrections are not required.

We find a conduction band minimum (CBM) at (0.316, 0.316, 0.316). This differs to that found by other authors around (0.66, 0.57, 0.57)[164, 168–170], and Larson who finds (0.381, 0.500, 0.500)[165].

To observe a sensible SCF minimisation cycle and bandstructure, we must treat the occupancies of the SR and FR cases differently. The former proceeded with a fixed occupancy, insulator treatment, whereas the latter was required to be treated as a metal. A FR, insulator treatment reported very slow convergence of the SCF cycle minimisation. The energy change between each iteration oscillated between positive and negative values, and did not converge on a reasonable minimum energy before the limit of 300 SCF iterations. On longer calculations, a bandstructure could be extracted that - despite an insulator treatment specified - indicated a metallic structure, inconsistent with other computational and experimental findings. The proximity of the highest valence band to the Fermi energy is noted as a possible cause to this. Further investigation into this phenomena would be of interest. Relaxation of the fixed occupancy treatment in the SR case would not be expected to alter its results.

4.4 Applied magnetic field

4.4.1 Expression

In the anticipation for its use in the evaluation of chemical shielding tensors later, we discuss here the implementation of an applied magnetic field. This affects the Hamiltonian via a perturbation, $\mathcal{V}_{\mathbf{B}}$,

$$\mathcal{V}_{\mathbf{B}} = \frac{1}{2} g \, \mathbf{S} \cdot \mathbf{B}, \tag{4.4}$$

which is the interaction of the electron spin with the magnetic field. This is the final term in equation 3.83. As $\mathbf{S} = \frac{1}{2}\boldsymbol{\sigma}$, we can evaluate the dot product to obtain a more explicit expression,

$$\mathcal{V}_{\mathbf{B}} = \frac{1}{4} g \begin{pmatrix} B_3 & B_1 - iB_2 \\ B_1 + iB_2 & -B_3 \end{pmatrix}, \tag{4.5}$$

where the three components of the applied field are labelled with B_1, B_2 and B_3. This is easily implementable and is appended to the local potential of the calculation, which induces a polarisation of the density matrix.

In energetic terms, this perturbation is very small, even for very large magnetic fields. For example, a back-of-the-envelope calculation of a 50 Tesla field corresponds to a perturbation, from the B_3 component, of around 2.9 meV. The magnetic fields used in experiment utilise resistive electromagnets and superconductors, the latter typically reach up to around 23.5 T. Hybrid techniques have been reported for material research up to around 100 T.[171]

4.4.2 Implementation

Figure 4.5 shows the magnetisation of the system,

$$\mathbf{m}_{\text{cell}} = \int_{\Omega_{\text{BZ}_1}} \mathbf{m}\left(\mathbf{r}\right) \mathrm{d}\mathbf{r}, \tag{4.6}$$

with respect to the applied magnetic field, $\mathbf{B}$, for the hydrogen halide molecules. The effects of SOC increase in the halide atom down the series, and is reflected by higher cell magnetisations for the heavier systems. The mixing of triplet and singlet state character by the SOC interaction gives the j-splitting of states required to polarise the spins.

The HF and HCl molecules, due to only containing light atoms, have very little spin density throughout the cell. This results in only small magnetisations, even at the very extreme end of the scale, where a 20 kT field is applied. HBr and HI, however, have respectively higher magnetisations. Both plots show noisy responses of magnetisation to small applied fields. Bromine takes noticeably longer to stabilise, which is thought to be due to its inclusion of its 3d electrons as valence. These states may complicate the potential energy surface, resulting in the SCF solver struggling to settle in the global minimum state until a strong enough magnetic field is applied.

The magnetisations for HBr and HI equilibrate roughly between 1.1 and 3.5 kT, shown by the shaded region. These fields would indicate a reasonable choice where a finite-field method could be implemented, and is used later in chapter 6 to study

the magnetic response of systems to an applied field. In this range, the effect of the field perturbs the system linearly and is an alternate model to perturbation theory.

Above this ideal range, higher order effects are seen and the plot shows quadratic scaling. At these values, the second-order terms in the expansion become non-negligible and the method described above would not be valid.

4.5 The implementation of the f-matrices

A central quantity discussed so far is the density, which is required for both the SCF cycle and NMR parts of the code. For scalar wavefunctions, it is defined in equation 3.67, and spinors, equation 3.126. One key difference between these equations is in the density-like term, equations 3.68 and 3.115, for scalars and spinors, respectively. In the latter are the f-matrices, equation 3.116. These contain the U-matrices, defined through equation 3.107, that provide a unitary rotation between the *complex* and a *chosen* set of spherical harmonics. The latter then appear in the charge augmentation, equation 3.120.

Importantly, the charge augmentation in the scalar case has already been implemented, equation 3.58. We must therefore be careful to ensure we construct the U-matrices that provide the correct rotation between the complex and this already-implemented set.[2] These spherical harmonics are outlined, with the appropriate U-matrix, in appendix B.

For convenience, the reader can also find the common choice of real spherical harmonics, and the appropriate U-matrix, in appendix B, too.

In the NMR sections of the CASTEP code, the chosen set happens to be complex. This reduces the unitary rotation matrix, $U^{\ell}_{m,m'} = \delta_{mm'} \; \forall \; \ell$. This new set of U and f-matrices were implemented for use in the NMR modules.

[2]The implementation of the unitary rotation matrix was incorrectly defined for a different set of chosen spherical harmonics in CASTEP version 16.1 (formerly 9.0; Biovia release 2016). This resulted in some very strange outputs. The application of a magnetic field in the x direction would polarise the spins in the y! And vice versa.

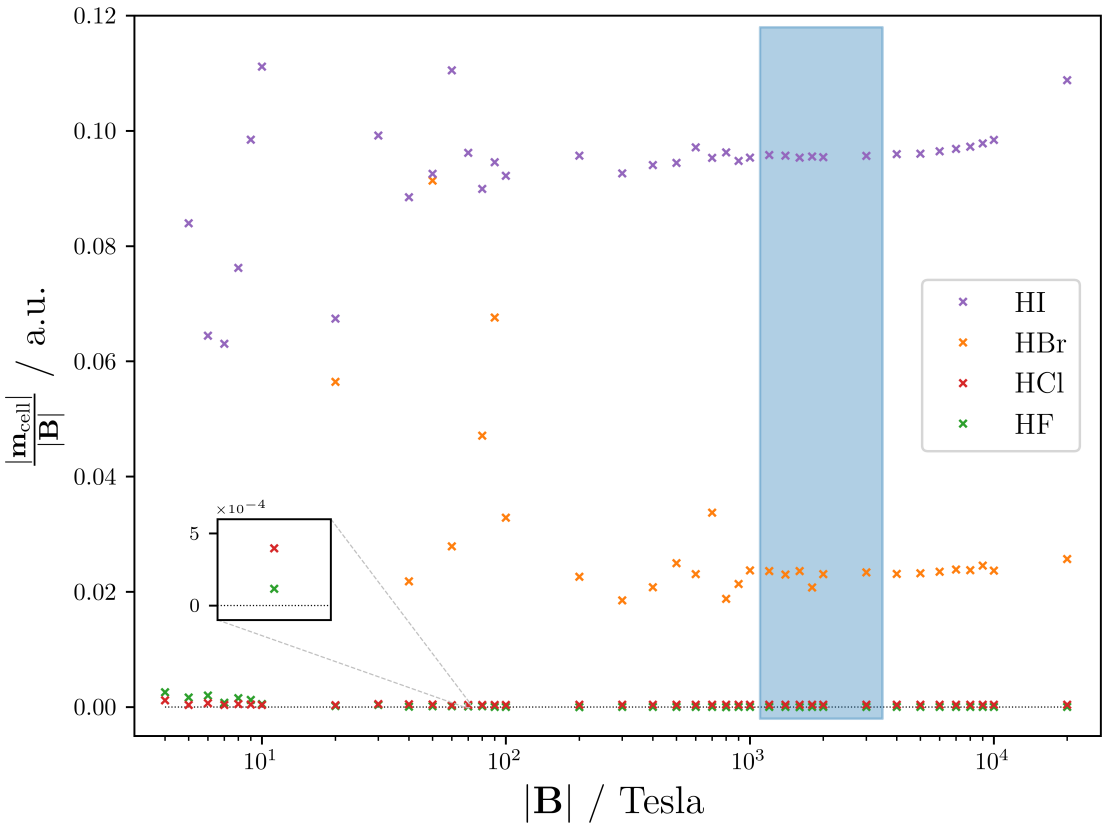


Figure 4.5: Magnetisation of the cell with respect to applied magnetic field for the hydrogen halide molecules. The effects of SOC increase down the group and result in greater magnetisation of the spins. At low field strengths the effects fluctuate due to noise. Higher order contributions increase at high field. The highlighted region, 1.1 kT to 3.5 kT, shows where the magnetic response has equilibrated to linear order.

4.6 Memory and calculation time considerations

When performing a FR calculation, one should be concerned in regard to the extra time and memory requirements due to spinor wavefunctions. In comparison to a NR or SR calculation, we would expect both the memory and calculation time requirements to increase. This is due to the use of two-component spinor wavefunctions and the additional computations required for operator matrix elements, respectively. Additionally, the spin is scalar in the NR/SR formalism, but a vector for a FR calculation. The j-splitting of eigenstates creates additional complexity for the non-local part of the potential; other than the s-state, the $\ell > 0$ angular momentum channel sizes will double.

Some singlepoint energy calculations were performed on boron nitride, BN, to investigate these extra computational demands. Figure 4.6 shows comparisons of time and memory requirements, for scalar and spinor calculations, both with respect to increasing cut-off energy, E_{cut}. The former shows the average length of one SCF cycle, and the latter reports the electronic energy minimisation data.

As expected, both the time and memory requirements increase with respect to E_{cut}. More interestingly, the ratio of FR to SR times per SCF cycle increase with respect to E_{cut}, and varied from around 2 up to 6. In the lower E_{cut} regimes, computations not involving the wavefunction will constitute a large portion of the calculation time, hence the ratio is below the 4-8 times that we would expect. The ratio between FR and SR memory requirements is constant at around 4 times. There exists additional baseline code and system data, that are equal in both regimes, that has been excluded.

As defined in equation 3.51, the cut-off energy, E_{cut}, defines the maximum $\mathbf{G}$ vector considered in the basis set, and as a result, defines the size of the arrays that store the wavefunction. One notable point is that E_{cut} defines a radius for a sphere of points in the reciprocal lattice to be considered in a calculation. The number of points therefore increases as the square of E_{cut}. This is reflected in the fitting of both the time and memory requirements.

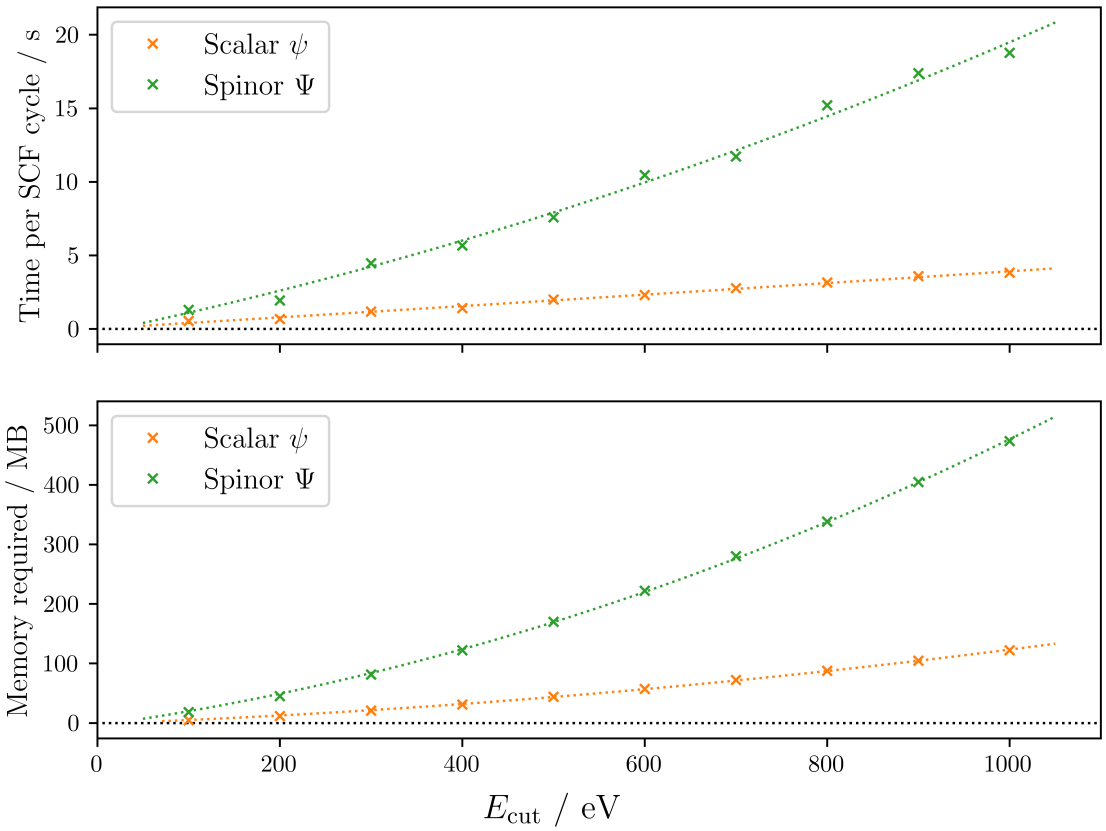


Figure 4.6: Comparison between scalar and spinor calculation self-consistent field cycle times and memory requirements, with increasing cut-off energy E_{cut}. Singlepoint energy calculations were performed on boron nitride using a $5 \times 5 \times 5$ **k**-point grid.

Whilst the wavefunction is stored on a reduced spherical grid, the key variables - such as the charge density, potential, etc. - map to reciprocal space grids of the unit cell. Amongst other variables, the former is therefore directly a function of the number of bands, whereas the latter is not. It is typical, therefore, for the memory of larger systems to be dominated by the wavefunction arrays, and for smaller systems, the reciprocal cell grids. In FR calculations, the two spinor components double the number of wavefunction arrays, furthering the memory dependence of FR calculations on the number of bands.

4.7 Symmetry breaking

In the NR and SR formulations, the treatment of spin is scalar; that is, the direction can always be chosen to be in **z**. There exists no coupling to the lattice, and as a result, the Hamiltonian reflects the geometric symmetry of the crystal.[172] Both the electronic density and magnetisation can therefore be obtained through a reduced **k**-point grid of the Brillouin zone, as outlined by Monkhorst and Pack.[117] **k**-points of opposite sign are also degenerate, which can (at best) half the number required for the calculation. This even holds for magnetic structures that do not obey time reversal symmetry.

On the introduction of SOC in the FR treatment, these symmetries are broken. The directional nature of the spin now couples it to the geometry of the lattice. Only the symmetry operations of the space group of the crystal, that do not affect the polarisation of the spin, are allowed. **k**-points of opposite sign must also be treated separately, as this would lead to the conclusion that the magnetisation is 0 for all space.

For example, the cubic T_d point group has 24 spatial rotations. NR and SR calculations can thus make use of all these symmetries, even when considering spin. However, for the FR case with spin in the [001] direction, only 8 of these are applicable, of which, correspond to the tetragonal point group.

Despite this, it may be possible to combine a spatial rotation and the time-reversal symmetry together, to result in an allowed transformation. For example, a

ferromagnetic structure may be mapped onto itself by a 180° rotation, followed by application of time-reversal symmetry (which inverts the magnetisation).

These considerations, along with those discussion in section 4.6, result in greater time and memory requirements for FR calculations.

4.8 Towards nuclear magnetic resonance calculations

Each progression of the theory up until now has been needed for the calculation of NMR parameters. The NR quantum mechanics allowed us to form a basis to the DFT theory, which has been implemented in the planewave electronic structure code, CASTEP. In this project, we needed to reevaluate the pseudopotential construction and PAW method to allow for spinors, which are solved using the FR Dirac equation. This implementation now allows us to account for SOC in our calculations of NMR parameters, of which, is of critical importance in systems that contain heavy elements. Ultimately, all of this work led to the expression of the electronic density; equations 3.67 and 3.126 for the NR/SR and FR theories, respectively. This is the key variable in the DFT theory, and also arises directly in the calculation of the electric field gradient parameter in the next section.

5 Electric field gradients

Contents

5.1 Electric field gradient expression 85
5.2 Implementation 88
5.2.1 Testing spinor wavefunctions 88
5.2.2 Testing norm-conserving pseudopotentials 88
5.2.3 Calculations with relativistic pseudopotentials 92
5.3 Results 92
5.3.1 Convergence testing 95
5.3.2 ^{133}Cs 96
5.3.3 ^{209}Bi 96

5.1 Electric field gradient expression

In this chapter, we will review the method, outlined by Profeta *et al.*,[57] to calculate the electric field gradient (EFG) tensor, $\overleftrightarrow{\mathcal{G}}(\mathbf{r})$. We will use the formalism, outlined by dal Corso and Conte,[144] to generalise the PAW approach to spinor wavefunctions that was discussed in section 3.5.8.

The EFG is a function of each point in space, $\mathbf{r}$, and is given by,

$$\overleftrightarrow{\mathcal{G}}(\mathbf{r}) = \frac{\partial \mathbf{E}(\mathbf{r})}{\partial \mathbf{r}} - \frac{1}{3}\mathbb{1}_3 \left[\boldsymbol{\nabla} \cdot \mathbf{E}(\mathbf{r})\right], \tag{5.1}$$

where $\mathbf{E}(\mathbf{r})$ is the electric field; that is,

$$\mathbf{E}(\mathbf{r}) = \int \frac{n(\mathbf{r}')}{|\mathbf{r}-\mathbf{r}'|^3}(\mathbf{r}-\mathbf{r}')\,\mathrm{d}\mathbf{r}'. \tag{5.2}$$

With the insertion of this expression into equation 5.1, we get,

$$\overleftrightarrow{\mathcal{G}}(\mathbf{r}) = \int \frac{n(\mathbf{r}')}{|\mathbf{r}-\mathbf{r}'|^3}\left[\mathbb{1}_3 - 3\frac{(\mathbf{r}-\mathbf{r}')\otimes(\mathbf{r}-\mathbf{r}')}{|\mathbf{r}-\mathbf{r}'|^2}\right]\mathrm{d}\mathbf{r}'. \tag{5.3}$$

The expression in brackets here is purely angular; that is it contains no radial dependence. In other words, it is a function of only *normalised* position vectors, $\frac{\mathbf{r}-\mathbf{r}'}{|\mathbf{r}-\mathbf{r}'|}$. This is known as a spherical tensor operator, and due to the Wigner-Eckart theorem, can be expressed with purely angular components. Its elements are expanded in terms of the complex spherical harmonics,

$$\delta_{\alpha\beta} - 3\frac{(r_\alpha - r'_\alpha)(r_\beta - r'_\beta)}{|\mathbf{r}-\mathbf{r}'|^2} = \sqrt{\frac{6\pi}{5}}\sum_{q=-2}^{2} C^q_{\alpha\beta} Y^q_2(\theta,\varphi), \tag{5.4}$$

where α and β run over the x, y, z directions. The vector, $\mathbf{C}_{\alpha\beta}$, contains sets of Clebsch-Gordan coefficients that recover the angular dependence. These are well known and given in appendix C with an example.

The final task is to obtain $n(\mathbf{r})$ and insert it into equation 5.3. The density is split into the ionic and electronic contributions, $n(\mathbf{r}) = n^{\mathrm{ion}}(\mathbf{r}) + n^{\mathrm{elec}}(\mathbf{r})$. The first returns the ionic EFG,

$$\mathcal{G}^{\mathrm{ion}}_{\alpha,\beta}(\mathbf{r}) = \sum_{\mathbf{R}} \frac{Z_{\mathbf{R}}}{|\mathbf{r}-\mathbf{R}|^3}\left[\delta_{\alpha\beta} - 3\frac{(r_\alpha - R_\alpha)(r_\beta - R_\beta)}{|\mathbf{r}-\mathbf{R}|^2}\right]. \tag{5.5}$$

This is evaluated for each ion in the system to obtain the tensor, $\overleftrightarrow{\mathcal{G}}^{\mathrm{ion}}_{\mathbf{R}}$, and follows an Ewald summation technique[173] as in Profeta *et al.*.

The electronic density was obtained, according to the pseudopotential and PAW scheme, as equation 3.126. Inserting its trace into 5.3, we get the pseudopotential contribution from the first term,

$$\mathcal{G}^{\mathrm{bare}}_{\alpha,\beta}(\mathbf{r}) = \sum_{\sigma}\int \frac{|\tilde{\Psi}^\sigma(\mathbf{r}')|^2}{|\mathbf{r}-\mathbf{r}'|^3}\left[\delta_{\alpha\beta} - 3\frac{(r_\alpha - r'_\alpha)(r_\beta - r'_\beta)}{|\mathbf{r}-\mathbf{r}'|^2}\right]\mathrm{d}\mathbf{r}'. \tag{5.6}$$

Following Profeta *et al.*, we calculate this in reciprocal space and evaluate the expression at each ionic position when performing the Fourier transform back to real space; obtaining $\overleftrightarrow{\mathcal{G}}^{\text{bare}}_{\mathbf{R}}$. The second term is the augmentation,

$$\mathcal{G}^{\text{aug}}_{\mathbf{R},\alpha,\beta} = \sum_{\tau,\ell,j,m} \sum_{\tau',\ell',j',m'} \sum_{\sigma} \rho^{\mathbf{R},\sigma,\sigma}_{\tau,\ell,j,m;\tau',\ell',j',m'} \, \Pi^{\mathbf{R}}_{\tau,\ell,j;\tau',\ell',j'} \sum_{q=-2}^{2} C^{q}_{\alpha\beta} \Gamma^{q}_{\ell,j;\ell',m'}, \tag{5.7}$$

where we have used the on-site approximation to evaluate this term for each ion at $\mathbf{R}$; see point 2 of the rules outlined in section 3.4.7. We have the purely atomic augmentation term,

$$\Pi^{\mathbf{R}}_{\tau,\ell,j;\tau',\ell',j'} = \int \frac{1}{r^3} \left[\phi^{\mathbf{R}}_{\tau,\ell,j}(r) \phi^{\mathbf{R}}_{\tau',\ell',j'}(r) - \tilde{\phi}^{\mathbf{R}}_{\tau,\ell,j}(r) \tilde{\phi}^{\mathbf{R}}_{\tau',\ell',j'}(r) \right] \mathrm{d}r, \tag{5.8}$$

which is only required to be computed for one of each ion and projector pair, and the analytical Gaunt integrals,

$$\Gamma^{q}_{\ell,j;\ell',m'} = \sqrt{\frac{6\pi}{5}} \int \int Y^{*}_{\ell,m}(\theta,\varphi) Y^{q}_{2}(\theta,\varphi) Y_{\ell',m'}(\theta,\varphi) \, \mathrm{d}\theta \, \mathrm{d}\varphi, \tag{5.9}$$

which are readily calculable and stored before the calculation of the EFG term. Recall, from section 3.5.8, that the *subscript m* denotes that any choice of harmonics are acceptable, providing the correct unitary rotation matrix is chosen; see equation 3.107. The augmentation term concerns the behaviour nearer the nucleus, and can therefore be expected to have the largest change due to SOC.

The total EFG tensor, for an ion at $\mathbf{R}$, is then,

$$\overleftrightarrow{\mathcal{G}}_{\mathbf{R}} = \overleftrightarrow{\mathcal{G}}^{\text{ion}}_{\mathbf{R}} + \overleftrightarrow{\mathcal{G}}^{\text{bare}}_{\mathbf{R}} + \overleftrightarrow{\mathcal{G}}^{\text{aug}}_{\mathbf{R}} \, . \tag{5.10}$$

The diagonal components of this tensor are characterised by two quantities: the quadrupolar coupling constant, C_Q, given in equation 2.20; and the asymmetry parameter, η_Q, given in equation 2.21. The former quantifies the magnitude of the interaction between a nucleus and its quadrupole moment. The latter describes the directional dependence of the interaction with regard to the Cartesian coordinates.

5.2 Implementation

5.2.1 Testing spinor wavefunctions

To ensure the generalisation of the code was implemented correctly, comparisons between scalar and spinor wavefunctions were performed.

In the construction of the atomic pseudopotentials, it is possible to solve for the radial, all-electron eigenspinors, $\Phi^{\mathbf{R}}_{\tau,\ell,j,m_j}(r)$, using the Schrödinger equation. Despite being a two-component spinor, it will contain no relativistic information. A pseudopotential can then be constructed, using the method of section 3.5.7, but will critically contain no effects of SOC. A non-collinear spin calculation can then be performed using this pseudopotential. In doing so, we will perform a NR calculation at the aforementioned 4-8 times the cost of an analogous scalar wavefunction calculation. However, it provides the advantage of running through the code with spinor objects, which should exactly reproduce the scalar code due to the neglect of relativity in both cases.

For validation, multiple systems were tested using this method. In figure 5.1, are 129 C_Q values obtained from spinor calculations, plotted against those from equivalent scalar calculations. A variety of molecular and crystalline materials were chosen. The calculations were performed using the PBE exchange-correlation functional, with an energy cut-off of 1000 eV. Three additional values of C_Q for the halides in HF, HBr and HI molecules, all of equal quality to the others, were obtained. However, these were omitted from the plot as their magnitudes were considerably larger and reduced the interpretability. We expect a linear $y = x$ line through each point; and this is what we obtain. From this, we can conclude that the generalised PAW approach to spinors, equation 5.7, has been implemented correctly.

5.2.2 Testing norm-conserving pseudopotentials

Before benchmarking the relativistic calculations, we ensure that the NCP set, designed for the Dirac solver, are suitably accurate when compared to the latest

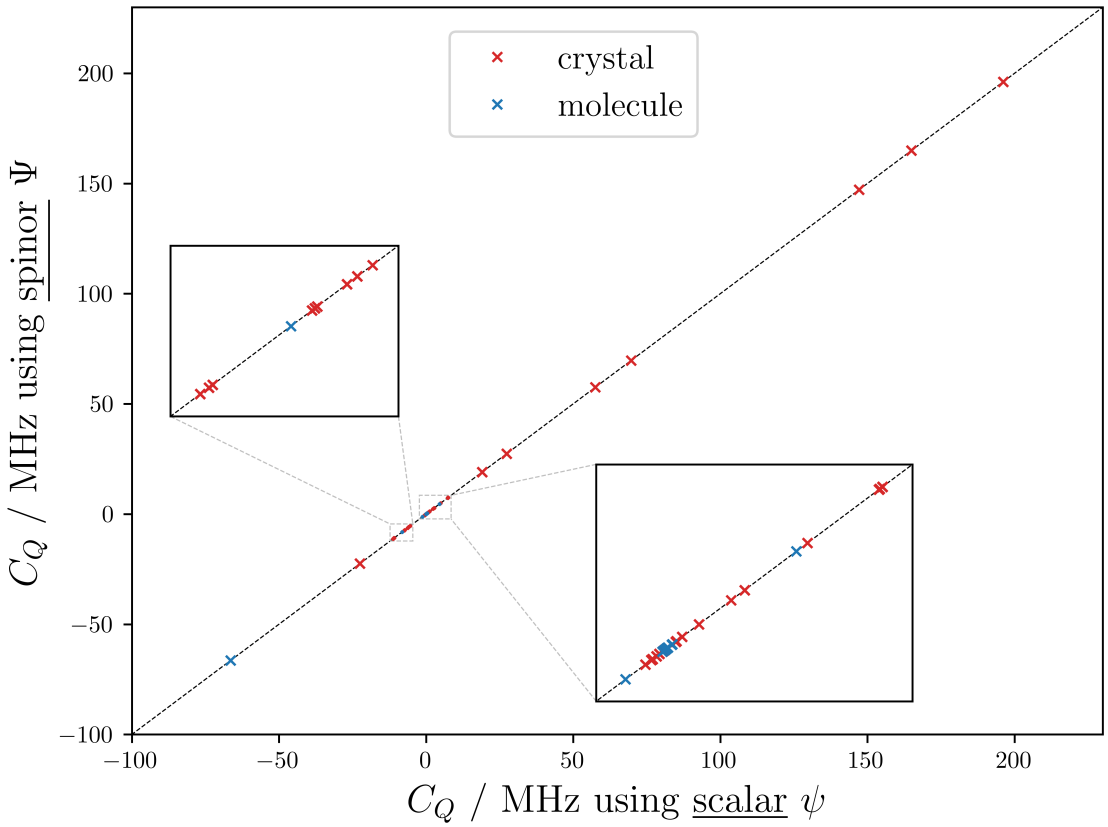


Figure 5.1: Validation of the spinor code for the calculation of C_Q values. The horizontal axis represents values computed from scalar wavefunctions, whilst the vertical axis represents those calculated in the spinor regime. Excluded data points are those of F, Br and I in their respective hydrogen halide molecules. Apart from numerical noise, the relative deviation was zero.

USPs. If they are, we use them when performing benchmarking calculations with the confidence that they are appropriately accurate.

Van Lenthe and Baerends document a set of EFG calculations for a range of halide-containing diatomic molecules.[174] Accompanying these are observed values, which we use for comparison here and name them the 'diatomic molecule set'. References for each of the values can be found inside reference [174].

Plotted in figure 5.2 is a comparison between the NCPs and USPs for C_Q values in the diatomic molecule set. These calculations were performed at the scalar-relativistic level of Koelling-Harmon, using the PBE exchange-correlation functional and a 1000 eV cut-off energy. As expected, the USPs perform slightly better overall. Tables D.1 and D.2 in appendix D represent the halide and metallic values for these data, respectively.

The halides report excellent agreement between the NCP and USP values, with median relative deviations of 3.348 % and 4.776 %, respectively. We see the heavier ^{127}I perform slightly worse than the lighter ^{35}Cl and ^{79}Br, but still within a suitable level of accuracy.

In the metals, we see a comparably worse performance from both sets of pseudopotentials, with median relative deviations of 19.09 % and 10.61 % for the NCPs and USPs, respectively. This is most likely due to the higher levels of correlation in these ions, as well as the close proximity of charge augmentation regions (which formally should not overlap) in the small diatomics. However, the root-mean-square (RMS) relative deviation for the USPs is 10.65 %, which is comparable to its halide value. See equation D.2 for the definition of RMS relative deviation. The NCP value is double its halide counterpart, however, which highlights that a set of relativistic USPs may be needed for publication-quality results of the EFGs. We proceed with the confidence that the NCP set is suitable for benchmark calculations, however.

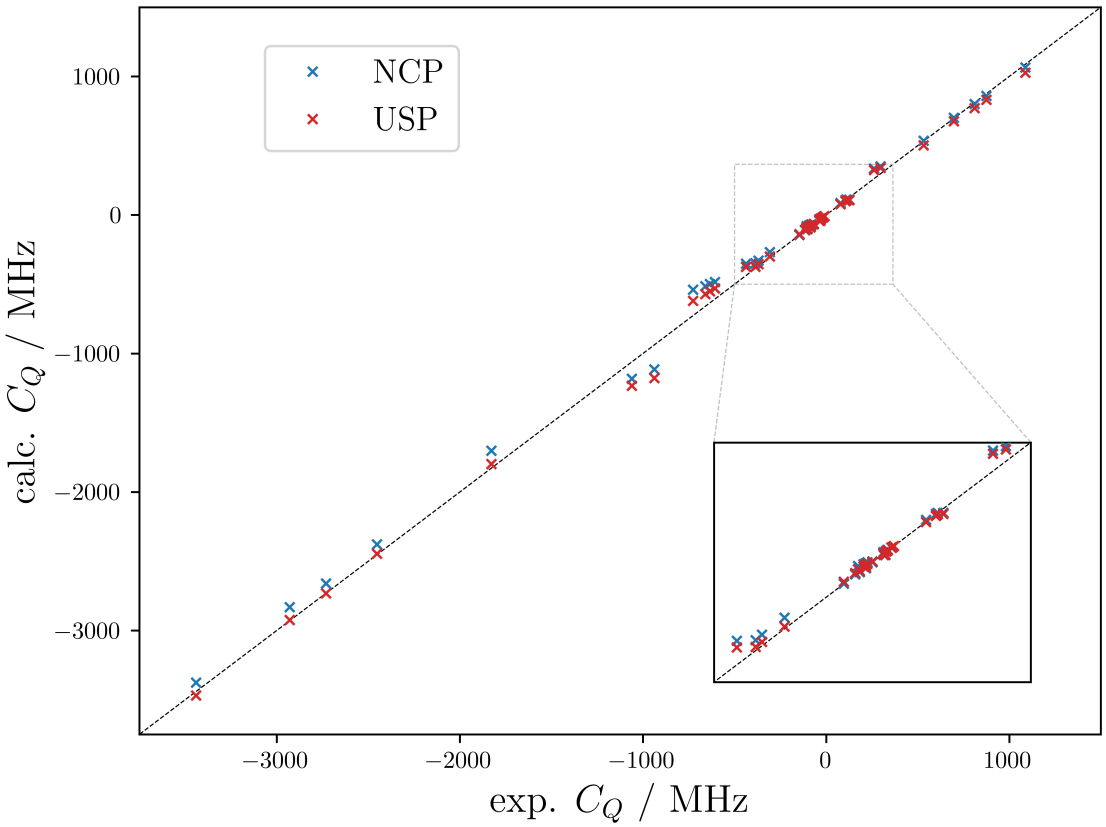


Figure 5.2: Comparison of pseudopotentials for C_Q values against experiment for a range of diatomic molecules. NCP: norm-conserving pseudopotential. USP: ultra-soft pseudopotentials. Experimental values taken from reference [174]. For halide C_Q values, the root-mean-square relative deviations were 10.82 % and 10.13 % for the NCP and USP values, respectively. For metallic C_Q values, the root-mean-square relative deviations were 19.43 % and 10.65 % for the NCP and USP values, respectively.

5.2.3 Calculations with relativistic pseudopotentials

We turn to calculations that use fully-relativistic (FR) pseudopotentials. Plotted in figure 5.3 are C_Q values of the diatomic molecule set, obtained from fully-relativistic calculations, against their experimental values. Figure 5.4 represents the same data with comparisons to non-relativistic (NR) and scalar-relativistic (SR) calculations. Tables D.3 and D.4 in appendix D detail the halide and metallic C_Q data, respectively. The NR treatment corresponds to Schrödinger equation, SR the Koelling-Harmon equation and FR the Dirac equation. All calculations use the PBE exchange-correlation functional and a 1000 eV cut-off energy.

In general, we see a systematic improvement on the obtained C_Q values between the theories. The NR solver consistently performs far worse than the SR and FR, as expected. Numerically, the halides have RMS relative deviations for NR, SR and FR approaches of 15.17 %, 10.82 % and 9.558 %, respectively. This shows that a SR approach is imperative for calculations of this nature. It also indicates that the contributions of spin-orbit coupling are smaller, but non-negligible.

The metallic ions evidence a similar story, with RMS relative deviations for NR, SR and FR approaches of 23.89 %, 19.43 % and 19.23 %, respectively. It is possible that relativistic effects may be lost due to noise with the lower accuracy of the NCPs.

We proceed by summarising that the FR approach implemented has favourable results in regard to experiment, and slightly improves upon the current SR theory. These effects of SOC are noted to be typically smaller than the corrections offered between the NR and SR theories. Users should thus consider the desired accuracy of results against the increased computation time for the FR spinor approach.

5.3 Results

The implemented methodology was use to explore the role of SOC in compounds containing heavy elements, namely ^{133}Cs and ^{209}Bi, with appropriate spins of 7/2 and 9/2, respectively.

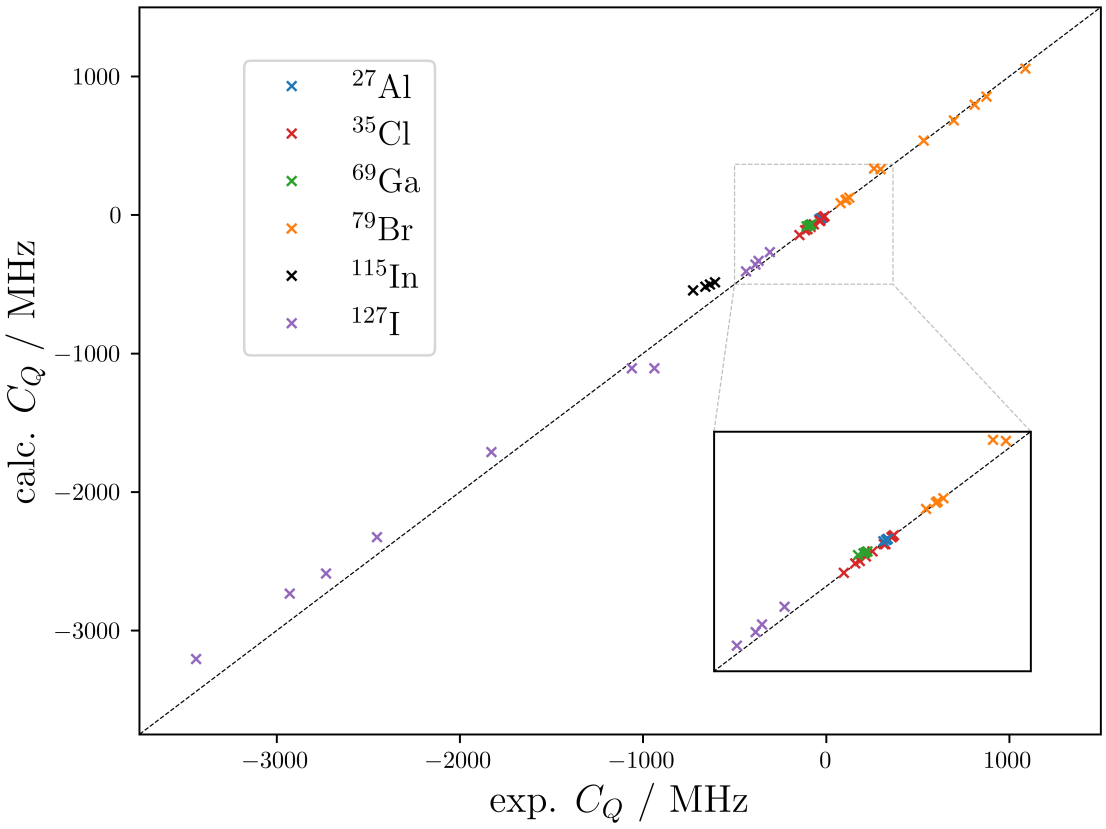


Figure 5.3: Comparison of C_Q values between fully-relativistic calculations and experiment for a range of diatomic molecules. Experimental values taken from reference [174]. The root-mean-square relative deviations were 9.558 % and 19.23 % for the halide and metallic C_Q values, respectively.

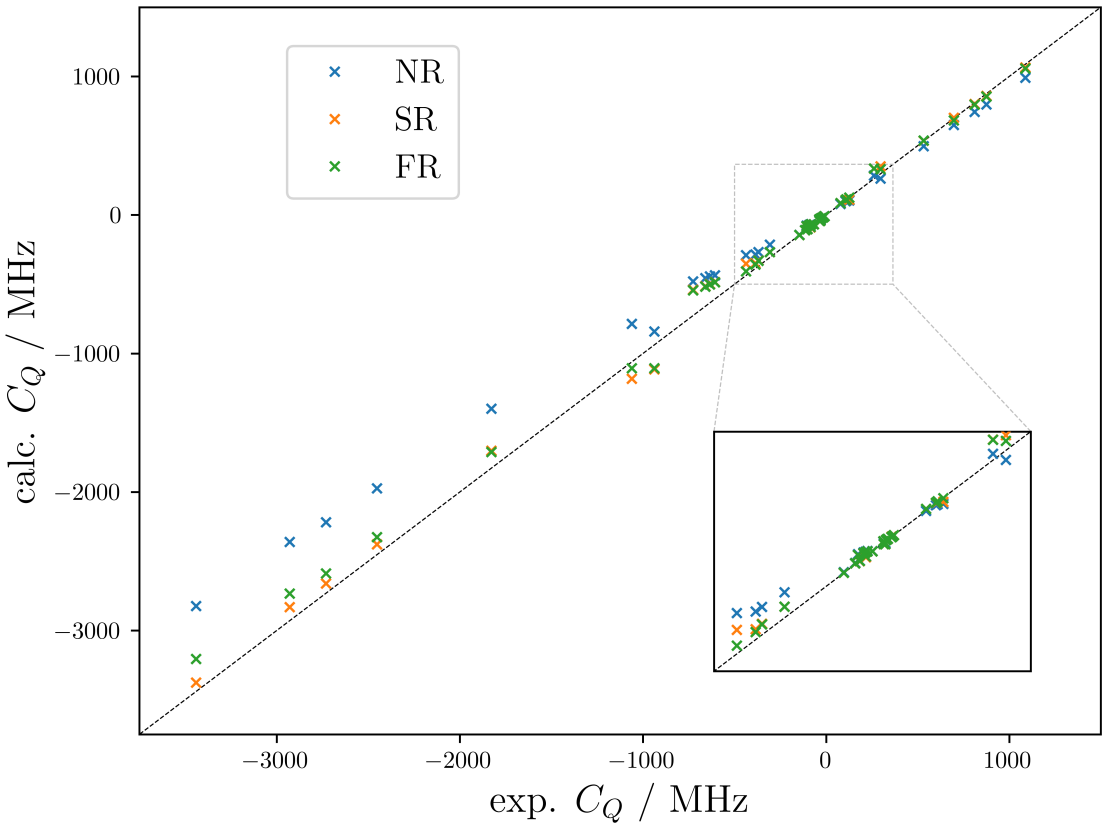


Figure 5.4: Comparison of the treatment of relativity for C_Q values for a range of diatomic molecules. NR: non-relativistic. SR: scalar-relativistic. FR: fully-relativistic. Experimental values taken from reference [174]. For the NR solver, the root-mean-square relative deviations were 15.17 % and 23.89 % for the halide and metallic C_Q values, respectively. For the SR solver, the root-mean-square relative deviations were 10.82 % and 19.43 % for the halide and metallic C_Q values, respectively. For the FR solver, the root-mean-square relative deviations were 9.558 % and 19.23 % for the halide and metallic C_Q values, respectively.

The calculations performed in this section used the LDA and PBE exchange-correlation functionals. Experimental and optimised geometries are used, and the latter were relaxed at the scalar-relativistic Koelling-Harmon level of theory, using the latest on-the-fly ultra-soft pseudopotentials. The unit cells were constrained under the optimisation process, allowing only the ions to move. The EFG calculations utilised a relativistic set of norm-conserving pseudopotentials, generated on-the-fly in CASTEP.

The range of experimental ^{209}Bi values are taken from Hamaed *et al.*[175] and Griffith *et al.*[176]. The former for BiOCl, BiOBr and BiOI, and the latter for $BiAlTeO_6$ and $BiGaTeO_6$. The experimental ^{133}Cs values are taken from Skibsted *et al.*, who investigated the caesium salts $CsClO_4$, Cs_2CO_3 and Cs_2SO_4.[177]

5.3.1 Convergence testing

Graphed in figures D.1 and D.2 in appendix D are the convergence of C_Q values in a subset of the ^{209}Bi and ^{133}Cs compounds, with respect to the cut-off energy, E_{cut}. This corresponds to increasing basis set size, as in equation 3.51. One of each lattice structure was chosen to test the convergence. It was deemed the C_Q values were converged at a cut off value of $E_{\text{cut}} = 1300$ eV. This was then used for all calculations that follow.

The Brillouin zone sampling was then considered for convergence. The density of **k**-points chosen can drastically affect the accuracy of the mapping of the Brillouin zone, which NMR parameters are highly sensitive to. Convergence of C_Q with respect to the chosen reciprocal grid is relatively straightforward to perform. At the converged value of $E_{\text{cut}} = 1300$ eV, several MP **k**-point grids (with increasing density) were investigated for the calculation subset. See graphs D.3 and D.4. The BiOCl system was deemed converged at a **k**-point spacing of 0.04 Å^{-1}, which corresponds to a grid of $7 \times 7 \times 4$. This was also used for the BiOBr and BiOI systems. The $BiAlTeO_6$ system was deemed converged at a **k**-point spacing of 0.04 Å^{-1}, which corresponds to a grid of $6 \times 6 \times 6$. This was also used for the $BiGaTeO_6$ system. The $CsClO_4$ system was deemed converged at a **k**-point spacing

of 0.05 Å^{-1}, which corresponds to a grid of $3 \times 4 \times 3$. The Cs_2SO_4 system was deemed converged at a **k**-point spacing of 0.04 Å^{-1}, which corresponds to a grid of $4 \times 3 \times 5$. The Cs_2CO_3 system was deemed converged at a **k**-point spacing of 0.05 Å^{-1}, which corresponds to a grid of $4 \times 2 \times 3$.

5.3.2 ^{133}Cs

Tables 5.1 and 5.2 show C_Q and η for the ^{133}Cs compounds. The geometries were optimised and the exchange-correlation functional was PBE. In each, compared are the three levels of relativistic theory: Schrödinger (NR), Koelling-Harmon (SR) and Dirac (FR). Only the latter was computed using spinor wavefunctions. The calculations perform relatively well with respect to the experiment, particularly in the C_Q parameter. It is worth noting that the sign of C_Q is not typically obtained via experimental NMR, and the anisotropy value, η, is often very sensitive the errors in a calculation.

The small magnitude of C_Q for ^{133}Cs arises from its 6s valence electron controlling its chemical properties. The spherical nature of s orbitals gives no gradient of the electric field, and does not contribute greatly to its C_Q value. Perturbations of the ^{133}Cs EFG come from its environment in the crystal, but are small because of cubic order decay of effects from other ions, and the weaker SOC interaction further from the ^{133}Cs ion. It is also worth noting that the valence s electron is not j-split in energy by the effects of SOC. This fact is emphasised by the large change between the NR Schrödinger and SR Koelling-Harmon values, but only a small impact by the FR Dirac solver. This results in the gradient of the electric field, and its anisotropy, mostly accounted for by the inclusion of SR effects.

5.3.3 ^{209}Bi

Geometry

The effect of geometry plays a very important role in NMR parameters and is often used as a technique to determine the validity of proposed compound structures.

Table 5.1: C_Q values for ^{133}Cs in the $CsClO_4$, Cs_2SO_4 and Cs_2CO_3 systems. The quadrupole moment used was, $Q(^{133}\text{Cs}) = -0.0034$ barn. Experimental values taken from reference [177].

Solver	$CsClO_4$	Cs_2SO_4		Cs_2CO_3	
		site 1	site 2	site 1	site 2
Schrödinger	-0.0790	-0.113	0.0390	-0.405	0.199
Koelling-Harmon	0.120	-0.180	0.056	-0.651	0.309
Dirac	0.122	-0.183	0.057	-0.663	0.313
exp.	0.1336(6)	0.261(1)	0.02(0.1)	0.695(14)	0.479(23)

Table 5.2: η values for ^{133}Cs in the $CsClO_4$, Cs_2SO_4 and Cs_2CO_3 systems. Experimental values taken from reference [177].

Solver	$CsClO_4$	Cs_2SO_4		Cs_2CO_3	
		site 1	site 2	site 1	site 2
Schrödinger	0.985	-0.113	0.0390	0.160	0.234
Koelling-Harmon	0.120	0.0646	0.527	0.153	0.220
Dirac	0.122	0.0637	0.527	0.153	0.220
exp.	0.11(1)	0.01(1)	0.27(11)	0.34(5)	0.58(7)

Figure 5.5 shows the calculated C_Q values with LDA using the experimental geometries against the obtained values by experiment. All three relativistic treatments for the calculated results are included. There is a roughly systematic difference in the calculated values being higher than those found by experiment. The FR results reinforce this as they are greater than the SR values in all cases. This may indicate that the ^{209}Bi nuclear quadrupole moment is slightly high.

We also test the differences in C_Q of the geometries optimised with the CASTEP package, and those used in the experimental studies. Figure 5.6 shows the former plotted against the latter with the LDA exchange-correlation functional. All three relativistic treatments are included. The root-mean-square deviation between the geometries is 6.455 MHz, which equates to 3.47 % to 10.49 % difference. The relaxed geometries were chosen to test the effects of the choice of exchange-correlation functional.

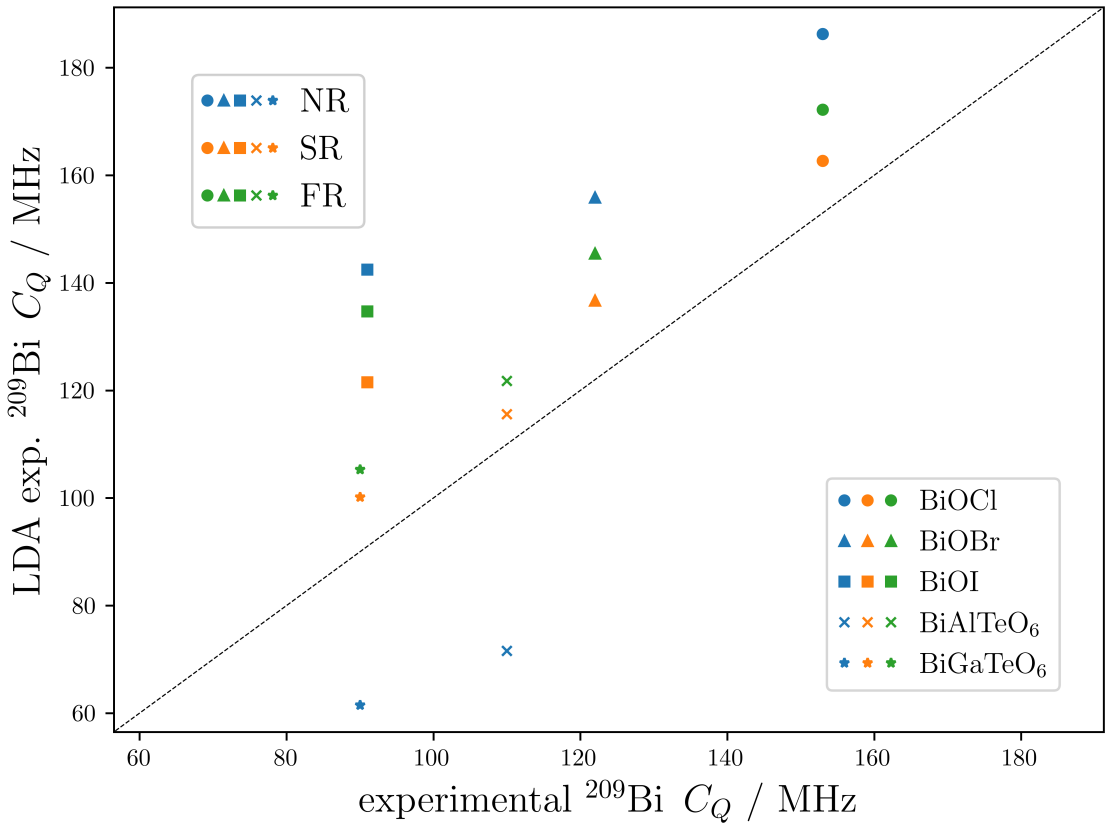


Figure 5.5: C_Q values calculated using the experimental geometry against those obtained by experiment for ^{209}Bi compounds. The LDA exchange-correlation functional was used and $Q(^{209}\text{Bi}) = -0.5160$ barn. NR: non-relativistic. SR: scalar-relativistic. FR: fully-relativistic.

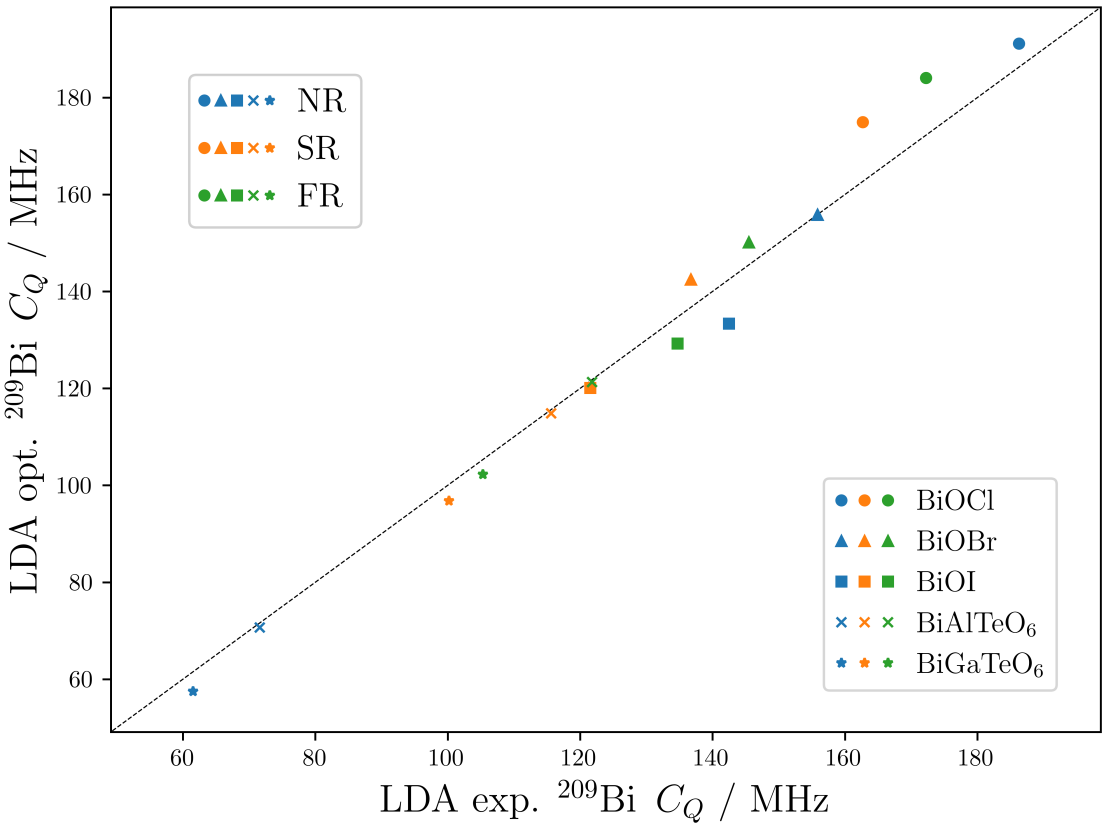


Figure 5.6: C_Q values of optimised against experimental geometries for ^{209}Bi compounds. The LDA exchange-correlation functional was used and $Q(^{209}\text{Bi}) = -0.5160$ barn. NR: non-relativistic. SR: scalar-relativistic. FR: fully-relativistic.

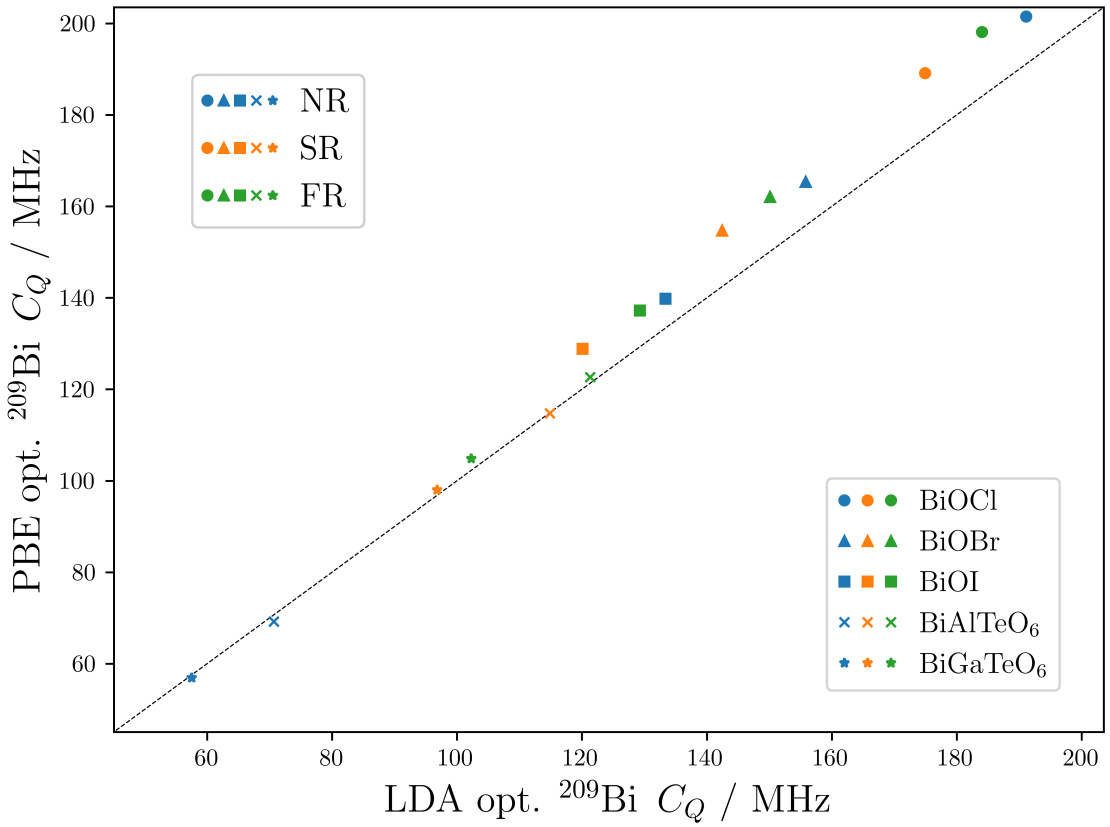


Figure 5.7: C_Q values using PBE against LDA functionals for ^{209}Bi compounds. The geometry optimised structures were used and $Q(^{209}\text{Bi}) = -0.5160$ barn. NR: non-relativistic. SR: scalar-relativistic. FR: fully-relativistic.

Exchange-correlation functional

The exchange-correlation functional is important in capturing the electronic correlation in ions, particularly that of heavy elements. As discussed in section 4.2, the current treatment of functionals for non-collinear spin in the CASTEP package is to use the locally collinear approach. The use of functionals above LDA may cause difficulties, due to their inclusion of electron density derivates in their definitions. Despite all converging, the PBE calculations performed in this study saw up to roughly twice the number of SCF cycles required to obtain a converged wavefunction, when compared to their respective LDA counterparts.

Plotted in figure 5.7 is the results for the PBE functional against LDA, both for the optimised geometry systems. The root-mean-square deviation between the functionals is 9.497 MHz, which equates to 4.97 % to 16.51 % difference. It is noted that the BiOX compounds lie consistently above the $y = x$ line. This may hint to some correlation effects that the PBE functional is picking up that the LDA has missed.

Relativistic effects

Table 5.3 details the EFG parameters, C_Q and η, for the BiOX compounds. Table 5.4 has similar data for the $BiMTe_6$ compounds. The geometries were optimised and the exchange-correlation functional was PBE. In each, compared are the three levels of relativistic theory: Schrödinger (NR), Koelling-Harmon (SR) and Dirac (FR). The effects of relativity are more prevalent in the ^{209}Bi compounds. There is a roughly systematic change in the C_Q values with respect to the relativistic treatment. FR calculations report higher values than the experimental for all compounds, and may indicate that the ^{209}Bi nuclear quadrupole moment is slightly high.

Nuclear quadrupole moment

It is noted that attaining an accurate value of nuclear quadrupole moments is an especially challenging problem. Calculations using a multi-configurational basis with the Dirac-Fock model on a neutral ^{209}Bi atom report a value of $Q(^{209}\text{Bi}) = -0.516(15)$

Table 5.3: EFG parameters for ^{209}Bi in the BiOCl, BiOBr and BiOI systems. The quadrupole moment used was, $Q(^{209}\text{Bi}) = -0.516$ barn. Experimental values taken from reference [175].

Solver	C_Q / MHz			η		
	BiOCl	BiOBr	BiOI	BiOCl	BiOBr	BiOI
Schrödinger	202	165	140	0.0	0.0	0.0
Koelling-Harmon	189	155	129	0.0	0.0	0.0
Dirac	198	162	137	0.0	0.0	0.0
exp.	153(3)	122(3)	91(3)	0.01(1)	0.03(3)	0.01(1)

barn,[178, 179] which the CASTEP package uses by default. However, more recent studies obtain values of $Q(^{209}\text{Bi}) = -0.420(8)$ barn[180] and $Q(^{209}\text{Bi}) = -0.4151$ barn[181]. Both investigated the EFG of BiN and BiP molecules in the coupled cluster scheme using the relativistic Dirac-Coulomb equation. Most notably, a recent set of calculations report a similar value of $Q(^{209}\text{Bi}) = -0.418(6)$ barn, obtained with the same approach as the previous two but on the neutral ^{209}Bi atom.[182]

Plotted in figure 5.8, is the $\mathcal{G}_{zz}$ component of the EFG tensor, for the ^{209}Bi compounds, against the experimental C_Q values. The optimised geometries and PBE functional were used. Using equation 2.20, we determine the nuclear quadrupole moment of ^{209}Bi through the gradient of the linear fit as $Q(^{209}\text{Bi}) = -0.406$ barn. This value supports the recent proposals of an update to the commonly used nuclear quadrupole moment of ^{209}Bi.

The critical generalisation of the PAW theory, applied to the calculation of EFG tensors, has allowed our work to extend the scope of the studied systems to solid-state compounds, which reinforce the previous molecular investigations. The good agreement of our obtained C_Q values for ^{209}Bi indicates the validity of the approach used, and promises the possibility of additional EFG studies on solid-state systems containing heavy compounds.

A final test for the validity of this work is the extension of the EFG calculations in the spinor PAW scheme with ultra-soft pseudopotentials. The new implementation

Table 5.4: EFG parameters for ^{209}Bi in the $BiAlTeO_6$ and $BiGaTeO_6$ systems. The quadrupole moment used was, $Q(^{209}\text{Bi}) = -0.516$ barn. Experimental values taken from reference [176].

Solver	C_Q / MHz		η	
	$BiAlTeO_6$	$BiGaTeO_6$	$BiAlTeO_6$	$BiGaTeO_6$
Schrödinger	69.2	56.9	0.0	0.0
Koelling-Harmon	115	98.0	0.0	0.0
Dirac	123	105	0.0	0.0
exp.	110(2)	90(2)	0.03(3)	0.02(2)

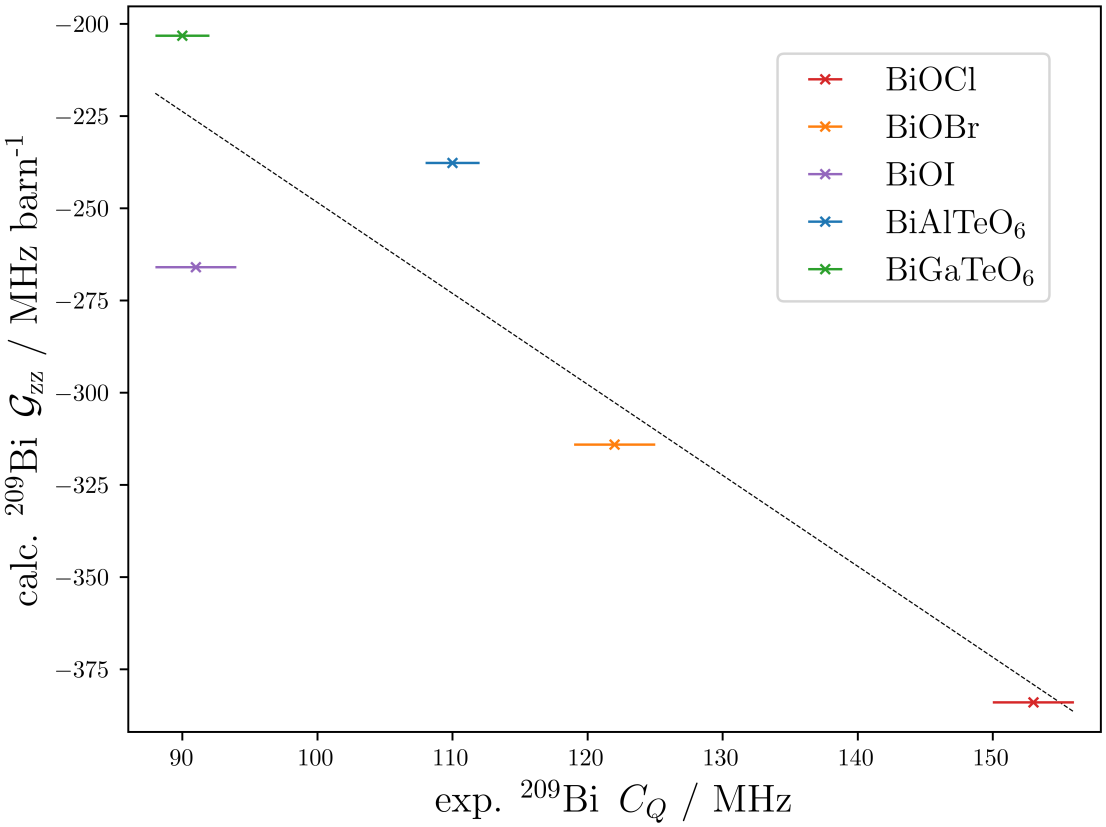


Figure 5.8: $\mathcal{G}_{zz}$ against experimental C_Q values for the ^{209}Bi compounds. The inverse of the gradient gives the ^{209}Bi nuclear quadrupole moment as $Q(^{209}\text{Bi}) = -0.406$ barn. $\mathcal{G}_{zz}$ values were calculated using optimised geometries and the PBE functional.

of the spinor EFG calculations does not require any further work, and is only subject to the ability to generate relativistic USPs on-the-fly in the CASTEP package.

It is also of worth to note that the method outlined here is applicable to materials that have magnetic ground states, such as metals or paramagnetic compounds with unpaired electrons. The former only requires the ability to impose fractional occupancies of states in the equations above, which is already accounted for in the implementation in the CASTEP code. The latter have been investigated by Cuny *et al.*,[183] using a collinear magnetism approach, where they found agreeable comparison of the method for paramagnetic compounds compared to diamagnetics. The work here would allow for the extension of the study to structures with non-collinear magnetic ground states. The use of USPs would be critical in achieving the desired accuracy for the complex electronic structures in these materials.

6
Magnetic shielding

Contents

6.1 Induced and applied magnetic fields 105
6.2 Gauge-including projector augmented-wave method . 107
6.3 Core shielding 108
6.3.1 Expression 108
6.3.2 Implementation 109
6.4 Orbital shielding 110
6.4.1 Expression 110
6.4.2 Implementation 121
6.5 Spin term 124
6.5.1 Expression 125
6.5.2 Implementation 128
6.6 Results 136
6.6.1 Hydrogen halide molecules 136
6.6.2 L-Cysteine 140
6.6.3 4-dimethylaminopyridinium halides 148

6.1 Induced and applied magnetic fields

The chemical shielding tensor, $\overleftrightarrow{\sigma}(\mathbf{r})$, is defined as the ratio of the induced field at each point in space, $\mathbf{B}^{\text{in}}(\mathbf{r})$, when given an applied field, $\mathbf{B}$,

$$\mathbf{B}^{\text{in}}(\mathbf{r}) = -\overleftrightarrow{\sigma}(\mathbf{r})\,\mathbf{B}. \tag{6.1}$$

The induced field arises due to two phenomena: an *orbital* contribution due to a current from the movement of electrons, and a *spin* contribution due to the magnetisation of electron spins,

$$\mathbf{B}^{\text{in}}(\mathbf{r}) = \mathbf{B}^{\text{orb}}(\mathbf{r}) + \mathbf{B}^{\text{spin}}(\mathbf{r}), \tag{6.2}$$

and notably there is no cross term present between the two contributions, meaning we can calculate them separately. For diamagnetic insulators, the latter term only becomes non-zero when SOC is incorporated into the calculation. This term depends on the magnetisation, $\mathbf{m}(\mathbf{r})$, of the spins, which is only finite if there is an energy level splitting between the spin states, as discussed in section 3.5. Mathematically, in a scalar calculation, the up and down spin density are equal, that is, $n_{\uparrow}(\mathbf{r}) = n_{\downarrow}(\mathbf{r})$, giving no magnetisation; see equation 4.1.

For the orbital term, we will present the generalisation of the gauge-including projector augmented-wave (GIPAW) method, first presented by Pickard *et al.*,[6] to work with spinor wavefunctions, by following the formalism, outlined in section 3.5.8, of dal Corso and Conte[144]. This uses perturbation theory (PT) to obtain an expression for the induced current upon application of a magnetic field.

In contrast, we shall use a finite-field method to calculate the response of the spin term. There is no need for the use of the GIPAW generalisation, despite the formalism involving an applied magnetic field, because their is no positional dependence of the spin operator that appears in the magnetisation, $\mathbf{m}(\mathbf{r})$. PT also requires the calculation of the exchange-correlation energy derivative with respect to the perturbation, which are additional complications not required in the finite-field method. The implementation of the PT approach would be a useful verification tool, and has also been used by d'Avezac *et al.* to calculate the NMR response in metals.[184]

The position operator, $\mathbf{r}$, that appears in the orbital angular momentum, $\mathbf{L} = \mathbf{r} \times \mathbf{p}$, cannot be represented in the periodic boundary conditions required for crystal calculations, meaning a finite-field approach for the orbital term is not viable. We

can calculate the contribution via the Biot-Savart law,

$$\mathbf{B}^{\mathrm{orb}}(\mathbf{r}) = \frac{1}{c}\int \mathbf{j}(\mathbf{r}') \times \frac{\mathbf{r}-\mathbf{r}'}{|\mathbf{r}-\mathbf{r}'|^3}\,\mathrm{d}\mathbf{r}', \tag{6.3}$$

with $\mathbf{j}(\mathbf{r}')$ the first-order induced electric current density. Formally, the exchange-correlation functional becomes dependent on the first-order current density on the application of a magnetic field. However, Wolff and Ziegler note that, even for heavy atoms, its effects on the functional can be neglected; this is known as *uncoupled* DFT.[68]

The choice of atomistic solver affects the form of the operators in the expressions that follow. For the tightly bound, highly negative energy core electrons, we need the Dirac equation to account for the strong SOC effects experienced. However, for the valence electrons, the previously discussed scalar ZORA approach is a good approximation to the Dirac equation, as they are not as tightly bound to the core region. We can therefore employ the ZORA formalism for the valence states but obtain the core contribution via the full Dirac equation.

One final note is to remind the reader that the subtleties of the notation used for spinor wavefunctions and spin-dependent operators are detailed explicitly for clarity in appendix A.

6.2 Gauge-including projector augmented-wave method

The main problem, that so far has not been encountered, is that of the gauge origin. The use of a finite basis set results in the dependence of the chosen origin of the vector potential, $\mathbf{A}$, which is defined through $\mathbf{B} = \boldsymbol{\nabla} \times \mathbf{A}$.

The applied field, $\mathbf{B}$, causes an additional phase factor on the wavefunction when the system is translated by some vector, $\mathbf{t}$,

$$\langle \mathbf{r}|\Psi\rangle = e^{\frac{i}{2c}\mathbf{r}\cdot\mathbf{t}\times\mathbf{B}}\langle \mathbf{r}-\mathbf{t}|\Psi\rangle. \tag{6.4}$$

The wavefunctions here have $\mathbf{k}$-point and band indices, $\mathbf{k}$ and i, but have been omitted, in this section, for brevity. The wavefunctions in the PAW translation

operator for spinors (equation 3.104), $\mathcal{T}$, do not satisfy the above relation, and thus must be modified to the field-dependent form,

$$|\Psi\rangle = |\tilde{\Psi}\rangle + \sum_{\mathbf{R}} \sum_{n} e^{\frac{i}{2c}\mathbf{r}\cdot\mathbf{R}\times\mathbf{B}} \left[|\Phi_n^{\mathbf{R}}\rangle - |\tilde{\Phi}_n^{\mathbf{R}}\rangle \right] \langle P_n^{\mathbf{R}}| e^{-\frac{i}{2c}\mathbf{r}\cdot\mathbf{R}\times\mathbf{B}} |\tilde{\Psi}\rangle, \tag{6.5}$$

where we shall use the composite indices n and m in this section, which correspond to τ, ℓ, j, m_j and $\tau', \ell', j', m_{j'}$, respectively.

We follow the same procedure as the previous PAW approaches, and define the field-dependent pseudo-operator now as $\mathcal{O}_{\mathbf{B}}$,

$$\begin{aligned} \langle \tilde{\Psi}|\mathcal{O}_{\mathbf{B}}|\tilde{\Psi}\rangle =& \langle \tilde{\Psi}|O|\tilde{\Psi}\rangle + \sum_{\mathbf{R}} \sum_{n,m} \langle \tilde{\Psi}|e^{i\vartheta}|P_n^{\mathbf{R}}\rangle \\ & \times \Big[\langle \Phi_n^{\mathbf{R}}|e^{-i\vartheta} O e^{i\vartheta}|\Phi_m^{\mathbf{R}}\rangle \\ & \quad - \langle \tilde{\Phi}_n^{\mathbf{R}}|e^{-i\vartheta} O e^{i\vartheta}|\tilde{\Phi}_m^{\mathbf{R}}\rangle \Big] \\ & \quad \times \langle p_m^{\mathbf{R}}|e^{-i\vartheta}|\tilde{\Psi}\rangle, \end{aligned} \tag{6.6}$$

where $\vartheta = \frac{1}{2c}\mathbf{r}\cdot\mathbf{R}\times\mathbf{B}$. We expand the exponential terms to first-order, that is $e^{\pm i\vartheta} \simeq 1 \pm i\vartheta$, and then insert the definitions of the spinor wavefunctions, 3.111. This obtains a definition akin to 3.113 with an additional commutation,

$$\langle \tilde{\Psi}|\mathcal{O}_{\mathbf{B}}|\tilde{\Psi}\rangle = \langle \tilde{\Psi}|O|\tilde{\Psi}\rangle + \sum_{\mathbf{R}} \sum_{n,m} \sum_{\sigma,\sigma'} \Theta_{n,m}^{\mathbf{R}} \rho_{n,m}^{\mathbf{R},\sigma,\sigma'} + \frac{1}{2ci} \left[\Theta_{n,m}^{\mathbf{R}} \rho_{n,m}^{\mathbf{R},\sigma,\sigma'}, \mathbf{r}\cdot\mathbf{R}\times\mathbf{B} \right], \tag{6.7}$$

where we ignore the first-order term in $\mathbf{B}$ if the operator in $\Theta_{n,m}^{\mathbf{R}}$ is first-order itself. The augmentation operator, $\Theta_{n,m}^{\mathbf{R}}$, is exactly that of equation 3.114, and the density-like term, $\rho_{n,m}^{\mathbf{R},\sigma,\sigma'}$, of 3.115.

These equations now define the form of any operator element in the spinor basis, $\mathcal{O}_{\mathbf{B}}$, that is gauge-invariant upon a translation.

6.3 Core shielding

6.3.1 Expression

We begin with the contribution from the core states, which are treated as frozen (see section 3.4.5). These states are spherically symmetric and contribute a purely

diamagnetic current, $\mathbf{j}_{\text{core}}(\mathbf{r}')$,

$$\mathbf{j}_{\text{core}}(\mathbf{r}') = \frac{n_{\text{core}}(\mathbf{r}')}{2c}\mathbf{B} \times \mathbf{r}', \tag{6.8}$$

where $n_{\text{core}}(\mathbf{r}')$ is the core electron density. These electrons are energetically tightly bound to the nucleus and do not participate in the chemistry between atom. In other words, the core chemical shielding value is unique only to the element, and not its environment. This can therefore be calculated with a purely atomic code where, as previously discussed, we must use the FR Dirac equation to capture the strong SOC effects.

On insertion of the above current into equation 6.3 and using 6.1 we can obtain the core chemical shielding tensor, $\overleftrightarrow{\sigma}^{\text{core}}_{\mathbf{R}}$, for some ion at $\mathbf{R}$,

$$\overleftrightarrow{\sigma}^{\text{core}}_{\mathbf{R}} = \frac{1}{2c^2}\int \frac{n_{\text{core}}(\mathbf{r}')}{|\mathbf{R}-\mathbf{r}'|}\left[\mathbb{1}_3 - \frac{(\mathbf{R}-\mathbf{r}')\otimes(\mathbf{R}-\mathbf{r}')}{|\mathbf{R}-\mathbf{r}'|^2}\right]\mathrm{d}\mathbf{r}'. \tag{6.9}$$

Its diagonal elements are all equal, and the isotropic core shielding, $\sigma^{\text{core}}_{\mathbf{R}}$, can therefore immediately be obtained with equation 2.12,

$$\sigma^{\text{core}}_{\mathbf{R}} = \frac{1}{3c^2}\int \frac{n_{\text{core}}(\mathbf{r}')}{|\mathbf{R}-\mathbf{r}'|}\,\mathrm{d}\mathbf{r}'. \tag{6.10}$$

6.3.2 Implementation

The only extension to the code for the relativistic case is generalising the calculation of $n_{\text{core}}(\mathbf{r}')$ for spinors. It is,

$$n_{\text{core}}(\mathbf{r}') = \sum_{n,\ell}^{\text{core}} |\Psi_{n,\ell}(\mathbf{r}')|^2 = \sum_{n,\ell}^{\text{core}}\sum_{\sigma} |\Psi^{\sigma}_{n,\ell}(\mathbf{r}')|^2, \tag{6.11}$$

where σ denotes the spinor component and we sum over core states only. As the core term is purely atomic, it is feasible to solve for the density in the all-electron case. The (GI)PAW approach is therefore not required and the density is not augmented. Conveniently, we solve for the all-electron atom when constructing the pseudopotential; see section 3.4.6.

We can check this code implementation by ensuring that $n_{\text{core}}(\mathbf{r}')$ integrates to the number of core electrons, N_{core},

$$N_{\text{core}} = \int n_{\text{core}}(\mathbf{r}')\,\mathrm{d}\mathbf{r}'. \tag{6.12}$$

Table 6.1: Calculated number of core electrons for a select set of atoms. Z is the atomic number. The valence electrons (defined by the choice of pseudopotential) and calculated core electrons should sum to Z.

Atom	Z	Valence e$^-$	$\int n_{\text{core}}(\mathbf{r}')\,\mathrm{d}\mathbf{r}'$
H	1	1	0.000
O	8	6	2.000
S	16	6	10.00
Se	34	16	18.00
Sn	50	14	36.00
Ba	56	10	46.00
Eu	63	17	46.00
Os	76	16	60.00
Pb	82	14	68.00

Table 6.1 presents the results, for a few select atoms, of the number of calculated core electrons. All values are correct; including, critically, the heavy atoms where the magnitude of the second spinor component is non-negligible.

Figure 6.1 evidences the increasing effects of relativity with respect to the atomic number, Z, on the core chemical shielding value. The FR calculations report higher values, which is due to the increase effect of the potential term with the inclusion of SOC. These core electrons feel a stronger attraction to the nucleus, increasing their shielding value.

6.4 Orbital shielding

6.4.1 Expression

We will need to know the form of the Hamiltonian in the GIPAW scheme for the expression of $\mathbf{j}(\mathbf{r}')$, which once obtained, leads to the induced field trivially through equation 6.3.

Magnetic pseudo-Hamiltonian

The expression for the vector potential,

$$\mathbf{A} = \frac{1}{2}\mathbf{B} \times (\mathbf{r} - \mathbf{d}), \tag{6.13}$$

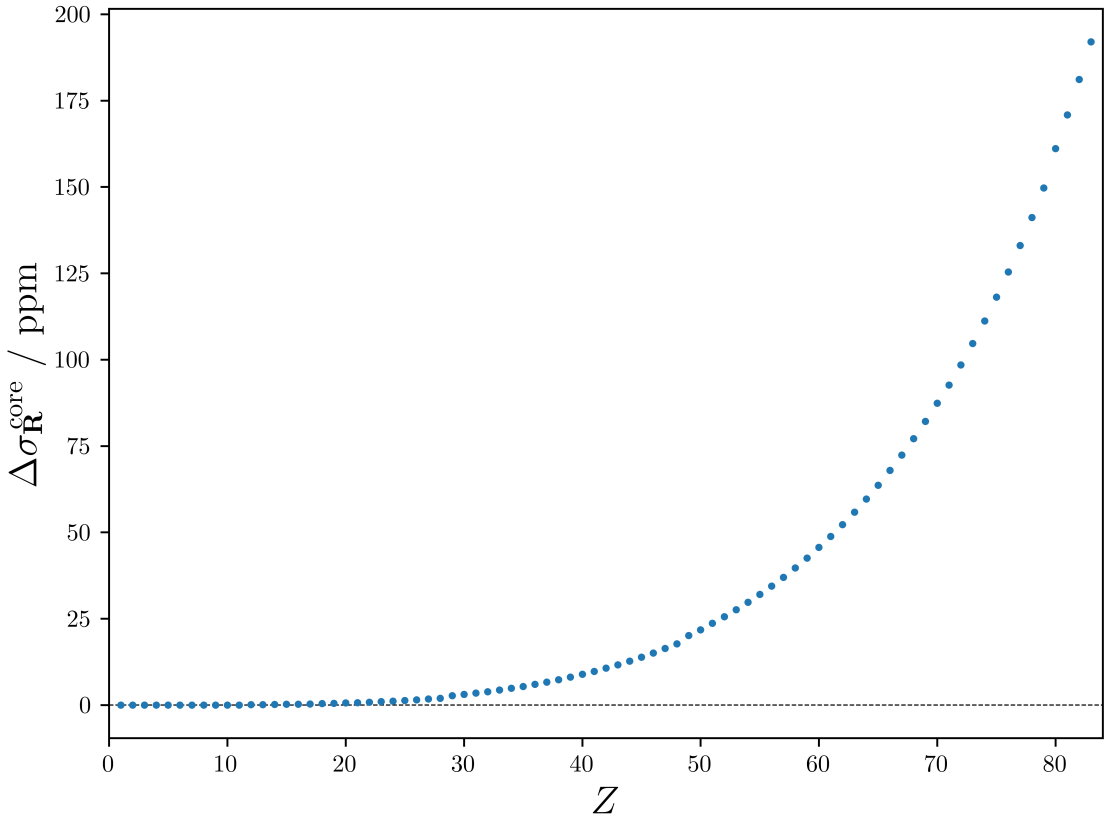


Figure 6.1: The difference between fully (FR) and scalar-relativistic (SR) calculations with respect to increasing atomic number, Z. The effects of relativity increase for the heavier elements, as expected. $\Delta\sigma_{\mathbf{R}}^{\mathrm{core}} = \Delta\sigma_{\mathbf{R}}^{\mathrm{core,FR}} - \Delta\sigma_{\mathbf{R}}^{\mathrm{core,SR}}$.

is known as the symmetric gauge with origin $\mathbf{d}$. Whilst the operators should not depend on $\mathbf{d}$, the chosen number of atomic wavefunctions to describe the selected pseudopotentials does. The number required is minimised for $\mathbf{d} = \mathbf{0}$, as this choice minimises the effect of the field on the augmentation region. Additionally, interaction between the core and valence states is minimised with this choice.[49]

Inserting $\mathbf{d} = \mathbf{0}$ into $\mathbf{A}$ and then into the ZORA Hamiltonian, equation 3.102, we get,

$$\mathcal{H}_{\text{ZORA}} = \mathbf{p} \cdot \frac{K}{2}\mathbf{p} + \frac{K}{4c}\mathbf{B} \cdot \mathbf{L} + \mathbf{B} \cdot \mathbf{L}\frac{K}{4c} + V, \tag{6.14}$$

where $\mathbf{L} = \mathbf{r} \times \mathbf{p}$ is the orbital angular momentum operator and we have omitted the term of second-order in $\mathbf{B}$. By insertion of the ZORA Hamiltonian into equation 6.7, we can obtain the form of the pseudo-Hamiltonian for GIPAW,

$$\tilde{\mathcal{H}}_{\mathbf{B}}^{\sigma,\sigma'} = \tilde{\mathcal{H}}_{\mathbf{B}}^{\sigma,\sigma',(0)} + \tilde{\mathcal{H}}_{\mathbf{B}}^{\sigma,\sigma',(1)}, \tag{6.15}$$

where the order of each quantity is its proportionality to the applied field, and those of second-order and above are omitted. The zeroth-order is identical to that given in equation 3.121. We choose the notation here to be,

$$\tilde{\mathcal{H}}_{\mathbf{B}}^{\sigma,\sigma',(0)} = \frac{p^2}{2} + \tilde{V}_{\text{loc}} + \sum_{\mathbf{R}} \tilde{\mathcal{V}}_{\text{non-loc}}^{\mathbf{R},\sigma,\sigma'}, \tag{6.16}$$

and the first-order change is,

$$\tilde{\mathcal{H}}_{\mathbf{B}}^{\sigma,\sigma',(1)} = \frac{1}{2c}\left(\delta_{\sigma\sigma'}\mathbf{L} + \frac{1}{i}\sum_{\mathbf{R}}\left[\tilde{\mathcal{V}}_{\text{non-loc}}^{\mathbf{R},\sigma,\sigma'}, \mathbf{r}\right] \times \mathbf{R} + \sum_{\mathbf{R}} \mathbf{L}_{\mathbf{R}}\mathcal{Q}_{\mathbf{R}}^{\sigma,\sigma'}\right) \cdot \mathbf{B}. \tag{6.17}$$

We have defined $\mathbf{L}_{\mathbf{R}} = (\mathbf{r} - \mathbf{R}) \times \mathbf{p}$ and $\mathcal{Q}_{\mathbf{R}}^{\sigma,\sigma'}$ has arisen due to the charge augmentation in the USPs, and is defined as,

$$\mathcal{Q}_{\mathbf{R}}^{\sigma,\sigma'} = \sum_{n,m} |p_n^{\mathbf{R}}\rangle \, q_{n,m}^{\mathbf{R},\sigma,\sigma'} \langle p_m^{\mathbf{R}}|, \tag{6.18}$$

with matrix notation $\mathcal{Q}_{\mathbf{R}}$. In this, $q_{n,m}^{\mathbf{R},\sigma,\sigma'}$ are defined in equation 3.118 and ultimately depend on $Q_{n;m}^{\mathbf{R}}$ in equation 3.120. We generalise $Q_{n;m}^{\mathbf{R}}$ for the ZORA Hamiltonian here,

$$\begin{aligned} Q_{n;m}^{\mathbf{R}}(\mathbf{r}) &= K^{\mathbf{R}}(r)\,\langle\phi_n^{\mathbf{R}}|\mathbf{r}\rangle\langle\mathbf{r}|\phi_m^{\mathbf{R}}\rangle - \langle\tilde{\phi}_n^{\mathbf{R}}|\mathbf{r}\rangle\langle\mathbf{r}|\tilde{\phi}_m^{\mathbf{R}}\rangle, \\ &= \left[K^{\mathbf{R}}(r)\,\phi_n^{\mathbf{R}}(r)\phi_m^{\mathbf{R}}(r) - \tilde{\phi}_n^{\mathbf{R}}(r)\tilde{\phi}_m^{\mathbf{R}}(r)\right] Y_n^*(\theta,\varphi)Y_m(\theta,\varphi), \end{aligned} \tag{6.19}$$

where $K^{\mathbf{R}}(r)$ is now $\mathbf{R}$ dependent as it is localised inside the augmentation sphere. As a result, it is also purely radial and can be calculated on an atom.

It is the first-order response of the Hamiltonian, with respect to the applied field, that will dictate the current response. The overlap matrix, obtained by inserting $\mathbb{1}$ into equation 6.7, has elements,

$$\mathcal{S}_{\mathbf{B}}^{\sigma,\sigma'} = \mathcal{S}_{\mathbf{B}}^{\sigma,\sigma',(0)} + \mathcal{S}_{\mathbf{B}}^{\sigma,\sigma',(1)}, \tag{6.20}$$

with the zeroth-order term identical to equation 3.117. We choose the notation here as,

$$\mathcal{S}_{\mathbf{B}}^{\sigma,\sigma',(0)} = \delta_{\sigma\sigma'} + \sum_{\mathbf{R}} \mathcal{Q}_{\mathbf{R}}^{\sigma,\sigma'}, \tag{6.21}$$

and its first-order change is,

$$\mathcal{S}_{\mathbf{B}}^{\sigma,\sigma',(1)} = \frac{1}{2ci} \sum_{\mathbf{R}} \left[\mathcal{Q}_{\mathbf{R}}^{\sigma,\sigma'}, \mathbf{r}\right] \times \mathbf{R} \cdot \mathbf{B}. \tag{6.22}$$

As always, the overlap matrix assures that the wavefunction bands are orthonormal. The encapsulation of the f-matrices inside the $q_{n,m}^{\mathbf{R},\sigma,\sigma'}$ term result in minimal changes needed to the augmentation charge, $\mathcal{Q}_{\mathbf{R}}^{\sigma,\sigma'}$, and overlap matrix, $\mathcal{S}_{\mathbf{B}}^{\sigma,\sigma'}$, inside the NMR code.

The final term to define is the atomic non-local potential, $\tilde{\mathcal{V}}_{\text{non-loc}}^{\mathbf{R},\sigma,\sigma'}$. Its sum over $\mathbf{R}$ is defined in equation 3.122 and we define its matrix notation as $\tilde{\mathcal{V}}_{\text{non-loc}}^{\mathbf{R}}$.

These definitions outline the pseudisation of the ZORA Hamiltonian in the GIPAW scheme. We now have the tools required to derive the response current density, $\mathbf{j}(\mathbf{r}')$, through PT.

GIPAW current operator

As in Yates *et al.*,[52] the current operator is $\mathbf{J}(\mathbf{r}') = K(\mathbf{r}') \left[\mathbf{J}^{\mathrm{d}}(\mathbf{r}') + \mathbf{J}^{\mathrm{p}}(\mathbf{r}')\right]$, and is composed of diamagnetic,

$$\mathbf{J}^{\mathrm{d}}(\mathbf{r}') = -\frac{\mathbf{B} \times \mathbf{r}'}{2c} |\mathbf{r}'\rangle\langle\mathbf{r}'|, \tag{6.23}$$

and paramagnetic,

$$\mathbf{J}^{\mathrm{p}}(\mathbf{r}') = -\frac{\mathbf{p}|\mathbf{r}'\rangle\langle\mathbf{r}'| + |\mathbf{r}'\rangle\langle\mathbf{r}'|\mathbf{p}}{2}, \tag{6.24}$$

parts. Noting that $\mathbf{J}^{\mathrm{p}}(\mathbf{r}')$ and $\mathbf{J}^{\mathrm{d}}(\mathbf{r}')$ are zeroth and first-order in $\mathbf{B}$, respectively, we can obtain the GIPAW current by inserting $\mathbf{J}(\mathbf{r}')$ into equation 6.7. The zeroth-order response is,

$$\langle\tilde{\Psi}|\boldsymbol{\mathcal{J}}^{(0)}_{\mathbf{B}}(\mathbf{r}')|\tilde{\Psi}\rangle = \langle\tilde{\Psi}|\mathbf{J}^{\mathrm{p}}(\mathbf{r}')|\tilde{\Psi}\rangle + \sum_{\mathbf{R}}\sum_{\sigma,\sigma'}\langle\tilde{\Psi}^{\sigma}|\Delta\mathbf{J}^{\mathrm{p},\sigma,\sigma'}_{\mathbf{R}}(\mathbf{r}')|\tilde{\Psi}^{\sigma'}\rangle, \tag{6.25}$$

and the first-order response is,

$$\begin{aligned}\langle\tilde{\Psi}|\boldsymbol{\mathcal{J}}^{(1)}_{\mathbf{B}}(\mathbf{r}')|\tilde{\Psi}\rangle =& \langle\tilde{\Psi}|\mathbf{J}^{\mathrm{d}}(\mathbf{r}')|\tilde{\Psi}\rangle \\ &+ \sum_{\mathbf{R}}\sum_{\sigma,\sigma'}\Big\{\langle\tilde{\Psi}^{\sigma}|\Delta\mathbf{J}^{\mathrm{d},\sigma,\sigma'}_{\mathbf{R}}(\mathbf{r}')|\tilde{\Psi}^{\sigma'}\rangle \\ &\quad + \frac{1}{2ci}\left[\mathbf{B}\times\mathbf{R}\cdot\mathbf{r}', \langle\tilde{\Psi}^{\sigma}|\Delta\mathbf{J}^{\mathrm{p},\sigma,\sigma'}_{\mathbf{R}}(\mathbf{r})|\tilde{\Psi}^{\sigma'}\rangle\right]\Big\}.\end{aligned} \tag{6.26}$$

We have defined,

$$\langle\tilde{\Psi}^{\sigma}|\Delta\mathbf{J}^{\mathrm{p},\sigma,\sigma'}_{\mathbf{R}}(\mathbf{r}')|\tilde{\Psi}^{\sigma'}\rangle = \sum_{n,m}\left[\langle\phi^{\mathbf{R}}_n|K^{\mathbf{R}}(r')\mathbf{J}^{\mathrm{p}}(\mathbf{r}')|\phi^{\mathbf{R}}_m\rangle - \langle\tilde{\phi}^{\mathbf{R}}_n|\mathbf{J}^{\mathrm{p}}(\mathbf{r}')|\tilde{\phi}^{\mathbf{R}}_m\rangle\right]\rho^{\mathbf{R},\sigma,\sigma'}_{n,m}, \tag{6.27}$$

as the paramagnetic current augmentation, and,

$$\langle\tilde{\Psi}^{\sigma}|\Delta\mathbf{J}^{\mathrm{d},\sigma,\sigma'}_{\mathbf{R}}(\mathbf{r}')|\tilde{\Psi}^{\sigma'}\rangle = \sum_{n,m}\left[\langle\phi^{\mathbf{R}}_n|K^{\mathbf{R}}(r')\mathbf{J}^{\mathrm{d}}(\mathbf{r}')|\phi^{\mathbf{R}}_m\rangle - \langle\tilde{\phi}^{\mathbf{R}}_n|\mathbf{J}^{\mathrm{d}}(\mathbf{r}')|\tilde{\phi}^{\mathbf{R}}_m\rangle\right]\rho^{\mathbf{R},\sigma,\sigma'}_{n,m}, \tag{6.28}$$

as the diamagnetic current augmentation.

Density functional perturbation theory

These operators follow the derivation of Pickard *et al.*, of whom, worked with NCPs.[6] The response of the current density, in this case, only arises due to the projection of the first-order wavefunction into the unoccupied state space. Yates *et al.* then showed that this derivation is also correct for USPs, but we encounter additional terms due to the first-order wavefunction response in the occupied state space, also. The current density, from the result of the above operators in PT, becomes,

$$\begin{aligned}\mathbf{j}(\mathbf{r}') =& \sum_{o}\Big[2\mathbb{R}\mathrm{e}\langle\tilde{\Psi}^{(0)}_o|\boldsymbol{\mathcal{J}}^{(0)}_{\mathbf{B}}(\mathbf{r}')|\tilde{\Psi}^{(1)}_o\rangle \\ &- \sum_{o'}\langle\tilde{\Psi}^{(0)}_o|\boldsymbol{\mathcal{J}}^{(0)}_{\mathbf{B}}(\mathbf{r}')|\tilde{\Psi}^{(0)}_{o'}\rangle\langle\tilde{\Psi}^{(0)}_{o'}|\mathcal{S}^{(1)}_{\mathbf{B}}|\tilde{\Psi}^{(0)}_o\rangle \\ &+ \langle\tilde{\Psi}^{(0)}_o|\boldsymbol{\mathcal{J}}^{(1)}_{\mathbf{B}}(\mathbf{r}')|\tilde{\Psi}^{(0)}_o\rangle\Big],\end{aligned} \tag{6.29}$$

where we have made explicit the summation over occupied states, with indices o and o'.

Linear response function

The first-order response of the wavefunction, $|\tilde{\Psi}_o^{(1)}\rangle$, in equation 6.29 is,

$$|\tilde{\Psi}_o^{(1)}\rangle = G\left(\varepsilon_o^{(0)}\right)\left(\tilde{\mathcal{H}}_{\mathbf{B}}^{(1)} - \varepsilon_o^{(0)}\mathcal{S}_{\mathbf{B}}^{(1)}\right)|\tilde{\Psi}_o^{(0)}\rangle, \tag{6.30}$$

where,

$$G\left(\varepsilon_o^{(0)}\right) = \sum_e \frac{|\tilde{\Psi}_e^{(0)}\rangle\langle\tilde{\Psi}_e^{(0)}|}{\varepsilon_o^{(0)} - \varepsilon_e^{(0)}}, \tag{6.31}$$

is the Green function that sums over empty states, indexed by e, only.

The induced current

Following that of Pickard *et al.*[6] and Yates *et al.*[52], we reorder the contributions to the response current, $\mathbf{j}(\mathbf{r}')$, as one due to the pseudised valence wavefunctions, $\mathbf{j}_{\text{bare}}(\mathbf{r}')$, one due to the augmentation to the diamagnetic component, $\mathbf{j}_{\Delta\text{d}}(\mathbf{r}')$, and one due to the augmentation to the paramagnetic component, $\mathbf{j}_{\Delta\text{p}}(\mathbf{r}')$,

$$\mathbf{j}(\mathbf{r}') = \mathbf{j}_{\text{bare}}(\mathbf{r}') + \mathbf{j}_{\Delta\text{d}}(\mathbf{r}') + \mathbf{j}_{\Delta\text{p}}(\mathbf{r}'). \tag{6.32}$$

The bare term is,

$$\begin{aligned}\mathbf{j}_{\text{bare}}(\mathbf{r}') = \sum_o \Big[& 2\mathbb{R}\text{e}\langle\tilde{\Psi}_o^{(0)}|\mathbf{J}^{\text{p}}(\mathbf{r}')|\tilde{\Psi}_o^{(1)}\rangle \\ & - \sum_{o'}\langle\tilde{\Psi}_o^{(0)}|\mathbf{J}^{\text{p}}(\mathbf{r}')|\tilde{\Psi}_{o'}^{(0)}\rangle\langle\tilde{\Psi}_{o'}^{(0)}|\mathcal{S}_{\mathbf{B}}^{(1)}|\tilde{\Psi}_o^{(0)}\rangle\Big] \\ & - \frac{1}{2c}n_{\text{soft}}(\mathbf{r}')\mathbf{B}\times\mathbf{r}',\end{aligned} \tag{6.33}$$

where $n_{\text{soft}}(\mathbf{r}')$ is the 'soft' ground-state density; that is the first term in equation 3.126,

$$n_{\text{soft}}(\mathbf{r}') = \sum_o \langle\tilde{\Psi}_o^{(0)}|\mathbf{r}'\rangle\langle\mathbf{r}'|\tilde{\Psi}_o^{(0)}\rangle. \tag{6.34}$$

The diamagnetic augmentation is,

$$\mathbf{j}_{\Delta\text{d}}(\mathbf{r}') = \sum_{\mathbf{R}}\sum_{\sigma,\sigma'}\sum_o \langle\tilde{\Psi}_o^{\sigma,(0)}|\Delta\mathbf{J}_{\mathbf{R}}^{\text{d},\sigma,\sigma'}(\mathbf{r}')|\tilde{\Psi}_o^{\sigma',(0)}\rangle, \tag{6.35}$$

and the paramagnetic augmentation is,

$$\begin{aligned}\mathbf{j}_{\Delta\mathrm{p}}(\mathbf{r}') = \sum_{\mathbf{R}}\sum_{\sigma,\sigma'}\sum_{o}\Big\{ & 2\mathbb{R}\mathrm{e}\langle\tilde{\Psi}_o^{\sigma,(0)}|\Delta\mathbf{J}_{\mathbf{R}}^{\mathrm{p},\sigma,\sigma'}(\mathbf{r}')|\tilde{\Psi}_o^{\sigma',(1)}\rangle \\ & - \sum_{\sigma_A,o'}\langle\tilde{\Psi}_o^{\sigma,(0)}|\Delta\mathbf{J}_{\mathbf{R}}^{\mathrm{p},\sigma,\sigma_A}(\mathbf{r}')|\tilde{\Psi}_{o'}^{\sigma_A,(0)}\rangle\langle\tilde{\Psi}_{o'}^{\sigma_A,(0)}|\mathcal{S}_{\mathbf{B}}^{\sigma_A\sigma',(1)}|\tilde{\Psi}_o^{\sigma',(0)}\rangle \\ & + \frac{1}{2ci}\left[\mathbf{B}\times\mathbf{R}\cdot\mathbf{r},\langle\tilde{\Psi}_o^{\sigma,(0)}|\Delta\mathbf{J}_{\mathbf{R}}^{\mathrm{p},\sigma,\sigma'}(\mathbf{r}')|\tilde{\Psi}_o^{\sigma',(0)}\rangle\right]\Big\}. \end{aligned} \tag{6.36}$$

Notice now that, with this notation, the $\mathbf{j}_{\Delta\mathrm{d}}(\mathbf{r}')$ and $\mathbf{j}_{\Delta\mathrm{p}}(\mathbf{r}')$ terms vanish outside the augmentation region.

Equations 6.33, 6.34, 6.35 and 6.36 fully define the response current by the applied field, required to obtain the induced field from equation 6.3.

Alternate molecular method

As the diamagnetic contribution is only concerned with the ground state wavefunctions, it will converge much faster - with respect to the basis set size - than the bare and paramagnetic terms, which involve the empty states as well. This stems from the gauge-origin problem, of which, is only present for finite basis sets. As done by Pickard *et al.*[6] and Yates *et al.*[52], we will reformulate the bare and paramagnetic currents such that they converge in parallel to the diamagnetic term.

We start by noting that the 'soft' density term in equation 6.33 can be rewritten,

$$-\frac{1}{2c}n_{\mathrm{soft}}(\mathbf{r}')\mathbf{B}\times\mathbf{r}' = -\frac{1}{2c}\sum_{o}\langle\tilde{\Psi}_o^{(0)}|\frac{1}{i}\left[\mathbf{B}\times\mathbf{r}'\cdot\mathbf{r},\mathbf{J}^{\mathrm{p}}(\mathbf{r}')\right]|\tilde{\Psi}_o^{(0)}\rangle, \tag{6.37}$$

and along with the generalised f-sum rule outlined in the appendix of Yates *et al.*[52],

$$\begin{aligned} & -2\sum_{o}\mathbb{R}\mathrm{e}\langle\tilde{\Psi}_o^{(0)}|\mathcal{O}G\left(\varepsilon_o^{(0)}\right)\left[\mathcal{E},\tilde{\mathcal{H}}_{\mathbf{B}}^{(0)}-\varepsilon_o^{(0)}\mathcal{S}_{\mathbf{B}}^{(0)}\right]|\tilde{\Psi}_o^{(0)}\rangle \\ & \quad = \sum_{o}\langle\tilde{\Psi}_o^{(0)}|\left[\mathcal{E},\mathcal{O}\right]|\tilde{\Psi}_o^{(0)}\rangle - \sum_{o,o'}\langle\tilde{\Psi}_o^{(0)}|\mathcal{O}|\tilde{\Psi}_{o'}^{(0)}\rangle\langle\tilde{\Psi}_{o'}^{(0)}|\left[\mathcal{E},\mathcal{S}_{\mathbf{B}}^{(0)}\right]|\tilde{\Psi}_o^{(0)}\rangle, \end{aligned} \tag{6.38}$$

where $\mathcal{E}$ operators are even and $\mathcal{O}$ are odd under time reversal symmetry, we can obtain,

$$\begin{aligned}\mathbf{j}_{\mathrm{bare}}(\mathbf{r}') = \sum_{o}\Big\{ & 2\mathbb{R}\mathrm{e}\left[\langle\tilde{\Psi}_o^{(0)}|\mathbf{J}^{\mathrm{p}}(\mathbf{r}')|\tilde{\Psi}_o^{(1)}\rangle - \langle\tilde{\Psi}_o^{(0)}|\mathbf{J}^{\mathrm{p}}(\mathbf{r}')|\bar{\Psi}_o^{(1)}\rangle\right] \\ & - \sum_{o'}\langle\tilde{\Psi}_o^{(0)}|\mathbf{J}^{\mathrm{p}}(\mathbf{r}')|\tilde{\Psi}_{o'}^{(0)}\rangle\langle\tilde{\Psi}_{o'}^{(0)}|\left(\mathbf{R}-\mathbf{r}'\right)\times\frac{1}{2ci}\left[\mathbf{r},\mathcal{Q}_{\mathbf{R}}\right]\cdot\mathbf{B}|\tilde{\Psi}_o^{(0)}\rangle\Big\}, \end{aligned} \tag{6.39}$$

and,

$$\begin{aligned}\mathbf{j}_{\Delta\mathrm{p}}(\mathbf{r}') = \sum_{\mathbf{R},o}\sum_{\sigma,\sigma'}\Big\{ & 2\mathbb{R}\mathrm{e}\left[\langle\tilde{\Psi}_o^{\sigma,(0)}|\Delta\mathbf{J}_{\mathbf{R}}^{\mathrm{p},\sigma,\sigma'}(\mathbf{r}')|\tilde{\Psi}_o^{\sigma',(1)}\rangle - \langle\tilde{\Psi}_o^{\sigma,(0)}|\Delta\mathbf{J}_{\mathbf{R}}^{\mathrm{p},\sigma,\sigma'}(\mathbf{r}')|\bar{\Psi}_o^{\sigma',(1)}\rangle\right] \\ & - \sum_{\mathbf{R}',o'}\sum_{\sigma_A}\Big[\langle\tilde{\Psi}_o^{\sigma,(0)}|\Delta\mathbf{J}_{\mathbf{R}}^{\mathrm{p},\sigma,\sigma_A}(\mathbf{r}')|\tilde{\Psi}_{o'}^{\sigma_A,(0)}\rangle \\ & \times\langle\tilde{\Psi}_{o'}^{\sigma_A,(0)}|\left(\mathbf{R}'-\mathbf{R}\right)\times\frac{1}{2ci}\left[\mathbf{r},\mathcal{Q}_{\mathbf{R}}^{\sigma_A,\sigma'}\right]\cdot\mathbf{B}|\tilde{\Psi}_o^{\sigma',(0)}\rangle\Big]\Big\},\end{aligned} \tag{6.40}$$

where we have defined,

$$|\bar{\Psi}_o^{(1)}\rangle = G\left(\varepsilon_o^{(0)}\right)\frac{\mathbf{B}\times\mathbf{r}'}{2c}\cdot\mathbf{v}\left(\varepsilon_o^{(0)}\right)|\tilde{\Psi}_o^{(0)}\rangle, \tag{6.41}$$

along with the velocity operator,

$$\mathbf{v}\left(\varepsilon_o^{(0)}\right) = \mathbf{p} - i\sum_{\mathbf{R}}\left[\mathbf{r},\left(\tilde{\mathcal{V}}_{\text{non-loc}}^{\mathbf{R}} - \varepsilon_o^{(0)}\mathcal{Q}_{\mathbf{R}}\right)\right]. \tag{6.42}$$

These equations map those of references [6] and [52], but are generalised for spinor wavefunctions.

Extended systems

The diamagnetic contribution, equation 6.35, can be applied to both molecular and extended systems without difficulty. However, equations 6.39 and 6.40 contain expectation values of position operators. Initially, one may deduce that these are incalculable for extended systems where these operators may not be well-defined. However, Pickard *et al.* showed that rewriting these equations highlights their dependence only on the *difference* of position operators.[6] These quantities do not diverge as fast as the Green function, paramagnetic augmentation operator and velocity operator go to 0. As a result, the product of these contributions vanish and do not cause the calculations to diverge.

Infinite systems

The final consideration for the calculation of the current is that of infinitely repeating systems. Pickard *et al.* outlined the approach and denoted it the *crystal* method. Again, we need only to generalise the bare and paramagnetic augmentation terms, both of which contain position operators, for those systems that repeat periodically.

We would define alike equations to 52 and 54 in reference [6], and 39 and 41 in reference [52]. These define q-dependent $\mathbf{S}_{\text{bare}}(\mathbf{r}', q)$ and $\mathbf{S}_{\Delta\text{p}}(\mathbf{r}', q)$ functions. These expressions map those of equations 6.39 and 6.40, but we replace the expectation values of position operators, $\mathbf{r}$, with e^{iqr_j} in each of the Cartesian directions, denoted with j. These exponential quantities are now conveniently periodic with respect to the position. In practice, we evaluate the Green function, paramagnetic and velocity operator quantities at $\mathbf{k}$-points shifted by q for each Cartesian direction. We then recover the current expressions by,

$$\mathbf{j}_{\text{bare}}(\mathbf{r}') = \lim_{q\to 0} \frac{\mathbf{S}_{\text{bare}}(\mathbf{r}', q) - \mathbf{S}_{\text{bare}}(\mathbf{r}', -q)}{2q}, \tag{6.43}$$

and,

$$\mathbf{j}_{\Delta\text{p}}(\mathbf{r}') = \lim_{q\to 0} \frac{\mathbf{S}_{\Delta\text{p}}(\mathbf{r}', q) - \mathbf{S}_{\Delta\text{p}}(\mathbf{r}', -q)}{2q}. \tag{6.44}$$

We must choose q to be small for these limits to hold, such that $e^{\pm iqr_j} \simeq 1 \pm iqr_j$. The generalised expressions for $\mathbf{S}_{\text{bare}}(\mathbf{r}', q)$ and $\mathbf{S}_{\Delta\text{p}}(\mathbf{r}', q)$ that are needed for this work need for us to only appreciate the spinor nature of the wavefunctions involved. The algebra required is only that of the generalisation of the expressions outlined here to arbitrary $\mathbf{k}$-points, which is not specific to this work. We continue without outlining the extension to infinite systems, but note to the reader that the generalisations given here for the molecular approaches outline all the key points needed.

Shielding tensors

We now have three methods to calculate the induced magnetic field from the response current, through equation 6.3, with spinor wavefunctions. The first is named the *molecular* method, defined by equations 6.33, 6.36 and 6.35. The second is named the *molecular sum-rule* method, defined by equations 6.39, 6.40 and 6.35. The third is named the *crystal* method, defined by equations 6.43, 6.44 and 6.35. Each current gives the respective magnetic field response through insertion into equation 6.3. We calculate each of the bare, diamagnetic and paramagnetic responses separately, rather than summing the currents and utilising equation 6.3.

This is because the augmentation terms, that describe the current near the nucleus, would require an extremely high charge augmentation grid.

By inserting 6.35 into 6.3 and then into 6.1, we obtain the diamagnetic chemical shielding tensor, $\overleftrightarrow{\sigma}^{\Delta \mathrm{d}}(\mathbf{r})$, as,

$$\overleftrightarrow{\sigma}^{\Delta \mathrm{d}}(\mathbf{r}) = \frac{1}{2c^2} \sum_{\mathbf{R}} \sum_{\sigma,\sigma'} \sum_{n,m} \rho_{n,m}^{\mathbf{R},\sigma,\sigma'} \int \frac{Q_{n;m}^{\mathbf{R}}(\mathbf{r}')}{|\mathbf{r}-\mathbf{r}'|} \left[\mathbb{1}_3 - \frac{(\mathbf{r}-\mathbf{r}') \otimes (\mathbf{r}-\mathbf{r}')}{|\mathbf{r}-\mathbf{r}'|^2} \right] \mathrm{d}\mathbf{r}', \quad 6.45$$

where $\rho_{n,m}^{\mathbf{R},\sigma,\sigma'}$ is defined in equation 3.115 and $Q_{n;m}^{\mathbf{R}}(\mathbf{r}')$ is equation 6.19. Much like the augmentation term found in the electric field gradients, this augmentation term has a spherical tensor operator in brackets. The elements of this can be expanded due to the Wigner-Eckart theorem,

$$\delta_{\alpha\beta} - \frac{(r_\alpha - r'_\alpha)(r_\beta - r'_\beta)}{|\mathbf{r}-\mathbf{r}'|^2} = \frac{4\sqrt{\pi}}{3} \delta_{\alpha\beta} Y_0^0(\theta,\varphi) + \sqrt{\frac{2\pi}{15}} \sum_{q=-2}^{2} C_{\alpha\beta}^q Y_2^q(\theta,\varphi). \quad 6.46$$

As before, α and β run over the x, y, z directions, and the vector $\mathbf{C}_{\alpha\beta}$ contains sets of Clebsch-Gordan coefficients that recover the required angular dependence. This term has diagonal components that take some portion of the $\ell = m = 0$ harmonic. See appendix C for the vector, $\mathbf{C}_{\alpha\beta}$.

As before, we can rewrite the tensor elements, $\sigma_{\mathbf{R},\alpha,\beta}^{\Delta \mathrm{d}}$, more compactly,

$$\sigma_{\mathbf{R},\alpha,\beta}^{\Delta \mathrm{d}} = \frac{1}{2c^2} \sum_{\sigma,\sigma'} \sum_{n,m} \rho_{n,m}^{\mathbf{R},\sigma,\sigma'} \Pi_{n,m}^{\mathbf{R}} \left[\delta_{\alpha\beta} \Gamma_{n;m}^0 + \sum_{q=-2}^{2} C_{\alpha\beta}^q \Gamma_{n;m}^q \right], \quad 6.47$$

where we have again used the on-site approximation to evaluate the expression at the ion at $\mathbf{R}$. We have the atomic term,

$$\Pi_{n,m}^{\mathbf{R}} = \int \frac{1}{r} \left[K^{\mathbf{R}}(r)\, \phi_n^{\mathbf{R}}(r) \phi_m^{\mathbf{R}}(r) - \tilde{\phi}_n^{\mathbf{R}}(r) \tilde{\phi}_m^{\mathbf{R}}(r) \right] \mathrm{d}r, \quad 6.48$$

and the Gaunt integrals,

$$\Gamma_{n;m}^0 = \frac{4\sqrt{\pi}}{3} \int\int Y_n^*(\theta,\varphi)\, Y_0^0(\theta,\varphi)\, Y_m(\theta,\varphi)\, \mathrm{d}\theta\, \mathrm{d}\varphi, \quad 6.49$$

and,

$$\Gamma_{n;m}^q = \sqrt{\frac{2\pi}{15}} \int\int Y_n^*(\theta,\varphi)\, Y_2^q(\theta,\varphi)\, Y_m(\theta,\varphi)\, \mathrm{d}\theta\, \mathrm{d}\varphi, \quad 6.50$$

where we re-emphasise that n and m are composite indices and map the spherical harmonics according to,

$$\begin{aligned} Y_n(\theta,\varphi) &\mapsto Y_{\ell,m}(\theta,\varphi), \\ Y_m(\theta,\varphi) &\mapsto Y_{\ell',m'}(\theta,\varphi), \end{aligned} \tag{6.51}$$

where ℓ, ℓ' and m, m' on the right-hand side are the well-known azimuthal and magnetic quantum numbers, respectively.

A similar process can be done for the paramagnetic augmentation tensor elements, $\sigma^{\Delta\mathrm{p}}_{\mathbf{R},\alpha,\beta}$,

$$\sigma^{\Delta\mathrm{p}}_{\mathbf{R},\alpha,\beta} = \frac{1}{c^2}\sum_{\sigma,\sigma'}\sum_{n,m}\bar{\rho}^{\mathbf{R},\sigma,\sigma',\alpha}_{n,m}\,\Pi^{\mathbf{R}}_{n,m}\,l^{\beta}_{n;m}, \tag{6.52}$$

where we use the bar decoration in $\bar{\rho}^{\mathbf{R},\sigma,\sigma',\alpha}_{n,m}$ to signify that its ket vector is that of a *perturbed* wavefunction; either of those in equations 6.30 or 6.41 depending on the approach used. The α index indicates the direction of the applied field, $\mathbf{B}$, inside those expressions. The atomic term in this case is,

$$\Pi^{\mathbf{R}}_{n;m} = \int \frac{1}{r^3}\left[K^{\mathbf{R}}(r)\,\phi^{\mathbf{R}}_n(r)\phi^{\mathbf{R}}_m(r) - \tilde{\phi}^{\mathbf{R}}_n(r)\tilde{\phi}^{\mathbf{R}}_m(r)\right]\mathrm{d}r. \tag{6.53}$$

And finally, $l^{\beta}_{n;m}$ are the eigenvalues of the orbital angular momentum operator, $\mathbf{L}^{\dagger} = \begin{pmatrix} L_x & L_y & L_z \end{pmatrix}$,

$$l^{\beta}_{\ell,m;\ell',m'} = \langle \Phi^{\mathbf{R}}_{\ell,m} | L_\beta | \Phi^{\mathbf{R}}_{\ell',m'} \rangle = \delta_{\ell\ell'} \begin{cases} \delta_{m,m'+1} l_+ + \delta_{m,m'-1} l_- & \beta \to x, \\ \delta_{m,m'+1} l_+ - \delta_{m,m'-1} l_- & \beta \to y, \\ \delta_{m,m'} m & \beta \to z, \end{cases} \tag{6.54}$$

where we have expanded the composite indices, and,

$$l_+ = \frac{\sqrt{\ell(\ell+1) - m(m+1)}}{2}, \qquad l_- = \frac{\sqrt{\ell(\ell+1) - m(m-1)}}{2}, \tag{6.55}$$

arise due to acting on the atomic wavefunctions with the raising and lowering operators in L_β. The former has eigenvalues, l_+, and latter, l_-.

The bare term is calculated in reciprocal space, and its $\mathbf{G} = \mathbf{0}$ point is related to the macroscopic magnetic susceptibility. A 'slow' Fourier transform is performed

back into real space at each ion in the system, giving $\overleftrightarrow{\sigma}^{\text{bare}}_{\mathbf{R}}$. We perform a 'slow' Fourier transform because only one point in space is required, which is faster than an external software package that is optimised to invert the whole charge density space.

The orbital chemical shielding tensor, $\overleftrightarrow{\sigma}^{\text{orb}}_{\mathbf{R}}$, is defined as the sum of these three terms,

$$\overleftrightarrow{\sigma}^{\text{orb}}_{\mathbf{R}}=\overleftrightarrow{\sigma}^{\text{bare}}_{\mathbf{R}} + \overleftrightarrow{\sigma}^{\Delta\text{d}}_{\mathbf{R}} + \overleftrightarrow{\sigma}^{\Delta\text{p}}_{\mathbf{R}}, \tag{6.56}$$

and its isotropic value, $\sigma^{\text{orb}}_{\mathbf{R}}$, given through equation 2.12.

6.4.2 Implementation

All three of the aforementioned orbital methods (two molecular and one crystal) were generalised in the CASTEP code to handle spinor wavefunctions. In principle, all should give equivalent results, as long as a converged basis set is chosen, that is the cut-off energy is high enough. It is also worth noting that the crystal method is a generalisation of the other two, and molecular currents can be computed via this method through a supercell approach.

We test a set of systems, comprised of molecules and crystals, on these three generalised codes. As with the electric field gradients, we can run the calculations under the scalar and spinor bases using the Schrödinger equation for both. We should obtain identical answers for the two cases as there are no relativistic effects, even in the spinor calculations. Figure 6.2 shows these computations for the crystal approach. Both the molecular approaches recover similar plots. We expect all values on these plots to pass through the $y = x$ line; which is what we obtain. For all remaining calculations in this text, the crystal method was used.

Figure 6.3 shows the calculated chemical shielding value for the each of the core and orbital terms for the heavy atom in the hydrogen halides. We compare the different relativistic treatments: Schrödinger (NR), Koelling-Harmon (SR) and Dirac (FR). The bare and diamagnetic augmentation terms are grouped because the latter is typically very small.

Only the sum of the shielding components (obtained through equation 6.56) is well-defined. This is because - subject to the ability to construct a reasonable

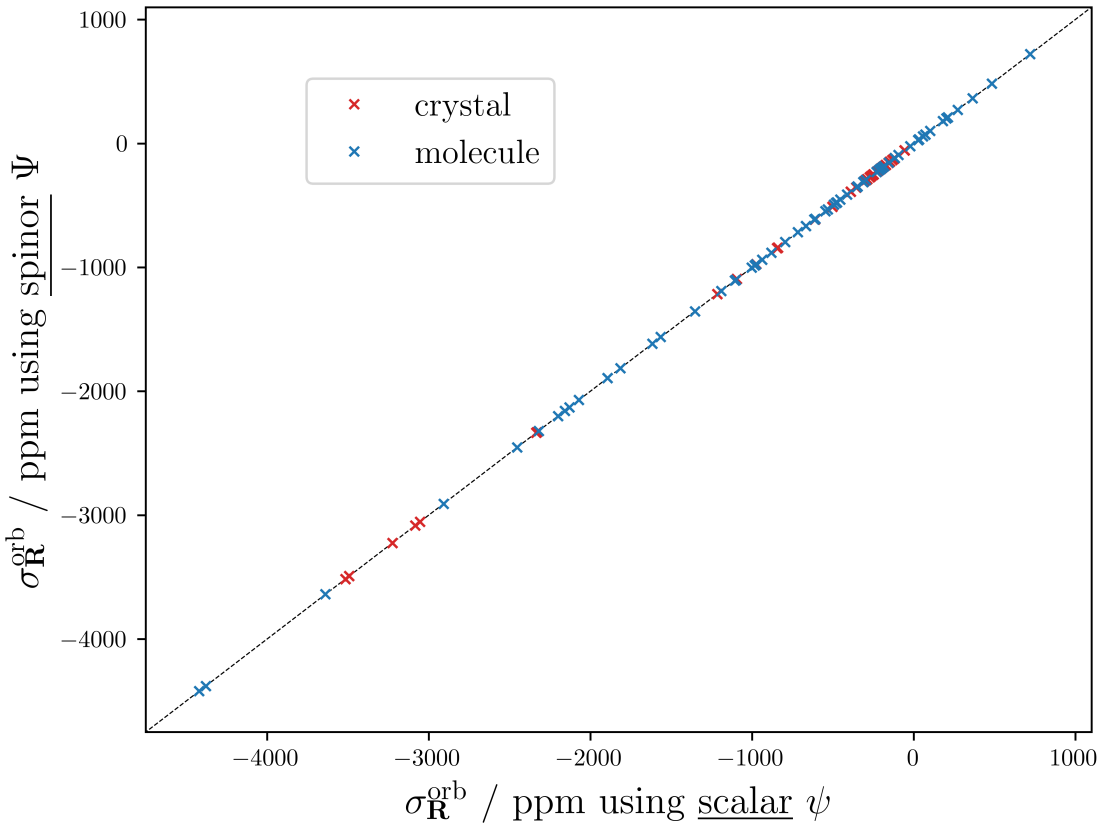


Figure 6.2: Validation of the spinor code for the calculation of orbital shielding values, $\sigma_{\mathbf{R}}^{\mathrm{orb}}$. The horizontal axis represents values computed from scalar wavefunctions, whilst the vertical axis represents those calculated in the spinor regime. Apart from numerical noise, the relative deviation was zero.

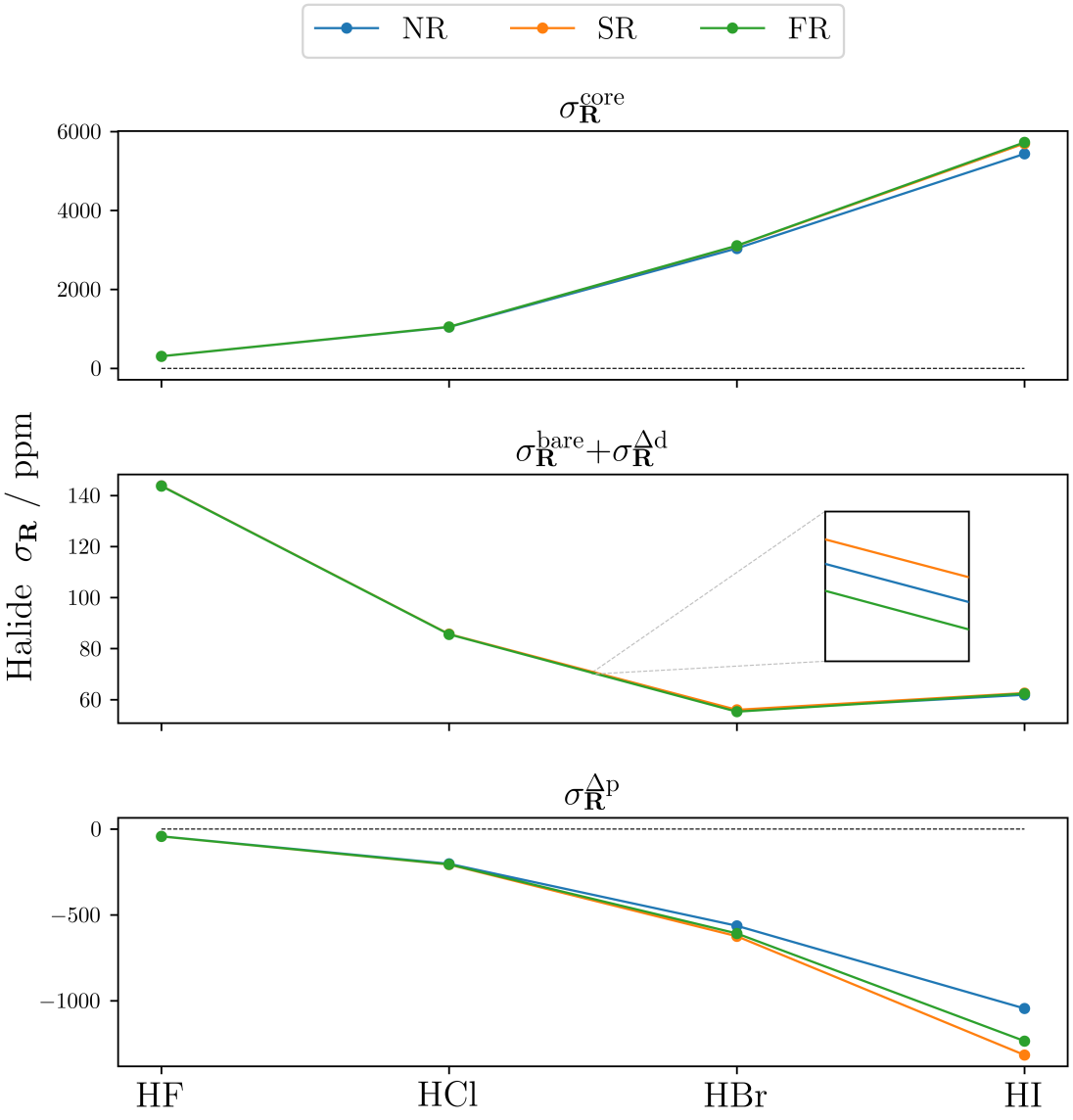


Figure 6.3: Effects of relativity on each of the chemical shielding core and orbital terms for the heavy atom in the hydrogen halides. The Schrödinger (non-relativistic), Koelling-Harmon (scalar-relativistic) and Dirac (fully-relativistic) solvers are compared. The $\sigma_{\mathbf{R}}^{\mathrm{bare}}$ and $\sigma_{\mathbf{R}}^{\Delta\mathrm{d}}$ terms are grouped because the latter is typically very small.

pseudopotential - the choice of which states are core and which are valence is arbitrary. In bromine, we consider its 3d states as valence, whereas in the other halides we only consider their highest energy s and p orbitals. The valence shielding is therefore much higher in bromine, but its core shielding appropriately lower. To observe trends in each of the components - and account for the different core-valence split in bromine - we also calculate the core shielding due to the 3d states of the isolated atom and add it to $\sigma_{\mathbf{R}}^{\text{core}}$ and subtract it from $\sigma_{\mathbf{R}}^{\text{bare}} + \sigma_{\mathbf{R}}^{\Delta\text{d}}$. This leaves $\sigma_{\mathbf{R}}^{\text{orb}}$ unaffected, but allows us to observe trends in each of its components.

As expected, heavier atoms give larger changes between each of the relativistic methods. We see very little change for the bare and diamagnetic augmentation. The latter is only a function of the charge density, which is only expected to vary slightly with the inclusion of SOC. The paramagnetic contribution dominates the change in chemical shift, and becomes more pronounced for the heavier atoms. Zilka *et al.* discuss how the chemical shifts are dominated by the local effects of the paramagnetic term for heavier atoms, whereas lighter elements are dominated by long range interactions.[185] For a given atom, the region considered local is that of its PAW augmentation, and the long range is simply the region outside these spheres. They found that the non-local contributions have a negligible difference between different atom types. This can be explained by considering an element of current, $\mathbf{j}(\mathbf{r}')$, at $\mathbf{r}'$. Through equation 6.3, the induced field at a nucleus at $\mathbf{r}$ is independent of the chemical species and only a function of distance, $|\mathbf{r} - \mathbf{r}'|$.

6.5 Spin term

In the presence of an externally applied magnetic field, SOC induces spin polarisation at nuclei; that is, it mixes some triplet state character into the singlet ground state. As discussed, it is heavy atoms that exhibit the greatest effects of SOC, and can thus perturb the electronic density of lighter atoms in close proximity. This occurs via two mechanisms, a Fermi-contact (FC) and spin-dipolar (SD). It is the FC term that typically dominates this effect,[186–188] which arises from any non-zero spin density at a given atomic nucleus. Only s-orbitals are nodeless at the atomic

origin, and thus only $\ell = 0$ states need to be considered for this term. The FC interaction with SOC is not isotropic (we observe non-zero off-diagonal terms in its tensor), and this is predominantly captured by the additional ZORA-FC (Z-FC) term that arises due to the ZORA scheme. This term is actually closer in similarity to the SD term, which captures anisotropic interactions (those that depend on the orientation of the applied magnetic field, $\mathbf{B}$).

We employ here the extended PAW approach for spinor wavefunctions by dal Corso and Conte,[144] as outlined in section 3.5.8.

6.5.1 Expression

Induced magnetic field

The spin contribution is comprised of the terms discussed above, $\mathbf{B}^{\mathrm{SD}}(\mathbf{r})$ and $\mathbf{B}^{\mathrm{FC}}(\mathbf{r})$,

$$\mathbf{B}^{\mathrm{spin}}(\mathbf{r}) = \mathbf{B}^{\mathrm{SD}}(\mathbf{r}) + \mathbf{B}^{\mathrm{FC}}(\mathbf{r}) + \mathbf{B}^{\text{Z-FC}}(\mathbf{r}), \tag{6.57}$$

where $\mathbf{B}^{\text{Z-FC}}(\mathbf{r})$ is an additional term that arises due to the ZORA scheme.

The SD term is,

$$\mathbf{B}^{\mathrm{SD}}(\mathbf{r}) = -\frac{1}{c^2}\int \frac{1}{|\mathbf{r}-\mathbf{r}'|^3}\left[\mathbb{1}_3 - 3\frac{(\mathbf{r}-\mathbf{r}')\otimes(\mathbf{r}-\mathbf{r}')}{|\mathbf{r}-\mathbf{r}'|^2}\right]\mathbf{m}(\mathbf{r}')\,\mathrm{d}\mathbf{r}', \tag{6.58}$$

where $Q^{\mathbf{R}}_{n;m}(\mathbf{r})$ in $\mathbf{m}(\mathbf{r}')$ are given in equation 6.19. The FC term is,

$$\mathbf{B}^{\mathrm{FC}}(\mathbf{r}) = \frac{1}{c^2}\frac{8\pi}{3}\int \delta(\mathbf{r}-\mathbf{r}')\mathbf{m}(\mathbf{r}')\,\mathrm{d}\mathbf{r}', \tag{6.59}$$

where $Q^{\mathbf{R}}_{n;m}(\mathbf{r})$ in $\mathbf{m}(\mathbf{r}')$ are,

$$\begin{aligned} Q^{\mathbf{R}}_{n;m}(\mathbf{r}) &= K^{\mathbf{R}}(r)\,\langle\phi^{\mathbf{R}}_n|\mathbf{r}\rangle\langle\mathbf{r}|\phi^{\mathbf{R}}_m\rangle, \\ &= K^{\mathbf{R}}(r)\,\phi^{\mathbf{R}}_n(r)\phi^{\mathbf{R}}_m(r)\,Y^*_n(\theta,\varphi)Y_m(\theta,\varphi). \end{aligned} \tag{6.60}$$

Finally, the Z-FC term is,

$$\mathbf{B}^{\text{Z-FC}}(\mathbf{r}) = -\frac{1}{c^2}\int \frac{1}{|\mathbf{r}-\mathbf{r}'|^2}\left[\mathbb{1}_3 - \frac{(\mathbf{r}-\mathbf{r}')\otimes(\mathbf{r}-\mathbf{r}')}{|\mathbf{r}-\mathbf{r}'|^2}\right]\mathbf{m}(\mathbf{r}')\,\mathrm{d}\mathbf{r}', \tag{6.61}$$

where the expressions of $Q^{\mathbf{R}}_{n;m}(\mathbf{r}')$ in $\mathbf{m}(\mathbf{r})$ are,

$$\begin{aligned} Q^{\mathbf{R}}_{n;m}(\mathbf{r}) &= \frac{\mathrm{d}K^{\mathbf{R}}(r)}{\mathrm{d}r}\langle\phi^{\mathbf{R}}_n|\mathbf{r}\rangle\langle\mathbf{r}|\phi^{\mathbf{R}}_m\rangle, \\ &= \frac{\mathrm{d}K^{\mathbf{R}}(r)}{\mathrm{d}r}\phi^{\mathbf{R}}_n(r)\phi^{\mathbf{R}}_m(r)\,Y^*_n(\theta,\varphi)Y_m(\theta,\varphi). \end{aligned} \tag{6.62}$$

See figure 3.4 for a plot of $\frac{\mathrm{d}K^{\mathbf{R}}(r)}{\mathrm{d}r}$ for lead, Pb.

Finite field approach

The goal is to obtain the spin magnetisation, $\mathbf{m}(\mathbf{r}')$,

$$\mathbf{m}(\mathbf{r}') = \frac{1}{2}\sum_{\sigma,\sigma'} n^{\sigma,\sigma'}(\mathbf{r}')\,\boldsymbol{\sigma}^{\sigma,\sigma'}, \tag{6.63}$$

which is induced due to the inclusion of SOC. Without it, the electronic density is not j-split, as discussed in section 3.5, and therefore the magnetisation is always $\mathbf{0}$. That is, $n_\uparrow(\mathbf{r}) = n_\downarrow(\mathbf{r})$; see equation 4.1. This excludes non-diamagnetic systems, which may have induced magnetisation due to open-shell states.

To do so, we will employ a finite-field method, whereby we explicitly apply a magnetic field into the calculation through the local potential, as discussed in section 4.4. This will give rise to a non-zero magnetisation, $\mathbf{m}(\mathbf{r}')$. To build the rows of the spin shielding tensor, we apply the external field in each of the three Cartesian directions. We solve for the wavefunction in each case and obtain the corresponding row of the tensor with the equations above. We must also normalise by the applied field to eliminate its dependence on the magnitude of the tensors.

This method is valid as long as the magnitude of $\mathcal{V}_{\mathbf{B}}$ is small, which is true even for magnetic fields of several hundred Tesla. It is also convenient in that nowhere in the expressions does the evaluation of the $\mathbf{r}$ operator arise. This means the method is transferable to extended and infinite systems without need for alteration.

Shielding tensors

Inserting $\mathbf{m}(\mathbf{r}')$ into the SD expression, equation 6.58, we obtain the pseudopotential contribution from the first term in equation 3.126,

$$\sigma_{\alpha,\beta}^{\text{SD-bare}}(\mathbf{r}) = -\frac{1}{|\mathbf{B}|}\frac{1}{2c^2}\sum_{\sigma,\sigma'}\int \frac{\langle\tilde{\Psi}_\alpha^\sigma|\mathbf{r}\rangle\langle\mathbf{r}|\tilde{\Psi}_\alpha^{\sigma'}\rangle}{|\mathbf{r}-\mathbf{r}'|^3}\left[\delta_{\alpha\beta} - 3\frac{(r_\alpha - r'_\alpha)\left(r_\beta - r'_\beta\right)}{|\mathbf{r}-\mathbf{r}'|^2}\right]\sigma_\beta^{\sigma,\sigma'}\,\mathrm{d}\mathbf{r}', \tag{6.64}$$

which is calculated in reciprocal space and evaluated at each ionic position, when performing the Fourier transform to real space, obtaining $\overleftrightarrow{\sigma}_{\mathbf{R}}^{\text{SD-bare}}$. The second term gives the augmentation,

$$\sigma_{\mathbf{R},\alpha,\beta}^{\text{SD-aug}} = -\frac{1}{|\mathbf{B}|}\frac{1}{2c^2}\sum_{n,m}\sum_{\sigma,\sigma'}\Pi_{n,m}^{\mathbf{R}}\,\bar{\rho}_{n;m}^{\mathbf{R},\sigma,\sigma',\alpha}\,\sigma_\beta^{\sigma,\sigma'}\sum_{q=-2}^{2}C_{\alpha\beta}^{q}\Gamma_{n;m}^{q}, \tag{6.65}$$

where α denotes the Cartesian direction in which the external magnetic field was applied when solving for that wavefunction. We use the bar decoration for $\bar{\rho}_{n;m}^{\mathbf{R},\sigma,\sigma',\alpha}$ to signify that the wavefunctions inside follow this same notation. The atomic term is the same as in equation 6.53 and the Gaunt integrals as in 5.9.

The FC term is,

$$\sigma_{\mathbf{R},\alpha,\beta}^{\mathrm{FC}} = \frac{1}{|\mathbf{B}|}\frac{1}{3c^2}\sum_{\sigma,\sigma'}\Pi_0^{\mathbf{R}}\,\bar{\rho}_{0;0}^{\mathbf{R},\sigma,\sigma',\alpha}\,\sigma_\beta^{\sigma,\sigma'}, \tag{6.66}$$

where, as only the s orbitals are non-zero at the origin, the 0 indices indicate $\ell = m = 0$. The atomic term is,

$$\Pi_0^{\mathbf{R}} = K^{\mathbf{R}}(0)\left[\phi_0^{\mathbf{R}}(0)\right]^2, \tag{6.67}$$

i.e the relativistically scaled amplitude of the atomic wavefunction at its origin.

Finally, the Z-FC term is,

$$\sigma_{\mathbf{R},\alpha,\beta}^{\text{Z-FC}} = -\frac{1}{|\mathbf{B}|}\frac{1}{2c^2}\sum_{n,m}\sum_{\sigma,\sigma'}\Pi_{n,m}^{\mathbf{R}}\,\bar{\rho}_{n;m}^{\mathbf{R},\sigma,\sigma',\alpha}\,\sigma_\beta^{\sigma,\sigma'}\sum_{q=-2}^{2}C_{\alpha\beta}^{q}\Gamma_{n;m}^{q}, \tag{6.68}$$

with the atomic term,

$$\Pi_{n,m}^{\mathbf{R}} = \int\frac{1}{r^2}\frac{\mathrm{d}K^{\mathbf{R}}(r)}{\mathrm{d}r}\phi_n^{\mathbf{R}}(r)\phi_m^{\mathbf{R}}(r)\,\mathrm{d}r, \tag{6.69}$$

and the Gaunt integrals given in equation 6.50.

We obtain only augmentation terms for the FC and Z-FC (i.e they do not have analogous equations to the SD-bare in 6.64) because they are both purely local operators. The Dirac delta function in FC operates only at the origin, and the $\frac{\mathrm{d}K^{\mathbf{R}}(r)}{\mathrm{d}r}$ term in Z-FC is 0 outside of the augmentation region.

The spin chemical shielding tensor, $\overleftrightarrow{\sigma}_{\mathbf{R}}^{\mathrm{spin}}$, is defined as the sum of these four terms,

$$\overleftrightarrow{\sigma}_{\mathbf{R}}^{\mathrm{spin}} = \overleftrightarrow{\sigma}_{\mathbf{R}}^{\text{SD-bare}} + \overleftrightarrow{\sigma}_{\mathbf{R}}^{\text{SD-aug}} + \overleftrightarrow{\sigma}_{\mathbf{R}}^{\mathrm{FC}} + \overleftrightarrow{\sigma}_{\mathbf{R}}^{\text{Z-FC}}, \tag{6.70}$$

and its isotropic value, $\sigma_{\mathbf{R}}^{\mathrm{spin}}$, given through equation 2.12.

Analogy with J-coupling

As discussed, heavy atoms perturb the electronic structure of lighter atoms in close proximity, via the spin density generated at its nucleus due to SOC. This is analogous to the indirect spin-spin (J) coupling phenomenon, which only differs in that the perturbing mechanism is from the magnetic moment of another nucleus. We therefore see similarities between the mathematical equations (e.g references [58, 59]) and the observed phenomena (e.g references [133, 189]). Figure 6.4 displays the similarity in mechanisms. This link was first noted by Nomura *et al.*[60] and has since been investigated multiple times via computational techniques (e.g reference [189]).

Some notable observed similarities of the mechanism to J-coupling are; A) the chemical shift of the perturbed atom is dependent on its s-orbital character in its valence shell; B) atoms that are further away from the perturbing nucleus are less affected; C) the magnitude of the shift of the perturbed atom will depend on the magnitude of the SOC on the perturbing atom e.g heavier elements (greater period/row) will cause a greater shift. One key difference is that the s-orbital character of the perturbing nucleus is not a major factor in the shift of the perturbed nuclei. This makes sense, as it is the effects of SOC that perturb the wavefunction of the system, which are governed by the atomic number, Z, rather than the Fermi-contact mechanism as in the J-coupling.

In regard to computational calculations, Joyce *et al.*[58] and Green *et al.*[59] note that they implicitly rotate over the magnetisation axis when calculating the J-coupling terms. This is because these formulations used non/scalar-relativistic theories. As discussed above, this method is not valid for the fully-relativistic case, and we compute the ground state wavefunction at three times; for the magnetic field aligned in each direction.

6.5.2 Implementation

The four previously discussed spin shielding tensors, equations 6.64, 6.65, 6.66 and 6.68, were implemented into the CASTEP electronic structure code.

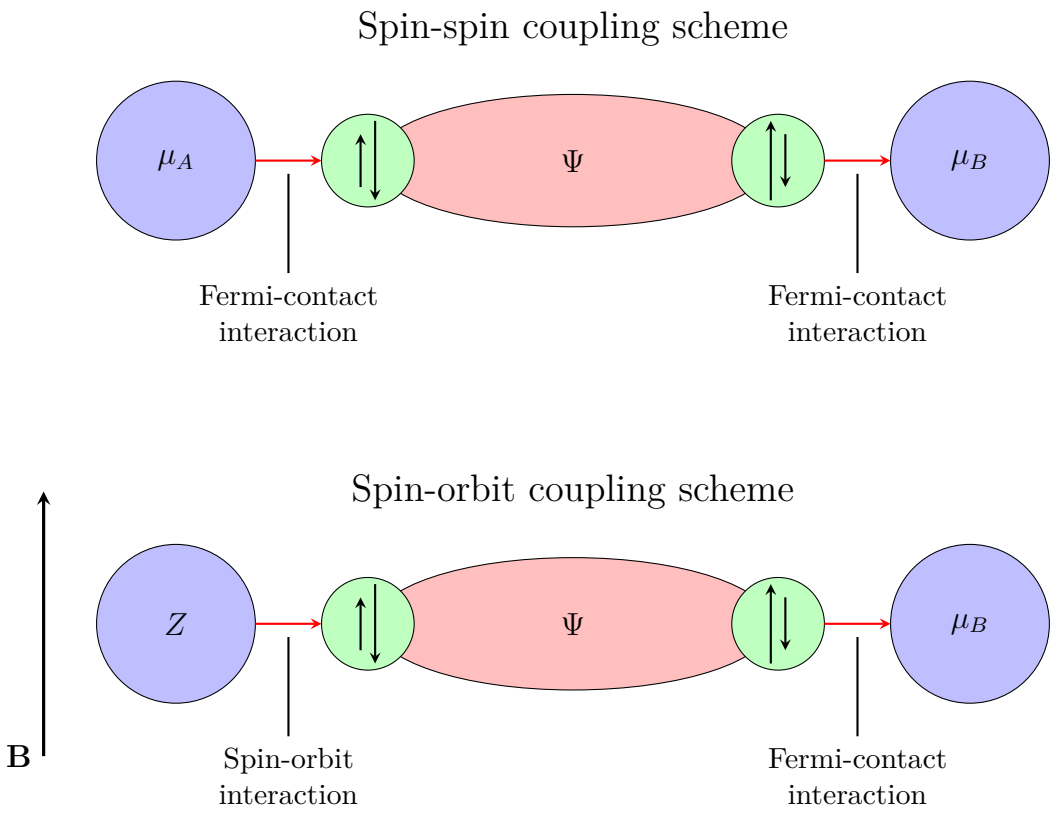


Figure 6.4: Comparison of the J-coupling and SOC effect on chemical shift mechanisms. This diagram is based off that in Kaupp *et al.*.[189] The processes occur left to right. In the J-coupling scheme, the Fermi-contact interaction creates a spin density at a nucleus, A. This propagates through the system (denoted by the wavefunction, Ψ) and creates a spin density at a neighbouring nucleus, B. Through another Fermi-contact interaction, this perturbs the magnetic moment of the B nucleus. The SOC scheme works similarly, but it is an applied field, $\mathbf{B}$, that causes a spin-orbit splitting of the ground state. This creates a spin density at nucleus A, and the process follows the same as the J-coupling case.

Divergence of the Dirac equation

One notable subtlety of the Dirac equation is that its solutions for hydrogen-like atoms are divergent at the origin; as $\phi(r) \sim r^{-1}$. Figure 6.5 shows the 1s atomic wavefunction for hydrogen, solved using the Schrödinger and Dirac equations. One can see that the origin in the NR case is bounded and defined, whilst the FR case diverges to infinity. Evaluation at the nucleus appears in the FC term, specifically in equation 6.67. Divergence of these points are avoided in the atomic code by storing $r\,\phi(r)$, meaning the $r = 0$ point is 0. The $\phi(0)$ term is then recovered via extrapolation from the 20 closest r values to the origin. In the FR scheme, this divergence is further avoided by the fact that $K^{\mathbf{R}}(0) = 0 \,\forall\, \mathbf{R}$ (see figure 3.4) and, as a result, equation 6.67 is 0 for all atoms.

Combining NR and FR pseudopotentials

We retain the FC term in the discussion for this section, despite it always equalling 0 in the FR case, as there is a possibility for the pseudopotentials for light atoms - where relativistic effects are small - to be solved non-relativistically. We do not implement this idea here, but propose it for possible future work. Figure 6.6 shows the relative difference for the atomic wavefunctions of several atoms. Those that exceed a difference of a pre-defined tolerance percentage (e.g 5 %) would be solved relativistically and thus require spinor wavefunctions. Those that are below this tolerance, however, could be solved using NR pseudopotentials, resulting in a lower computational expense due to the use of scalar wavefunctions. The effects of SOC on the chemical shift at the light atom are retained as long as we treat the heavy atoms of the system fully-relativistically. The light atom spin shielding effects are then still calculable through equation 6.70, but where we use the NR forms of the operators therein; that is $K^{\mathbf{R}} \to 1$ and thus $\frac{\mathrm{d}K^{\mathbf{R}}}{\mathrm{d}r} \to 0$. The Z-FC term would therefore disappear, and the expressions reduce to the well-known NR hyperfine operators (e.g references [190–192]).

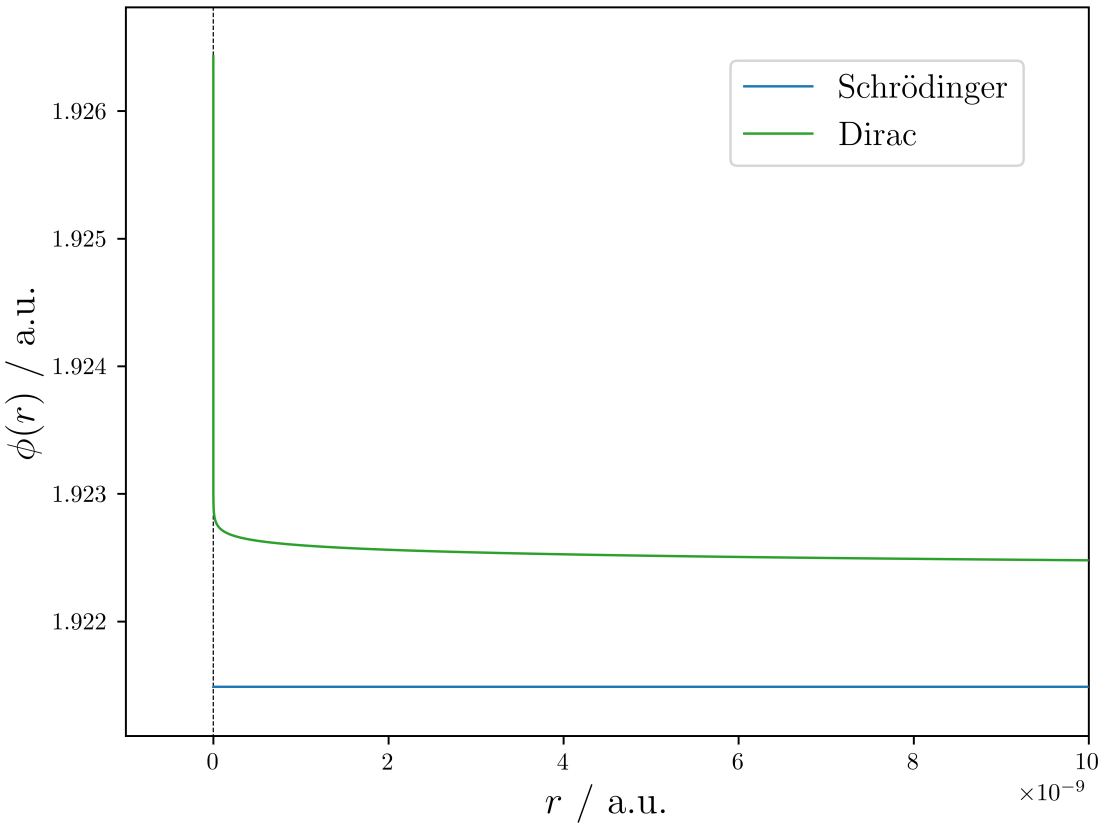


Figure 6.5: Non-relativistic (Schrödinger) and fully-relativistic (Dirac) 1s atomic wavefunctions for hydrogen, H. The value of the wavefunction tends towards a well-defined point in the NR case, but diverges to infinity for the FR case. The exact $r = 0$ point is omitted in these plots. An incredibly dense grid was used for these calculations, totalling 23039 points (the default for hydrogen is typically 2879), to capture the behaviour near the origin better. Note also that logarithmic grids are used for the all-electron calculations, meaning the density of points nearer the origin is higher than elsewhere.

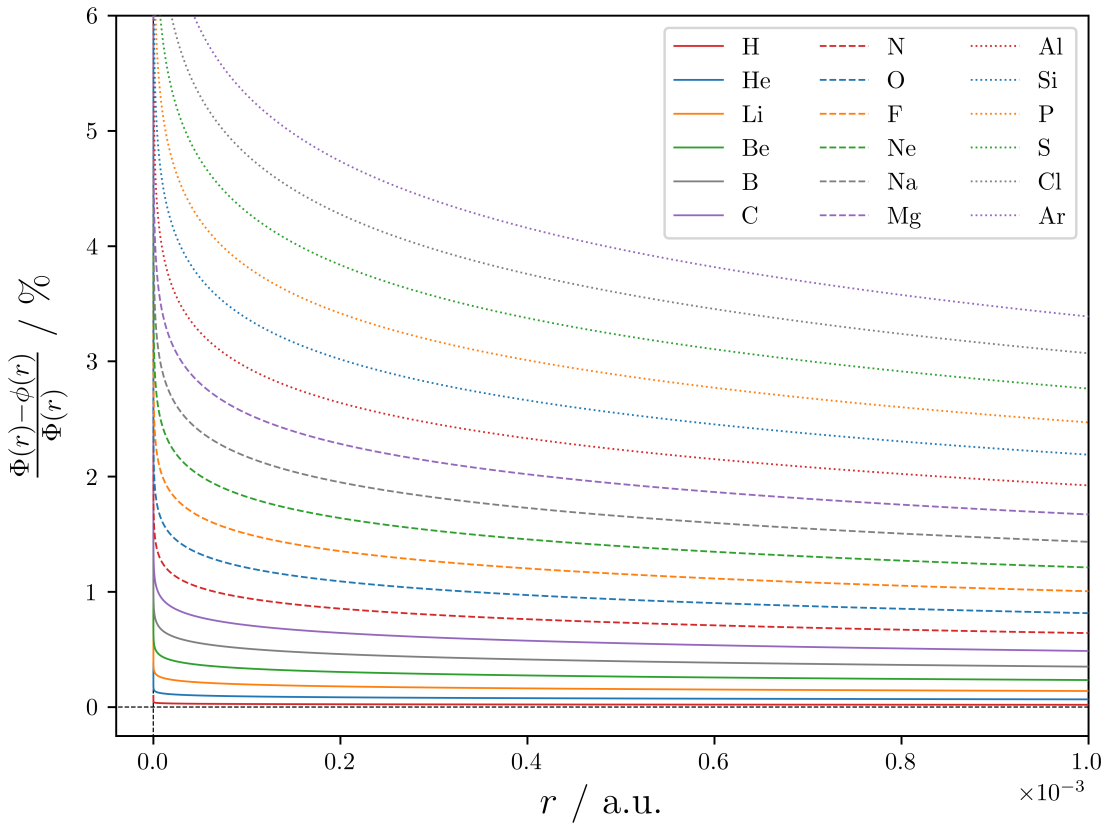


Figure 6.6: Relative difference between fully-relativistic and non-relativistic atomic wavefunctions. Up to roughly magnesium, Mg, we notice that the percentage difference between the wavefunctions remains below 5 %. This threshold could be used to declare these atoms be treated sufficiently with NR (or SR) pseudopotentials. The origin point, which is ill-defined for all atoms in the FR scheme, has been omitted.

Ground-state spin densities

Non-collinear magnetism has more degrees of freedom for the spins to relax into, due to the fact that spin is a three-vector. The energy landscape, with respect to the spin, is therefore very complex and may have a multitude of local minima. The size of basis set and electronic energy tolerance of the SCF cycle therefore have to be carefully considered for NCM calculations, particularly in the case of applying an external magnetic field. It is wise to check that a ground-state (no external field) calculation returns a vector spin density of approximately zero for a non-spin-polarised system. Using too small of a basis set or too lenient a choice of SCF cycle tolerance may result in the spin vectors not relaxing to their true minima, despite the energy being converged. The former may simply be investigated by the previously outlined systematic increase in cut-off energy, E_{cut}, where one may realise that a higher value is required to obtain $\mathbf{S} \simeq \mathbf{0}$. The latter can also be made stricter by a systematic method, and it was found that an electronic energy tolerance of around 10^{-11} eV / atom was appropriate to obtain converged zero spin densities in the ground state. This contrasts the current default CASTEP value for NMR calculations of 10^{-9} eV / atom. If a non-converged basis set or tolerance is chosen, the perturbed calculations (non-zero applied magnetic field) may have some spurious spin density embedded in them, giving fallacious results.

It is also appropriate to consider the size of applied magnetic field in the finite-field method. Investigation of the cell magnetisation with respect to the applied magnetic field is shown in figure 4.5 in chapter 4. In this, the magnetisation of the cell stabilised in the 10^3-10^4 Tesla range. This scale was found to be reasonably robust and transferable for the systems studied in section 6.6, but it may be wise for a user to test a number of applied fields for their system with the same considerations as us.

The initialisation of the wavefunction is typically random[1] (subject to certain constraints, such as normalisation). As a result, the starting spin configuration can

[1]CASTEP will perform a quick calculation using an initially randomised wavefunction, but with a much smaller basis set (lower cut-off energy). The resultant wavefunction from this is then used as the starting point for the requested full basis set calculation. This has been shown to considerably speed up the process of solving for the wavefunction.[193]

be heavily polarised, which may cause the solver to converge down an energetically favourable but spin biased path. Woods *et al.* note that there is no widely successful method for an initial guess of the spin densities in polarised systems.[193] Forcing the spin density to be exactly 0 for the first few SCF cycles (and in the initial approximate wavefunction calculation performed by CASTEP) was therefore tested as a method to encourage the wavefunction solver to explore the energy landscape from a non-spin-polarised initial point. However, it was found that the level of spin polarisation obtained at the end of the SCF cycle was almost identical in either case.

Convergence of orbital and spin terms

The convergence of the orbital GIPAW and spin finite-field methods were investigated with respect to the basis set size, defined by the cut-off energy. Figure 6.7 shows the $\sigma_{\mathbf{R}}^{\mathrm{orb}}$ and $\sigma_{\mathbf{R}}^{\mathrm{spin}}$ shielding values with respect to E_{cut} for ^{1}H in a hydrogen iodide molecule. They both follow a similar trend with increasing basis set size, and the convergence of both terms is deemed comparable. A user can therefore conduct convergence tests on either or both values, with the additional considerations for the spin term as above.

This behaviour is expected as we have used the PAW approach, which results in only augmentation terms for the FC and Z-FC operators. These are in the atomic basis, which are solved on radial grids and therefore do not present challenges in mapping the origin point. This contrasts to Gaussian basis sets, of which, do not represent the steep nature of the origin well, and therefore observe slower convergence.[194] Gaussian basis sets, designed specifically for electric and magnetic properties, are common.

The spin term is noticeably noisier, which is expected given the very high sensitivity of the term with respect to the spin density at the nucleus. Obtaining a value at a specific point will naturally incur more noise than a quantity that takes an integral average over space. Around 1000 eV to 1200 eV, the variation between runs is of the order of 0.1 ppm. This is relatively small, but not negligible for ^{1}H shielding values, and should therefore be taken into account when considering the

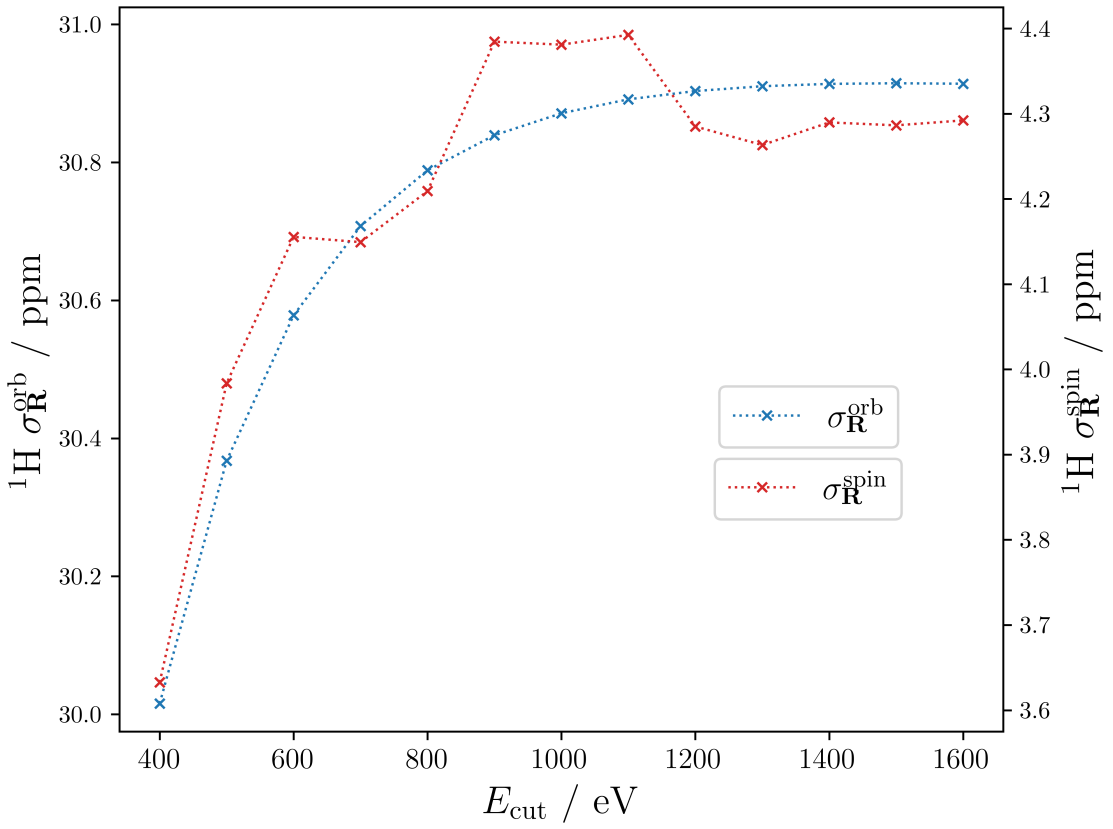


Figure 6.7: Convergence of the isotropic orbital and spin chemical shielding values with respect to cut-off energy, E_{cut}, for ^{1}H in hydrogen iodide. $\sigma_{\mathbf{R}}^{\mathrm{orb}}$ follows the blue curve with its y axis given on the left, and $\sigma_{\mathbf{R}}^{\mathrm{spin}}$ follows the red curve with its y axis given on the right.

error in a FR NMR calculation. Only at incredibly high E_{cut} energies of around 1500 eV do we see reliable convergence of the spin term. This is mainly due to the use of norm-conserving pseudopotentials, which require larger basis sets to achieve good convergence. The implementation of ultra-soft pseudopotentials with FR calculations in CASTEP will hopefully allow these high basis set requirements to be relaxed, whilst still achieving converged results.

6.6 Results

The total chemical shielding tensor, $\overleftrightarrow{\sigma}_{\mathbf{R}}$, for a given ion at $\mathbf{R}$, is the sum of the three previously discussed,

$$\overleftrightarrow{\sigma}_{\mathbf{R}} = \overleftrightarrow{\sigma}^{\text{core}}_{\mathbf{R}} + \overleftrightarrow{\sigma}^{\text{orb}}_{\mathbf{R}} + \overleftrightarrow{\sigma}^{\text{spin}}_{\mathbf{R}}, \tag{6.71}$$

and its isotropic value, $\sigma_{\mathbf{R}}$, given by equation 2.12.

6.6.1 Hydrogen halide molecules

The molecular hydrogen halides, HX (X = F, Cl, Br, I) are a simple yet informative set of systems to study the effects of SOC. The halide atom polarises the spin density at the hydrogen nucleus, through the Fermi-contact interaction, affecting the ^{1}H value. A trend of increasing shift change on both atoms, with respect to the halide atomic number, Z, can be observed.

NR formulations report chemical shielding values of all ^{1}H atoms in the HX set as roughly 30 ppm. Whilst accurate for HF and HCl, this value quickly deviates for the experimentally reported shifts of 34.96 ppm and 43.96 ppm for ^{1}H in HBr and HI, respectively.[195] These differences are well understood to be due to the neglect of SOC that is only incorporated through the use of a FR approach.[60, 61]

There have been a very large number of studies on the HX set, as well as the similar methyl halide molecules, of which, are often used as benchmark tests for developed methodologies. For example, Ballard *et al.* used the unrestricted Hartree-Fock method, with inclusion of the spin-orbit operator, to calculate the SOC effects on the HX chemical shifts.[188] Malkin *et al.*[67] and Wolff and Ziegler[68,

69] both used DFT methods, differing in their choice of basis orbitals and treatment of the SOC term. Melo *et al.* also developed a FR method, starting from the Breit Hamiltonian.[196, 197] Komorovský *et al.* developed a scheme that utilised Dirac-Kohn-Sham formulation,[198] and Kantola *et al.* then performed an advanced study, with the inclusion of anharmonic and harmonic vibrational corrections, using DFT with the SOC effects accounted for by the Breit-Pauli perturbation.[199]

Figure 6.8 compares the different levels of relativistic treatment against experiment for the ^{1}H chemical shielding value in the hydrogen halide molecules. All calculations used the PBE exchange-correlation functional and a set of relativistic NCPs constructed on-the-fly. As expected, the NR and SR schemes perform poorly, and obtain a roughly constant value of the ^{1}H chemical shielding value down the HX molecules. The FR calculations perform slightly better, but clearly do not account for the whole difference between the NR/SR and experimental values. It is possible that the spin density at ^{1}H is missing some level of perturbation from the heavy atom SOC effect. This could be due to additional polarisation of the core electrons, which are treated as frozen in the current implementation. One possibility, to account for this, is to apply a magnetic field to the core states when solving the all-electron atom and obtain spin-dependent pseudopotentials. These would then introduce any additional spin polarisation offered by the core region of the heavy atom, and possibly account for the difference in magnitude seen in the NMR spin response at the light atom. In this approach, the spin response of the core states would be obtained non-self-consistently. In other words, the polarisation of the core would be determined and fixed, and any effect this has on the valence states would not be reciprocated back to the core. This approximation could be investigated with self-consistent pseudopotentials,[126] of which, are determined atomically, but then allowed to undergo an SCF cycle with the valence states.

Table 6.2 shows the different contributions to the chemical shielding value of the FR calculations. The FC contribution is $0 \; \forall \; \mathbf{R}$ and the SD-aug term is 0 for hydrogen. Both the SD-bare and Z-FC values increase in magnitude down the HX series, as expected, due to the larger effect of SOC in the heavy atom. The

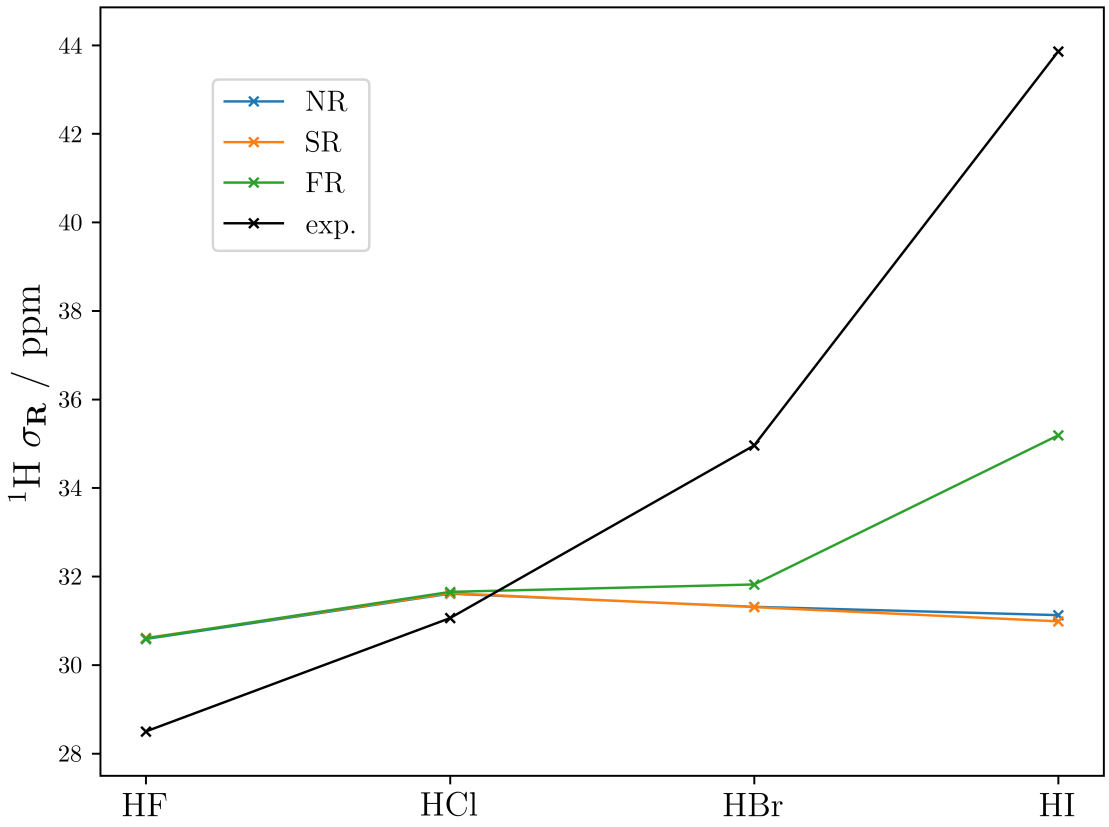


Figure 6.8: Comparison of relativistic treatments on the ^{1}H chemical shielding value in the hydrogen halide molecules. All calculations used the PBE exchange correlation functional and the same set of relativistic norm-conserving pseudopotentials. NR: non-relativistic. SR: scalar-relativistic. FR: fully-relativistic. Experimental values from reference [195] that were compiled in [201].

Table 6.2: ^{1}H chemical shielding values for the hydrogen halides from fully-relativistic calculations, broken down into the orbital term, 6.56, and the spin contributions from equations 6.64 and 6.68. The SD-aug term is 0 for hydrogen. The exchange-correlation functional was PBE. Experimental values from reference [195] that were compiled in [201].

Molecule	Chemical shielding / ppm					
	$\sigma_{\mathbf{R}}^{\text{orb}}$	$\sigma_{\mathbf{R}}^{\text{SD-bare}}$	$\sigma_{\mathbf{R}}^{\text{Z-FC}}$	$\sigma_{\mathbf{R}}^{\text{spin}}$	$\sigma_{\mathbf{R}}$	exp.
HF	30.61	0.000	-0.012	-0.012	30.60	28.50
HCl	31.62	0.001	0.028	0.029	31.65	31.06
HBr	31.30	0.012	0.506	0.518	31.82	34.96
HI	30.90	0.030	4.255	4.285	35.19	43.86

most dominant contribution to $\sigma_{\mathbf{R}}^{\text{spin}}$ is from the Z-FC term, which represents the polarisation of spin density at the nucleus. This has been well known to be the most important term in calculating the SOC contribution to chemical shielding, and often the spin dipolar parts are ignored.[66, 200]

The chemical shielding value at the H atom was investigated as a function of the core-valence split of the I atom in HI. The question of whether the core electrons in I contribute to the level of polarisation observed at H could be better understood if the I 4d electrons were included in the valence states, rather than in the core, which is the case in the results in table 6.2 and figure 6.8. Table 6.3 shows the comparison with and without the I 4d states as valence. The additional shielding value observed at the H atom is small, and certainly does not account for a large portion of the difference with experiment. A point that is not noted in the table, is that the I chemical shielding value increases greatly with the addition of the 4d as valence electrons. However, this does not correspond to additional polarisation observed, but simply that the core term is smaller by an equivalent magnitude.

Table 6.3: Comparison of the ^{1}H spin chemical shielding value with and without the 4d states treated as valence on the I atom for fully-relativistic calculations. The exchange-correlation functional was PBE.

Molecule	Valence states	Chemical shielding / ppm		
		$\sigma_{\mathbf{R}}^{\text{SD-bare}}$	$\sigma_{\mathbf{R}}^{\text{Z-FC}}$	$\sigma_{\mathbf{R}}^{\text{spin}}$
HI	5s 5p	0.030	4.255	4.285
	4d 5s 5p	0.021	4.394	4.415

To visualise the HALA effect, a tool was created to plot the vector spin densities of the cell in three-dimensional space, which is shown in figure 6.9. The SOC effect at the I atom induces spin density on application of the external magnetic field, of which, in this case was along the bond direction. This polarises the spin across the bond and induces density at the H nucleus, altering its chemical shielding value; this is the heavy-atom light-atom effect. This is captured predominantly by the Fermi-contact operators.

6.6.2 L-Cysteine

The molecular crystal L-cysteine was considered to determine its ^{1}H NMR shielding values with the newly implemented FR approach. The heavy S atom in L-cysteine contributes additional shift effects to its bonded H atom due to its spin-orbit interaction. Acquiring accurate shielding values of the light atom bonded to S has been proven to be a difficult but required task.[202] Rusakov and Rusakova have showed that the S can shift ^{13}C shielding values by up to almost 8 ppm.[203]

Recent work has been done by Dračínský *et al.*, by performing SR calculations on the L-cysteine crystal, as well as other compounds.[204] Using the GIPAW approach within DFT, they then added a spin-orbit correction, which is calculated on the isolated molecule. They found these corrections to account for around 0.56 ppm, which is large compared to the ^{1}H shift range of about 0-12 ppm. Additional to this, Dračínský *et al.* also considered the use of hybrid functionals, such as PBE0, to better account for the exchange-correlation effects. These functionals use a portion of the exact exchange derived in the Hartree-Fock theory. The corrections were also calculated on the isolated molecule, as solid-state calculations can suffer from high time and memory requirements with hybrid functionals. These corrections have been shown to improve reported shielding values.[53, 205–208] They also added molecular corrections through the coupled-cluster method, and nuclear quantum effects (such as tunnelling) were taken into account by a path integral molecular dynamics technique. Altogether, the authors saw a decrease in the root-mean-square deviations of ^{1}H shifts to 0.21 ppm, which was about half that of the standard

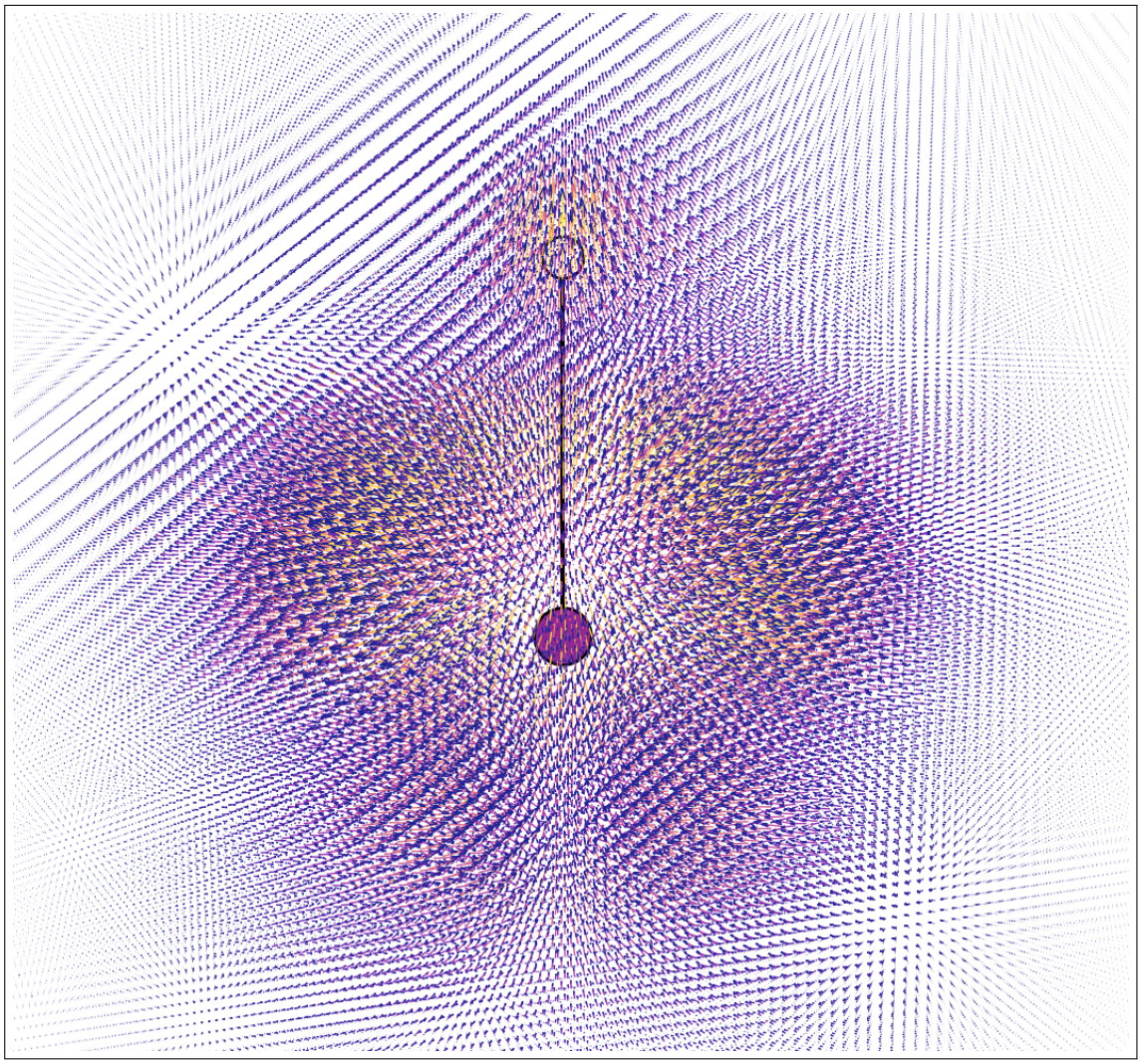


Figure 6.9: Spin density in the hydrogen iodide molecule, where an external magnetic field has been applied along the bond. The H atom is in white and the I atom is in purple. A plasma colour mapping shows the areas of high spin densities.

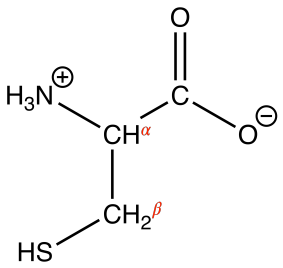


Figure 6.10: Molecular structure of L-cysteine, with the H^{α} and H^{β} atoms labelled.

GIPAW approach. The SOC effect was shown to be, for the vast majority of the terms, the largest correction required to obtain accurate shielding values.

One possible shortcoming of the Dračínský *et al.* method is the neglect of solid-state effects by using correction terms based on molecular calculations. The authors noted that these types of corrections ignore many-body effects, which are inherently accounted for in the exchange-correlation functional of the DFT theory in solids. The newly implemented FR approach to NMR calculations should allow for the computation of the full shielding values of the crystal, without the need for additional correction terms.

Conformers

The molecular structure of L-cysteine is shown in figure 6.10. It has been reported that there exists a phase transition between two conformers of L-cysteine.[209] Kolesov *et al.* report that, at ambient temperature, the thiol group preferentially hydrogen bonds to O atoms over S atoms, whereas at low temperature, the reverse is true. The structures for both of these conformations are shown in figures 6.11 and 6.12. The nature of the crystal and hydrogen bonding present is shown in both.

Following Dračínský *et al.*, we perform SR singlepoint calculations for both structures to obtain their energies. The PBE functional and latest ultra-soft on-the-fly pseudopotentials were used. The final energies were −8181.486 eV and −8181.374 eV for the low and high temperature conformers, respectively. Boltzmann's distribution is,

$$\frac{p_{\text{high}}}{p_{\text{low}}} = e^{-\frac{\Delta E}{k_{\text{B}}T}}, \tag{6.72}$$

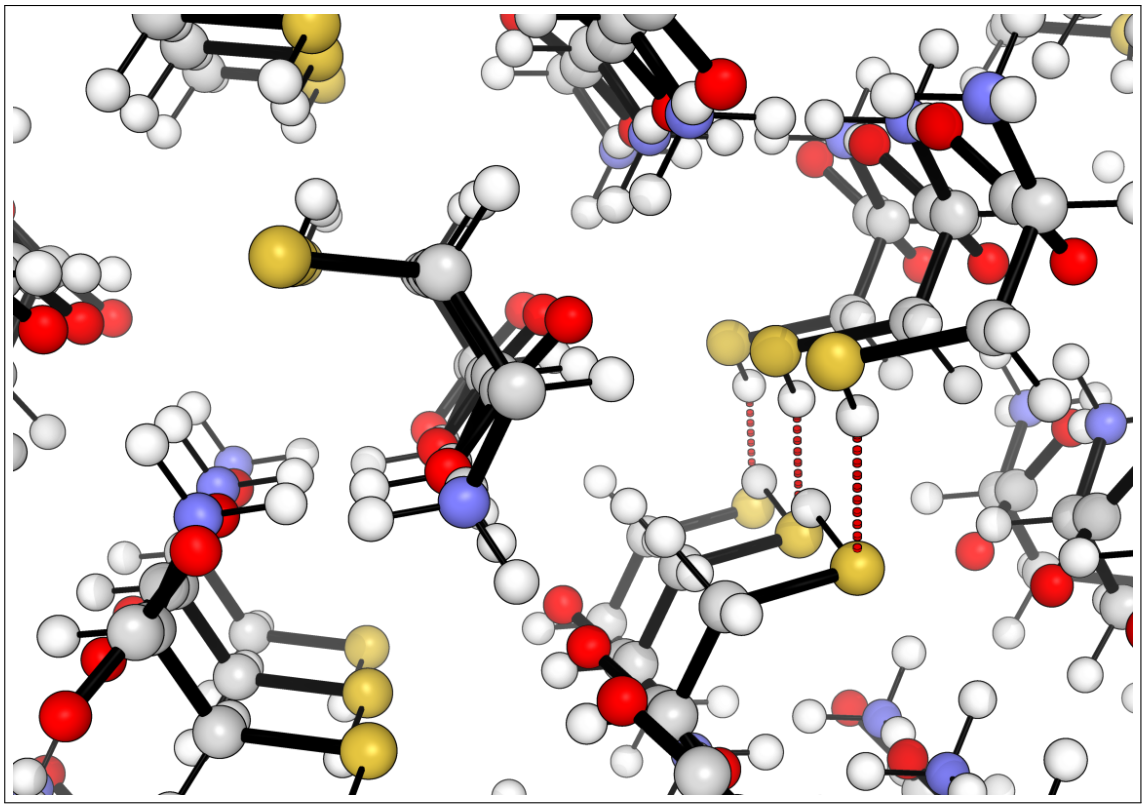


Figure 6.11: Structure of L-cysteine at low temperature, with S-H$\cdots$S hydrogen bonding shown as a dashed red bond.

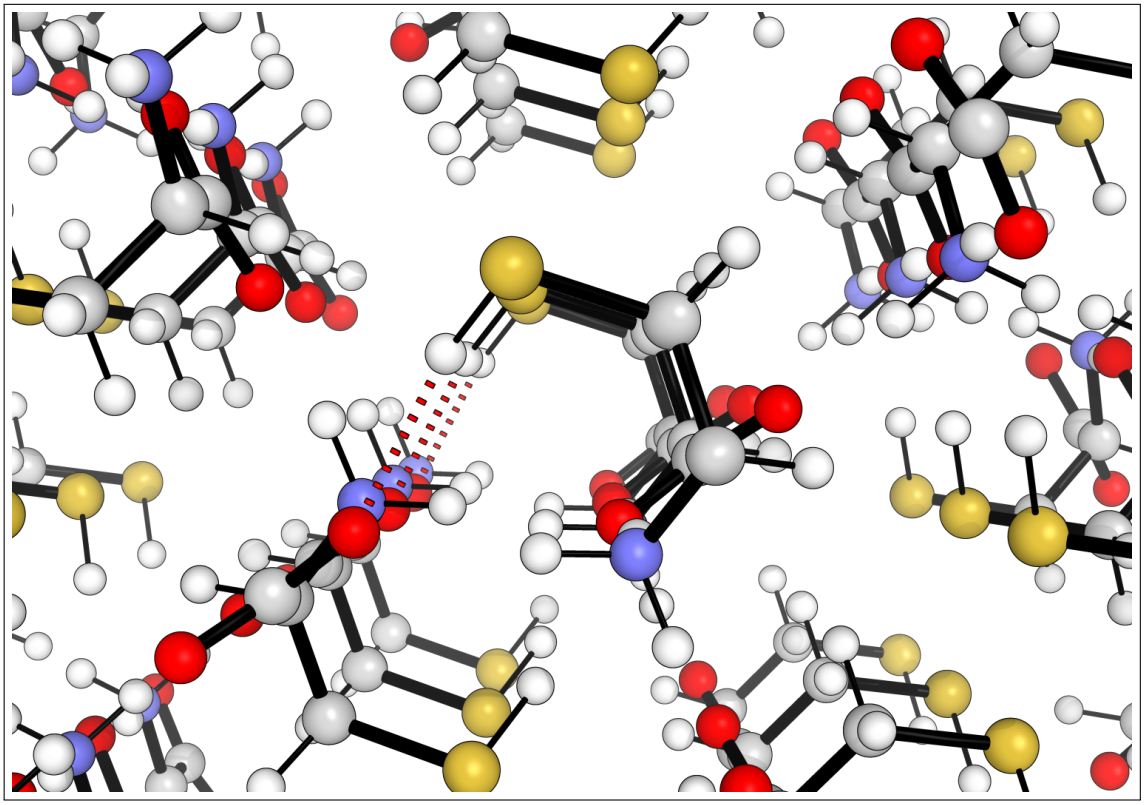


Figure 6.12: Structure of L-cysteine at high temperature, with S-H$\cdots$O hydrogen bonding shown as a dashed red bond.

where p_{i} is the proportion of conformer i, ΔE is the energy difference between the conformers, k_{B} is Boltzmann's constant and T is ambient temperature. Using this equation, and the fact that $p_{\mathrm{high}} + p_{\mathrm{low}} = 1$, we obtain the values $p_{\mathrm{high}} = 25$ % and $p_{\mathrm{low}} = 75$ %. This follows closely with the results of Dračínský *et al.*, who obtain $p_{\mathrm{high}} = 32$ % and $p_{\mathrm{low}} = 68$ %. We perform the NMR calculations on both conformers, and weight the results using the proportions found.

Calculations

Both high and low temperature conformer structures were obtained from reference [185] and subjected to geometry optimisations using the PBE functional, SR solver and latest set of on-the-fly USPs in CASTEP. Both calculations reported the structures converged after one cycle and were subsequently used for all NMR calculations.

Sets of NMR calculations were performed using the Schrödinger (NR), Koelling-Harmon (SR) and Dirac (FR) solvers. Calculation of the orbital term was performed for all three, but only the latter required the computation of the spin term, where a 2 kT external magnetic field was used for the finite-field method. All NMR calculations used the same set of relativistic NCPs. These runs were performed for both the LDA and PBE exchange-correlation functionals, however, the latter had problems of convergence for the FR calculations. This was most likely due to the locally collinear implementation of the exchange-correlation functionals for non-collinear magnetism,[151] discussed in section 4.2. The LDA results were used for the remainder of the study.

Results

Using equation 2.13, we can plot the calculated isotropic chemical shielding in ppm, σ_{iso}, against the experimental shift, δ_{iso}. This should give a slope of -1 and intercept equal to the reference in ppm, σ_{ref}. In figure 6.13, we plot this for the SR calculations, but omit the ^{1}H thiol group value from the linear fitting because it results in a poor value for the gradient. This illustrates the poor performance of the SR method for the thiol group containing the heavy S atom, reaffirming the findings of Dračínský *et al.*. We obtain a slope of -1.097 and intercept of 30.29 ppm. The

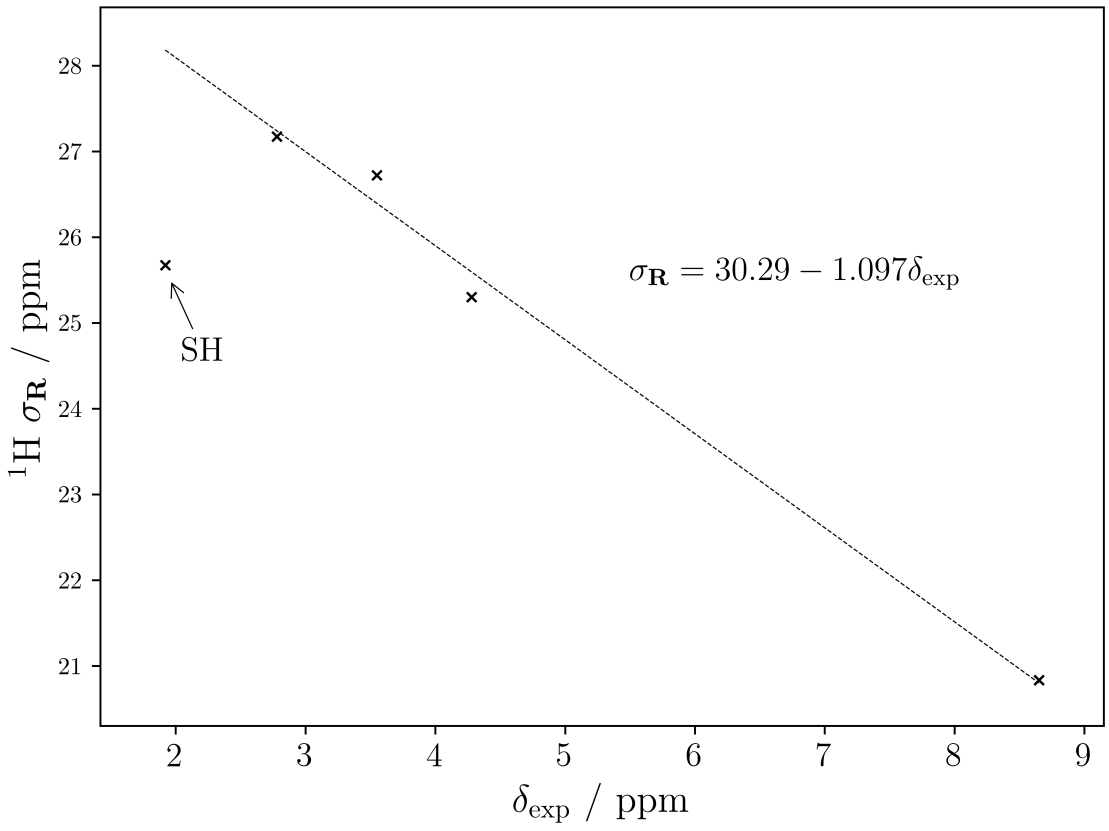


Figure 6.13: Correlation between calculated ^{1}H chemical shielding values against experimental shifts for L-cysteine. Scalar-relativistic calculations were performed with the LDA exchange-correlation functional. The SH value was excluded from the line of best fit, which had slope -1.097 and intercept 30.29 ppm.

Table 6.4: ^{1}H chemical shielding values for the L-cysteine crystal from fully-relativistic calculations, broken down into the orbital term, 6.56, and the spin contributions from equations 6.64 and 6.68. The SD-aug term is 0 for hydrogen. The exchange-correlation functional was LDA. Experimental values from reference [204]. Our shieldings, $\sigma_{\mathbf{R}}$, are converted to shifts, $\delta_{\mathbf{R}}$, with the equation in figure 6.13.

H atom	Chemical shielding / ppm						
	$\sigma_{\mathbf{R}}^{\text{orb}}$	$\sigma_{\mathbf{R}}^{\text{SD-bare}}$	$\sigma_{\mathbf{R}}^{\text{Z-FC}}$	$\sigma_{\mathbf{R}}^{\text{spin}}$	$\sigma_{\mathbf{R}}$	$\delta_{\mathbf{R}}$	exp.
SH	25.68	0.0030	0.0091	0.0121	25.69	4.19	1.92
H^{α}	25.30	0.0001	0.0008	0.0009	25.30	4.54	4.28
$H^{\beta 1}$	26.72	-0.0001	-0.0001	-0.0002	26.72	3.25	3.55
$H^{\beta 2}$	27.18	-0.0001	-0.0001	-0.0002	27.18	2.84	2.78
NH_3	20.83	-0.0001	0.0001	0.0000	20.83	8.62	8.65

difference between the thiol ^{1}H and the fitted line is around 2.5 ppm. The NR solver reports similar findings, with a slope of -1.099 and intercept of 30.31 ppm. The SR calculations are performed to indicate the atoms that may need a FR treatment to obtain the correct shielding values. We now proceed with FR calculations in the hope to rectify the incorrect shielding values for the thiol group ^{1}H atom.

Table 6.4 reports the break down of the individual contributions to the chemical shielding using the FR approach. As with the hydrogen halide molecules, we do not see the correct magnitude that we expect for the spin term. We convert our chemical shielding values from calculation, $\sigma_{\mathbf{R}}$, to shifts, $\delta_{\mathbf{R}}$, with the equation in figure 6.13. The effects of SOC would be expected to give $\sigma_{\mathbf{R}}^{\text{spin}} \simeq 2.5$ ppm, to bring the shift value in line with that found by experiment. The possible reasons for the lower values obtained were discussed in section 6.6.1. One additional note with these results is that, as discussed, the LDA exchange-correlation functional was used for all NMR calculations. The use of a higher order functional would not be expected to account for the errors found in the spin term here, but may account for a smaller portion of the differences. Despite the incorrect magnitude of shift found, we still observe the expected trends. The thiol H has a contribution from the spin term that is orders of magnitude greater than the other H atoms in the crystal.

One interesting feature is that the H^{α} spin shift found is around five times larger than the H^{β} values. This contrasts the results found by Dračínský *et al.*, of whom, find all of the spin-orbit correction terms for H^{α} and H^{β} to be comparable.

As discussed, their method implemented the SOC corrections via a calculation on the isolated molecule. Whilst they observed favourable shift changes through this method, it does not account for the spatial effects of the crystal. The molecular structure in figure 6.10 implies that the H^{α} is far from the S atom. However, the three-dimensional geometry of the crystal, pictured in figure 6.14, shows that it is in fact very close to the S atom, which may contribute additional spin density at the H^{α} nucleus. These proximities would not be accounted for in the molecular method, and their effects would only be considered in a solid-state NMR calculation. This reinforces the necessity for the implementation of a FR GIPAW technique.

Visualisation

Figure 6.15 shows a plot of the spin density for a unit cell of the L-cysteine molecular crystal. This helps to visualise the higher levels of spin density around the heavy S atoms, which is due to their additional spin-orbit interactions. These effects polarise the spin density at the bonded H atom, via the Fermi-contact coupling mechanism discussed in section 6.5.1, shifting its chemical shielding value. Higher spin density is also noticeable at the oxygen atoms, and may contribute through space to the higher H^{α} spin shielding term.

6.6.3 4-dimethylaminopyridinium halides

It is well-known that the interactions between weakly bonded atoms, such as in hydrogen bonding or van der Waals forces, can affect the observed NMR shifts.[210, 211] However, the relativistic nature of the interaction, which is expected to be of appreciable size if one of the atoms if heavy, has been studied less. This *through-space* interaction has been noted by recent authors to be considerable in some cases,[212, 213] and the effects from the heavy atom are not restricted to only strong covalent bonds; as was the case in the L-cysteine study, for example. As discussed in section 6.5.1, the spin-orbit effect on the chemical shift follows analogously to that of the J-coupling phenomenon. It is no surprise, therefore, that through-space J-coupling interactions have been observed.[214–217]

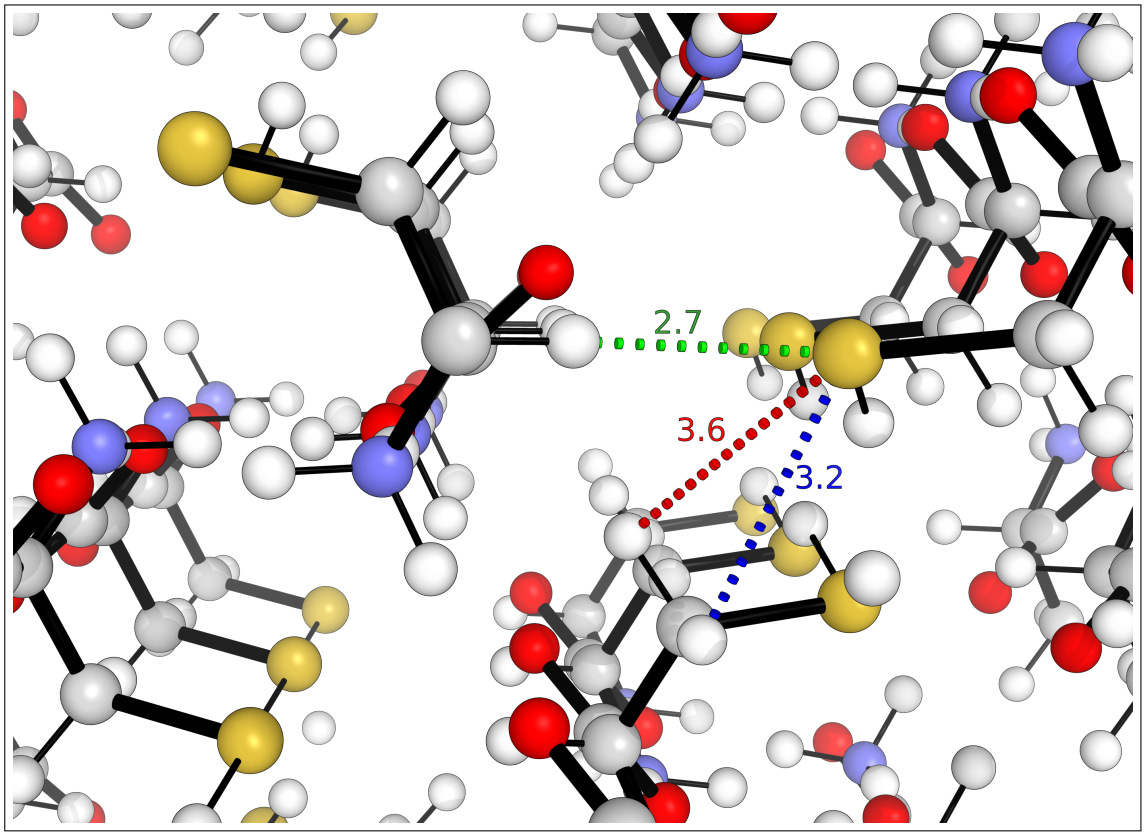


Figure 6.14: Distances in Å of hydrogen atoms to sulphur in the molecular crystal L-cysteine for the low temperature conformer. The red and blue dashed lines show the H^{β} distances, which are 3.6 Å and 3.2 Å, respectively. The green dashed line shows the H^{α} distance, which is 2.7 Å.

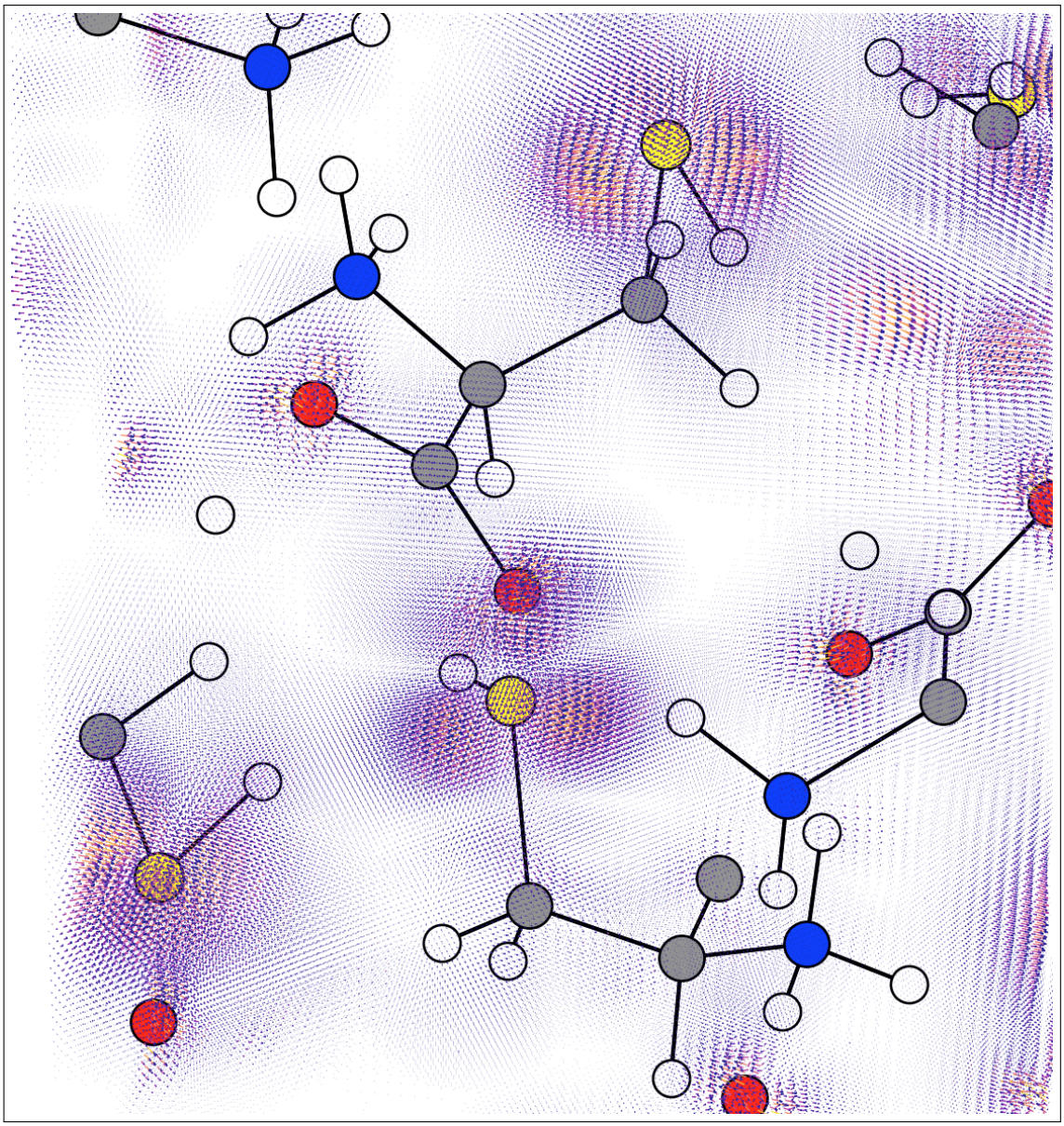


Figure 6.15: Spin density in molecular crystal L-cysteine for the low temperature conformer. Higher polarisation is seen near the heavy S atoms (yellow circles) due to the SOC effect. This causes spin density at the adjoining H (white circles) nuclei. Carbon atoms are grey, oxygen are red and nitrogen are blue.

Ariai and Saielli used the ZORA method in DFT to investigate the relativistic effects on the NMR shifts of ^{1}H, ^{13}C and ^{15}N in the 1-methylpyridinium halide and 1-butyl-3-methylpyridinium trihalide ionic liquids.[212] The heavy anions, Cl^-, Br^- and I^-, contributed to shift changes at ^{1}H atoms of around 1 ppm, and noted that atoms closer to the halide were more greatly affected. They urged further work to be done on the HALA effect in the absence of covalent bonds.

Vícha *et al.* looked at a similar set of compounds: the 4-dimethylaminopyridinium halides $[DMAPH]^+X^-$ (X = Cl, Br, I).[213] These salts have a similar hydrogen bond interaction between the NH group and the halide ion. They computed the NMR shieldings using the GIPAW method in the crystal, and then considered hybrid functional and SOC corrections for the isolated molecule. They found that the H near the heavy atoms experienced shifts of up to around 0.5 ppm in the iodide case. They also noted that the bromide and chloride induce H shifts but to a smaller extent, keeping in line with the HALA trends seen for covalent interactions.

Following these studies, we investigate the 4-dimethylaminopyridinium halides with the newly implemented FR GIPAW approach. This method has the benefit of being able to compute the NMR shieldings for the crystal, without the need for molecular corrections.

Structures

The structures of the three $[DMAPH]^+X^-$ salts are given in figure 6.16 with their hydrogen bond distances labelled. Due to the sizes of the ions, the distances increase with respect to the halide down the group. Figure 6.17 shows a three-dimensional view for the I^- salt, illustrating the repeating crystal structure and the spatial interactions between the pyridinium and iodide ions. From this, we can see that the I^- ion is nested between the pyridinium layers, as a result of their π-stacking.

Keeping in line with the study by Vícha *et al.*, we also consider the hydrated structure of $[DMAPH]^+Cl^-\cdot H_2O$. They note that, due to the strong hygroscopic nature of $[DMAPH]^+Cl^-$, the sample recrystallised as a monohydrate during the experimental process. They were able to obtain experimental ^{1}H shifts for the NH

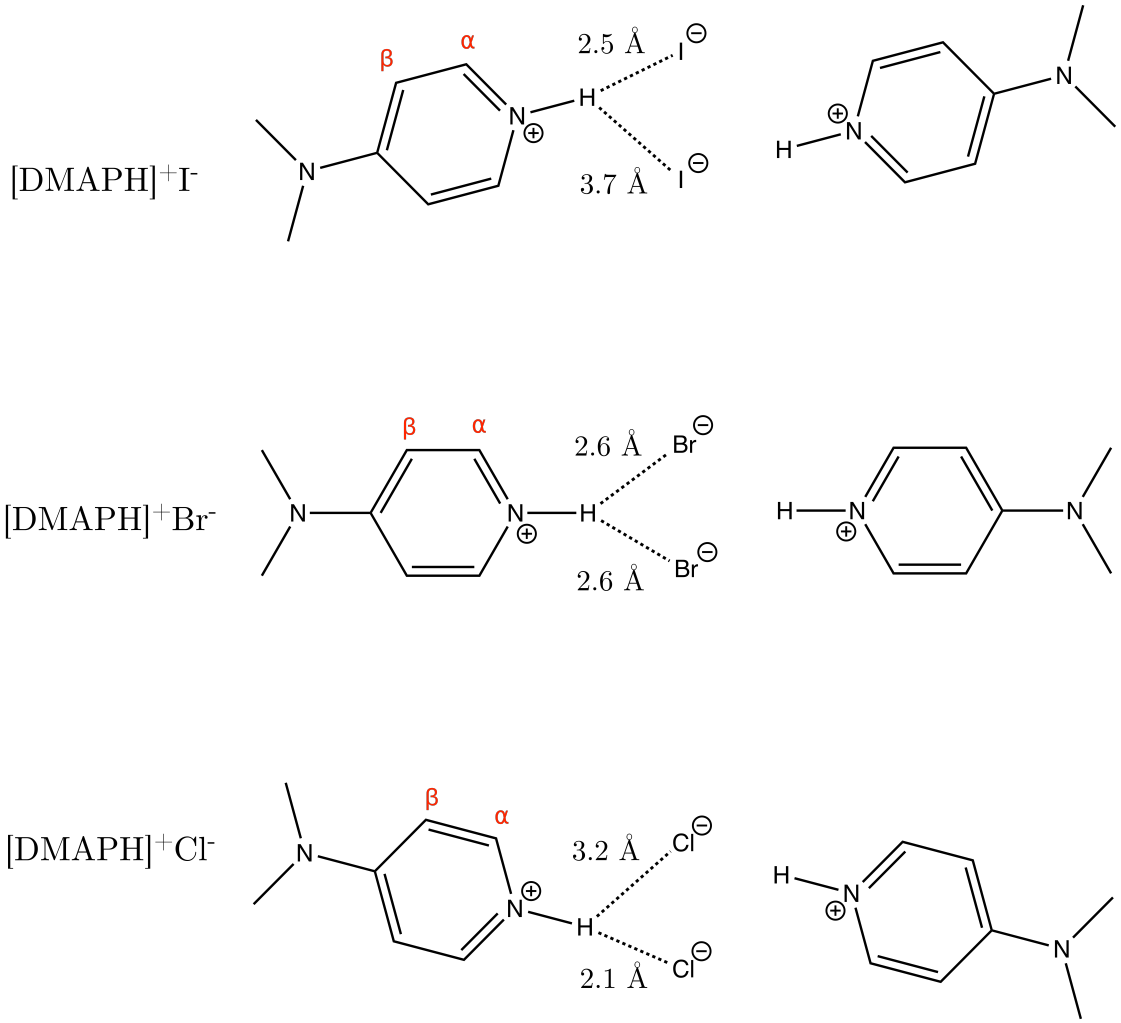


Figure 6.16: Molecular structures of the 4-dimethylaminopyridinium halides with the hydrogen bond distances labelled in Å. Labels of H^{α} and H^{β}, given in red next to their respective C atoms, are given to the H atoms in the aromatic ring.

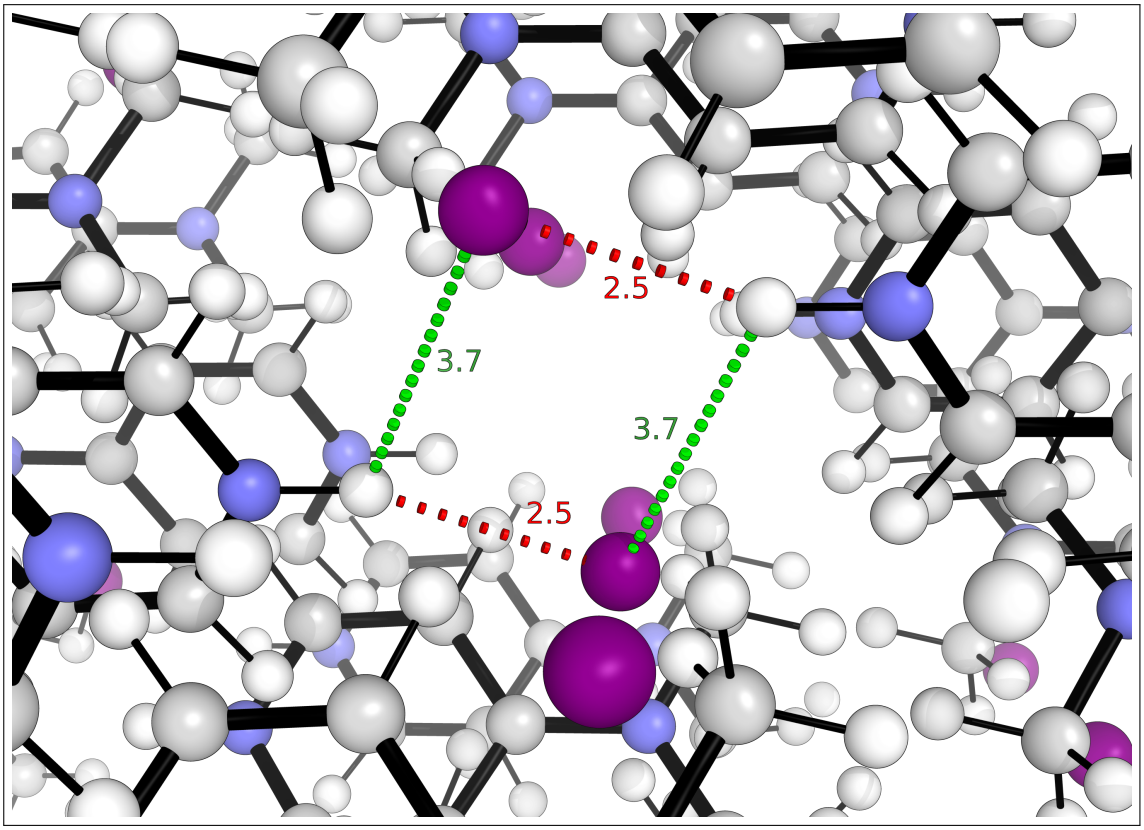


Figure 6.17: Structure of the molecular crystal 4-dimethylaminopyridinium iodide. Distances in Å of the H atom in the NH group to the I ion are shown. The iodide is nested between the pyridinium stacks at a slight offset, meaning there are two hydrogen bond distances of 2.5 Å in red and 3.7 Å in green.

group in both structures, but only the other H atoms for the hydrated form. We consider both forms for this study to better compare results.

Calculations

All four $[DMAPH]^+X^-$ structures followed that of Vícha *et al.*, and were subjected to geometry optimisations using the PBE functional, SR solver and latest set of on-the-fly USPs. All calculations reported the structures as converged, and were subsequently used for all NMR calculations.

Sets of NMR calculations were performed using the Schrödinger (NR), Koelling-Harmon (SR) and Dirac (FR) solvers. Calculation of the orbital term was performed for all three, but only the latter required the computation of the spin term, where a 2 kT external magnetic field was used for the finite-field method. All NMR calculations used the same set of relativistic NCPs. These runs were performed for both the LDA and PBE exchange-correlation functionals, however, the $[DMAPH]^+Br^-$ salt had problems with convergence in the PBE FR calculations. As previously discussed, this was most likely due to the locally collinear implementation of the exchange-correlation functionals for non-collinear magnetism,[151] discussed in section 4.2. The LDA results were used for the remainder of the study.

Results

In figure 6.18, we plot the SR calculation results for LDA against the experimental values obtained from reference [213]. We have omitted the ^1H chemical shielding values of the NH groups from the line of best fit, which has a slope of -0.995 and intercept of 29.52 ppm. The salts with Br and Cl halides performed better than the I halide salt, of which, had a difference between itself and the fitted line of around 1 ppm. The NR solver reports similar values of a slope of -0.996 and intercept of 29.53 ppm.

Table 6.5 reports the break down of the individual contributions to the chemical shielding using the FR approach for all of the $[DMAPH]^+X^-$ compounds. As expected, we notice that the highest contributing spin term is the Z-FC, especially for the heavier halides. As before, we do not see the correct magnitude that

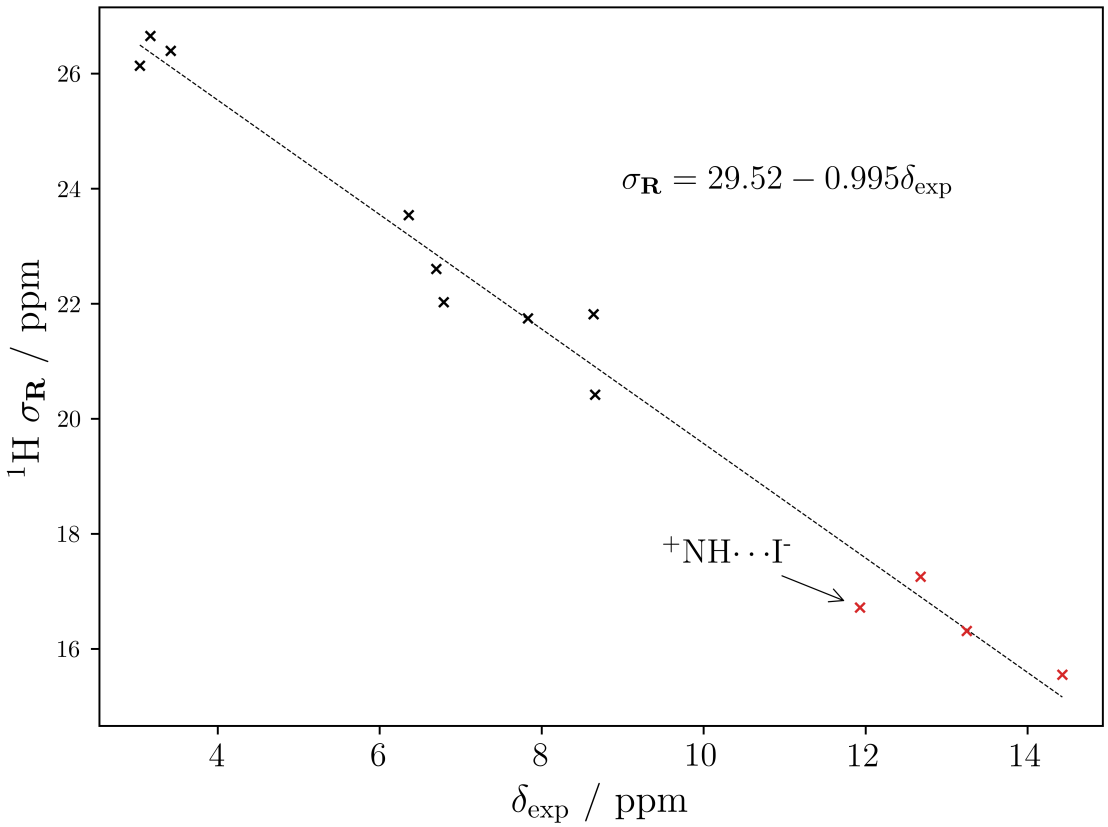


Figure 6.18: Correlation between calculated ^{1}H chemical shielding values against experimental shifts for the 4-dimethylaminopyridinium halides. Scalar-relativistic calculations were performed with the LDA exchange-correlation functional. The NH values were excluded from the line of best fit, of which, had slope -0.995 and intercept 29.52 ppm.

Table 6.5: ^{1}H chemical shielding values for the 4-dimethylaminopyridinium halides from fully-relativistic calculations, broken down into the orbital term, 6.56, and the spin contributions from equations 6.64 and 6.68. The SD-aug term is 0 for hydrogen. The exchange-correlation functional was LDA. Experimental values from reference [213]. Our shieldings, $\sigma_{\mathbf{R}}$, are converted to shifts, $\delta_{\mathbf{R}}$, with the equation in figure 6.18. The H^{α} and H^{β} positions are given in figure 6.16. The hy. Cl^- and an. Cl^- entries are the hydrated and anhydrous forms of $[DMAPH]^+Cl^-$, respectively.

Halide ion & H atom		Chemical shielding / ppm						
		$\sigma_{\mathbf{R}}^{\text{orb}}$	$\sigma_{\mathbf{R}}^{\text{SD-bare}}$	$\sigma_{\mathbf{R}}^{\text{Z-FC}}$	$\sigma_{\mathbf{R}}^{\text{spin}}$	$\sigma_{\mathbf{R}}$	$\delta_{\mathbf{R}}$	exp.
I^-	NH	16.72	0.0009	0.0691	0.0700	16.79	12.81	11.93
	H^{α}	21.82	0.0012	-0.0076	-0.0064	21.81	7.82	8.64
	H^{β}	22.60	0.0010	0.0066	0.0076	22.61	7.02	6.70
	CH_3	26.65	0.0010	-0.0060	-0.0051	26.65	3.01	3.17
Br^-	NH	17.26	-0.0002	0.0071	0.0069	17.26	12.34	12.68
	H^{α}	20.42	-0.0003	-0.0018	-0.0020	20.42	9.21	8.66
	H^{β}	22.03	0.0000	0.0004	0.0004	22.03	7.60	6.79
	CH_3	26.14	0.0003	-0.0020	-0.0017	26.14	3.51	3.04
hy. Cl^-	NH	16.31	0.0000	0.0007	0.0007	16.31	13.29	13.25
	H^{α}	21.75	0.0000	0.0000	0.0000	21.75	7.88	7.83
	H^{β}	23.54	0.0000	0.0000	0.0001	23.54	6.10	6.36
	CH_3	26.40	0.0000	0.0000	0.0000	26.40	3.25	3.42
an. Cl^-	NH	15.55	0.0000	0.0008	0.0009	15.55	14.04	14.43
	H^{α}	21.83	0.0000	0.0000	0.0000	21.83	7.80	-
	H^{β}	21.50	0.0000	0.0001	0.0001	21.50	8.12	-
	CH_3	27.04	0.0000	0.0000	0.0000	27.04	2.62	-

we expect, but observe the trend found by Vícha *et al.* that the heavier halide constitutes a greater spin chemical shift change at the NH group. This highlights that a polarisation of the spin density at the ^{1}H nucleus occurs via the aforementioned through-space interaction. The other H atoms realise some level of polarisation for the heavier halides, but of approximately an order of magnitude less. We convert our chemical shielding values from calculation, $\sigma_{\mathbf{R}}$, to shifts, $\delta_{\mathbf{R}}$, with the equation in figure 6.18. The effects of SOC would be expected to give $\sigma_{\mathbf{R}}^{\text{spin}} \simeq 1$ ppm to bring the shift value in line with that found by experiment. The reasons for the possible lower values obtained were discussed in 6.6.1 and 6.6.2. Vícha *et al.* find spin-orbit shifts of -0.05 ppm and -0.39 ppm for the bromide and iodide salts, respectively. Notably, these are of the opposite sign to our findings.

One other feature of the results, that emphasises the critical importance of the spin-orbit interaction, is that the spin shielding is higher for the heavier halides, despite them having greater hydrogen bond distances to the NH group. This highlights that, for this set of compounds at least, the increasing effect of SOC down the periodic table has a greater impact on the electronic structure than the bonding geometry. This emphasises that the inclusion of SOC for compounds with heavy elements is just as significant as the well-known sensitivity of NMR to the system geometry.

Another feature worth note, is that through-space effects are very commonly found in the solid-state. Molecular crystals often possess weakly interacting ions that exhibit features discussed here, which only re-emphasises the importance of the progression of this work and theory.

7

Conclusions and future work

In this thesis, the planewave pseudopotential method was extended for fully-relativistic calculations of solid-state NMR parameters, namely the electric field gradient and magnetic shielding. The current capabilities and limitations were outlined in detail, and the implementation of the extended approach was discussed with benchmark calculations and case studies of appropriate systems.

This comprised of outlining the generalisation of the projector augmented-wave method for spinor wavefunctions, as discussed by dal Corso and Conte.[144] This allowed the extension of the calculation of the electric field gradient tensor, previously outlined by Profeta *et al.*[57]. We then extended the gauge-including projector augmented-wave method[6] for spinors, to allow for the calculation of the orbital NMR term. Finally, we introduced the new spin shielding terms, that also utilised the extended PAW method, that arise only when fully-relativistic effects are performed.

With the new formalisms, the EFG parameters of ^{133}Cs and ^{209}Bi solid-state compounds were investigated. We proposed an alternative nuclear quadrupole moment for the latter, of which, supported highly accurate recent calculations by other authors. Investigations into paramagnetic and metallic materials are suggested as future work, which do not require any further considerations to the implementation presented here.

The extended GIPAW theory allowed for the study of the magnetic shielding in the L-cysteine and 4-dimethylaminopyridinium halide solid-state molecular crystals. We found that the method indicates confidently the light atoms most affected by the spin-orbit effect from the heavy atoms, but did not account fully for the magnitude of the interaction. Possible causes for this, including missing polarisation effects from the heavy atom core electrons, were proposed and discussed. It is possible that a theory beyond the frozen core approximation could be required, which may be solved by the application of magnetic fields to the core electrons, generating spin-dependent pseudopotentials. It was highlighted that current approaches, of which, calculate the spin-orbit contribution via a molecular correction method, lack the consideration of through-space effects present in solids. These methods also only work for molecular crystals, and would not be able to study inorganic solids that are not comprised of repeating molecular fragments. These points emphasise the importance of the work presented here, and prompt further study for a complete method.

One overarching requirement to extend this work is for the generation of on-the-fly fully-relativistic ultra-soft pseudopotentials in the CASTEP package. This would allow for higher accuracy calculations, at lower computational cost. This is particularly important for the calculations discussed in this work, due to their increased time and memory requirements due to two-spinor wavefunctions and loss of spatial and temporal symmetries.

Other future work of note is the extension of the locally collinear approach to non-collinear magnetism in the evaluation of the exchange-correlation functionals, which has been outlined by Pu *et al.*.[157] This would allow for higher order functionals to be used more robustly in achieving the ground-state electronic structure of fully-relativistic calculations. Extension of the Hubbard model would also allow for a wider scope of solids to be considered, particularly those across the d and f blocks.[218] Naturally, solid-state compounds contain a large number of these elements and may require the on-site DFT+U term for accurate modelling of the physics involved. Finally, the effects of temperature are an important consideration in any NMR study, and can often be the highest factor of error in many cases.

Path integral methods, to account for nuclear quantum effects, have been utilised by the community to better model experiment,[219] and may be an interesting consideration to improve on computational errors in the current models.

Appendices

A
Notation

Contents

A.1 Spinors 165
A.2 Pauli vector matrix elements, $\boldsymbol{\sigma}^{\sigma,\sigma'}$ 167

A.1 Spinors

For complete clarity, we outline here the notation subtleties of the use of spinors. In this text, all spinor wavefunctions typically use capitalised versions of their scalar counterparts. For example, spinor wavefunctions are denoted with $|\Psi\rangle$, whereas scalar use $|\psi\rangle$. Spinor projectors use $|P\rangle$, whereas scalar use $|p\rangle$. Spinor, atomic wavefunctions use $|\Phi\rangle$ but scalar $|\phi\rangle$. The pseudised versions of quantities follow the same pattern but with tilde decorations. When we refer to a single component of these spinors, we use the index σ or σ'. For example, spinor wavefunctions look like,

$$|\Psi\rangle = \begin{pmatrix} |\Psi^1\rangle \\ |\Psi^2\rangle \end{pmatrix}, \tag{A.1}$$

where we can write a specific element of the right-hand side as $|\Psi^\sigma\rangle$. Here, σ could be 1 or 2. One could think of this object as acting just like a scalar wavefunction itself.

Operators in the spinor basis will be written in calligraphic form; that is $\mathcal{O}$ as opposed to the scalar O, for example. These are 2×2 matrices, and look like,

$$\mathcal{O} = \begin{pmatrix} \mathcal{O}^{1,1} & \mathcal{O}^{1,2} \\ \mathcal{O}^{2,1} & \mathcal{O}^{2,2} \end{pmatrix}, \tag{A.2}$$

where we can write a specific element of the matrix on the right-hand side as $\mathcal{O}^{\sigma,\sigma'}$. Again, σ and σ' can equal 1 or 2.

The expectation value of these matrix operators looks like,

$$\langle\Psi|\mathcal{O}|\Psi\rangle = \begin{pmatrix} \langle\Psi^1| & \langle\Psi^2| \end{pmatrix} \begin{pmatrix} \mathcal{O}^{1,1} & \mathcal{O}^{1,2} \\ \mathcal{O}^{2,1} & \mathcal{O}^{2,2} \end{pmatrix} \begin{pmatrix} |\Psi^1\rangle \\ |\Psi^2\rangle \end{pmatrix}, \tag{A.3}$$

which can be expanded using the usual matrix operations,

$$\langle\Psi|\mathcal{O}|\Psi\rangle = \langle\Psi^1|\mathcal{O}^{1,1}|\Psi^1\rangle + \langle\Psi^1|\mathcal{O}^{1,2}|\Psi^2\rangle + \langle\Psi^2|\mathcal{O}^{2,1}|\Psi^1\rangle + \langle\Psi^2|\mathcal{O}^{2,2}|\Psi^2\rangle. \tag{A.4}$$

This is simply four of the usual scalar expectation values summed together. We can write this compactly as,

$$\langle\Psi|\mathcal{O}|\Psi\rangle = \sum_{\sigma,\sigma'} \langle\Psi^\sigma|\mathcal{O}^{\sigma,\sigma'}|\Psi^{\sigma'}\rangle, \tag{A.5}$$

which is present throughout the text.

One final note is that of the expectation value of scalar operators, like O, under spinor wavefunctions, like $|\Psi\rangle$. For example,

$$\langle\Psi|O|\Psi\rangle. \tag{A.6}$$

Notice that we have a scalar operator, O, but a two-component spinor wavefunction, $|\Psi\rangle$. The above equation actually corresponds to the quantity,

$$\langle\Psi|O\mathbb{1}_2|\Psi\rangle, \tag{A.7}$$

where $\mathbb{1}_2$ is the 2×2 matrix identity,

$$\mathbb{1}_2 = \begin{pmatrix} 1 & 0 \\ 0 & 1 \end{pmatrix}. \tag{A.8}$$

Equation A.6 is therefore a simplification of the notation, and is equivalent to,

$$\langle\Psi| \begin{pmatrix} O & 0 \\ 0 & O \end{pmatrix} |\Psi\rangle, \tag{A.9}$$

which is evaluated in exactly the same way as equation A.4, but with the off-diagonal elements making no contribution.

A.2 Pauli vector matrix elements, $\boldsymbol{\sigma}^{\sigma,\sigma'}$

The Pauli vector, $\boldsymbol{\sigma}$, is,

$$\boldsymbol{\sigma} = \begin{pmatrix} \sigma_1 \\ \sigma_2 \\ \sigma_3 \end{pmatrix}, \tag{A.10}$$

where the Pauli matrices are,

$$\sigma_1 = \begin{pmatrix} 0 & 1 \\ 1 & 0 \end{pmatrix}, \qquad \sigma_2 = \begin{pmatrix} 0 & -i \\ i & 0 \end{pmatrix}, \qquad \sigma_3 = \begin{pmatrix} 1 & 0 \\ 0 & -1 \end{pmatrix}. \tag{A.11}$$

The notation, $\boldsymbol{\sigma}^{\sigma,\sigma'}$, denotes the three-vector that contains the element from row σ and column σ' of each Pauli matrix,

$$\boldsymbol{\sigma}^{\sigma,\sigma'} \equiv \begin{pmatrix} \sigma_1^{\sigma,\sigma'} \\ \sigma_2^{\sigma,\sigma'} \\ \sigma_3^{\sigma,\sigma'} \end{pmatrix}. \tag{A.12}$$

Both σ and σ' can take the value of 1 or 2.

For example, suppose $\sigma = 2$ and $\sigma' = 1$. The value in the 2$^{\text{nd}}$ row and 1$^{\text{st}}$ column in σ_1 is 1. For σ_2 it is i and in σ_3 it is 0. Therefore,

$$\boldsymbol{\sigma}^{2,1} = \begin{pmatrix} \sigma_1^{2,1} \\ \sigma_2^{2,1} \\ \sigma_3^{2,1} \end{pmatrix} = \begin{pmatrix} 1 \\ i \\ 0 \end{pmatrix}. \tag{A.13}$$

For the magnetisation equation,

$$\mathbf{m}(\mathbf{r}) = \frac{1}{2} \sum_{\sigma,\sigma'} n^{\sigma,\sigma'}(\mathbf{r})\, \boldsymbol{\sigma}^{\sigma,\sigma'}, \tag{A.14}$$

we can explicitly perform the summation,

$$\mathbf{m}(\mathbf{r}) = \frac{1}{2} n^{1,1}(\mathbf{r}) \begin{pmatrix} \sigma_1^{1,1} \\ \sigma_2^{1,1} \\ \sigma_3^{1,1} \end{pmatrix} + \frac{1}{2} n^{1,2}(\mathbf{r}) \begin{pmatrix} \sigma_1^{1,2} \\ \sigma_2^{1,2} \\ \sigma_3^{1,2} \end{pmatrix} + \frac{1}{2} n^{2,1}(\mathbf{r}) \begin{pmatrix} \sigma_1^{2,1} \\ \sigma_2^{2,1} \\ \sigma_3^{2,1} \end{pmatrix} + \frac{1}{2} n^{2,2}(\mathbf{r}) \begin{pmatrix} \sigma_1^{2,2} \\ \sigma_2^{2,2} \\ \sigma_3^{2,2} \end{pmatrix}, \tag{A.15}$$

and then inserting the matrix elements as described above gives,

$$\mathbf{m}(\mathbf{r}) = \frac{1}{2} \begin{pmatrix} n^{1,2}(\mathbf{r}) + n^{2,1}(\mathbf{r}) \\ -i[n^{1,2}(\mathbf{r}) - n^{2,1}(\mathbf{r})] \\ n^{1,1}(\mathbf{r}) - n^{2,2}(\mathbf{r}) \end{pmatrix}. \tag{A.16}$$

B

The rotation matrix, $\mathbf{U}^{\ell}$

Contents

B.1 Spherical coordinate system 169
B.2 Complex spherical harmonics 170
B.3 CASTEP choice of real spherical harmonics 171
B.4 Common choice of real spherical harmonics 173

For an excellent overview of spherical harmonics and their transformations, see reference [220].

B.1 Spherical coordinate system

We define the spherical coordinates as,

$$x = r\cos\varphi\sin\theta, \tag{B.1}$$

$$y = r\sin\varphi\sin\theta, \tag{B.2}$$

$$z = r\cos\theta, \tag{B.3}$$

with φ and θ the azimuth and inclination angles, respectively.

B.2 Complex spherical harmonics

The complex spherical harmonics are the eigenfunctions of the orbital angular momentum. Up to $\ell = 3$, they are,

$$
\begin{aligned}
Y_0^0(\theta,\varphi) &= \frac{1}{2}\frac{1}{\sqrt{\pi}}, \\
Y_1^{-1}(\theta,\varphi) &= \frac{1}{2}\sqrt{\frac{3}{2\pi}}\cdot\frac{(x-iy)}{r}, \\
Y_1^0(\theta,\varphi) &= \frac{1}{2}\sqrt{\frac{3}{\pi}}\cdot\frac{z}{r}, \\
Y_1^1(\theta,\varphi) &= -\frac{1}{2}\sqrt{\frac{3}{2\pi}}\cdot\frac{(x+iy)}{r}, \\
Y_2^{-2}(\theta,\varphi) &= \frac{1}{4}\sqrt{\frac{15}{2\pi}}\cdot\frac{(x-iy)^2}{r^2}, \\
Y_2^{-1}(\theta,\varphi) &= \frac{1}{2}\sqrt{\frac{15}{2\pi}}\cdot\frac{(x-iy)\cdot z}{r^2}, \\
Y_2^0(\theta,\varphi) &= \frac{1}{4}\sqrt{\frac{5}{\pi}}\cdot\frac{(3z^2-r^2)}{r^2}, \\
Y_2^1(\theta,\varphi) &= -\frac{1}{2}\sqrt{\frac{15}{2\pi}}\cdot\frac{(x+iy)\cdot z}{r^2}, \\
Y_2^2(\theta,\varphi) &= \frac{1}{4}\sqrt{\frac{15}{2\pi}}\cdot\frac{(x+iy)^2}{r^2}, \\
Y_3^{-3}(\theta,\varphi) &= \frac{1}{8}\sqrt{\frac{35}{\pi}}\cdot\frac{(x-iy)^3}{r^3}, \\
Y_3^{-2}(\theta,\varphi) &= \frac{1}{4}\sqrt{\frac{105}{2\pi}}\cdot\frac{(x-iy)^2\cdot z}{r^3}, \\
Y_3^{-1}(\theta,\varphi) &= \frac{1}{8}\sqrt{\frac{21}{\pi}}\cdot\frac{(x-iy)\cdot(5z^2-r^2)}{r^3}, \\
Y_3^0(\theta,\varphi) &= \frac{1}{4}\sqrt{\frac{7}{\pi}}\cdot\frac{(5z^3-3zr^2)}{r^3}, \\
Y_3^1(\theta,\varphi) &= -\frac{1}{8}\sqrt{\frac{21}{\pi}}\cdot\frac{(x+iy)\cdot(5z^2-r^2)}{r^3}, \\
Y_3^2(\theta,\varphi) &= \frac{1}{4}\sqrt{\frac{105}{2\pi}}\cdot\frac{(x+iy)^2\cdot z}{r^3}, \\
Y_3^3(\theta,\varphi) &= -\frac{1}{8}\sqrt{\frac{35}{\pi}}\cdot\frac{(x+iy)^3}{r^3}.
\end{aligned}
$$

B.3 CASTEP choice of real spherical harmonics

In the self-consistent field cycle of CASTEP, we use a slightly different choice of real harmonics than what is found in most texts,

$$Y_{\ell,m}(\theta,\varphi) = \begin{cases} \frac{(-i)^m}{\sqrt{2}}\left[Y_\ell^m + Y_\ell^{-m}\right] & m > 0, \\ Y_\ell^m & m = 0, \\ \frac{i(i)^m}{\sqrt{2}}\left[Y_\ell^m - Y_\ell^{-m}\right] & m < 0. \end{cases} \tag{B.4}$$

Note that the *superscript* m denotes a complex spherical harmonic, and *subscript* m a real.

The unitary $\mathbf{U}^{\ell}$ matrix, that expands the complex form into the real form above, is,

$$\mathbf{U}^{\ell} = \begin{array}{c} {}^{m}_{\downarrow}\backslash m' \rightarrow \\ -\ell \\ \vdots \\ -2 \\ -1 \\ 0 \\ +1 \\ +2 \\ \vdots \\ +\ell \end{array} \begin{array}{c} \begin{array}{ccccccccc} -\ell & \cdots & -2 & -1 & 0 & +1 & +2 & \cdots & +\ell \end{array} \\ \begin{pmatrix} \frac{(-i)i^{\ell}}{\sqrt{2}} & \cdots & 0 & 0 & 0 & 0 & 0 & \cdots & \frac{i^{\ell}}{\sqrt{2}} \\ \vdots & & \vdots & \vdots & \vdots & \vdots & \vdots & & \vdots \\ 0 & \cdots & \frac{(-i)i^{2}}{\sqrt{2}} & 0 & 0 & 0 & \frac{i^{2}}{\sqrt{2}} & \cdots & 0 \\ 0 & \cdots & 0 & \frac{(-i)i^{1}}{\sqrt{2}} & 0 & \frac{i^{1}}{\sqrt{2}} & 0 & \cdots & 0 \\ 0 & \cdots & 0 & 0 & 1 & 0 & 0 & \cdots & 0 \\ 0 & \cdots & 0 & \frac{(i)i^{1}}{\sqrt{2}} & 0 & \frac{i^{1}}{\sqrt{2}} & 0 & \cdots & 0 \\ 0 & \cdots & \frac{(i)i^{2}}{\sqrt{2}} & 0 & 0 & 0 & \frac{i^{2}}{\sqrt{2}} & \cdots & 0 \\ \vdots & & \vdots & \vdots & \vdots & \vdots & \vdots & & \vdots \\ \frac{(i)i^{\ell}}{\sqrt{2}} & \cdots & 0 & 0 & 0 & 0 & 0 & \cdots & \frac{i^{\ell}}{\sqrt{2}} \end{pmatrix} \end{array}. \tag{B.5}$$

The real harmonics defined by equation B.4, up to $\ell = 3$, are,

$$
\begin{aligned}
Y_{0,0}(\theta,\varphi) = s &= \frac{1}{2}\frac{1}{\sqrt{\pi}}, \\
\\
Y_{1,-1}(\theta,\varphi) = p_x &= \frac{1}{2}\sqrt{\frac{3}{\pi}}\cdot\frac{x}{r}, \\
Y_{1,0}(\theta,\varphi) = p_z &= \frac{1}{2}\sqrt{\frac{3}{\pi}}\cdot\frac{z}{r}, \\
Y^{1}_{1,1}(\theta,\varphi) = p_y &= -\frac{1}{2}\sqrt{\frac{3}{\pi}}\cdot\frac{y}{r}, \\
\\
Y_{2,-2}(\theta,\varphi) = d_{xy} &= -\frac{1}{2}\sqrt{\frac{15}{\pi}}\cdot\frac{x\cdot y}{r^2}, \\
Y_{2,-1}(\theta,\varphi) = d_{xz} &= \frac{1}{2}\sqrt{\frac{15}{\pi}}\cdot\frac{x\cdot z}{r^2}, \\
Y_{2,0}(\theta,\varphi) = d_{z^2} &= \frac{1}{4}\sqrt{\frac{5}{\pi}}\cdot\frac{3z^2-r^2}{r^2}, \\
Y_{2,1}(\theta,\varphi) = d_{yz} &= -\frac{1}{2}\sqrt{\frac{15}{\pi}}\cdot\frac{y\cdot z}{r^2}, \\
Y_{2,2}(\theta,\varphi) = d_{x^2-y^2} &= -\frac{1}{4}\sqrt{\frac{15}{\pi}}\cdot\frac{x^2-y^2}{r^2}, \\
\\
Y_{3,-3}(\theta,\varphi) = f_{x(x^2-3y^2)} &= -\frac{1}{4}\sqrt{\frac{35}{2\pi}}\cdot\frac{x\cdot(x^2-3y^2)}{r^3}, \\
Y_{3,-2}(\theta,\varphi) = f_{xyz} &= -\frac{1}{2}\sqrt{\frac{105}{\pi}}\cdot\frac{x\cdot y\cdot z}{r^3}, \\
Y_{3,-1}(\theta,\varphi) = f_{xz^2} &= \frac{1}{4}\sqrt{\frac{21}{2\pi}}\cdot\frac{x\cdot(5z^2-r^2)}{r^3}, \\
Y_{3,0}(\theta,\varphi) = f_{z^3} &= \frac{1}{4}\sqrt{\frac{7}{\pi}}\cdot\frac{z\cdot(5z^2-3r^2)}{r^3}, \\
Y_{3,1}(\theta,\varphi) = f_{yz^2} &= -\frac{1}{4}\sqrt{\frac{21}{2\pi}}\cdot\frac{y\cdot(5z^2-r^2)}{r^3}, \\
Y_{3,2}(\theta,\varphi) = f_{(x^2-y^2)z} &= -\frac{1}{4}\sqrt{\frac{105}{\pi}}\cdot\frac{(x^2-y^2)\cdot z}{r^3}, \\
Y_{3,3}(\theta,\varphi) = f_{(3x^2-y^2)y} &= \frac{1}{4}\sqrt{\frac{35}{2\pi}}\cdot\frac{(3x^2-y^2)\cdot y}{r^3}.
\end{aligned}
$$

B.4 Common choice of real spherical harmonics

A common choice of real spherical harmonics is,

$$Y_{\ell,m}(\theta,\varphi) = \begin{cases} \frac{1}{\sqrt{2}}\left[(-1)^m Y_\ell^m + Y_\ell^{-m}\right] & m > 0, \\ Y_\ell^m & m = 0, \\ \frac{i}{\sqrt{2}}\left[Y_\ell^m - (-1)^m Y_\ell^{-m}\right] & m < 0. \end{cases} \tag{B.6}$$

Note that the *superscript* m denotes a complex spherical harmonic, and *subscript* m a real.

The unitary $\mathbf{U}^\ell$ matrix, that expands the complex form into the real form above, is,

$$\mathbf{U}^\ell = \begin{array}{c} {\scriptstyle m \downarrow \backslash m' \rightarrow} \\ -\ell \\ \vdots \\ -2 \\ -1 \\ 0 \\ +1 \\ +2 \\ \vdots \\ +\ell \end{array} \begin{array}{c} \begin{array}{ccccccccc} -\ell & \cdots & -2 & -1 & 0 & +1 & +2 & \cdots & +\ell \end{array} \\ \begin{pmatrix} \frac{-i}{\sqrt{2}} & \cdots & 0 & 0 & 0 & 0 & 0 & \cdots & \frac{1}{\sqrt{2}} \\ \vdots & & \vdots & \vdots & \vdots & \vdots & \vdots & & \vdots \\ 0 & \cdots & \frac{-i}{\sqrt{2}} & 0 & 0 & 0 & \frac{1}{\sqrt{2}} & \cdots & 0 \\ 0 & \cdots & 0 & \frac{-i}{\sqrt{2}} & 0 & \frac{1}{\sqrt{2}} & 0 & \cdots & 0 \\ 0 & \cdots & 0 & 0 & 1 & 0 & 0 & \cdots & 0 \\ 0 & \cdots & 0 & \frac{i(-1)^1}{\sqrt{2}} & 0 & \frac{(-1)^1}{\sqrt{2}} & 0 & \cdots & 0 \\ 0 & \cdots & \frac{i(-1)^2}{\sqrt{2}} & 0 & 0 & 0 & \frac{(-1)^2}{\sqrt{2}} & \cdots & 0 \\ \vdots & & \vdots & \vdots & \vdots & \vdots & \vdots & & \vdots \\ \frac{i(-1)^\ell}{\sqrt{2}} & \cdots & 0 & 0 & 0 & 0 & 0 & \cdots & \frac{(-1)^\ell}{\sqrt{2}} \end{pmatrix} \end{array}. \tag{B.7}$$

The real harmonics defined by equation B.6, up to $\ell = 3$, are,

$$
\begin{aligned}
Y_{0,0}(\theta,\varphi) = s &= \frac{1}{2}\frac{1}{\sqrt{\pi}}, \\
\\
Y_{1,-1}(\theta,\varphi) = p_y &= \frac{1}{2}\sqrt{\frac{3}{\pi}}\cdot\frac{y}{r}, \\
Y_{1,0}(\theta,\varphi) = p_z &= \frac{1}{2}\sqrt{\frac{3}{\pi}}\cdot\frac{z}{r}, \\
Y^1_{1,1}(\theta,\varphi) = p_x &= \frac{1}{2}\sqrt{\frac{3}{\pi}}\cdot\frac{x}{r}, \\
\\
Y_{2,-2}(\theta,\varphi) = d_{xy} &= \frac{1}{2}\sqrt{\frac{15}{\pi}}\cdot\frac{x\cdot y}{r^2}, \\
Y_{2,-1}(\theta,\varphi) = d_{yz} &= \frac{1}{2}\sqrt{\frac{15}{\pi}}\cdot\frac{y\cdot z}{r^2}, \\
Y_{2,0}(\theta,\varphi) = d_{z^2} &= \frac{1}{4}\sqrt{\frac{5}{\pi}}\cdot\frac{3z^2-r^2}{r^2}, \\
Y_{2,1}(\theta,\varphi) = d_{xz} &= \frac{1}{2}\sqrt{\frac{15}{\pi}}\cdot\frac{x\cdot z}{r^2}, \\
Y_{2,2}(\theta,\varphi) = d_{x^2-y^2} &= \frac{1}{4}\sqrt{\frac{15}{\pi}}\cdot\frac{x^2-y^2}{r^2}, \\
\\
Y_{3,-3}(\theta,\varphi) = f_{(3x^2-y^2)y} &= \frac{1}{4}\sqrt{\frac{35}{2\pi}}\cdot\frac{(3x^2-y^2)\cdot y}{r^3}, \\
Y_{3,-2}(\theta,\varphi) = f_{xyz} &= \frac{1}{2}\sqrt{\frac{105}{\pi}}\cdot\frac{x\cdot y\cdot z}{r^3}, \\
Y_{3,-1}(\theta,\varphi) = f_{yz^2} &= \frac{1}{4}\sqrt{\frac{21}{2\pi}}\cdot\frac{y\cdot(5z^2-r^2)}{r^3}, \\
Y_{3,0}(\theta,\varphi) = f_{z^3} &= \frac{1}{4}\sqrt{\frac{7}{\pi}}\cdot\frac{z\cdot(5z^2-3r^2)}{r^3}, \\
Y_{3,1}(\theta,\varphi) = f_{xz^2} &= \frac{1}{4}\sqrt{\frac{21}{2\pi}}\cdot\frac{x\cdot(5z^2-r^2)}{r^3}, \\
Y_{3,2}(\theta,\varphi) = f_{(x^2-y^2)z} &= \frac{1}{4}\sqrt{\frac{105}{\pi}}\cdot\frac{(x^2-y^2)\cdot z}{r^3}, \\
Y_{3,3}(\theta,\varphi) = f_{x(x^2-3y^2)} &= \frac{1}{4}\sqrt{\frac{35}{2\pi}}\cdot\frac{x\cdot(x^2-3y^2)}{r^3}.
\end{aligned}
$$

C

The $\mathbf{C}_{\alpha\beta}$ vector

Contents

C.1 Definition 175
C.2 Spherical operator form 176

C.1 Definition

A spherical tensor operator element, $\Omega_{\alpha\beta}$, with indices α and β that run over the Cartesian axes, may be expanded,

$$\Omega_{\alpha\beta} = \delta_{\alpha\beta} - \kappa\frac{r_\alpha r_\beta}{r^2} = \begin{cases} \sqrt{\dfrac{2\pi}{15}}\displaystyle\sum_{q=-2}^{2} C^q_{\alpha\beta} Y^q_2(\theta,\varphi) + \dfrac{4\sqrt{\pi}}{3}\delta_{\alpha\beta} Y^0_0(\theta,\varphi) & \kappa = 1, \\ \sqrt{\dfrac{6\pi}{5}}\displaystyle\sum_{q=-2}^{2} C^q_{\alpha\beta} Y^q_2(\theta,\varphi) & \kappa = 3, \end{cases} \tag{C.1}$$

where $Y^m_\ell(\theta,\varphi)$ are complex spherical harmonics. $\mathbf{C}_{\alpha\beta}$ is a vector of coefficients and is given below. For the operators found in this work, κ takes the values of 1 or 3. The coordinate system is,

$$r_1 = x = r\sin\theta\cos\varphi, \tag{C.2}$$

$$r_2 = y = r\sin\theta\sin\varphi, \tag{C.3}$$

$$r_3 = z = r\cos\theta. \tag{C.4}$$

C.2 Spherical operator form

The expansion vector, $\mathbf{C}_{\alpha\beta}$, is given by,

$$\mathbf{C}_{\alpha\beta} = \begin{pmatrix} [\delta_{\alpha\beta}(2\alpha-3) - \delta_{1\gamma}(1-\delta_{3\beta})i]\,(1-\delta_{3\alpha}) & q=-2 \\ -[\delta_{2\gamma} + \delta_{1\gamma}(1-\delta_{1\alpha})(1-\delta_{1\beta})i] & q=-1 \\ \delta_{\alpha\beta}\,[1-3\delta_{3\alpha}]\,\sqrt{6}/3 & q=0 \\ [\delta_{2\gamma} - \delta_{1\gamma}(1-\delta_{1\alpha})(1-\delta_{1\beta})i] & q=+1 \\ [\delta_{\alpha\beta}(2\alpha-3) + \delta_{1\gamma}(1-\delta_{3\beta})i]\,(1-\delta_{3\alpha}) & q=+2 \end{pmatrix}, \tag{C.5}$$

where $\gamma = |\alpha - \beta|$.

Example one

Suppose that,

$$\Omega_{\alpha\beta} = \delta_{\alpha\beta} - 3\frac{r_\alpha r_\beta}{r^2}. \tag{C.6}$$

Then, for example, if $\alpha = 1$ and $\beta = 3$, the operator is,

$$\Omega_{13} = \delta_{13} - 3\frac{r_1 r_3}{r^2} = -3\frac{xz}{r^2}. \tag{C.7}$$

We can recover this using the expansion in equation C.1 for $\kappa = 3$,

$$\begin{aligned} \Omega_{13} &= \sqrt{\frac{6\pi}{5}} \sum_{q=-2}^{2} C_{13}^{q} Y_2^q(\theta,\varphi), \\ &= \sqrt{\frac{6\pi}{5}} \begin{pmatrix} [\delta_{13}(2\cdot 1-3) - \delta_{12}(1-\delta_{33})i]\,(1-\delta_{31}) \\ -[\delta_{22} + \delta_{12}(1-\delta_{11})(1-\delta_{13})i] \\ \delta_{13}\,[1-3\delta_{31}]\,\sqrt{6}/3 \\ [\delta_{22} - \delta_{12}(1-\delta_{11})(1-\delta_{13})i] \\ [\delta_{13}(2\cdot 1-3) + \delta_{12}(1-\delta_{33})i]\,(1-\delta_{31}) \end{pmatrix} \cdot \begin{pmatrix} Y_2^{-2}(\theta,\varphi) \\ Y_2^{-1}(\theta,\varphi) \\ Y_2^{0}(\theta,\varphi) \\ Y_2^{1}(\theta,\varphi) \\ Y_2^{2}(\theta,\varphi) \end{pmatrix}, \end{aligned} \tag{C.8}$$

where we have inserted $\gamma = |1-3| = 2$. Thus, using the definitions of the spherical coordinate system,

$$\begin{aligned}
\Omega_{13} &= \sqrt{\frac{6\pi}{5}} \begin{pmatrix} 0 \\ -1 \\ 0 \\ 1 \\ 0 \end{pmatrix} \cdot \begin{pmatrix} Y_2^{-2}(\theta,\varphi) \\ Y_2^{-1}(\theta,\varphi) \\ Y_2^{0}(\theta,\varphi) \\ Y_2^{1}(\theta,\varphi) \\ Y_2^{2}(\theta,\varphi) \end{pmatrix}, \\
&= \sqrt{\frac{6\pi}{5}} \left[Y_2^1(\theta,\varphi) - Y_2^{-1}(\theta,\varphi) \right], \\
&= \sqrt{\frac{6\pi}{5}} \left[-\frac{1}{2}\sqrt{\frac{15}{2\pi}} e^{i\varphi} \sin\theta\cos\theta - \frac{1}{2}\sqrt{\frac{15}{2\pi}} e^{-i\varphi} \sin\theta\cos\theta \right], \\
&= -3\cos\varphi \sin\theta\cos\theta, \\
&= -3\frac{xz}{r^2}, \qquad \text{C.9}
\end{aligned}$$

as required.

Example two

Suppose that,

$$\Omega_{\alpha\beta} = \delta_{\alpha\beta} - \frac{r_\alpha r_\beta}{r^2}. \qquad \text{C.10}$$

Then, for example, if $\alpha = \beta = 2$, the operator is,

$$\Omega_{22} = \delta_{22} - \frac{r_2 r_2}{r^2} = 1 - \frac{y^2}{r^2}. \qquad \text{C.11}$$

We can recover this using the expansion in equation C.1 for $\kappa = 1$,

$$\begin{aligned}
\Omega_{22} &= \sqrt{\frac{2\pi}{15}} \sum_{q=-2}^{2} C_{22}^q Y_2^q(\theta,\varphi) + \frac{4\sqrt{\pi}}{3}\delta_{22} Y_0^0(\theta,\varphi), \\
&= \sqrt{\frac{2\pi}{15}} \begin{pmatrix} \left[\delta_{22}(2\cdot 2-3) - \delta_{10}(1-\delta_{32})i\right](1-\delta_{32}) \\ -\left[\delta_{20} + \delta_{10}(1-\delta_{12})(1-\delta_{12})i\right] \\ \delta_{22}\left[1-3\delta_{32}\right]\sqrt{6}/3 \\ \left[\delta_{20} - \delta_{10}(1-\delta_{12})(1-\delta_{12})i\right] \\ \left[\delta_{22}(2\cdot 2-3) + \delta_{10}(1-\delta_{32})i\right](1-\delta_{32}) \end{pmatrix} \cdot \begin{pmatrix} Y_2^{-2}(\theta,\varphi) \\ Y_2^{-1}(\theta,\varphi) \\ Y_2^{0}(\theta,\varphi) \\ Y_2^{1}(\theta,\varphi) \\ Y_2^{2}(\theta,\varphi) \end{pmatrix} + \frac{2}{3}, \qquad \text{C.12}
\end{aligned}$$

where we have inserted $\gamma = |2-2| = 0$. Thus, using the definitions of the spherical coordinate system,

$$\begin{aligned}
\Omega_{22} &= \sqrt{\frac{2\pi}{15}} \begin{pmatrix} 1 \\ 0 \\ \sqrt{6}/3 \\ 0 \\ 1 \end{pmatrix} \cdot \begin{pmatrix} Y_2^{-2}(\theta,\varphi) \\ Y_2^{-1}(\theta,\varphi) \\ Y_2^{0}(\theta,\varphi) \\ Y_2^{1}(\theta,\varphi) \\ Y_2^{2}(\theta,\varphi) \end{pmatrix} + \frac{2}{3}, \\
&= \sqrt{\frac{2\pi}{15}} \left[Y_2^2(\theta,\varphi) + Y_2^{-2}(\theta,\varphi) + \frac{\sqrt{6}}{3} Y_2^0(\theta,\varphi) \right] + \frac{2}{3}, \\
&= \sqrt{\frac{2\pi}{15}} \left[\frac{1}{4}\sqrt{\frac{15}{2\pi}} e^{2i\varphi} \sin^2\theta + \frac{1}{4}\sqrt{\frac{15}{2\pi}} e^{-2i\varphi} \sin^2\theta + \frac{\sqrt{6}}{3}\frac{1}{4}\sqrt{\frac{5}{\pi}} \left(3\cos^2\theta - 1\right) \right] + \frac{2}{3}, \\
&= \frac{1}{2}\cos 2\varphi \sin^2\theta + \frac{1}{6}\left(3\cos^2\theta - 1\right) + \frac{2}{3}, \\
&= 1 - \frac{y^2}{r^2}, \qquad \text{C.13}
\end{aligned}$$

where we have used,

$$\frac{x^2}{r^2} + \frac{z^2}{r^2} = 1 - \frac{y^2}{r^2}. \qquad \text{C.14}$$

D

Electric field gradient data

The relative C_Q deviation, ΔC_Q^i, of data point, i, is calculated by,

$$\Delta C_Q^i = \frac{C_Q^{i,\mathrm{cal}} - C_Q^{i,\mathrm{exp}}}{C_Q^{i,\mathrm{exp}}}, \tag{D.1}$$

where $C_Q^{i,\mathrm{cal}}$ is the calculated and $C_Q^{i,\mathrm{exp}}$ the experimental value.

The mean and median relative deviations in the following tables then follow from these ΔC_Q^i values, and the root-mean-square (RMS) is calculated by,

$$C_Q^{\mathrm{RMS}} = \sqrt{\frac{1}{N_{C_Q}} \sum_i \left(\Delta C_Q^i\right)^2}, \tag{D.2}$$

where N_{C_Q} is the number of C_Q values.

Table D.1: Comparison of pseudopotentials for C_Q values of halides against experiment for a range of diatomic molecules. All values in MHz. Experimental values taken from reference [174]. The nuclear quadrupole moments used were taken from reference [174], $Q(^{35}\mathrm{Cl}) = -0.08165$ barn, $Q(^{79}\mathrm{Br}) = 0.30$ barn and $Q(^{127}\mathrm{I}) = -0.69$ barn.

Structure	Ion	exp.	NCP	USP
AlCl	^{35}Cl	-8.829	-8.995	-8.442
GaCl	^{35}Cl	-13.20	-13.55	-12.83
InCl	^{35}Cl	-13.30	-13.89	-13.30
TlCl	^{35}Cl	-15.75	-14.26	-13.79
CuCl	^{35}Cl	-32.12	-41.24	-40.12
AgCl	^{35}Cl	-36.44	-41.24	-40.12
HCl	^{35}Cl	-67.46	-67.48	-63.99
ICl	^{35}Cl	-85.80	-88.62	-84.88
BrCl	^{35}Cl	-102.4	-102.6	-98.01
Cl_2	^{35}Cl	-115.0	-110.5	-106.0
ClF	^{35}Cl	-145.9	-144.3	-137.6
AlBr	^{79}Br	78.71	85.82	77.90
GaBr	^{79}Br	105.8	107.5	100.3
InBr	^{79}Br	110.4	111.5	105.8
TlBr	^{79}Br	126.1	111.5	107.3
CuBr	^{79}Br	261.2	335.9	324.4
AgBr	^{79}Br	296.8	352.0	340.2
HBr	^{79}Br	532.2	536.6	503.2
IBr	^{79}Br	696.9	701.5	676.8
Br_2	^{79}Br	810.0	800.6	771.3
BrCl	^{79}Br	875.1	859.3	831.2
BrF	^{79}Br	1087	1065	1028
AlI	^{127}I	-307.4	-267.2	-299.5
GaI	^{127}I	-369.4	-328.5	-354.2
InI	^{127}I	-386.4	-348.6	-373.2
TlI	^{127}I	-438.1	-351.0	-374.3
CuI	^{127}I	-938.1	-1113	-1178
AgI	^{127}I	-1061	-1182	-1233
HI	^{127}I	-1828	-1702	-1798
I_2	^{127}I	-2453	-2377	-2445
IBr	^{127}I	-2731	-2660	-2731
ICl	^{127}I	-2929	-2831	-2924
IF	^{127}I	-3441	-3376	-3468
	median absolute deviation		9.363	8.224
	mean relative deviation		7.492 %	7.137 %
	median relative deviation		3.348 %	4.776 %
	RMS relative deviation		10.82 %	10.13 %

Table D.2: Comparison of pseudopotentials for C_Q values of metals against experiment for a range of diatomic molecules. All values in MHz. Experimental values taken from reference [174]. The nuclear quadrupole moments used were taken from reference [174], $Q(^{27}\mathrm{Al}) = 0.1466$ barn, $Q(^{69}\mathrm{Ga}) = 0.165$ barn and $Q(^{115}\mathrm{In}) = 0.74$ barn.

Structure	Ion	exp.	NCP	USP
AlF	^{27}Al	-37.75	-31.10	-35.57
AlCl	^{27}Al	-30.41	-25.99	-28.80
AlBr	^{27}Al	-28.01	-23.76	-26.18
AlI	^{27}Al	-25.55	-22.26	-24.23
GaF	^{69}Ga	-107.1	-80.71	-92.75
GaCl	^{69}Ga	-92.10	-74.52	-82.32
GaBr	^{69}Ga	-86.68	-71.17	-78.01
GaI	^{69}Ga	-81.29	-67.44	-73.10
InF	^{115}In	-727.1	-539.9	-619.4
InCl	^{115}In	-659.6	-513.2	-571.4
InBr	^{115}In	-634.7	-497.5	-550.2
InI	^{115}In	-607.5	-484.4	-530.2
	median absolute deviation		17.58	9.776
	mean relative deviation		19.05 %	10.09 %
	median relative deviation		19.09 %	10.61 %
	RMS relative deviation		19.43 %	10.65 %

Table D.3: Comparison of relativistic treatments for C_Q values of halides against experiment for a range of diatomic molecules. All values in MHz. Experimental values taken from reference [174]. The nuclear quadrupole moments used were taken from reference [174], $Q(^{35}\mathrm{Cl}) = -0.08165$ barn, $Q(^{79}\mathrm{Br}) = 0.30$ barn and $Q(^{127}\mathrm{I}) = -0.69$ barn.

Structure	Ion	exp.	NR	SR	FR
AlCl	^{35}Cl	-8.829	-8.867	-8.995	-8.990
GaCl	^{35}Cl	-13.20	-13.34	-13.55	-13.57
InCl	^{35}Cl	-13.30	-13.56	-13.89	-14.07
TlCl	^{35}Cl	-15.75	-13.95	-14.26	-15.87
CuCl	^{35}Cl	-32.12	-37.07	-41.24	-41.23
AgCl	^{35}Cl	-36.44	-37.07	-41.24	-41.23
HCl	^{35}Cl	-67.46	-66.40	-67.48	-67.48
ICl	^{35}Cl	-85.80	-86.87	-88.62	-85.29
BrCl	^{35}Cl	-102.4	-101.2	-102.6	-102.1
Cl_2	^{35}Cl	-115.0	-108.9	-110.5	-110.5
ClF	^{35}Cl	-145.9	-142.3	-144.3	-144.3
AlBr	^{79}Br	78.71	79.14	85.82	85.81
GaBr	^{79}Br	105.8	99.71	107.5	107.9
InBr	^{79}Br	110.4	103.2	111.5	113.3
TlBr	^{79}Br	126.1	104.5	111.5	124.8
CuBr	^{79}Br	261.2	285.3	335.9	335.7
AgBr	^{79}Br	296.8	262.5	352.0	331.5
HBr	^{79}Br	532.2	496.2	536.6	537.0
IBr	^{79}Br	696.9	649.4	701.5	682.9
Br_2	^{79}Br	810.0	744.4	800.6	797.3
BrCl	^{79}Br	875.1	798.6	859.3	855.1
BrF	^{79}Br	1087	991.6	1065	1057
AlI	^{127}I	-307.4	-214.5	-267.2	-267.2
GaI	^{127}I	-369.4	-267.7	-328.5	-331.0
InI	^{127}I	-386.4	-284.4	-348.6	-358.4
TlI	^{127}I	-438.1	-290.0	-351.0	-407.2
CuI	^{127}I	-938.1	-840.9	-1113	-1106
AgI	^{127}I	-1061	-785.0	-1182	-1106
HI	^{127}I	-1828	-1398	-1702	-1710
I_2	^{127}I	-2453	-1973	-2377	-2325
IBr	^{127}I	-2731	-2218	-2660	-2587
ICl	^{127}I	-2929	-2360	-2831	-2732
IF	^{127}I	-3441	-2822	-3376	-3205
	median absolute deviation		34.33	9.363	12.75
	mean relative deviation		11.73 %	7.492 %	6.473 %
	median relative deviation		8.771 %	3.348 %	4.251 %
	RMS relative deviation		15.17 %	10.82 %	9.558 %

Table D.4: Comparison of relativistic treatments for C_Q values of metals against experiment for a range of diatomic molecules. All values in MHz. Experimental values taken from reference [174]. The nuclear quadrupole moments used were taken from reference [174], $Q(^{27}\mathrm{Al}) = 0.1466$ barn, $Q(^{69}\mathrm{Ga}) = 0.165$ barn and $Q(^{115}\mathrm{In}) = 0.74$ barn.

Structure	Ion	exp.	NR	SR	FR
AlF	^{27}Al	-37.75	-30.90	-31.10	-31.10
AlCl	^{27}Al	-30.41	-25.87	-25.99	-25.99
AlBr	^{27}Al	-28.01	-23.78	-23.76	-23.74
AlI	^{27}Al	-25.55	-22.52	-22.26	-22.15
GaF	^{69}Ga	-107.1	-77.25	-80.71	-80.83
GaCl	^{69}Ga	-92.10	-71.40	-74.52	-74.64
GaBr	^{69}Ga	-86.68	-68.47	-71.17	-71.22
GaI	^{69}Ga	-81.29	-65.48	-67.44	-67.24
InF	^{115}In	-727.1	-479.8	-539.9	-544.6
InCl	^{115}In	-659.6	-455.9	-513.2	-517.9
InBr	^{115}In	-634.7	-443.1	-497.5	-501.5
InI	^{115}In	-607.5	-434.8	-484.4	-486.3
	median absolute deviation		20.70	17.58	17.46
	mean relative deviation		22.86 %	19.05 %	18.90 %
	median relative deviation		22.47 %	19.09 %	18.96 %
	RMS relative deviation		23.89 %	19.43 %	19.23 %

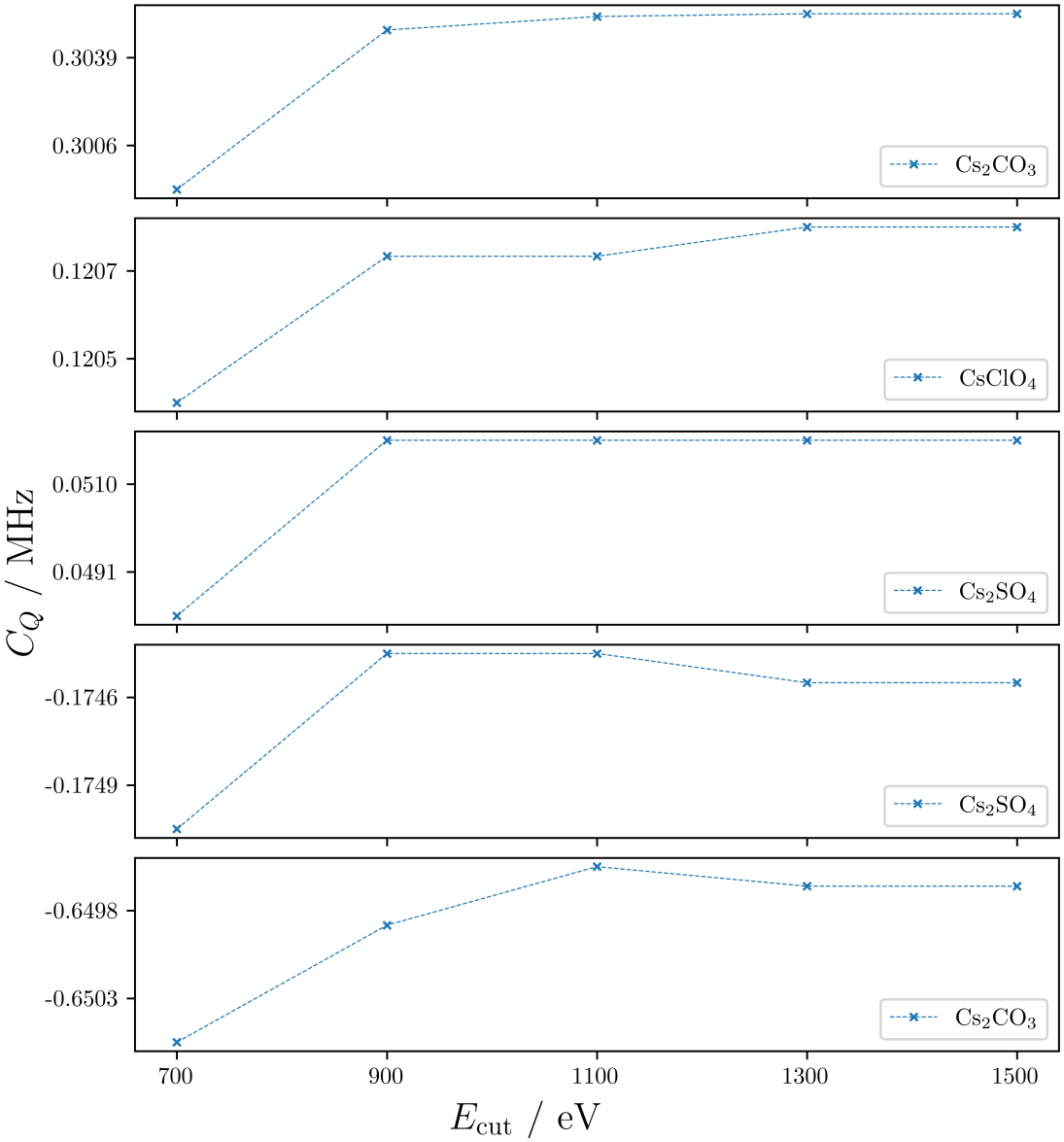


Figure D.1: Convergence of ^{133}Cs C_Q values with respect to E_{cut}.

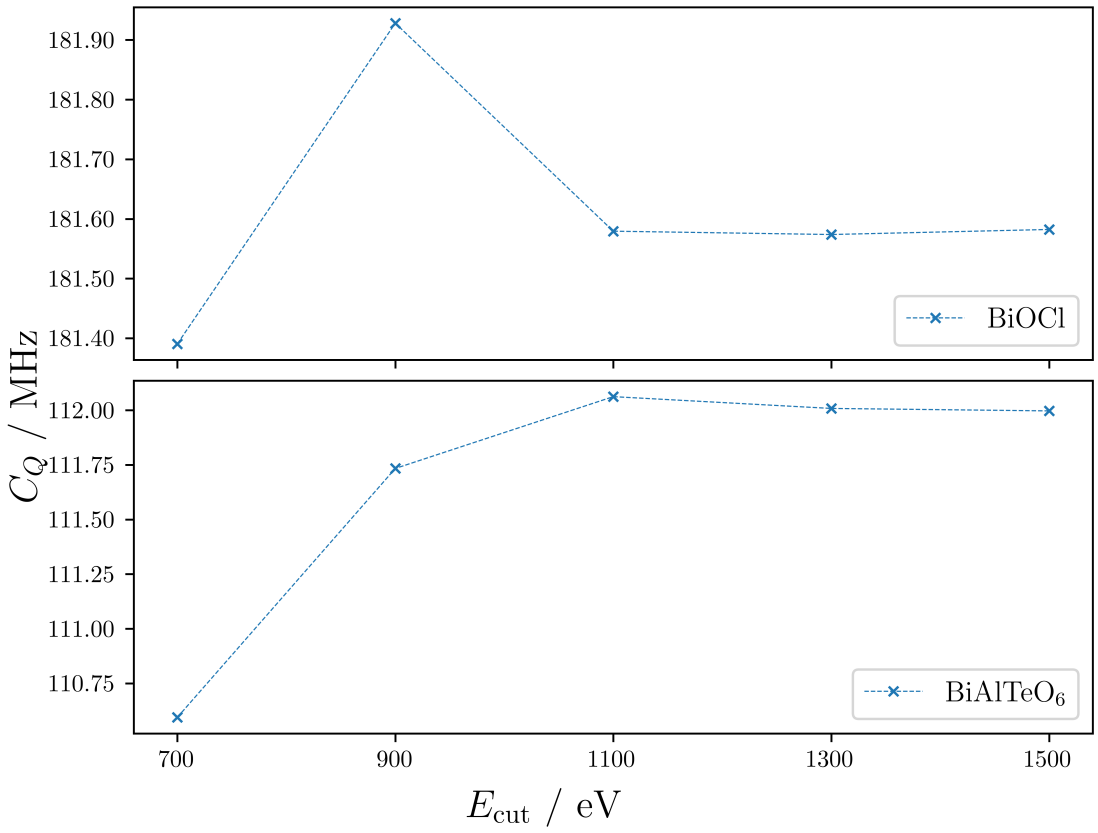


Figure D.2: Convergence of ^{209}Bi C_Q values with respect to E_{cut}.

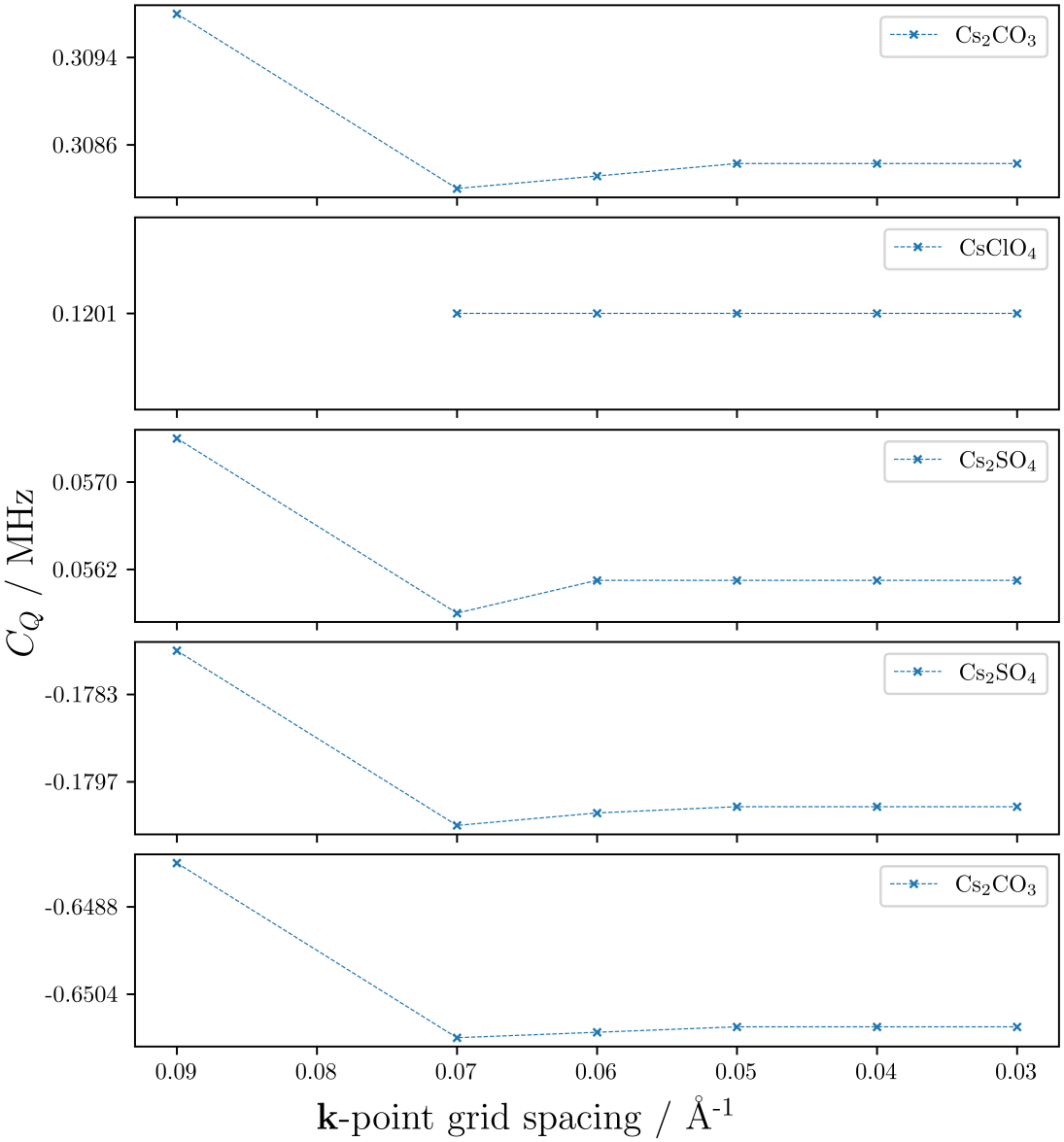


Figure D.3: Convergence of ^{133}Cs C_Q values with respect to **k**-point grid spacing.

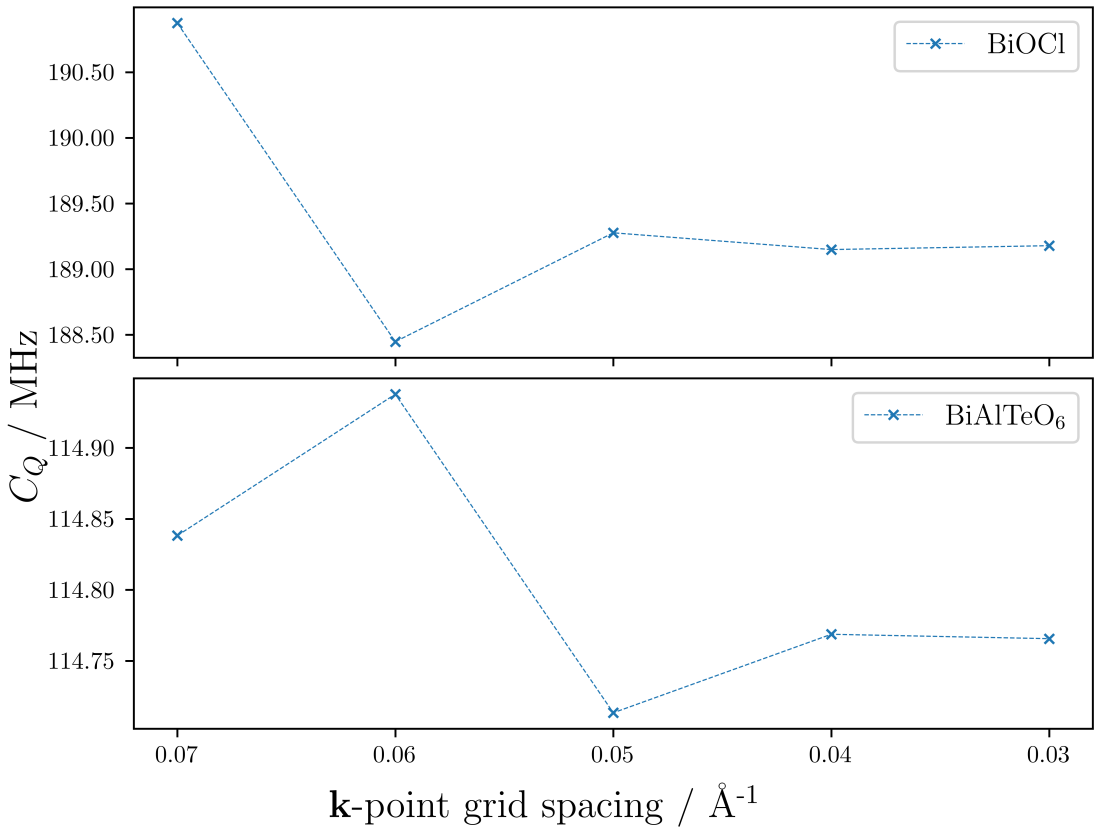


Figure D.4: Convergence of ^{209}Bi C_Q values with respect to **k**-point grid spacing.

References

(1) I. I. Rabi, J. R. Zacharias, S. Millman and P. Kusch, *Physical Review*, 1938, **53**, 318–318.

(2) E. M. Purcell, H. C. Torrey and R. V. Pound, *Physical Review*, 1946, **69**, 37–38.

(3) F. Bloch, W. W. Hansen and M. Packard, *Physical Review*, 1946, **69**, 127–127.

(4) P. Hohenberg and W. Kohn, *Physical Review*, 1964, **136**, B864–B871.

(5) W. Kohn and L. J. Sham, *Physical Review*, 1965, **140**, A1133–A1138.

(6) C. J. Pickard and F. Mauri, *Physical Review B*, 2001, **63**, 245101.

(7) M. D. Segall, J. D. L. Philip, M. J. Probert, C. J. Pickard, P. J. Hasnip, S. J. Clark and M. C. Payne, *Journal of Physics: Condensed Matter*, 2002, **14**, 2717.

(8) S. J. Clark, M. D. Segall, C. J. Pickard, P. J. Hasnip, M. I. J. Probert, K. Refson and M. C. Payne, *Zeitschrift für Kristallographie - Crystalline Materials*, 2005, **220**, 567–570.

(9) W. D. Knight, *Physical Review*, 1949, **76**, 1259–1260.

(10) W. C. Dickinson, *Physical Review*, 1950, **77**, 736–737.

(11) G. Lindström, *Physical Review*, 1950, **78**, 817–818.

(12) W. G. Proctor and F. C. Yu, *Physical Review*, 1950, **77**, 717–717.

(13) H. A. Thomas, *Physical Review*, 1950, **80**, 901–902.

(14) J. T. Arnold, S. S. Dharmatti and M. E. Packard, *The Journal of Chemical Physics*, 1951, **19**, 507–507.

(15) R. R. Ernst and W. A. Anderson, *Review of Scientific Instruments*, 1966, **37**, 93–102.

(16) U. Haeberlen, in *High resolution NMR in solids*, ed. J. S. Waugh, Academic Press, New York, 1976.

(17) H. W. Spiess, *Rotation of molecules and nuclear spin relaxation*, Conference Paper, 1978.

(18) M. Mehring, *Principles of high-resolution NMR in solids*, Springer-Verlag, Berlin, 2nd ed., 1983.

(19) D. C. Apperley, R. K. Harris and P. Hodgkinson, *Solid-State NMR: Basic Principles and Practice*, Momentum Press, New York, 2012.

(20) C. Bonhomme, C. Gervais, F. Babonneau, C. Coelho, F. Pourpoint, T. Azaïs, S. E. Ashbrook, J. M. Griffin, J. R. Yates, F. Mauri and C. J. Pickard, *Chemical Reviews*, 2012, **112**, 5733–5779.

(21) E. R. Andrew, A. Bradbury and R. G. Eades, *Nature*, 1958, **182**, 1659–1659.

(22) I. J. Lowe, *Physical Review Letters*, 1959, **2**, 285–287.

(23) E. Vinogradov, P. K. Madhu and S. Vega, *Chemical Physics Letters*, 1999, **314**, 443–450.

(24) D. Sakellariou, A. Lesage, P. Hodgkinson and L. Emsley, *Chemical Physics Letters*, 2000, **319**, 253–260.

(25) A. Lesage, D. Sakellariou, S. Hediger, B. Eléna, P. Charmont, S. Steuernagel and L. Emsley, *Journal of Magnetic Resonance*, 2003, **163**, 105–113.

(26) S. R. Hartmann and E. L. Hahn, *Physical Review*, 1962, **128**, 2042–2053.

(27) A. Pines, M. G. Gibby and J. S. Waugh, *The Journal of Chemical Physics*, 1972, **56**, 1776–1777.

(28) A. Samoson, E. Lippmaa and A. Pines, *Molecular Physics*, 1988, **65**, 1013–1018.

(29) Y. Wu, B. Q. Sun, A. Pines, A. Samoson and E. Lippmaa, *Journal of Magnetic Resonance*, 1990, **89**, 297–309.

(30) A. Llor and J. Virlet, *Chemical Physics Letters*, 1988, **152**, 248–253.

(31) K. T. Mueller, B. Q. Sun, G. C. Chingas, J. W. Zwanziger, T. Terao and A. Pines, *Journal of Magnetic Resonance*, 1990, **86**, 470–487.

(32) L. Frydman and J. S. Harwood, *Journal of the American Chemical Society*, 1995, **117**, 5367–5368.

(33) Z. Gan, *Journal of the American Chemical Society*, 2000, **122**, 3242–3243.

(34) S. E. Ashbrook and D. McKay, *Chemical Communications*, 2016, **52**, 7186–7204.

(35) C. Martineau, A. Cadiau, B. Bouchevreau, J. Senker, F. Taulelle and K. Adil, *Dalton Transactions*, 2012, **41**, 6232–6241.

(36) F. A. Perras and D. L. Bryce, *The Journal of Physical Chemistry C*, 2012, **116**, 19472–19482.

(37) C. J. Pickard and R. J. Needs, *Physical Review Letters*, 2006, **97**, 045504.

(38) N. F. Ramsey, *Physical Review*, 1950, **77**, 567–567.

(39) N. F. Ramsey, *Physical Review*, 1950, **78**, 699–703.

(40) N. F. Ramsey, *Physical Review*, 1953, **91**, 303–307.

(41) R. Ditchfield, *Molecular Physics*, 1974, **27**, 789–807.

(42) W. Kutzelnigg, *Israel Journal of Chemistry*, 1980, **19**, 193–200.

(43) A. E. Hansen and T. D. Bouman, *The Journal of Chemical Physics*, 1985, **82**, 5035–5047.

(44) M. Schindler and W. Kutzelnigg, *The Journal of Chemical Physics*, 1982, **76**, 1919–1933.

(45) F. London, *Journal de Physique et le Radium*, 1937, **8**, 397–409.

(46) H. F. Hameka, *Molecular Physics*, 1958, **1**, 203–215.

(47) R. Ditchfield, *The Journal of Chemical Physics*, 1972, **56**, 5688–5691.

(48) F. Mauri, B. G. Pfrommer and S. G. Louie, *Physical Review Letters*, 1996, **77**, 5300–5303.

(49) T. Gregor, F. Mauri and R. Car, *The Journal of Chemical Physics*, 1999, **111**, 1815–1822.

(50) P. E. Blöchl, *Physical Review B*, 1994, **50**, 17953–17979.

(51) J. R. Yates, C. J. Pickard, M. C. Payne and F. Mauri, *The Journal of Chemical Physics*, 2003, **118**, 5746–5753.

(52) J. R. Yates, C. J. Pickard and F. Mauri, *Physical Review B*, 2007, **76**, 024401.

(53) M. Dračínský, P. Unzueta and G. J. O. Beran, *Physical Chemistry Chemical Physics*, 2019, **21**, 14992–15000.

(54) J. D. Hartman and J. K. Harper, *Solid State Nuclear Magnetic Resonance*, 2022, **122**, 101832.

(55) P. Blaha, K. Schwarz and P. Herzig, *Physical Review Letters*, 1985, **54**, 1192–1195.

(56) H. M. Petrilli, P. E. Blöchl, P. Blaha and K. Schwarz, *Physical Review B*, 1998, **57**, 14690–14697.

(57) M. Profeta, F. Mauri and C. J. Pickard, *Journal of the American Chemical Society*, 2003, **125**, 541–548.

(58) S. A. Joyce, J. R. Yates, C. J. Pickard and F. Mauri, *The Journal of Chemical Physics*, 2007, **127**, 204107.

(59) T. F. Green and J. R. Yates, *The Journal of Chemical Physics*, 2014, **140**, 234106.

(60) Y. Nomura, Y. Takeuchi and N. Nakagawa, *Tetrahedron Letters*, 1969, **10**, 639–642.

(61) I. Morishima, K. Endo and T. Yonezawa, *The Journal of Chemical Physics*, 1973, **59**, 3356–3364.

(62) A. A. Cheremisin and P. V. Schastnev, *Journal of Magnetic Resonance*, 1980, **40**, 459–468.

(63) P. Pyykkö, *Chemical Physics*, 1983, **74**, 1–7.

(64) Z. C. Zhang and G. A. Webb, *Journal of Molecular Structure: THEOCHEM*, 1983, **104**, 439–444.

(65) P. Pyykkö, A. Görling and N. Rösch, *Molecular Physics*, 1987, **61**, 195–205.

(66) J. Vícha, J. Novotný, S. Komorovsky, M. Straka, M. Kaupp and R. Marek, *Chemical Reviews*, 2020, **120**, 7065–7103.

(67) V. G. Malkin, O. L. Malkina and D. R. Salahub, *Chemical Physics Letters*, 1996, **261**, 335–345.

(68) S. K. Wolff and T. Ziegler, *The Journal of Chemical Physics*, 1998, **109**, 895–905.

(69) S. K. Wolff, T. Ziegler, E. v. Lenthe and E. J. Baerends, *The Journal of Chemical Physics*, 1999, **110**, 7689–7698.

(70) E. Schrödinger, *Physical Review*, 1926, **28**, 1049–1070.

(71) D. R. Hartree, *Mathematical Proceedings of the Cambridge Philosophical Society*, 1928, **24**, 89–110.

(72) J. A. Pople and R. K. Nesbet, *The Journal of Chemical Physics*, 1954, **22**, 571–572.

(73) A. Szabo and N. S. Ostlund, *Modern Quantum Chemistry: Introduction to Advanced Electronic Structure Theory*, Dover Publications, Mineola, 1996.

(74) J. Čížek, *The Journal of Chemical Physics*, 1966, **45**, 4256–4266.

(75) R. F. Bishop and H. G. Kümmel, *Physics Today*, 1987, **40**, 52–60.

(76) I. Shavitt and R. J. Bartlett, *Many-Body Methods in Chemistry and Physics: MBPT and Coupled-Cluster Theory*, Cambridge University Press, Cambridge, 2009.

(77) C. Møller and M. S. Plesset, *Physical Review*, 1934, **46**, 618–622.

(78) F. Giustino, *Materials Modelling Using Density Functional Theory: Properties and Predictions*, Oxford University Press, Oxford, 2014.

(79) D. M. Ceperley and B. J. Alder, *Physical Review Letters*, 1980, **45**, 566–569.

(80) W. E. Pickett and J. Q. Broughton, *Physical Review B*, 1993, **48**, 14859–14867.

(81) G. Ortiz and P. Ballone, *Physical Review B*, 1994, **50**, 1391–1405.

(82) S. H. Vosko, L. Wilk and M. Nusair, *Canadian Journal of Physics*, 1980, **59**, 1200.

(83) J. P. Perdew and A. Zunger, *Physical Review B*, 1981, **23**, 5048–5079.

(84) J. P. Perdew and Y. Wang, *Physical Review B*, 1992, **45**, 13244–13249.

(85) L. A. Curtiss, K. Raghavachari, P. C. Redfern and J. A. Pople, *The Journal of Chemical Physics*, 1997, **106**, 1063–1079.

(86) M. Rasolt and H. Davis, *Physics Letters A*, 1981, **86**, 45–47.

(87) M. Rasolt and D. J. W. Geldart, *Physical Review B*, 1986, **34**, 1325–1328.

(88) L. Kleinman and S. Lee, *Physical Review B*, 1988, **37**, 4634–4636.

(89) W. Koch and M. C. Holthausen, in *A Chemist's Guide to Density Functional Theory*, 2001, pp. 19–28.

(90) D. C. Langreth and J. P. Perdew, *Physical Review B*, 1980, **21**, 5469–5493.

(91) D. C. Langreth and M. J. Mehl, *Physical Review B*, 1983, **28**, 1809–1834.

(92) C. Hu and D. C. Langreth, *Physica Scripta*, 1985, **32**, 391.

(93) J. P. Perdew, *Physical Review Letters*, 1985, **55**, 1665–1668.

(94) J. P. Perdew and W. Yue, *Physical Review B*, 1986, **33**, 8800–8802.

(95) A. D. Becke, *Physical Review A*, 1988, **38**, 3098–3100.

(96) B. Hammer, L. B. Hansen and J. K. Nørskov, *Physical Review B*, 1999, **59**, 7413–7421.

(97) Z. Wu and R. E. Cohen, *Physical Review B*, 2006, **73**, 235116.

(98) J. P. Perdew, *Electronic structure of solids '91*, Akademie Verlag, Berlin, 1991.

(99) J. P. Perdew, K. Burke and M. Ernzerhof, *Physical Review Letters*, 1996, **77**, 3865–3868.

(100) J. Tao, J. P. Perdew, V. N. Staroverov and G. E. Scuseria, *Physical Review Letters*, 2003, **91**, 146401.

(101) F. Tran and P. Blaha, *Physical Review Letters*, 2009, **102**, 226401.

(102) J. Sun, A. Ruzsinszky and J. P. Perdew, *Physical Review Letters*, 2015, **115**, 036402.

(103) A. P. Bartók and J. R. Yates, *The Journal of Chemical Physics*, 2019, **150**, 161101.

(104) J. P. Perdew, M. Ernzerhof and K. Burke, *The Journal of Chemical Physics*, 1996, **105**, 9982–9985.

(105) C. Adamo and V. Barone, *The Journal of Chemical Physics*, 1999, **110**, 6158–6170.

(106) J. Heyd, G. E. Scuseria and M. Ernzerhof, *The Journal of Chemical Physics*, 2003, **118**, 8207–8215.

(107) A. V. Krukau, O. A. Vydrov, A. F. Izmaylov and G. E. Scuseria, *The Journal of Chemical Physics*, 2006, **125**, 224106.

(108) E. Brémond, I. Ciofini, J. C. Sancho-García and C. Adamo, *Accounts of Chemical Research*, 2016, **49**, 1503–1513.

(109) V. I. Anisimov, J. Zaanen and O. K. Andersen, *Physical Review B*, 1991, **44**, 943–954.

(110) D. Wu, Q. Zhang and M. Tao, *Physical Review B*, 2006, **73**, 235206.

(111) F. Ortmann, F. Bechstedt and W. G. Schmidt, *Physical Review B*, 2006, **73**, 205101.

(112) S. Grimme, *Journal of Computational Chemistry*, 2006, **27**, 1787–1799.

(113) A. Tkatchenko and M. Scheffler, *Physical Review Letters*, 2009, **102**, 073005.

(114) W. Reckien, F. Janetzko, M. F. Peintinger and T. Bredow, *Journal of Computational Chemistry*, 2012, **33**, 2023–31.

(115) A. Ambrosetti, A. M. Reilly, R. J. A. DiStasio and A. Tkatchenko, *The Journal of Chemical Physics*, 2014, **140**, 18A508.

(116) N. Mardirossian and M. Head-Gordon, *Molecular Physics*, 2017, **115**, 2315–2372.

(117) H. J. Monkhorst and J. D. Pack, *Physical Review B*, 1976, **13**, 5188–5192.

(118) U. von Barth and C. D. Gelatt, *Physical Review B*, 1980, **21**, 2222–2228.

(119) M. Fuchs and M. Scheffler, *Computer Physics Communications*, 1999, **119**, 67–98.

(120) H. Hellmann, *The Journal of Chemical Physics*, 1935, **3**, 61–61.

(121) H. Hellmann and W. Kassatotschkin, *The Journal of Chemical Physics*, 1936, **4**, 324–325.

(122) E. Antončík, *Cechoslovackij Fiziceskij Zurnal*, 1954, **4**, 439–451.

(123) E. Antončík, *Journal of Physics and Chemistry of Solids*, 1959, **10**, 314–320.

(124) J. C. Phillips and L. Kleinman, *Physical Review*, 1959, **116**, 287–294.

(125) N. Troullier and J. Martins, *Solid State Communications*, 1990, **74**, 613–616.

(126) D. Vanderbilt, *Physical Review B*, 1990, **41**, 7892–7895.

(127) K. Laasonen, A. Pasquarello, R. Car, C. Lee and D. Vanderbilt, *Physical Review B*, 1993, **47**, 10142–10153.

(128) C. G. Van de Walle and P. E. Blöchl, *Physical Review B*, 1993, **47**, 4244–4255.

(129) P. Pyykkö, *Chemical Reviews*, 1988, **88**, 563–594.

(130) P. Pyykkö, *Annual Review of Physical Chemistry*, 2012, **63**, 45–64.

(131) J. Autschbach, *The Journal of Chemical Physics*, 2012, **136**, 150902.

(132) W. Liu, *The Journal of Chemical Physics*, 2020, **152**, 180901.

(133) J. Autschbach and T. Ziegler, *Encyclopedia of Nuclear Magnetic Resonance*, 2002, **9**, 306–323.

(134) J. Autschbach and S. Zheng, in *Annual Reports on NMR Spectroscopy*, ed. G. A. Webb, Academic Press, 2009, vol. 67, pp. 1–95.

(135) I. Alkorta, J. Elguero, M. Yáñez, O. Mó and M. M. Montero-Campillo, *Molecules*, 2019, **24**, 4399.

(136) P. A. M. Dirac, *Proceedings of the Royal Society of London. Series A, Containing Papers of a Mathematical and Physical Character*, 1928, **117**, 610–624.

(137) C. D. Anderson, *Physical Review*, 1933, **43**, 491–494.

(138) L. L. Foldy and S. A. Wouthuysen, *Physical Review*, 1950, **78**, 29–36.

(139) E. v. Lenthe, E. J. Baerends and J. G. Snijders, *The Journal of Chemical Physics*, 1993, **99**, 4597–4610.

(140) J.-M. Lévy-Leblond, *Communications in Mathematical Physics*, 1967, **6**, 286–311.

(141) J.-M. Lévy-Leblond, *Annals of Physics*, 1970, **57**, 481–495.

(142) D. D. Koelling and B. N. Harmon, *Journal of Physics C: Solid State Physics*, 1977, **10**, 3107–3114.

(143) E. L. Shirley, D. C. Allan, R. M. Martin and J. D. Joannopoulos, *Physical Review B*, 1989, **40**, 3652–3660.

(144) A. D. Corso and A. M. Conte, *Physical Review B*, 2005, **71**, 115106.

(145) L. A. Hemstreet, C. Y. Fong and J. S. Nelson, *Physical Review B*, 1993, **47**, 4238–4243.

(146) G. Theurich and N. A. Hill, *Physical Review B*, 2001, **64**, 073106.

(147) M. C. Payne, M. P. Teter, D. C. Allan, T. A. Arias and J. D. Joannopoulos, *Reviews of Modern Physics*, 1992, **64**, 1045–1097.

(148) R. Car and M. Parrinello, *Physical Review Letters*, 1985, **55**, 2471–2474.

(149) M. P. Teter, M. C. Payne and D. C. Allan, *Physical Review B*, 1989, **40**, 12255–12263.

(150) L. Kleinman, *Physical Review B*, 1980, **21**, 2630–2631.

(151) J. Kubler, K. H. Hock, J. Sticht and A. R. Williams, *Journal of Physics F: Metal Physics*, 1988, **18**, 469.

(152) T. Oda, A. Pasquarello and R. Car, *Physical Review Letters*, 1998, **80**, 3622–3625.

(153) C. Van Wüllen, *Journal of Computational Chemistry*, 2002, **23**, 779–785.

(154) F. Wang and T. Ziegler, *The Journal of Chemical Physics*, 2004, **121**, 12191–12196.

(155) I. W. Bulik, G. Scalmani, M. J. Frisch and G. E. Scuseria, *Physical Review B*, 2013, **87**, 035117.

(156) F. Egidi, S. Sun, J. J. Goings, G. Scalmani, M. J. Frisch and X. Li, *Journal of Chemical Theory and Computation*, 2017, **13**, 2591–2603.

(157) Z. Pu, H. Li, N. Zhang, H. Jiang, Y. Gao, Y. Xiao, Q. Sun, Y. Zhang and S. Shao, *Physical Review Research*, 2023, **5**, 013036.

(158) K. Lejaeghere, G. Bihlmayer, T. Björkman, P. Blaha, S. Blügel, V. Blum, D. Caliste, I. E. Castelli, S. J. Clark, A. Dal Corso, S. de Gironcoli, T. Deutsch, J. K. Dewhurst, I. Di Marco, C. Draxl, M. Dułak, O. Eriksson, J. A. Flores-Livas, K. F. Garrity, L. Genovese, P. Giannozzi, M. Giantomassi, S. Goedecker, X. Gonze, O. Grånäs, E. K. U. Gross, A. Gulans, F. Gygi, D. R. Hamann, P. J. Hasnip, N. A. W. Holzwarth, D. Iuşan, D. B. Jochym, F. Jollet, D. Jones, G. Kresse, K. Koepernik, E. Küçükbenli, Y. O. Kvashnin, I. L. M. Locht, S. Lubeck, M. Marsman, N. Marzari, U. Nitzsche, L. Nordström, T. Ozaki, L. Paulatto, C. J. Pickard, W. Poelmans, M. I. J. Probert, K. Refson, M. Richter, G.-M. Rignanese, S. Saha, M. Scheffler, M. Schlipf, K. Schwarz, S. Sharma, F. Tavazza, P. Thunström, A. Tkatchenko, M. Torrent, D. Vanderbilt, M. J. van Setten, V. Van Speybroeck, J. M. Wills, J. R. Yates, G.-X. Zhang and S. Cottenier, *Science*, 2016, **351**, aad3000.

(159) M. J. Verstraete, M. Torrent, F. Jollet, G. Zérah and X. Gonze, *Physical Review B*, 2008, **78**, 045119.

(160) R. Sehr and L. R. Testardi, *Journal of Physics and Chemistry of Solids*, 1962, **23**, 1219–1224.

(161) D. L. Greenaway and G. Harbeke, *Journal of Physics and Chemistry of Solids*, 1965, **26**, 1585–1604.

(162) G. A. Thomas, D. H. Rapkine, R. B. Van Dover, L. F. Mattheiss, W. A. Sunder, L. F. Schneemeyer and J. V. Waszczak, *Physical Review B*, 1992, **46**, 1553–1556.

(163) J. P. Perdew and M. Levy, *Physical Review Letters*, 1983, **51**, 1884–1887.

(164) S. J. Youn and A. J. Freeman, *Physical Review B*, 2001, **63**, 085112.

(165) P. Larson, *Physical Review B*, 2003, **68**, 155121.

(166) D. M. Bylander and L. Kleinman, *Physical Review B*, 1990, **41**, 7868–7871.

(167) S. K. Mishra, S. Satpathy and O. Jepsen, *Journal of Physics: Condensed Matter*, 1997, **9**, 461.

(168) T. J. Scheidemantel, C. Ambrosch-Draxl, T. Thonhauser, J. V. Badding and J. O. Sofo, *Physical Review B*, 2003, **68**, 125210.

(169) B.-L. Huang and M. Kaviany, *Physical Review B*, 2008, **77**, 125209.

(170) M. Kim, A. J. Freeman and C. B. Geller, *Physical Review B*, 2005, **72**, 035205.

(171) E. Moser, E. Laistler, F. Schmitt and G. Kontaxis, *Frontiers in Physics*, 2017, **5**, 33.

(172) G. Theurich and N. A. Hill, *Physical Review B*, 2002, **66**, 115208.

(173) A. Honma, *Science of Light (Tokyo)*, 1976, **25**, 41–55.

(174) E. v. Lenthe and E. J. Baerends, *The Journal of Chemical Physics*, 2000, **112**, 8279–8292.

(175) H. Hamaed, M. W. Laschuk, V. V. Terskikh and R. W. Schurko, *Journal of the American Chemical Society*, 2009, **131**, 8271–8279.

(176) K. J. Griffith, F. Ding and S. Flynn, *Magnetic Resonance in Chemistry*, 2021, **59**, 1077–1088.

(177) J. Skibsted, T. Vosegaard, H. Bildsøe and H. J. Jakobsen, *The Journal of Physical Chemistry*, 1996, **100**, 14872–14881.

(178) J. Bieroń and P. Pyykkö, *Physical Review Letters*, 2001, **87**, 133003.

(179) P. Pyykkö, *Molecular Physics*, 2018, **116**, 1328–1338.

(180) T. Q. Teodoro and R. L. A. Haiduke, *Physical Review A*, 2013, **88**, 052504.

(181) A. Shee, L. Visscher and T. Saue, *The Journal of Chemical Physics*, 2016, **145**, 184107.

(182) L. V. Skripnikov, A. V. Oleynichenko, A. V. Zaitsevskii, D. E. Maison and A. E. Barzakh, *Physical Review C*, 2021, **104**, 034316.

(183) J. Cuny, J. Yates, R. Gautier, E. Furet, E. Le Fur and L. Le Pollès, *Magnetic Resonance in Chemistry*, 2010, **48**, S171–S175.

(184) M. d'Avezac, N. Marzari and F. Mauri, *Physical Review B*, 2007, **76**, 165122.

(185) M. Zilka, S. Sturniolo, S. P. Brown and J. R. Yates, *The Journal of Chemical Physics*, 2017, **147**, 144203.

(186) H. Nakatsuji, H. Takashima and M. Hada, *Chemical Physics Letters*, 1995, **233**, 95–101.

(187) H. Takashima, M. Hada and H. Nakatsuji, *Chemical Physics Letters*, 1995, **235**, 13–16.

(188) C. C. Ballard, M. Hada, H. Kaneko and H. Nakatsuji, *Chemical Physics Letters*, 1996, **254**, 170–178.

(189) M. Kaupp, O. L. Malkina, V. G. Malkin and P. Pyykkö, *Chemistry – A European Journal*, 1998, **4**, 118–126.

(190) C. G. Van de Walle and P. E. Blöchl, *Physical Review B*, 1993, **47**, 4244–4255.

(191) A. V. Arbuznikov, J. Vaara and M. Kaupp, *The Journal of Chemical Physics*, 2004, **120**, 2127–2139.

(192) J. Autschbach, S. Patchkovskii and B. Pritchard, *Journal of Chemical Theory and Computation*, 2011, **7**, 2175–2188.

(193) N. D. Woods, M. C. Payne and P. J. Hasnip, *Journal of Physics: Condensed Matter*, 2019, **31**, 453001.

(194) E. D. Hedegård, J. Kongsted and S. P. A. Sauer, *Journal of Chemical Theory and Computation*, 2011, **7**, 4077–4087.

(195) W. G. Schneider, H. J. Bernstein and J. A. Pople, *The Journal of Chemical Physics*, 1958, **28**, 601–607.

(196) J. I. Melo, M. C. R. d. Azua, C. G. Giribet, G. A. Aucar and R. H. Romero, *The Journal of Chemical Physics*, 2003, **118**, 471–486.

(197) J. I. Melo, M. C. R. d. Azua, C. G. Giribet, G. A. Aucar and P. F. Provasi, *The Journal of Chemical Physics*, 2004, **121**, 6798–6808.

(198) S. Komorovský, M. Repiský, O. L. Malkina, V. G. Malkin, I. M. Ondík and M. Kaupp, *The Journal of Chemical Physics*, 2008, **128**, 104101.

(199) A. M. Kantola, P. Lantto, J. Vaara and J. Jokisaari, *Physical Chemistry Chemical Physics*, 2010, **12**, 2679–2692.

(200) J. Vaara, K. Ruud, O. Vahtras, H. Ågren and J. Jokisaari, *The Journal of Chemical Physics*, 1998, **109**, 1212–1222.

(201) S. Komorovský, M. Repiský, O. L. Malkina and V. G. Malkin, *The Journal of Chemical Physics*, 2010, **132**, 154101.

(202) P. Lantto, J. Vaara, A. M. Kantola, V.-V. Telkki, B. Schimmelpfennig, K. Ruud and J. Jokisaari, *Journal of the American Chemical Society*, 2002, **124**, 2762–2771.

(203) Y. Rusakov and I. Rusakova, *Magnetic Resonance in Chemistry*, 2018, **56**, 716–726.

(204) M. Dračínský, J. Vícha, K. Bártová and P. Hodgkinson, *ChemPhysChem*, 2020, **21**, 2075–2083.

(205) J. D. Hartman, G. M. Day and G. J. O. Beran, *Crystal Growth & Design*, 2016, **16**, 6479–6493.

(206) J. D. Hartman, R. A. Kudla, G. M. Day, L. J. Mueller and G. J. O. Beran, *Physical Chemistry Chemical Physics*, 2016, **18**, 21686–21709.

(207) J. D. Hartman, A. Balaji and G. J. O. Beran, *Journal of Chemical Theory and Computation*, 2017, **13**, 6043–6051.

(208) J. D. Hartman and G. J. O. Beran, *Solid State Nuclear Magnetic Resonance*, 2018, **96**, 10–18.

(209) B. A. Kolesov, V. S. Minkov, E. V. Boldyreva and T. N. Drebushchak, *The Journal of Physical Chemistry B*, 2008, **112**, 12827–12839.

(210) J. S. Lomas, *Magnetic Resonance in Chemistry*, 2016, **54**, 28–38.

(211) K. Sutter, G. A. Aucar and J. Autschbach, *Chemistry – A European Journal*, 2015, **21**, 18138–18155.

(212) J. Ariai and G. Saielli, *ChemPhysChem*, 2019, **20**, 108–115.

(213) J. Vícha, P. Švec, Z. Růžičková, M. A. Samsonov, K. Bártová, A. Růžička, M. Straka and M. Dračínský, *Chemistry – A European Journal*, 2020, **26**, 8698–8702.

(214) O. W. Howarth, J. Nelson and V. McKee, *Chemical Communications*, 2000, 21–22.

(215) A. Bagno, F. Rastrelli and G. Saielli, *Progress in Nuclear Magnetic Resonance Spectroscopy*, 2005, **47**, 41–93.

(216) J.-C. Hierso, *Chemical Reviews*, 2014, **114**, 4838–4867.

(217) R. Mokrai, J. Barrett, D. C. Apperley, A. S. Batsanov, Z. Benkő and D. Heift, *Chemistry – A European Journal*, 2019, **25**, 4017–4024.

(218) S. L. Dudarev, P. Liu, D. A. Andersson, C. R. Stanek, T. Ozaki and C. Franchini, *Physical Review Materials*, 2019, **3**, 083802.

(219) M. Dračínský, P. Bouř and P. Hodgkinson, *Journal of Chemical Theory and Computation*, 2016, **12**, 968–973.

(220) M. A. Blanco, M. Flórez and M. Bermejo, *Journal of Molecular Structure: THEOCHEM*, 1997, **419**, 19–27.